ANL/APS/TB-38

Experimental Facilities Division / User Program Division

TECHNICAL PROGRESS REPORT 1999-2000

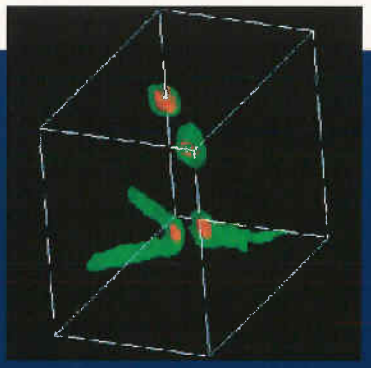

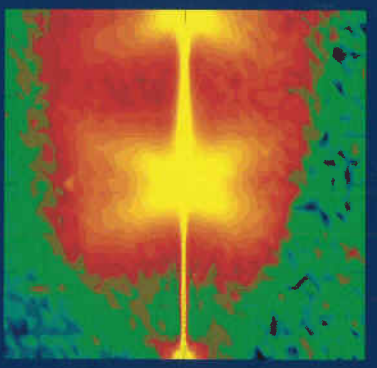

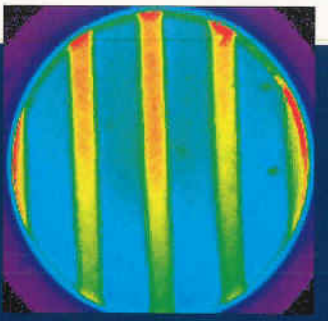

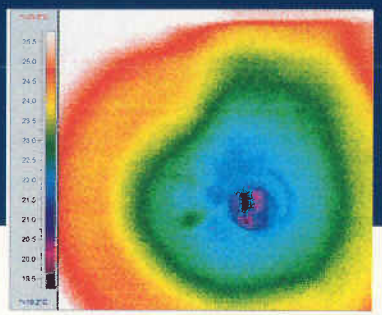

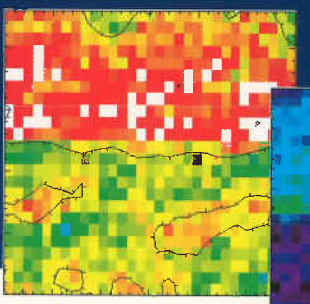

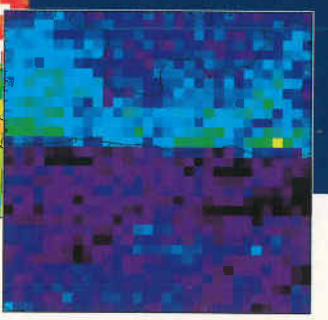

Advanced Photon Source

Argonne National Laboratory

Argonne National Laboratory, with facilities in the states of Illinois and Idaho, is owned by the United States Government and operated by The University of Chicago under the provisions of a contract with the Department of Energy.

DISCLAIMER

This report was prepared as an account of work sponsored by an agency of the United States Government. Neither the United States Government nor any agency thereof, nor The University of Chicago, nor any of their employees or officers, makes any warranty, express or implied, or assumes any legal liability or responsibility for the accuracy, completeness, or usefulness of any information, apparatus, product, or process disclosed, or represents that its use would not infringe privately owned rights. Reference herein to any specific commercial product, process, or service by trade name, trademark, manufacturer, or otherwise, does not necessarily constitute or imply its endorsement, recommendation, or favoring by the United States Government or any agency thereof. The views and opinions of document authors expressed herein do not necessarily state or reflect those of the United States Government or any agency thereof, Argonne National Laboratory, or The University of Chicago.

Available electronically at http://www.doe.gov/bridge

Available for a processing fee to U.S. Department of Energy and its contractors, in paper, from:

U.S. Department of Energy
Office of Scientific and Technical Information
P.O. Box 62
Oak Ridge, TN 37831-0062
phone: (865) 576-8401
fax: (865) 576-5728
email: reports@adonis.osti.gov

ANL/APS/TB-38

Experimental Facilities Division / User Program Division

TECHNICAL PROGRESS REPORT 1999-2000

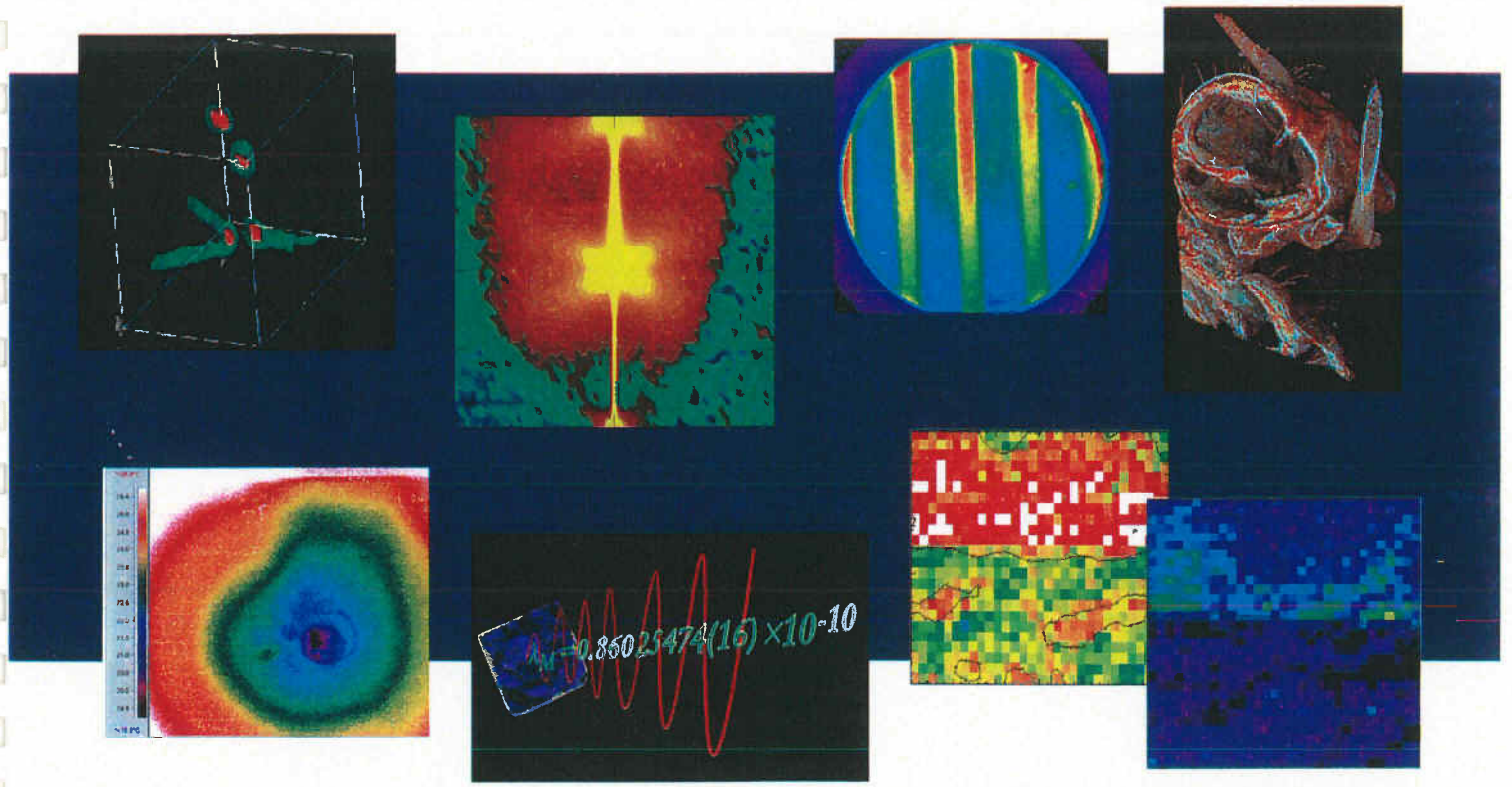

Figures:

Top, left to right: Three-dimensional image of a two-level integrated circuit interconnect obtained by scanning soft x-ray microtomography. The displayed volume is 8 µm x 5 µm x 5 µm,. ○ Charge melting and polaron collapse in $La_{1.2}Sr_{1.8}Mn_2O_7$: Recent studies carried out on beamline 1-ID-C provide important new insights into the relation of polarons to colossal magnetoresistance. ○ X-ray photoelectron image of 1 µm Pd stripes on a Si wafer. This image displays a 15 µm field of view and was acquired with a 12 bit CCD camera. ○ A rendered image from a three-dimensional tomographic cricket reconstruction, digitally cut at different planes to show the internal structures of the cricket's head.

Bottom, left to right: Image of the new white-beam photon shutter prior to accepting beam. The small purple square in the lower center of the image is the strike surface of the shutter. ○ Setting the standard for atomic scale measurements: X-ray beams from the APS and HASYLAB in Hamburg have been used to set a potential new standard of length for short distances, based on radiation from the excited nuclei of iron atoms. Further improvements may make this standard an important tool for probing the structure of matter, where physicists must gauge the separations between nuclei with an accuracy of millionths of an Ångstrom. ○ Two-dimensional mappings of a $HoFe_2$ crystal for a field of 0.43 Tesla, applied with opposite orientations. The magnitude of the field was sufficient to align the sample parallel to the applied field. The flipping ratio changed sign.

Contents

Acronyms Used vii

1 Introduction 1

1.1 Background 1
1.2 Mission of the Experimental Facilities Division 1
1.3 Mission of the User Program Division 2
1.4 XFD and UPD Organization 3
1.5 SRI CAT and R&D in Support of Users 3
1.6 APS Free-Electron Laser Developments 5
1.7 User Technical Support 6
1.8 Collaborative Work 6
1.9 Long-Term R&D Plans 7

2 SRI-CAT Beamlines, Technical Developments, and Scientific Applications ... 9

2.1 Mission of SRI CAT 9
2.2 SRI-CAT Beamline Layout and General Description of Activities 10
2.3 X-ray Imaging and Microfocusing 15
2.3.1 A New Facility: the 2-ID-E X-ray Fluorescence Microprobe 15
2.3.1.1 2-ID-E side-branch beamline 15
2.3.1.2 Optimized design 16
2.3.1.3 Performance 16
2.3.2 A High-Throughput X-ray Microtomography System 17
2.3.2.1 System architecture 17
2.3.2.2 Data acquisition system 17
2.3.2.3 Control software 19
2.3.2.4 Performance 19
2.3.2.5 Local parallel processing 20
2.3.3 Stacked Zone Plates 24
2.3.3.1 Near-field stacking of zone plates 24
2.3.3.2 Microfocusing with stacked zone plates 25
2.3.4 Imaging and Microfocusing Applications 27
2.3.4.1 Biological and medical applications 27
2.3.4.2 Environmental and geosciences 28
2.3.4.3 Nuclear materials studies 30
2.3.4.4 Nanotomography of chips 32
2.3.4.5 Noninterferometric quantitative x-ray phase imaging 34
2.3.4.6 Interferometry 39
2.4 Microfabrication and Deep X-ray Lithography 41
2.4.1 Novel X-ray Optical Elements 41
2.4.2 Zone Plate Fabrication by Focused Ion Beams 43

2.5 High-Energy X-ray Scattering 44
2.5.1 A New Bent-Crystal High-Throughput Monochromator 46
2.5.2 High-Energy Applications 47
2.5.2.1 Polaron studies 47
2.5.2.2 Confined fluids 50
2.5.2.3 High-temperature powder diffraction 52
2.6 High-Resolution X-ray Scattering 57
2.6.1 Nuclear Resonant Scattering 57
2.6.1.1 High-pressure applications 57
2.6.1.2 Biological materials and organic molecules: Dynamics of proteins 60
2.6.1.3 Thin films, multilayers, and amorphous materials 61
2.6.2 Inelastic X-ray Scattering 62
2.6.2.1 A new spectrometer with 2 meV resolution for inelastic x-ray scattering 62
2.6.2.2 Inelastic x-ray measurements on liquid aluminum 64
2.6.2.3 Investigation of collective excitation in lithium-ammonia mixtures 65
2.6.3 Fundamental Measurements 66
2.6.3.1 Normal incidence diffraction in Si and Al_2O_3 66
2.6.3.2 X-ray wavelength standard 67
2.6.3.3 Instrumentation development 68
2.7 Polarization Studies 68
2.7.1 A Microfocused Circularly Polarized X-ray Probe for Energies between 5 and 10 keV 69
2.7.2 Temperature Dependence of the X-ray Magnetic Circular Dichroism Signal at the RE L_3 Edge in $REFe_2$ 73
2.7.3 Interfacial Structure and Magnetism in Fe/Gd Multilayers 76
2.7.4 Exploring Magnetic Anisotrophy Using Polarized X-rays 77
2.7.5 Microspectroscopy and Imaging with Photoelectron Microscopy 78
2.7.6 X-ray-Excited Optical Luminescence Studies of Oxidized Porous Silicon 80
2.7.7 Changes of a Ferromagnet/Insulator Interface upon Thermal Annealing 81
2.8 Time-Resolved X-ray Techniques Development 82
2.8.1 Fuel Spray Studies 83
2.8.2 Polymer Thin-Film Dynamics and X-ray Damage 85
2.8.2.1 Polymer thin-film dynamics 85
2.8.2.2 X-ray damage in polymer thin films 86
2.8.3 Time-Resolved X-ray Absorption Near-Edge Spectroscopy (XANES) 88
2.8.4 X-ray Beam Chopper Development at SRI CAT 88
2.9 References 91

3 User Technical Support 95

3.1 Insertion Devices 95
3.1.1 Circularly Polarized Undulator 96
3.1.2 Fabrication of a New Gap Separation Mechanism for Insertion Devices 98

3.1.3 Insertion Device Vacuum Chamber Development and Fabrication 99
3.1.3.1 BESSY insertion device vacuum chamber fabrication 99
3.1.3.2 DESY FEL vacuum chamber fabrication 99
3.1.3.3 SLS insertion device vacuum chamber design and fabrication 99
3.2 High-Heat-Load-Optics 100
3.2.1 Cryogenically Cooled Silicon Monochromators 100
3.2.2 Diamond High-Heat-Load Tests 102
3.3 Synchrotron Radiation Instrumentation Engineering 104
3.3.1 Undulator-Only Front End 104
3.3.2 Double-Undulator Split Beamlines 105
3.3.3 Impact Studies on the Bending Magnet Front Ends for a 6-mm Lattice Offset 108
3.3.4 Beamline Components Development 109
3.3.4.1 New XBPM development 109
3.3.4.2 Wide-angle monochromatic photon shutter 109
3.3.4.3 Technology developments for white-beam components 109
3.3.4.4 High-resolution and precision instrumentation 113
3.4 X-ray Optics Fabrication and Metrology 115
3.4.1 X-ray Optics Metrology Laboratory 116
3.4.1.1 Recent enhancements in the metrology cleanroom 116
3.4.1.2 Mirror metrology 116
3.4.1.3 Atomic force microscope 117
3.4.2 International Workshop on Metrology for X-ray and Neutron Optics 118
3.4.3 Deposition Laboratory 119
3.4.3.1 Microfocusing mirrors 121
3.4.3.2 Graded multilayer deposition 122
3.4.3.3 Double-multilayer monochromator for beamline 2-BM 123
3.4.3.4 Reactive sputter deposition 123
3.4.4 Fabrication Laboratories 124
3.4.5 X-ray Characterization Laboratory 125
3.5. Beamline Controls and Data Acquisition 126
3.5.1 Overview and General Remarks 126
3.5.2 Scan-Related Software 127
3.5.3 EPICS String-Sequence Record 129
3.5.4 EPICS Optical Table Record 129
3.5.5 Java Interface to EPICS Channel-Access Library 129
3.5.6 Conversion to EPICS Message Passing Facility 129
3.5.7 Merging Third-Party Software 129
3.5.8 CCD Image-Grabber Software 130
3.5.9 Insertion Device Support 131
3.5.10 Progress toward a Standard Scripting Language 131
3.5.11 Parameter Management Software 131
3.5.12 Motor Support 131
3.5.13 System/Network Administration 132
3.6 References 132

4. Major Plans for the Future 135

4.1 Plans for Future Instrumentation and Technique Development 135
4.1.1 X-ray Imaging and Microscopy 135
4.1.2 High-Energy X-ray Scattering 135
4.1.3 High-Resolution X-ray Scattering 135
4.1.4 Polarization Techniques 136
4.1.5 Time-Resolved Program 136
4.2 User Support 137
4.2.1 Synchrotron Radiation Instrumentation Engineering 137
4.2.2 Insertion Devices 137
4.2.3 Optics Fabrication and Metrology 137
4.2.4 High-Heat-Load Optics 138
4.3 New Initiatives 138
4.3.1 Center for Nanoscale Materials 138
4.3.2 Inelastic X-ray Scattering (IXS) CAT 139
4.3.3 Normal Incidence Diffraction Beamline at Sector 1 139
4.3.4 High-Energy X-ray (HEX) CAT 140

Appendix 1: 1999 & 2000 XFD and UPD Publications 141

Appendix 2: 1999-2000 Presentations by XFD and UPD Staff 155

Appendix 3: SRI CAT 163

Acronyms Used

2D	Two Dimensional
3D	Three Dimensional
ADC	Analog-to-Digital Converter
ADP	Atomic Displacement Parameters
AFM	Atomic Force Microscope
ANL	Argonne National Laboratory
AOD	APS Operations Division
APD	Avalanche Photodiode
APS	Advanced Photon Source
ASD	Accelerator Systems Division
ASRP	Australian Synchrotron Radiation Project
BA	Born Approximation
BCDA	Beamline Controls and Data Acquisition
BCTF	Beamline Components Test Facility
BESSY	Berliner Elektronenspeicherring-Gesellschaft fur Synchrotronstrahlung (Germany)
BINP	Budker Institute of Nuclear Physics (Russia)
BM	Bending Magnet
BWR	Boiling Water Reactors
CAT	Collaborative Access Team
CCD	Charge Coupled Device
CCST	Coordination Council for Science and Technology
CMR	Colossal Magnetoresistance
CNM	Center for Nanoscale Materials
CPU	Circularly Polarized Undulator
CVD	Chemical Vapor Deposition
DAC	Digital-to-Analog Converter
DESY	Deutsches Elektronen-Synchrotron (Germany)
DMM	Double-Multilayer Monochromator
DOE	Department of Energy
DOS	Density of States
EDX	Energy Dispersive X-ray
EPICS	Experimental Physics and Industrial Control System
ESRF	European Synchrotron Radiation Facility (France)
FEL	Free-Electron Laser
FIB	Focused Ion Beam
FM	Ferromagnetic

FOE	First Optics Enclosure
FWHM	Full Width Half Maximum
FZP	Fresnel Zone Plate
GPIB	General Purpose Interface Bus
GSAS	General Structure Analysis System
HASYLAB	Hamburger Synchrotronstrahlungslabor (Germany)
HDF	Hierarchical Data Format
HEX	High-Energy X-ray
HHL	High Heat Load
HP	High Pressure
I	Insulating Layer
ID	Insertion Device
IDL	Interactive Data Language
IXS	Inelastic X-ray Scattering
JCA	Java Channel Access
KB	Kirkpatrick Baez
KEK	Japanese High Energy Accelerator Research Organization
LCLS	Linac Coherent Light Source
LDRD	Laboratory Directed Research & Development
LEGe	Low-Energy Germanium
LEUTL	Low-Energy Undulator Test Line
LLL	Triple Laue
LTP	Long Trace Profiler
Mb	Myoglobin
MDA	Multidimensional Archive
MCS	Mathematics and Computer Science Division at ANL
ML	Multilayer
MPF	Message Passing Facility
MPI	Message Passing Interface
MR	Magnetoresistance
MRAM	Magnetic Random Access Memory
MSD	Materials Science Division at ANL
MTJ	Magnetic Tunneling Junctions
Nano	Nanoscience
NIST	National Institute of Standards and Technology
NRIXS	Nuclear Resonant Inelastic X-ray Scattering
NRS	Nuclear Resonant Scattering
NSLS	National Synchrotron Light Source

OFM	Optics Fabrication and Metrology
OMCTS	Octamethylcyclotetrasiloxane
ORNL	Oak Ridge National Laboratory
OSA	Order-Sorting Aperture
PEEM	Photoelectron Microscope
PEM-FC	Polymer-Electrolyte Membrane Fuel Cell
PID	Proportional Integral Differential
PLY	Partial Luminescence Yield
PMMA	Polymethylmethacrylate
PTBA	Poly(Tert-Butyl Acrylate)
PWR	Pressurized Water Reactors
PZT	Piezoelectric Transducer
R&D	Research & Development
RE	Rare Earth
SAM	Self-Assembled Monolayers
SASE	Self-Amplified Spontaneous Emission
SFA	Surface Force Apparatus
SIRT	Simultaneous Iterative Reconstruction Technique
SLS	Swiss Light Source (Switzerland)
SPring	Super Photon Ring – 8 GeV (Japan)
SRI	Synchrotron Radiation Instrumentation
SSRL	Stanford Synchrotron Radiation Laboratory
STXM	Scanning Transmission X-ray Microscope
TEM	Transmission Electron Microscopy
TFY	Total X-ray Fluorescence Yield
TLY	Total Luminescence Yield
TM	Transition Metal
TTU	Topo Test Unit
UPD	User Program Division
VUV	Vacuum Ultraviolet
XANES	X-ray Absorption Near-Edge Spectroscopy
XAS	X-ray Absorption Spectroscopy
XBPM	X-ray Beam Position Monitor
XFD	Experimental Facilities Division
XMCD	X-ray Magnetic Circular Dichroism
XMLD	X-ray Magnetic Linear Dichroism
XMLL	X-ray Magnetic Linear Loop
XRF	X-ray Fluorescence
XRMS	X-ray Resonant Magnetic Scattering

1 INTRODUCTION

1.1 Background

In October 1999, the two divisions of the Advanced Photon Source (APS), the Accelerator Systems Division (ASD) and the Experimental Facilities Division (XFD), were reorganized into four divisions (see high-level APS organizational chart, Fig. 1.1). In addition to ASD and XFD, two new divisions were created, the APS Operations Division (AOD), to oversee APS operations, and the User Program Division (UPD), to serve the APS user community by developing and maintaining the highest quality user technical and administration support. Previous XFD *Progress Reports* (ANL/APS/TB-30 and ANL/APS/TB-34) covered a much broader base, including APS user administrative support and what was previously XFD operations (front ends, interlocks, etc.) This *Progress Report* summarizes the main scientific and technical activities of XFD, and the technical support, research and development (R&D) activities of UPD from October 1998 through November 2000.

The report is divided into four major sections, 1) Introduction, 2) SRI-CAT Beamlines, Technical Developments, and Scientific Applications, 3) User Technical Support, and 4) Major Plans for the Future. Sections 2 and 3 describe the technical activities and research accomplishments of the XFD and UPD personnel in supporting the synchrotron radiation instrumentation (SRI) collaborative access team (CAT) and the general APS user community. Also included in this report is a comprehensive list of publications (Appendix 1) and presentations (Appendix 2) by XFD and UPD staff during the time period covered by this report.

The organization of section 2, SRI CAT Beamlines, Technical Developments, and Scientific Applications has been made along scientific techniques/disciplines and not "geographical" boundaries of the sectors in which the work was performed. Therefore items under the subsection X-ray Imaging and Microfocusing could have been (and were) performed on several different beamlines by staff in different divisions. The management of SRI CAT encourages this type of cross-fertilization among the staff responsible for different beamlines and feels that this approach will ultimately result in the best scientific output.

The section on User Technical Support, on the other hand, is laid out more closely along group lines, namely insertion devices, high-heat-load optics, instrumentation engineering, optics fabrication and metrology, and beamline controls and data acquisition.

1.2 Mission of the Experimental Facilities Division

The mission of XFD is to develop and build state-of-the-art synchrotron radiation instrumentation and use it in a safe and environmentally sound manner to conduct world-class research at the forefront of

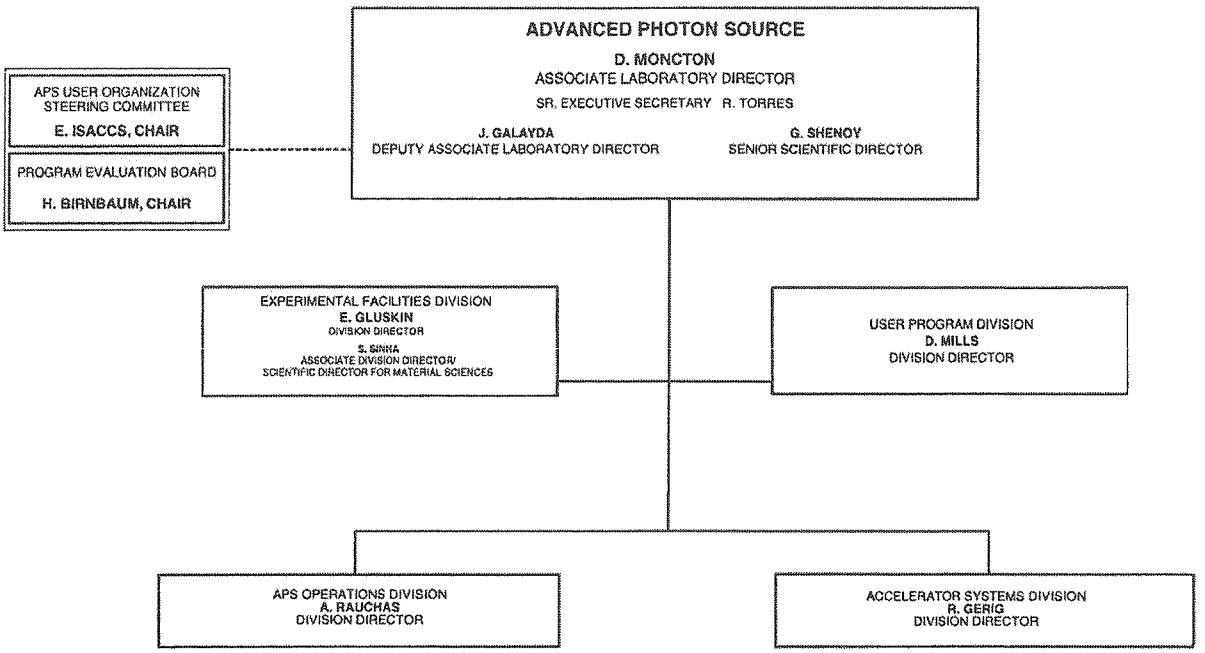

Fig. 1.1. High-level APS organizational chart showing the four divisions.

science and technology. This will enable the success of the APS as a preeminent synchrotron radiation user facility.

Specifically, the mission of XFD is to:

- Develop novel ways of using synchrotron radiation to explore the frontiers of x-ray physics and new scientific applications.
- Develop and build novel radiation sources for the APS and for the next generation of synchrotron radiation sources.
- Develop and build innovative instrumentation for front ends, beamlines, and experiment stations, for the APS and for the next generation of synchrotron radiation sources.
- Provide continuous technical support to APS users by sharing the technical capabilities, as well as the scientific and technical developments of the division.

1.3 Mission of the User Program Division

The mission of UPD is to serve the APS user community by developing and maintaining the highest quality user technical and administration support and through innovative R&D in support of the scientific programs at the APS.

This mission can be best achieved through the following principles:

- Developing a thorough understanding of the users' needs and goals and striving to exceed them.
- Creating an enriching, fulfilling, and collaborative R&D environment for the UPD staff and APS users to facilitate the development of new synchrotron radiation instrumentation and techniques that will enhance and ensure the long-term success of the APS.
- Engendering new areas of scientific research at the APS and educating and nurturing new research communities in the uses and applications of synchrotron radiation.
- Assuring the safety and well-being of APS users, APS/UPD personnel, visitors, and the environment.

1.4 XFD and UPD Organization

The XFD and UPD organization has two functional areas as shown in Fig 1.2. This *Progress Report* (and the review) will cover the technical support and R&D areas. These include the XFD and UPD organization structures, shown in Fig 1.3, which define various groups by specialization. This structure enables excellent communication and interaction across the boundaries of the groups to meet both the groups' and APS's objectives. Although most activities within a division are line managed, SRI CAT, which pulls its membership from both divisions (as well as from outside Argonne National Laboratory), is managed in a matrix fashion.

Although neither of these divisions has direct responsibility for the day-to-day operation of the facility, needless to say there is close communications between XFD/UPD and ASD/AOD. SRI CAT staff provide first-hand information to APS management through the XFD and UPD division directors on the performance of the storage ring. This information is used as diagnostics by the operations staff for further enhancement of the storage ring performance.

1.5 SRI CAT and R&D in Support of Users

The SRI CAT divides its membership into two categories, Developers and Scientific Members. Developers are financial contributors to the SRI CAT and consist of members from XFD and UPD, staff from several U.S. universities and national laboratories (X-ray Physics Group), and members of the Australian Synchrotron Radiation Project (ASRP). Scientific Members are non-paying members that are proposed by the Developers as close scientific collaborators. (A list of Developers and Scientific Members of the SRI CAT during this time period can be found in Appendix 3.) Through Scientific Members, SRI CAT has been able to reach out to a larger community to draw on their scientific expertise to further enhance the scientific output of the CAT.

SRI CAT Developers have made a major impact on the development of new synchrotron radiation optics, instrumentation, and techniques and continue to provide R&D support, advice, and guidance to the other APS CATs in these areas. And over the past two years, Scientific Members of SRI CAT have participated extensively with the XFD and UPD staff in performing

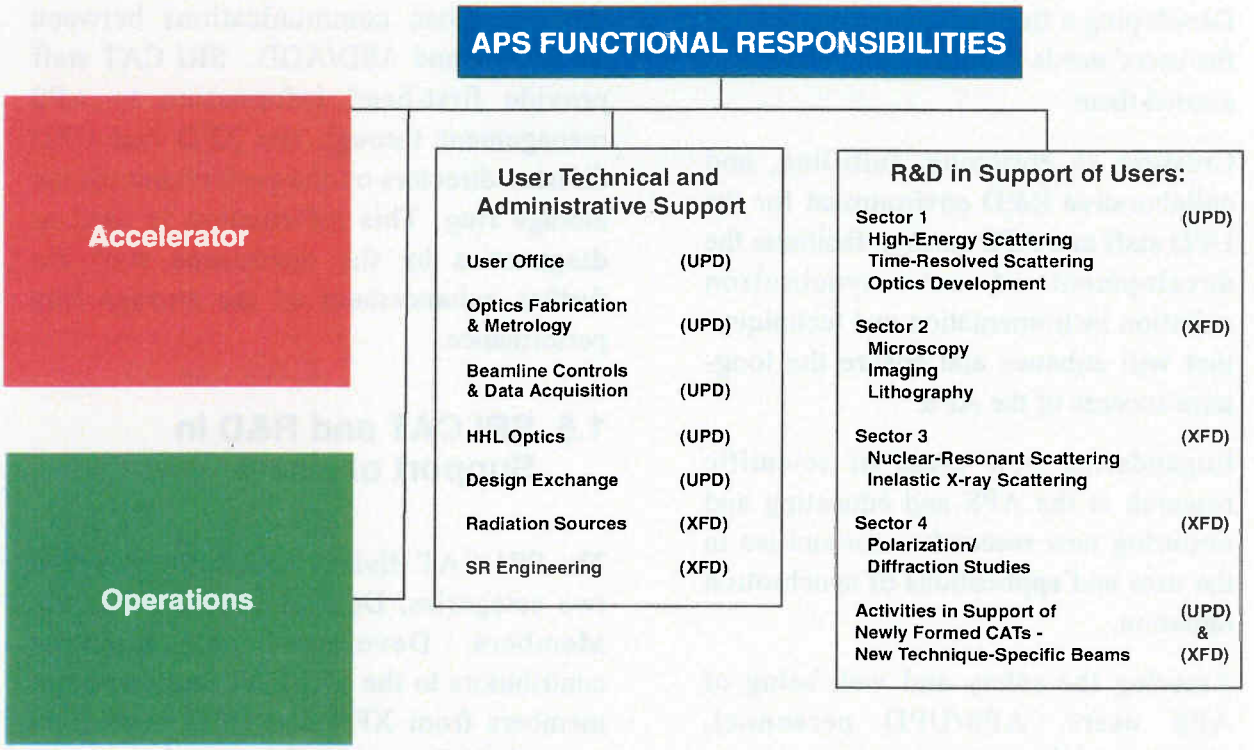

Fig. 1.2. APS functional responsibilities. This report will cover: user technical support and R&D in support of user operations and science.

frontier scientific research utilizing these new instruments and techniques. More details of the accomplishments of SRI CATcan be found in the next section of this report.

Besides instrumentation development, SRI CAT has served the synchrotron radiation community in other ways as well. Although SRI CAT is not directly involved in APS operations, it has made considerable contributions in this area too. SRI CAT often serves as a test-bed for new accelerator concepts, such as the canted undulator scheme for producing two beamlines from a single straight section which we have implemented in sector 4. The SRI CAT played an important part in better understanding the effect of top-up on photon beam stability and how these effects can be mitigated through gating techniques. And recently the storage ring was reconfigured in sectors 2, 3, and 4 to implement the so-called Decker distortion for improved insertion device beam position monitor reliability that should eventually lead to improved beam stability through the development of local feedback schemes.

The SRI CAT was the first CAT to accept independent investigator proposals for beam time, and, during the time covered by this report, we have hosted approximately 120

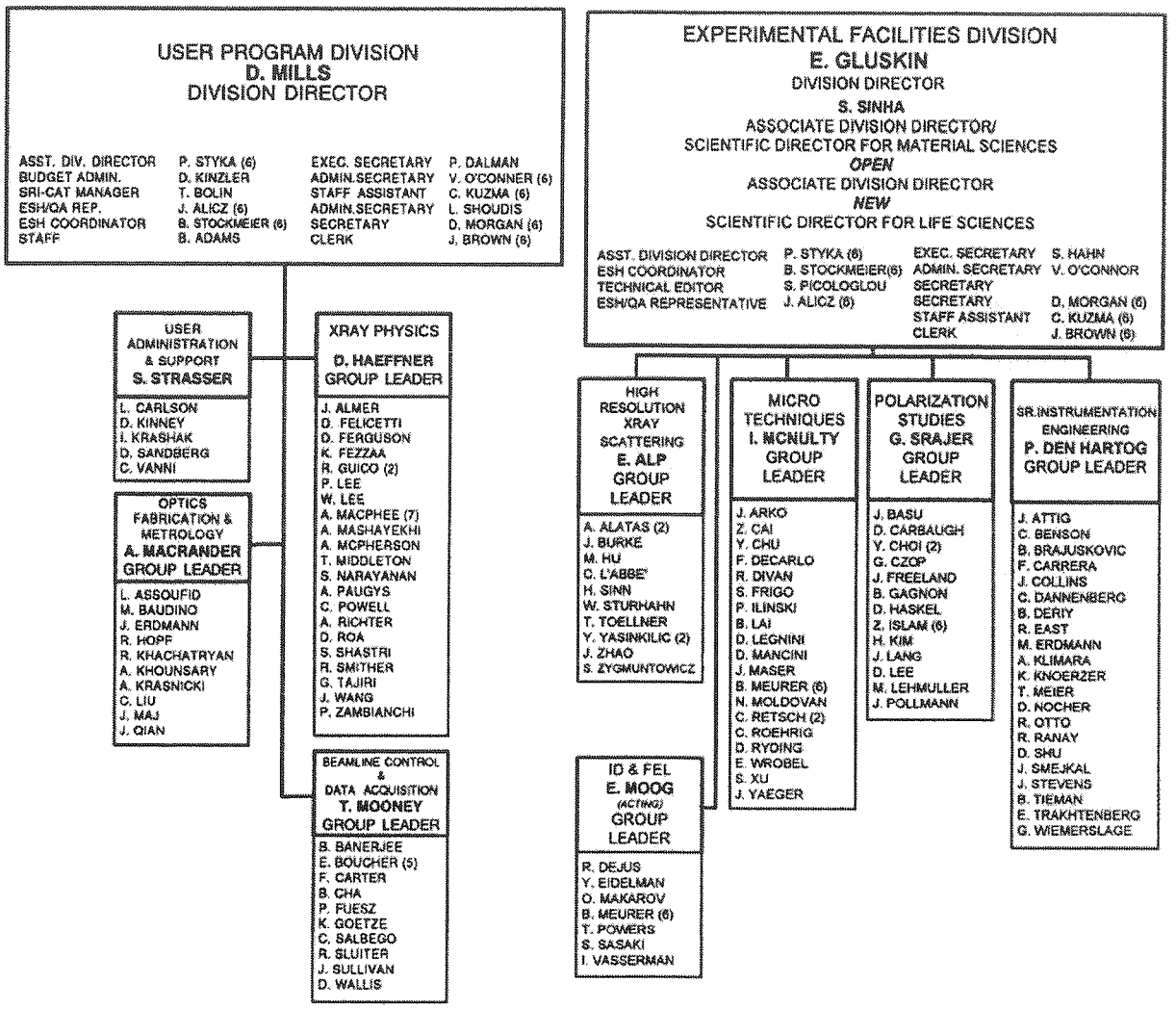

Fig. 1.3. UPD and XFD Organizational Charts.

independent investigators on our beamlines. Members of SRI CAT have also played important roles (Scientific Co-Director and Laboratory Coordinator) in the development and running of the National School for Neutron and X-ray Scattering, which has been hosted by Argonne National Laboratory (ANL) the last two summers. The goal of the school is to provide training for graduate students in the utilization of national user facilities, such as the APS. In addition to the organizational aspects of the school, many of the SRI CAT staff lectured and participated in the laboratory experiments that were performed on APS beamlines.

1.6 APS Free-Electron Laser Developments

In the last several years, the APS has been developing a new type of radiation source based on the self-amplified spontaneous

emission (SASE) process. The synchrotron radiation community recognizes that this type of source ultimately will be the next-generation synchrotron radiation source. Previous XFD *Progress Reports* contained information on the status of these developments.

In close collaboration with ASD, XFD continues to play a major part in the APS efforts to develop, characterize and use a novel SASE free-electron laser (FEL) source as a basis for the next-generation of synchrotron radiation sources. Recently it was a remarkable technical breakthrough in this area when for the first time the record high amplification has been achieved and experimental observation of the saturation process took place. XFD staff contributed to this success by designing and building the undulator-based amplifier and radiation diagnostics equipment.

Although in the last two years these activities have been a substantial part of XFD effort, they will not be covered in this report. A special comprehensive report on the SASE FEL will be generated by ASD and XFD in the near future.

1.7 User Technical Support

User technical support is distributed between the Experimental Facilities and User Program Divisions. The role of the user technical support groups is not only to provide services to users on a daily basis but also to anticipate future problems that might arise and to initiate the appropriate R&D programs now so that solutions can be found in a timely manner. Anticipation of future problems can only be achieved if the technical groups are in close contact with the research scientists, such as those of SRI CAT. This close integration of the SRI CAT members and technical support staffs has been achieved by distributing staff from both activities into XFD and UPD and not isolating the two activities in two separate divisions.

X-ray optics support, the APS Design Exchange, and support for beamlines controls is located in UPD, while insertion device development and beamline component engineering is performed primarily in XFD.

1.8 Collaborative Work

The XFD and UPD actively collaborate with other divisions within ANL and with other synchrotron radiation facilities. One of the formal ways to develop collaborations within the laboratory is through the use of Laboratory Directed Research and Development (LDRD) funds. One type of LDRD, the Coordination Council for Science and Technology (CCST) encourages collaborations between basic and applied programs, and we have participated in that program through a proposal entitled "Application of Synchrotron Radiation for Diesel Fuel Spray Characterization." Another funded LDRD proposal, "High-Throughput Biomolecular Structure Determination," has members from both XFD and UPD along with staff from the Biological Sciences, Mathematics and Computer Science, and Environmental Research Divisions. Similarly the "X-ray Magnetic Microscopy Development" LDRD was coauthored by SRI CAT staff and

Materials Science Division (MSD) personnel.

The XFD and UPD also received funding through the "4th-Generation Light Source Development" LDRD. This funding permitted collaboration with other national laboratories and international collaborations as well. As a result of collaborations with Stanford Synchrotron Radiation Laboratory (SSRL) on the Linac Coherent Light Source (LCLS) project and with Hamburger Synchrotronstrahlungslabor (HASYLAB) on the TESLA project, novel insertion devices (IDs) and ID vacuum chambers have been developed. In collaboration with the TESLA FEL facility at Deutsches Elektronen-Synchrotron (DESY) a conceptual design and cost estimate for a fourth-generation beamline has been developed. A similar collaboration has recently been undertaken with the LCLS Project.

Non-LDRD funded collaborations include those with Berliner Elektronenspeicherring-Gesellschaft für Synchrotronstrahlung (BESSY) and the Swiss Light Source (SLS) for the development and construction of ID vacuum chambers for these facilities. And several high-heat-load front-end components have been developed for the European Synchrotron Radiation Facility (ESRF) and Super Photon Ring – 8 GeV (SPring-8) in Japan. We also have an ongoing collaboration with the National High Magnetic Field Laboratory to explore the possibility of developing a high magnetic field facility on one of the SRI CAT beamlines.

1.9 Long-Term R&D Plans

The long-term R&D plans for the technical staff of both divisions fall into three categories, continued cutting-edge instrumentation and technique development to pursue state-of-the-art science in sectors 1-4, conceiving and designing "second-generation" beamlines for proposed new CATS at the APS, and preparing the way with both instrumentation and scientific applications for a fourth-generation synchrotron radiation source, namely an x–ray FEL.

Keeping the quality of the instrumentation and technique development on the SRI CAT at a world-class status will remain a high priority within XFD and UPD. We look forward to the commissioning of the soft x–ray circularly polarized undulator (CPU) and to improvements in high-energy-resolution monochromator and analyzer development for inelastic x-ray scattering. Considerable effort will be applied to push the current x-ray microprobes into the realm of nanoprobes. Development of the backscattering beamline on sector 1 will continue for use in fundamental studies of the physics of Bragg scattering at exactly 90° and the applications of such a backscattered beam. These and other new instrument developments will permit the staff to continue to pursue forefront science and become respected scientific innovators and leaders in their fields.

Several of the SRI CAT staff have become involved with newly formed CATS, such as the inelastic x-ray scattering (IXS) CAT, the

high-energy x-ray (HEX) CAT, and the nanoscience (Nano) CAT. The instrumentation and techniques around which all three of these CATs are based has been developed at SRI CAT. But rather than duplicate an existing beamline design for these proposed CATs, we plan to build on the experience gained in construction and operation of SRI CAT beamlines to develop "second-generation" beamlines for these CATs with source and beamline characteristics improved over the existing APS beamlines. These new beamlines will require R&D on specialized insertion devices, improved optical components, and enhanced instrumentation development. Because of the close relationship between these proposed beamlines and the current SRI CAT lines, much of the R&D on the new beamline components can be performed on the existing SRI CAT beamlines while the new beamlines are under construction.

Anticipating that the LCLS construction project will be funded, we are laying the foundations for our involvement in this project and eventually in a fourth-generation light source facility. In that regards, we plan to continue R&D programs that will keep us in the forefront of the science and technology required for these projects. This includes insertion device development, optics for x–ray FELs, ultrafast pump/probe techniques, and the use and applications of fully coherent x-ray beams.

These are a few of the future technical R&D challenges that we see on the horizon. An equal challenge will be how to accomplish this R&D in a way so as to maintain our high level of operational support for scientists using SRI CAT and the overall technical support for the APS user community.

2 SRI-CAT BEAMLINES, TECHNICAL DEVELOPMENTS, AND SCIENTIFIC APPLICATIONS

2.1 Mission of SRI CAT

The SRI CAT is composed of members from XFD and UPD, as well as non-APS researchers. These outside members are divided into two categories, Developers, who provide financial support, and Scientific Members, who bring intellectual capital to the CAT. A current list of SRI-CAT members can be found in Appendix 3.

The stated mission of the SRI CAT is:

> To conduct R&D activities towards the improvements of insertion devices, standard components, high-heat-load optics, and other novel x-ray optical components, and to develop innovative techniques useful to the entire community of APS CATs.
>
> To develop and implement strategic instrumentation programs that will open up new areas of research at the APS.
>
> To attract, educate, and foster new research communities in the uses for and applications of synchrotron radiation.

The SRI CAT continues to develop novel instrumentation that is of use to the APS community. In addition the SRI CAT still serves as a test bed for accelerator developments, such as top-off studies and lattice distortions to improve x–ray beam position monitor performance, and a variety other technical components.

More recently, our emphasis has evolved towards the latter two points of the mission statement. In that regard, we are proud to say that our strategic instrumentation programs, namely the hard x-ray microfocusing program, inelastic scattering program and 0.5 to 3 keV program have flourished. In fact these programs have nucleated new CATs, the IXS CAT, for instance, and have served as a valuable resource for the development of the Nano-CAT. The success of the polarization program has lead us to spin off a beamline dedicated to the use and applications of polarized x-rays from 0.5 to 100 keV, and our experience gained in the area of use and applications of high-energy x-rays has prompted us to consider a beamline dedicated to this purpose.

From the beginning of our beamline operations, SRI CAT has provided beam time to other CATs for testing beamline components and to jumpstart their core science programs while their beamlines are under construction. We continue to provide this opportunity to some of the newer CATs, most recently, the high pressure (HP) CAT.

We believe we have also been successful in educating existing communities and bringing in new communities to use synchrotron radiation. Members of SRI CAT have played important roles (Scientific Co-Director and Laboratory Coordinator) in the development and running of the National School for Neutron and X-ray Scattering,

hosted by ANL the last two summers. The goal of the school is to provide training for graduate students in the utilization of national user facilities such as the APS. In addition to the organizational aspects of the school, many of the SRI CAT staff participated in the laboratory experiments that were performed on the APS beamlines. Inside Argonne, we have nurtured collaborations with the Energy Systems Division at ANL to develop novel techniques for the study of diesel fuel spray for automotive applications and the Environmental Division to look at interesting specimens, including a strand of Beethoven's hair. We routinely host researchers from the fields of biology, environmental science, and the medical sciences on our imaging and microfocusing beamlines, and, under our guidance, scientists from the Adler planetarium, The University of Chicago Oriental Institute, and the Field Museum have all participated in experiments on the SRI CAT beamlines.

2.2 SRI-CAT Beamline Layout and General Description of Activities

With the completion of the construction of the sector 4 insertion device beamline, the SRI CAT now operates four insertion device lines and two bending magnet lines in four sectors. All the beamlines in sectors 1, 2 and 3 are fully operational and open to CAT members and independent investigators alike. During the last 24 months, we have hosted over 120 independent investigators on the beamlines.

Both the insertion device beamline and the bending magnet beamline have been constructed in sector 1 (see Fig. 2.1.). These beamlines were originally conceived as place of development for optics (high heat load, polarizing, high energy, etc.) and instrumentation related to time-resolved experiments. A standard APS 3.3-cm undulator (2.4 m long) is the radiation source, although we have temporarily installed a second standard undulator for high-heat-load optics testing. With the program in high-heat-load optics decreasing and the polarization program moved to sector 4, the mission of this sector has become slightly more directed. Optics development still continues, but high-heat-load testing has given way in large part to programs in x-ray interferometry and optics/instrumentation development for fourth-generation FEL sources. The major thrust in the high-energy optics program is to increase flux through the use of bent Laue monochromators. Use of the insertion device beamline for high-energy applications continues to grow, in fact to the point where we feel the time is ripe for the development of a sector devoted to the use of high-energy x-rays. This beamline continues to remain the home of the SRI CAT time-resolved program with a dispersive monochromator in place on the bending magnet beamline. An interesting synergy has emerged between the high-energy program and the time-resolved program with the application of high-energy, time-resolved powder diffraction to study phase transitions at temperatures in excess of 1000 °C.

Sector 2 (see Fig. 2.2) is the home of two of SRI CAT's strategic instruments, the hard x-ray microprobe and soft x-ray imaging

programs. Two independent (collinear) insertion devices provide the radiation for those programs, a standard APS undulator for the hard x-ray activities and a one-of-a-kind 5.5-cm-period undulator for soft x-rays. This beamline is run either with the hard x–ray undulator or the soft x-ray undulator, i.e., not simultaneously. In the past, the soft x-ray beam was further split between a spectroscopy/reflectivity program and the imaging program. The spectroscopy/ reflectivity branch line was recently relocated to sector 4 thus allowing increased beam time to the flourishing x-ray microprobe and imaging programs. The x–ray microprobe and soft x-ray imaging are powerful research tools and have been applied to the study of infectious disease, drug effectiveness, contaminated environments, and integrated circuits. Recently, the x-ray microscopy program was recognized by *Research and Development* magazine with an R&D 100 award for the development of a hard x-ray scanning microprobe.

The SRI CAT inelastic x-ray scattering program resides in sector 3 (see Fig. 2.3). The program has two major components, inelastic nuclear resonant scattering (NRS) and milli-eV (meV) resolution inelastic x-ray scattering. The meV resolution team has recently completed the first phase for the development of a new 2 meV spectrometer for momentum-resolved inelastic x-ray scattering. Users have been scheduled on a regular basis on this new instrument, although further development work is still a strong component of the schedule. The pursuit for high-energy resolution continues, and a world record of 0.143 meV at 24 keV has been achieved, corresponding to a $\Delta E/E$ of less than 6×10^{-9}. This program has generated a considerable user base, and plans are now being laid out to develop a dedicated inelastic x-ray scattering sector. Beam time for inelastic NRS experiments is also heavily subscribed. Applications of NRS have been extended to the study of dynamical properties of biological materials and of materials under high pressure with the use of a Kirkpatrick Baez mirror pair that can focus the 2 meV beam to less than 5 microns. This beamline currently has two 2.7 cm undulators in the straight section, one 2.4 m in length and the other 2.0 m long. The bending magnet beamline has not been constructed on this sector.

The focus of the sector 4 program is use of polarized x-rays from 0.5 to 100 keV. This is accomplished on sector 4 through a first in synchrotron radiation technology: the operation of two independent beamlines from two canted undulators in a single storage ring straight section (see Fig. 2.4). A 270 microradian separation is introduced between the two IDs, a standard 3.3 cm undulator for the production of hard x-rays and a special CPU for the soft x-ray regime. The 3.3 cm ID is installed and operational, and we are hoping for a December installation of the CPU. X-ray polarization-based scattering studies have led to a collaboration with the microprobe scientists of sector 2 to produce a circularly polarized x-ray microprobe for the study of domains in magnetic materials, particularly buried magnetic materials. Studies of magnetic circular dichroism and magnetic roughness are also underway on sector 4. As with sector 3, the bending magnet beamline at sector 4 has not been built.

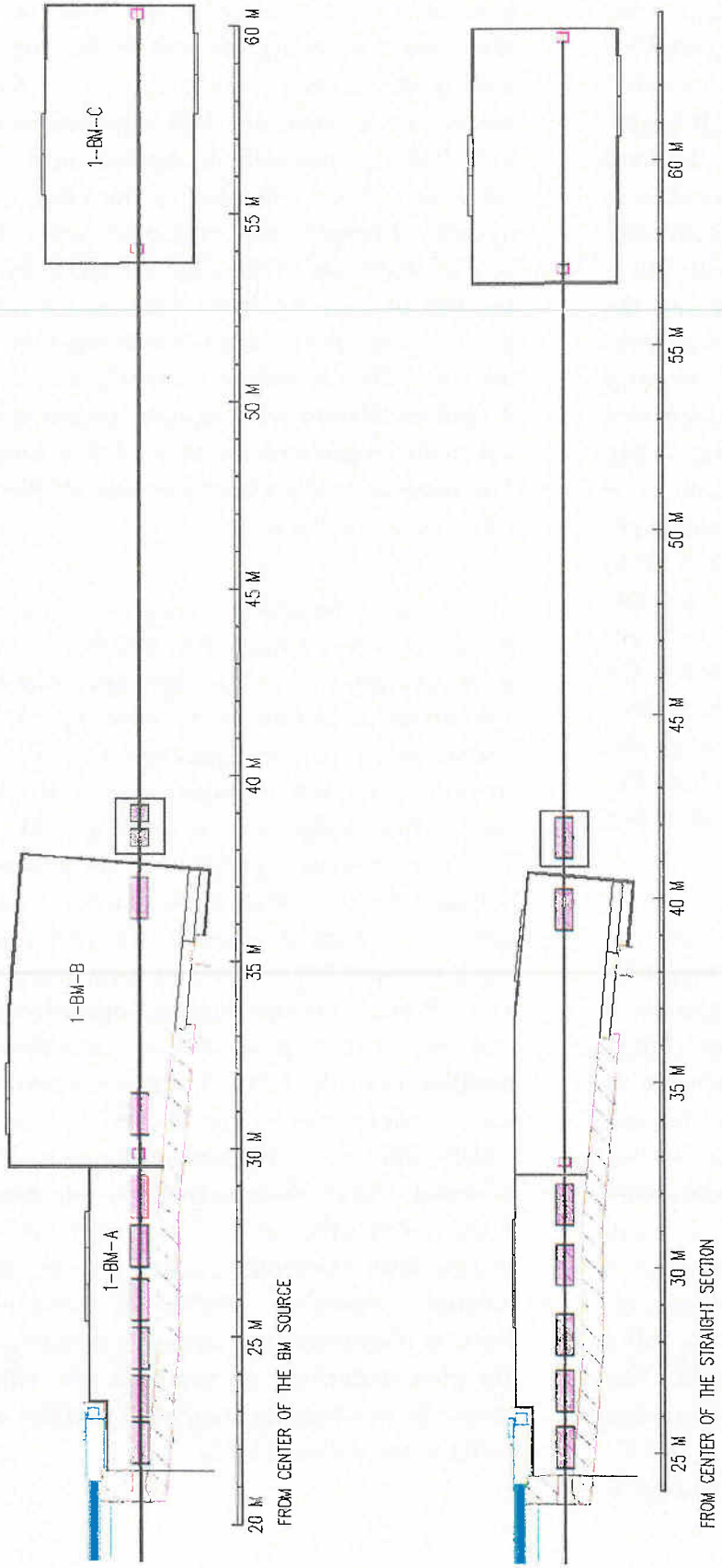

Fig 2.1. Top – General layout of bending magnet beamline at sector 1. Bottom – General layout of insertion device beamline at sector 1.

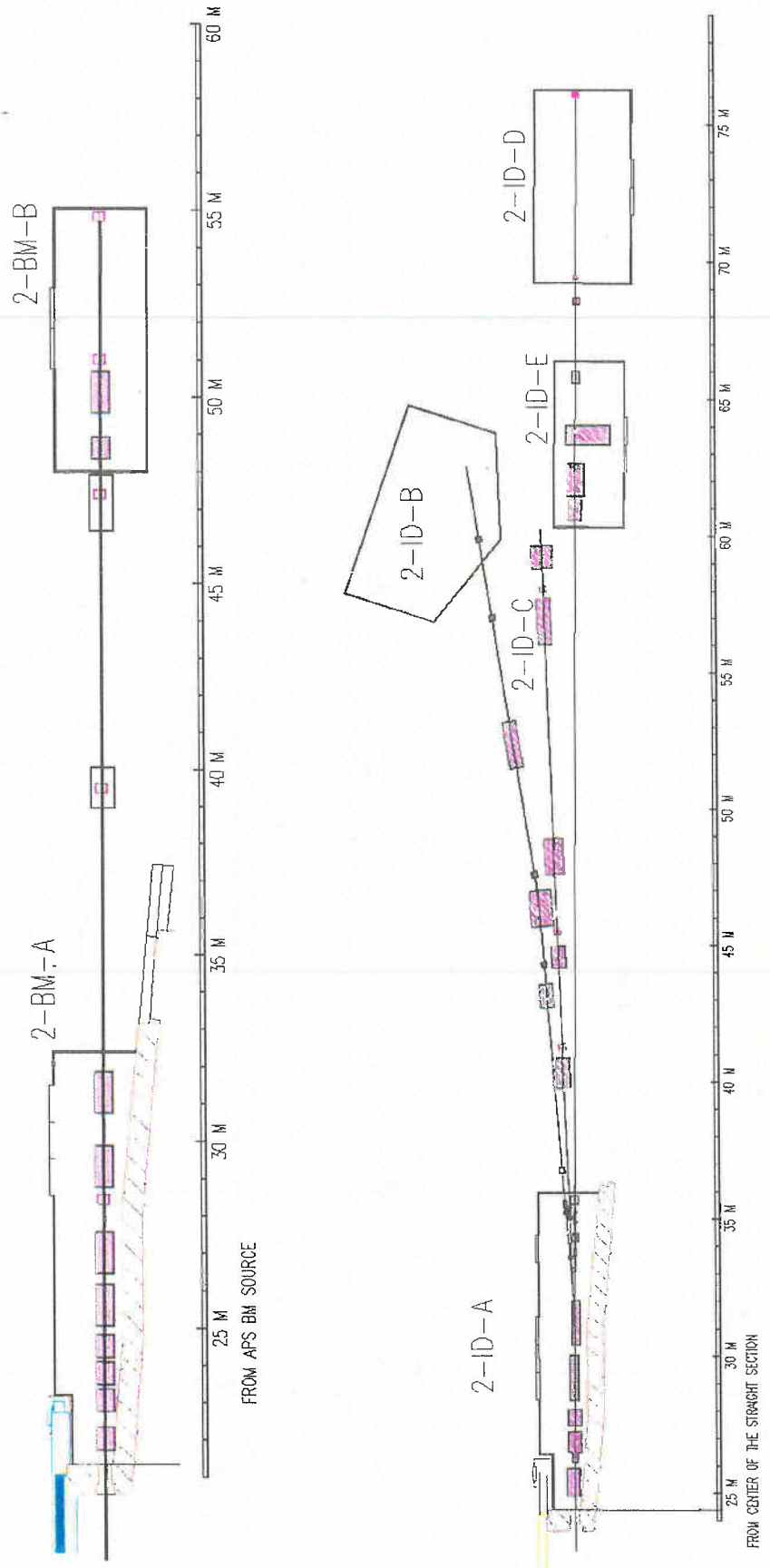

Fig 2.2. Top – General layout of bending magnet beamline at sector 2. Bottom – General layout of insertion device beamline at sector 2.

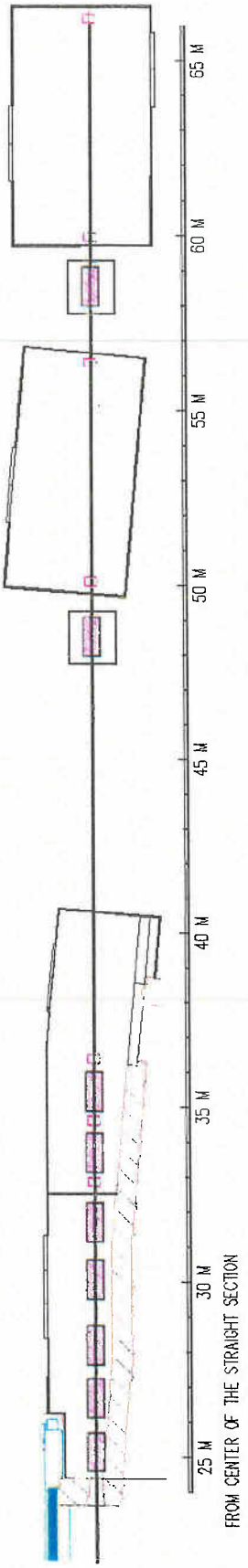

Fig 2.3. General layout of insertion device beamline at sector 3.

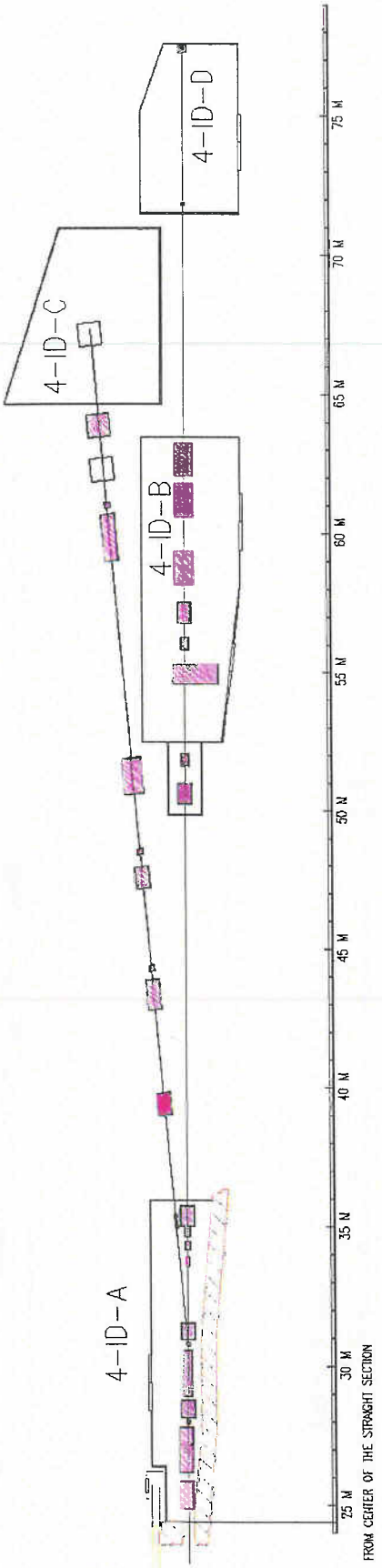

Fig 2.4. General layout of insertion device beamline at sector 4.

2.3. X-ray Imaging and Microfocusing

The thrust of the x-ray imaging and microfocusing program in SRI CAT is to develop state-of-the-art x-ray focusing optics and techniques, and to apply them to outstanding problems in the materials, environmental, biological, and biomedical fields. Our effort in these areas is roughly evenly split between development of novel microfocusing and imaging optics, instrumentation, and techniques with unprecedented capabilities that capitalize on the high brilliance of APS sources, and their application to problems that are either less efficiently studied or simply cannot be addressed by other means. The most mature and heavily subscribed of these instruments are the hard and soft *x-ray scanning microprobes*, which enable imaging and spectroscopic study of samples at high spatial resolution, currently down to 150 nm at 8 keV and 60 nm at 2 keV, using absorption and fluorescence contrast mechanisms. The hard x-ray scanning microprobe was one of three Argonne projects that won the Year 2000 R&D 100 Award sponsored by *R&D Magazine*. It was developed by B. Lai, Z. Cai, J. Maser, P. Ilinski, D. Legnini, and W. Yun. The newest such instrument operating in SRI CAT is the x-ray fluorescence microprobe located in the 2-ID-E experimental station. Zone-plate lenses are the key optical elements used to form the tightly focused x-ray microprobes in these instruments. Improving both the x-ray focusing resolution and efficiency of zone plates is a central goal of the SRI-CAT imaging program. In particular, *stacked zone plates* offer a practical means to realize both high efficiency and high resolution, most notably for high-energy x-rays. The scanning microprobes are primarily used for two-dimensional (2D) imaging. Other 2D imaging methods, including interferometric and noninterferometric *phase contrast imaging*, are also being developed as part of this program. *High-throughput tomography*, on the other hand, offers fully three-dimensional (3D) imaging on time scales of minutes down to the 1 μm spatial resolution scale. The raw speed of this method makes possible the dynamic study of nonstatic samples as they evolve in 3D or enables study of a large number of samples in 3D.

2.3.1 A New Facility: the 2-ID-E X-ray Fluorescence Microprobe

Sector 2 at the APS is dedicated to microbeam applications using zone-plate optics. Zone plates take advantage of the high brilliance of third-generation light sources by using the spatially coherent fraction of the beam and focusing it into a diffraction-limited spot of suboptical dimensions. When using zone plates to achieve highest x-ray optical resolution, only a small part of a typical undulator beam can be used. By dividing the wavefront of the beam, several x-ray microprobes can be operated in parallel at a small cost in flux density, spatial resolution and flexibility. Parallelizing of operation is particularly useful for elemental mapping using x-ray fluorescence, where small data rates limit the number of experiments that can be performed in a reasonable amount of time.

2.3.1.1 2-ID-E side-branch beamline

To make use of additional coherent modes in the undulator beam, we have developed a side-branch beamline with a dedicated x-ray

fluorescence microprobe in the 2-ID-E experimental station. This branch line is operated in parallel to the 2-ID-D end station. To divide the wavefront of the undulator, a beam-splitting crystal is positioned 0.3 mm from the center of the beam at a distance of 62 m from the source. The crystal deflects the outboard part of the undulator beam into the branch station, while letting the center of the beam pass through to the 2-ID-D end station. The flux density of the deflected beam is 15% - 20% less than in the beam center, thus providing quite reasonable conditions for micro-fluorescence studies.

2.3.1.2 Optimized design

Since the 2-ID-E microprobe is designed to operate only in x-ray fluorescence mode, significant optimization of the design could be achieved. A three-element low-energy germanium (LEGe) detector with a resolution of 150 eV collects the fluorescence spectra. Two zone plates with different x-ray optical resolution are mounted next to each other and can be changed at the push of a button. This allows a change of magnification and resolution similar to a change of objective lenses in an optical microscope and gives the user a choice between operation at highest resolution (0.25 μm) or an order-of-magnitude increase in photon flux at lower resolution. The specimen is mounted on a standardized kinematic mount in a chamber of leaded acrylic. This specimen chamber both serves to shield against the x-ray background in the 2-ID-E hutch and provides a gas-tight environment. During data acquisition, the specimen chamber is flooded with helium to both minimize Ar fluorescence from air and reduce absorption of the fluorescence of low-Z elements. Kinematic specimen holders allow fast and precise mounting. Using an adaptor, the specimen holder can be mounted kinematically on a state-of-the-art optical microscope, allowing survey of the specimen prior to x-ray mapping, as well as accurate prealignment with respect to the x-ray beam. This is invaluable when pre-positioning thin specimens with little x-ray absorption, such as cells and thin films. Significant attention has been paid recently to developing an intuitive user interface. This screen includes "in/out" buttons for exchange of x-ray optics and specimen, and a first version of tools that align the x-ray optics of the microprobe automatically at the push of a button. Users from fields like medical sciences, biology or environmental materials sciences, who are typically not familiar with the operation of complex synchrotron instrumentation, are able to operate independently after only a few hours of training.

2.3.1.3 Performance

With closed white-beam slits and optimized undulator gap, the 2-ID-E microprobe operates with a spatial resolution of 0.5 μm × 0.25 μm and focused flux of 10^8 ph/s (see Fig. 2.5). Opening the white-beam slits increases the spot size to 1.2 μm × 0.3 μm and yields a focused flux of 10^9 ph/s. Using the second zone plate, with a focal length of 40 cm and an outermost zone width of 250 nm, a focused flux of 2×10^{10} ph/s is obtained with open white-beam slits.

We have begun to build a user program in both biomedical and materials sciences. Experiments performed in the first six months of operation include mapping of the

trace metal distribution in eukaryotic cells and tissues, study of metals distributions in different organisms in the marine food chain (from copepods to bacteria), study of plants, both wild-type and genetically engineered, the study of trace element distributions in optical fibers, and characterization of the composition of Zr alloys in cladding for nuclear fuel rods.

Significant effort has been invested in different instrumentation issues, in particular, the characterization of and use of near-field stacking of zone plates, which significantly increases the diffraction efficiency, and commissioning of a multi-element detector. Significant progress has also been made in efficiently collecting full fluorescence spectra for each image pixel and using principal component analysis for data analysis.

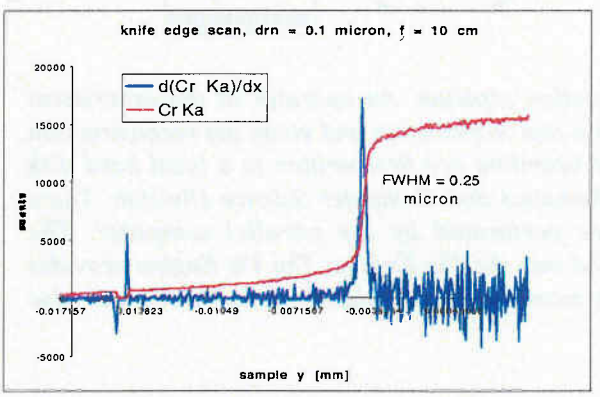

Fig. 2.5. Resolution measurement using a Cr knife-edge. X-ray fluorescence of the knife-edge is collected using an energy-dispersive LEGe detector. Fitting of the data with an error function and derivation of the measured curve yield a resolution of 0.25 μm.

2.3.2 A High-Throughput X-ray Microtomography System

2.3.2.1 System architecture

A third-generation synchrotron radiation source provides enough brilliance to acquire complete tomographic data sets at 100 nm or better resolution in a few minutes. To take advantage of such high-brilliance sources at the APS, we have constructed a pipelined data acquisition and analysis system (Fig. 2.6) in collaboration with the Argonne Mathematics and Computer Science Division (MCS). The system combines a fast detector, high-speed data networks, and massively parallel computers to rapidly acquire the projection data then remotely perform the preprocessing, reconstruction, and rendering calculations (Wang et al., 1999).

2.3.2.2 Data acquisition system

The high-throughput tomography data acquisition system is based at the 2-BM beamline. It uses a straight-ray projection imaging scheme and monochromatic x-rays of energies between 5 and 20 keV to produce an absorption contrast image on a scintillator screen. A visible-light objective lens and charge-coupled device (CCD) camera acquire the visible light image produced on the scintillator screen for each angular orientation of the sample as it is rotated about the vertical axis. Typically with our system configuration, we acquire 1024 × 1024 pixels projection every 0.25 - 0.50° of sample rotation, producing up to 720 projections. Once the data set is available, a software preprocessing algorithm normalizes the data using whitefield images (sample removed from

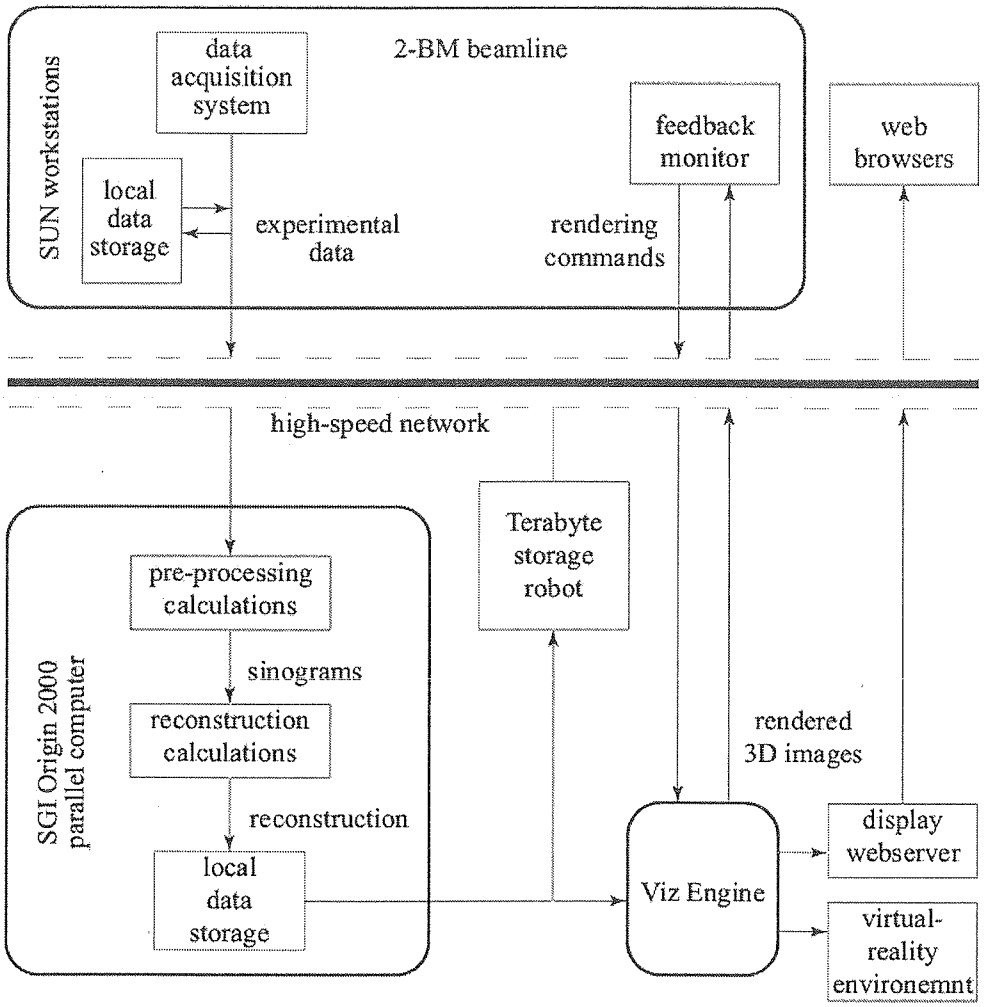

Fig. 2.6. Illustration of the data acquisition and computation pipeline. An operator at the experiment station in the APS controls the data acquisition system on a Sun workstation and views the reconstruction result on the feedback monitor. The data acquired at the beamline are first written to a local hard disk and then transferred via a 100 Mb/s network to the Mathematics and Computer Science Division. There the preprocessing and reconstruction calculations are performed by the parallel computer. The reconstruction results are saved to a hard disk then loaded into the Viz Engine. The Viz Engine provides rendered images interactively to the beamline feedback monitor via the high-speed network and also periodically writes rendered still images to a web server.

beam) and blackfield images (background with beam off), as well as aligns all the projections to a common rotation axis.

The user has a choice of two Princeton Instruments CCD cameras, depending on the exposure times and readout rate required. One camera uses a 1317 × 1025 pixel Kodak CCD (6.8 μm square pixels), thermo-electrically cooled to -15°C and driven by a ST-133 controller with 12 bits/pixel at 1 MHz. The other is a 1024 × 1024 pixel-thinned backside-illuminated SITE CCD (24 μm square pixels), cooled by liquid nitrogen to -100°C and driven by a ST-138 controller with 16 bits/pixel at 240 KHz. The latter

camera is the more sensitive but slower of the two.

For scintillator screens we use either a $CdWO_4$ crystal or a YAG crystal with a 5-μm-thick Ce doped active layer. The $CdWO_4$ screen delivers a resolution of ~3 μm using a 5X objective lens with NA = 0.1 with the Kodak CCD. The resolution of the YAG screen is higher, depending on the objective lens and CCD camera used. Using the YAG screen, SITE CCD, and various objectives from 4X to 40X in magnification, we achieved a resolution of 0.8 to 6 μm and sample image field size of 0.6 to 6 mm. The efficiency of the $CdWO_4$ screen is about four times that of the YAG screen.

2.3.2.3 Control software

All functions performed during a tomography experiment are automatically controlled by an interactive data language (IDL) language graphical user interface and script that uses Experimental Physics and Industrial Control System (EPICS) channel access routines to move motors and actuate the shutter, as well as to page the user when the data set is completed. Another important task performed by the IDL script is to log all the experimentally relevant information into a file as part of the data set. The projection data is stored in the data set (one file per projection) in the highly portable hierarchical data format (HDF) created by the National Center for Supercomputing Applications.

2.3.2.4 Performance

Using this system, complete tomographic data sets can be obtained in tens of minutes to hours depending on the resolution and contrast desired. Immediately after each image in the data set is acquired, it is transferred to a massively parallel supercomputer (Silicon Graphics Inc. Origin 2000 with 128 nodes) at the MCS building for normalization, filtering, and alignment calculations. The aligned projection images are then assembled into sinogram format for reconstruction calculations. Using 80 nodes, a data set containing 720 projections, each with 1024×1024 pixels, takes about 17 minutes to reconstruct with the filtered back-projection method. A smaller data set with 360 projections with 512×512 pixels takes less than 1 minute. When the reconstruction calculations are complete, a visualization computer loads the results and performs rendering calculations in hardware, makes rendered images available to the beamline users, and allows the users to manipulate the rendering interactively. This system is capable of examining a large number of samples at submicrometer 3D resolution or studying the full 3D structure of a dynamically evolving sample on a 10 minute temporal scale. Test results obtained with the instrument, showing 3D images of a cricket's head, are shown in Figs. 2.7 and 2.8.

We are currently improving on two limitations of the system: a new broadband multilayer monochromator will be used for fast tomography instead of the double-crystal monochromator currently in use, which has an unnecessarily narrow energy bandwidth, and a new CCD camera with a 10 frame/s transfer rate is under test to use in place of the slower cameras. These two improvements should increase the time resolution to the 1 min scale. A full-field imaging-type x-ray microscope using zone plate optics is currently being developed at

the 2-ID-B beamline and has demonstrated 100 nm spatial resolution. We plan to integrate this microscope with the high-throughput reconstruction infrastructure to perform high-throughput *nanotomography*.

2.3.2.5 Local parallel processing

One of the major problems to be solved when dealing with high-throughput tomography data is the scale and complexity

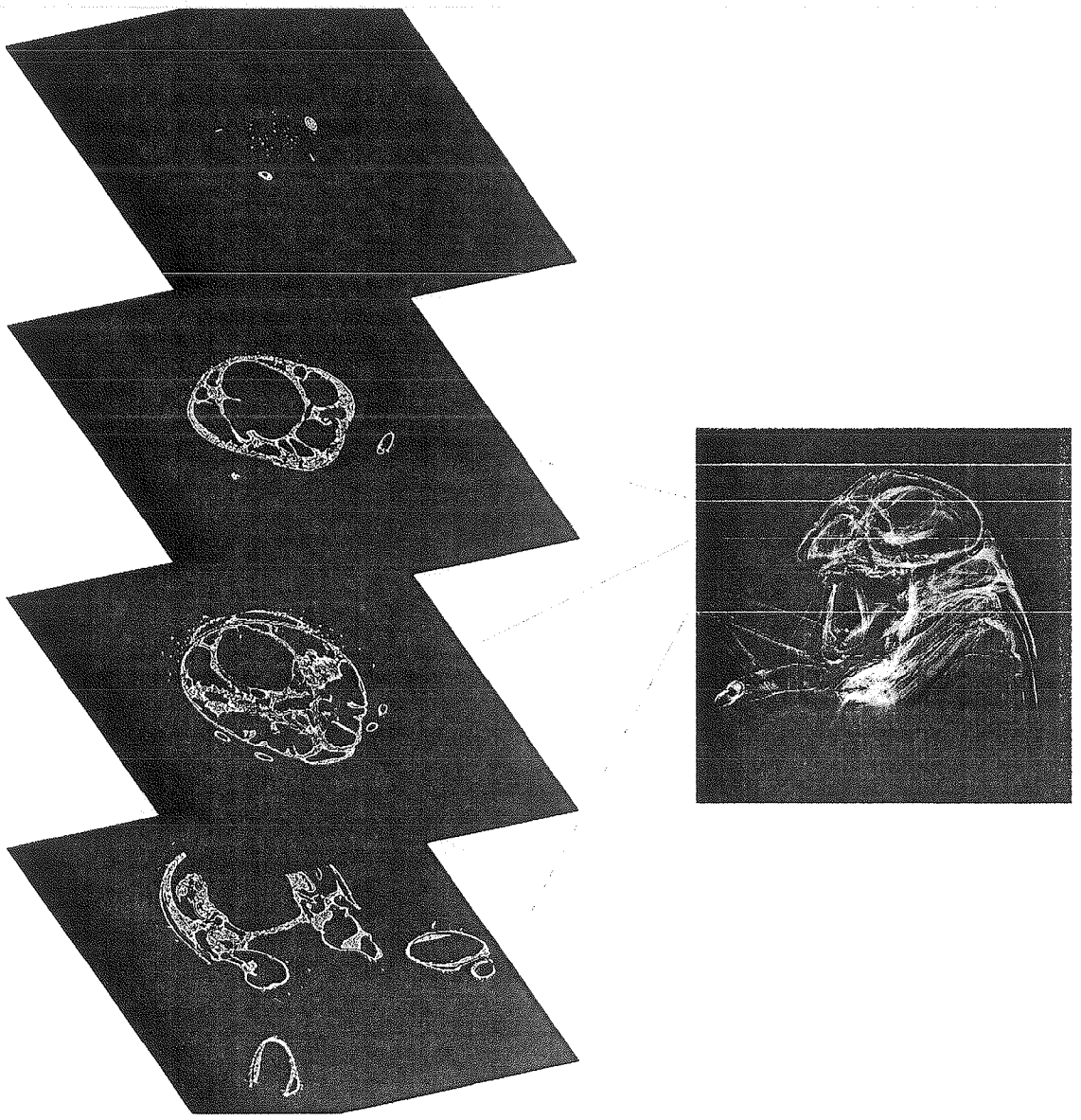

Fig. 2.7. Reconstructed sections from the cricket data. Four sections of the reconstruction volume as indicated on the projection image are shown. The fine features, such as individual hair and details in the skeletal structure including small cracks, are clearly visible.

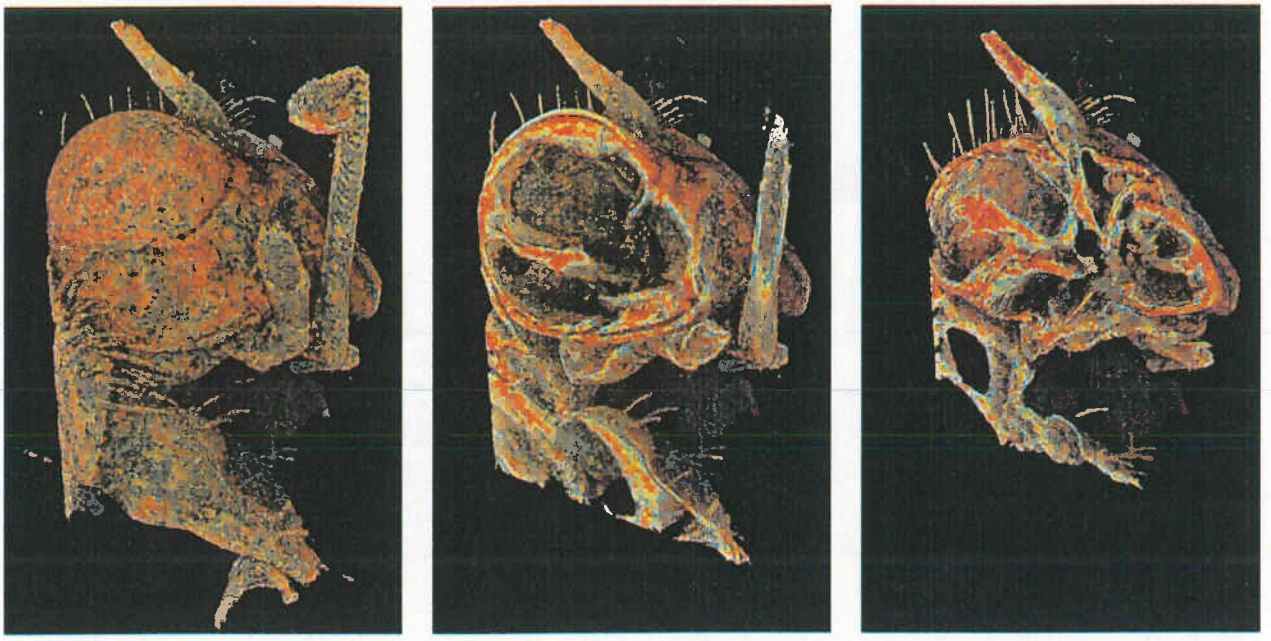

Fig. 2.8. Three rendered images from the cricket reconstruction, digitally cut at different planes to show the internal structures of the cricket's head.

of the data analysis, which requires rapid preprocessing, sinogram generation, 3D reconstruction, and visualization. In addition to supercomputer-based data analysis, we have developed a new method that uses the Message Passing Interface (MPI) software standard to combine multiple PC-class computers into a powerful yet locally available parallel computing system. Among the advantages of this approach are its accessibility, portability, ease of use, and relatively low cost.

MPI system

MPI is a library specification for message passing designed for both massively parallel machines and workstation clusters widely available, with free and vendor-supplied implementations. Key benefits of employing the MPI standard are its ease of use and wide portability (it runs under Unix including AIX, Digital Unix, FreeBSD, HP-UX, IRIX, LINUX, Solaris, and SunOS, as well as Windows 95/NT and MAC OS).

We used MPICH for our implementation of the MPI standard. MPICH is a freely available, portable implementation of the Message-Passing Interface Standard developed by the Argonne Mathematics and Computer Science Division for Windows NT and other operating systems. It was chosen to implement a client-server model for performing reconstructions. In this model, a single process acts as a server to hand out jobs to many clients running on individual Windows NT workstations on the network (Fig. 2.9).

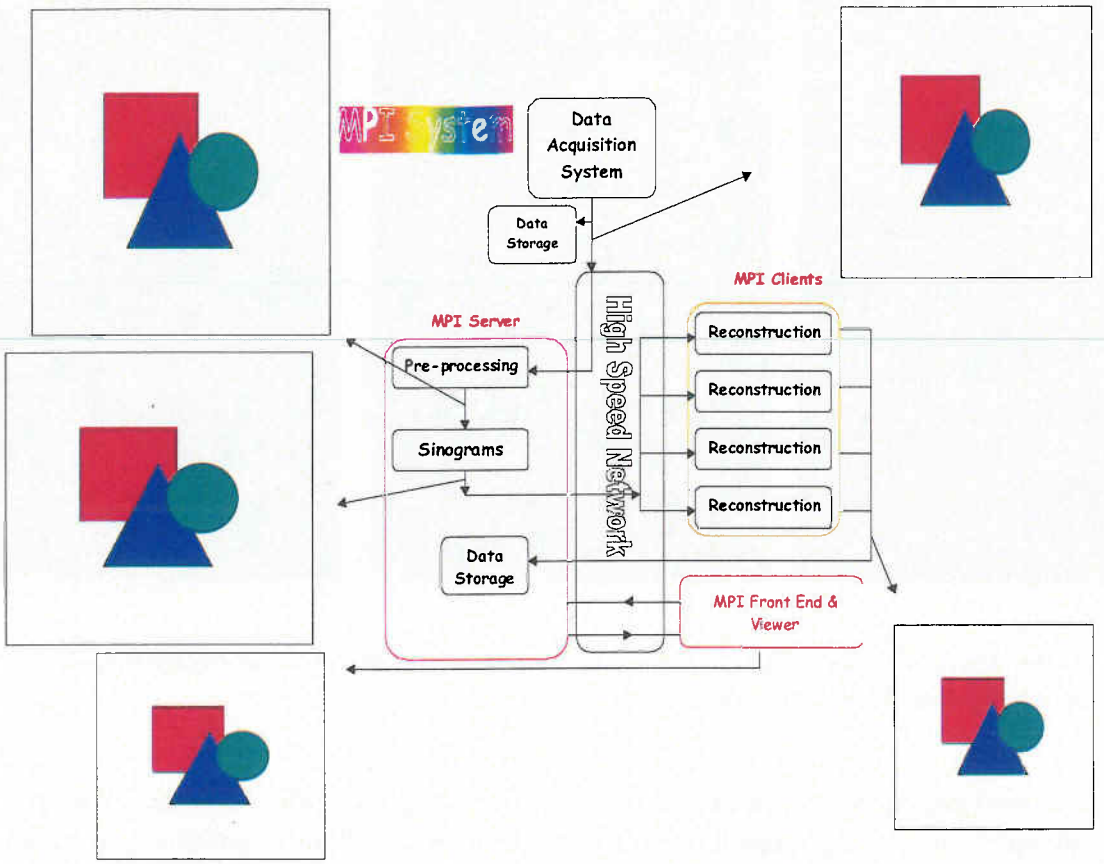

Fig. 2.9. The MPI client/server system used for tomography reconstruction.

The clients are typically the calculation engines of the system and perform a simple loop of operations: request a new sinogram. perform the reconstruction of the sinogram, send the server the completed reconstruction, then request a new sinogram. The clients perform these tasks in parallel to one another, since each client is typically running on its own processor.

The server's job is to respond to requests from the various clients and coordinate the flow of data from the disk system over the network and back to disk. The server first creates a number of sinograms from the preprocessed files on disk. Once this is done, it waits for individual clients to make requests. The sinograms are handed out on a first-request, first-served basis to the clients. The server also performs the task of collecting the completed reconstruction and writing it to disk.

A specialized client has also been written to serve as a front end to the system. The front end makes requests of the server to alter various system parameters or to get information to display to the user about the current state of the system.

A simple configuration file allows the user a way to start up the entire system from a single machine. This configuration file dictates which processors on the network will be used as the server, the front end, or the many clients. This client/server approach to parallelize time-consuming calculations was straightforward to implement and can be readily applied to a wider range of calculation intensive problems. To view tomography data, we developed a simple viewer that recovers all the experimentally relevant information from the tomography data set and allows the user to easily browse the raw data, as well as normalized data, sinograms, and reconstructed slices.

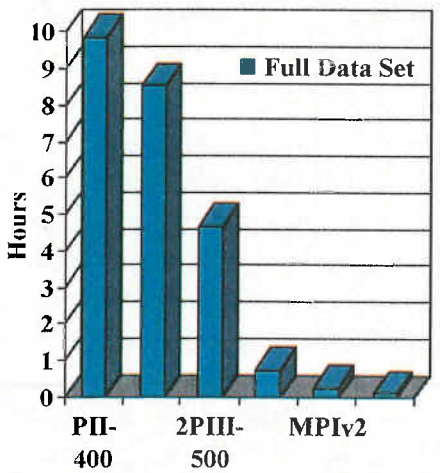

Fig. 2.10. Total reconstruction time (h) for a 360 projection set of 512x512 pixel projections. MPIv3 completes a reconstruction of the full data set in 7 min.

System performance

A first demonstration of the MPI system shows that the reconstruction time reduces proportionally with the number of processors used. At this stage, the network and disk data transport do not yet limit the calculation speed, although we expect this to be the main limitation for a system with 20 or more processors. The results are shown in Figs. 2.10 and 2.11. Setup of a larger NT cluster (>20 PCs) is ongoing. We anticipate that these developments will provide the user with a powerful analysis tool for high-throughput tomography experiments.

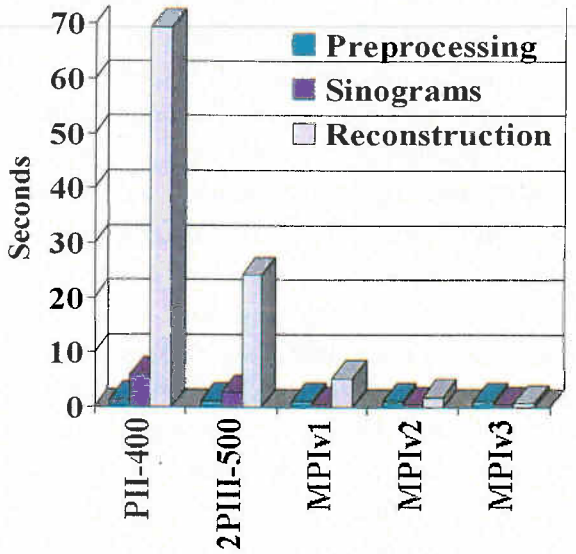

Machine	Processor (Type/MHz)
Xfdid10	2xPIII-500
Olive	PII-266
Mushroom	PII-400
Glorfindel	2xPIII-500
Pepperoni	PII-400
Crust	PII-300
B0302	P-120
Titania	2xPIII-500
Oscar	PII-400
Ipd31	PIII-500

Fig. 2.11. Average reconstruction time (s) per 512x512 pixel slice. For the MPI cluster defined in the table (bottom), we obtained an almost linear reduction of the time to reconstruct a single slice. MPIv1-2-3 refers *to a progression of three system upgrades. MPIv3 shows an average of 0.7 s/slice.*

2.3.3 Stacked Zone Plates

2.3.3.1 Near-field stacking of zone plates

We use Fresnel zone plates as focusing and imaging elements in hard x-ray microprobes at photon energies typically between 6 and 30 keV. While zone plates have allowed us to push the spatial resolution of hard x-ray microprobes towards the 0.1 μm region, highest resolution can currently be obtained only at reduced diffraction efficiency due to manufacturing limitations with respect to the aspect ratios of zone plates. To increase the effective thickness of zone plates, we have begun to stack several identical zone plates on-axis in close proximity. If the zone plates are aligned laterally to within better than one outermost zone width and longitudinally within optical near-field, they form a single optical element of larger effective thickness and improved efficiency and signal/noise ratio. This allows us both to use zone plates of moderate outermost zone width in the hard x-ray range and to increase the efficiency of zone plates with small outermost zone widths for the multi-keV range.

For lateral alignment dr_n of two zone plates, we require the typical accuracy $\delta_l < 1/3\ dr_n$, where dr_n is the outermost zone width. To quantify the required proximity p between two zone plates, we request that both zone plates are aligned to within optical near-field. For two zone plates with outermost zone width dr_n, the near-field condition can be written as $p < dr_n^2/\lambda$. To match the above condition for the lateral alignment δ_l, we require that $p < 1/3 \cdot dr_n^2/\lambda$ for the proximity between two zone plates. Table 2.1 shows the required proximity for zone plates with outermost zone widths of 50 nm, 100 nm and 250 nm, for photon energies between 8 and 100 keV. For example, stacking two zone plates with an outermost zone width of 50 nm at a photon energy of 8 keV requires a proximity of 5.4 μm and a lateral alignment of 17 nm.

Experimental results for the increase of efficiency obtained from stacking two zone plates with an outermost zone width of 100 nm is shown in Fig. 2.12. We have developed a compact holder for stacking two such zone plates and use this system regularly in the 2-ID-E microprobe. Lateral alignment of the two zone plates is achieved by observing the Moire pattern from the two zone plates in real time and maximizing the fringe spacing by moving one of the zone plates. The zone plate stack is stable to within better than one zone width for the full duration of a 5-6 day run.

To quantify the proximity condition p, we have performed dynamical calculations of wave propagation through two stacked zone plates using coupled wave theory. Two identical gold zone plates with an outermost zone width of 100 nm were considered. A photon energy of 8 keV was chosen. A plane wave was assumed to impinge on the first zone plate. Both zone plates were assumed to be laterally aligned. The complex amplitudes of the electromagnetic field were calculated for the back side of the first zone plate, with a thickness of 1 μm, then used as input for propagation through the vacuum region of thickness t_2, and the resulting amplitude used in turn used as input for calculation of the wave amplitudes at the rear side of the second zone plate. From the complex amplitudes, a total diffraction efficiency of the stack was calculated. Figure 2.13 shows results for a stack of two

Table 2.1. Proximity requirements for near-field stacking of zone plate lenses with three outermost zone widths for three hard x-ray energies.

dr_n [nm]	50			100			250		
energy [keV]	8	40	100	8	40	100	8	40	100
p [μm]	5.4	27	67	21	108	270	134	672	1680

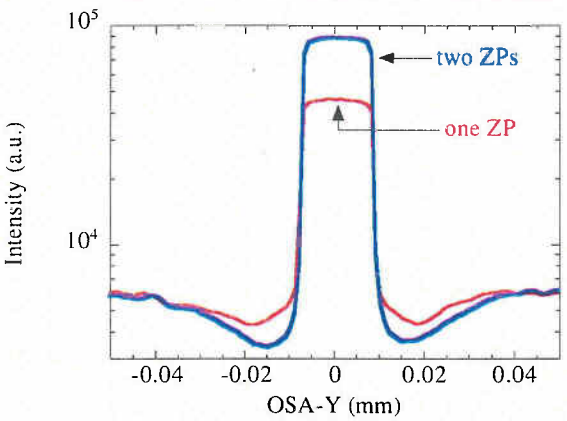

Fig. 2.12. Relative performance of one zone plate (ZP) vs. two stacked zone plates with outermost zone widths of 100 nm, at an energy of 8 keV.

zone plates with varying proximity parameter p.

2.3.3.2 Microfocusing with stacked zone plates

The focusing of x-rays to micron and even submicron dimensions has become routine at relatively low x-ray energies (< 20 keV) but is much more challenging at higher energies (40-100 keV). Motivated by possible applications, such as trace heavy-element detection by K-shell spectroscopy, fluorescence from dense materials, and bulk microdiffraction for stress measurements, an attempt to focus 50 keV undulator radiation using two closely juxtaposed zone plates was carried out. The high-quality zone plates typically used for microfocusing are not thick enough to produce the desired phase shift at higher energies. The "stacking" of two zone plates effectively creates a thicker zone plate, but it is essential to control the placement of the zone plates to very high precision so that the outer zones will be in registry.

The microfocusing optics configuration is sketched in Fig. 2.14. In order for the two zone plates to behave as one, the second zone plate must be placed well within the near-field diffraction distance of the first, and their relative transverse positions must be adjusted to within a few hundred nanometers. The 50 keV undulator radiation incident on the zone plates was delivered by a Si (111) double-crystal monochromator. The two zone plates were separated by a few millimeters and located 60 m from the undulator source. This setup produced a focal spot of 9 x 7 microns with a focal distance of 1 m. The flux density gain was a factor of 24. Improvement of the performance should be possible by additional optimization of the zone-plate parameters.

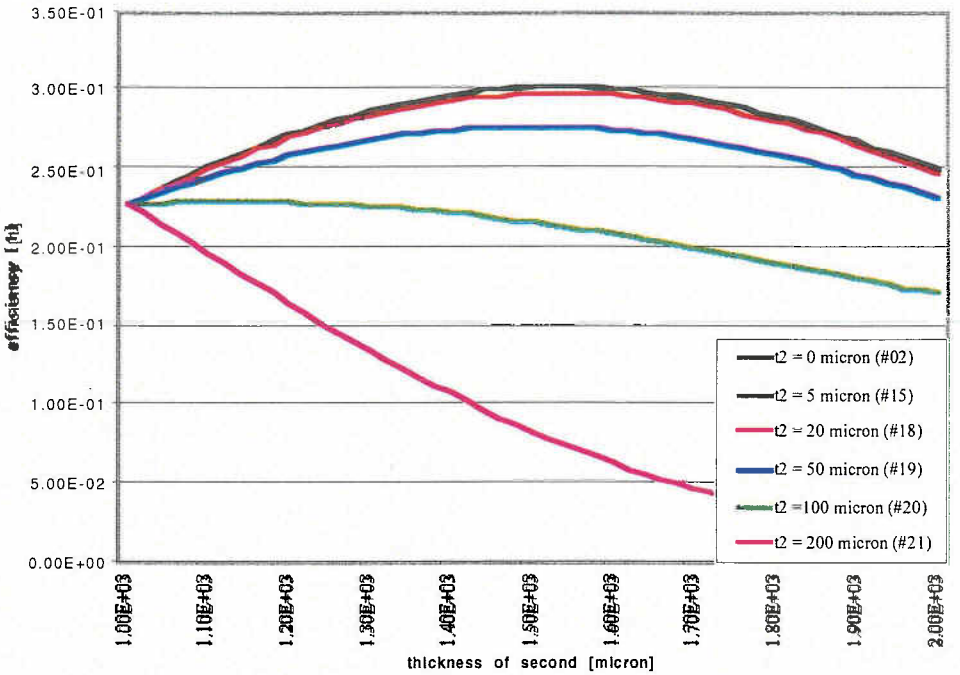

Fig. 2.13. Total efficiency of a stack of two zone plates with an outermost zone width of 100 nm, at a photon energy of 8 keV. The total efficiency of the stack is shown as function of the thickness of the second zone plate for different proximity parameter p. A fixed thickness of 1 μm was assumed for the first zone plate. Calculations for proximity parameters 0 μm, 5 μm, 20 μm, 50 μm, 100 μm and 200 μm are shown. Good agreement with the required proximity parameter of 20 nm, as derived from Fresnel diffraction, is demonstrated.

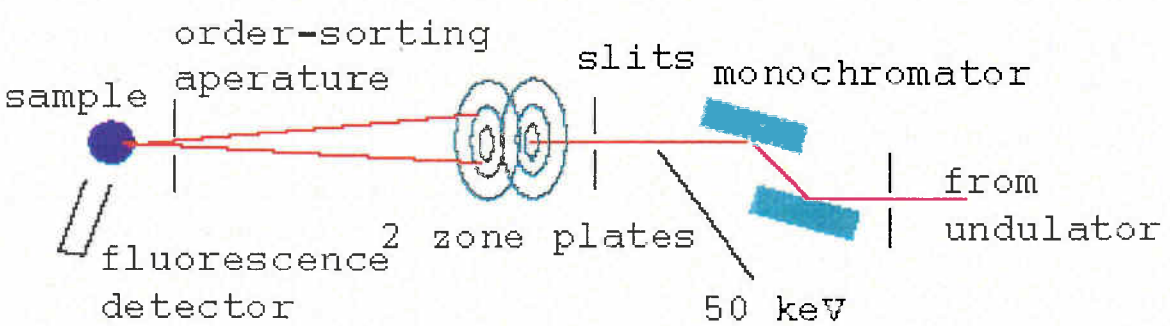

Fig. 2.14. Setup for stacked zone-plate experiment.

2.3.4 Imaging and Microfocusing Applications

2.3.4.1 Biological and medical applications

Two pathogenic mycobacteria, *Mycobacterium tuberculosis* and *Mycobacterium avium*, are intracellular pathogens that infect mainly mononuclear phagocytes and mucosal epithelial cells and survive within tissue macrophages. Tuberculosis is responsible for millions of deaths annually and one-fifth of all deaths of adults in developing countries. *M. avium* is the most common bacterial pathogen in AIDS patients managed in industrialized countries. The importance of macrophages for the survival and replication of both *M. tuberculosis* and *M. avium* in the host is widely appreciated, but little is known about the intracellular environment that permits intracellular survival and replication.

Once ingested by macrophages, *M. tuberculosis* and *M. avium* are present within membrane-bound inclusions that do not acidify or fuse with lysosomes. These phagosomes, although representing a stage of maturation between early and late phagosomes contain very similar host proteins as encountered in phagosomes that form around latex beads. Therefore, the reasons for the arrest of the vacuole maturation are unknown but are very likely due to the mycobacterial interference with the mammalian cell function. The intravacuolar localization of these mycobacteria suggests that they obtain sufficient nutrients required for intracellular multiplication, possibly by manipulating the macrophage to provide these nutrients.

Intracellular mycobacteria express a protein profile that is significantly different than that obtained when these organisms are cultured *in vitro*. It seems plausible that the expression of a number of these bacterial proteins is regulated by the conditions encountered within the vacuoles. These conditions would include the presence, absence, or actual concentration of particular elements like calcium, magnesium, iron, manganese, copper, potassium, and others that are important and necessary for the survival and replication of every organism.

We used the 2-ID-D hard x-ray microprobe to perform initial studies of the trace element distribution of metals in mycobacteria. By measuring and mapping the trace element distribution in the phagosome, we have taken first steps in investigating whether and how the concentration of particular elements might be related to the intracellular survival of pathogenic mycobacteria. This approach is supported by the fact that several cationic transporter genes have been found in the genomes of both *M. tuberculosis* and *M. avium*. By measuring the concentration of the particular elements in the phagosome infected by these pathogenic mycobacteria (*M. tuberculosis* and *M. avium*) and comparing it to the surrounding cytoplasm of the macrophage or to the concentration in phagosomes infected with an apathogenic mycobacterium (*M. smegmatis*) during the process of infection, we are gaining a first insight into the ability of pathogenic mycobacteria to aquire particular elements. By comparing differences in the ability to acquire particular elements in both pathogenic and apathogenic mycobacteria, we are also hoping to gain insight into how

this is related to the ability to cause disease. Due to the high elemental sensitivity and suboptical resolution of the microprobe and to the high penetration power of 10 keV x-rays, no other method method that we are aware of is capable of this type of study.

2.3.4.2 Environmental and geosciences

The microenvironment at and adjacent to actively metabolizing cell surfaces can be significantly different from the bulk environment. Cell surface polymers (lipopolysaccharides, extracellular polysaccharides), metabolic products, etc., can set up steep chemical gradients over very short distances. The behavior of contaminant radionuclides and metals in such microenvironments is currently difficult to predict because the chemistry of these environments has been difficult or impossible to define. The behavior of contaminants in such microenvironments can ultimately affect their macroscopic fates. Information about biogeochemical interactions at the microbe-geosurface microenvironment is paramount for predicting the fate of contaminants and effectively designing bioremediation approaches. State-of-the-art x-ray fluorescence (XRF) microimaging and spectromicroscopy are powerful techniques for resolving the distribution and speciation of contaminants on a microscopic scale. The objectives of our studies are (1) to determine the spatial distribution and chemical speciation of metals near bacteria-geosurface interfaces, and (2) to use this information to identify the interactions occurring near these interfaces among the metals, mineral surfaces, and bacterially produced extracellular materials under a variety of conditions.

We have used hard x-ray phase zone plates to produce x-ray microbeams at the APS to investigate the spatial distribution of 3*d* elements in a single hydrated *Pseudomonas fluorescens* bacterium adhered to a Kapton film. The zone plate used in these microscopy experiments produced a focal spot size of 150 nm. The elements were mapped by scanning this sample in 150 nm steps through the focused monochromatic x-ray beam and integrating the selected Kα fluorescence intensity.

Figure 2.15 shows results of the x-ray microprobe measurements, qualitatively indicating the spatial distributions of K, Cr, Fe, Ni, Cu, and Zn in and near a hydrated *P. fluorescens* bacterium, adhered to a Kapton film at ambient temperature, that was exposed for 6 h to Cr 1000 ppm in solution. Observation of these images indicates that monitoring the spatial distribution of the K Kα fluorescence radiation coming from the sample enabled identification of the rod-shaped *P. fluorescens*, as well as the extracellular exudes associated with it. In addition, comparison of the distribution of Cr with that of K indicates that the majority of the Cr in this sample was associated extracellularly. Studies also have taken advantage of the ability to perform microspectroscopy experiments with the x-ray microbeam to create spatially resolved chemical speciation maps. These studies have identified the valence state of Cr adhered to the biofilm to be 3+, indicating a

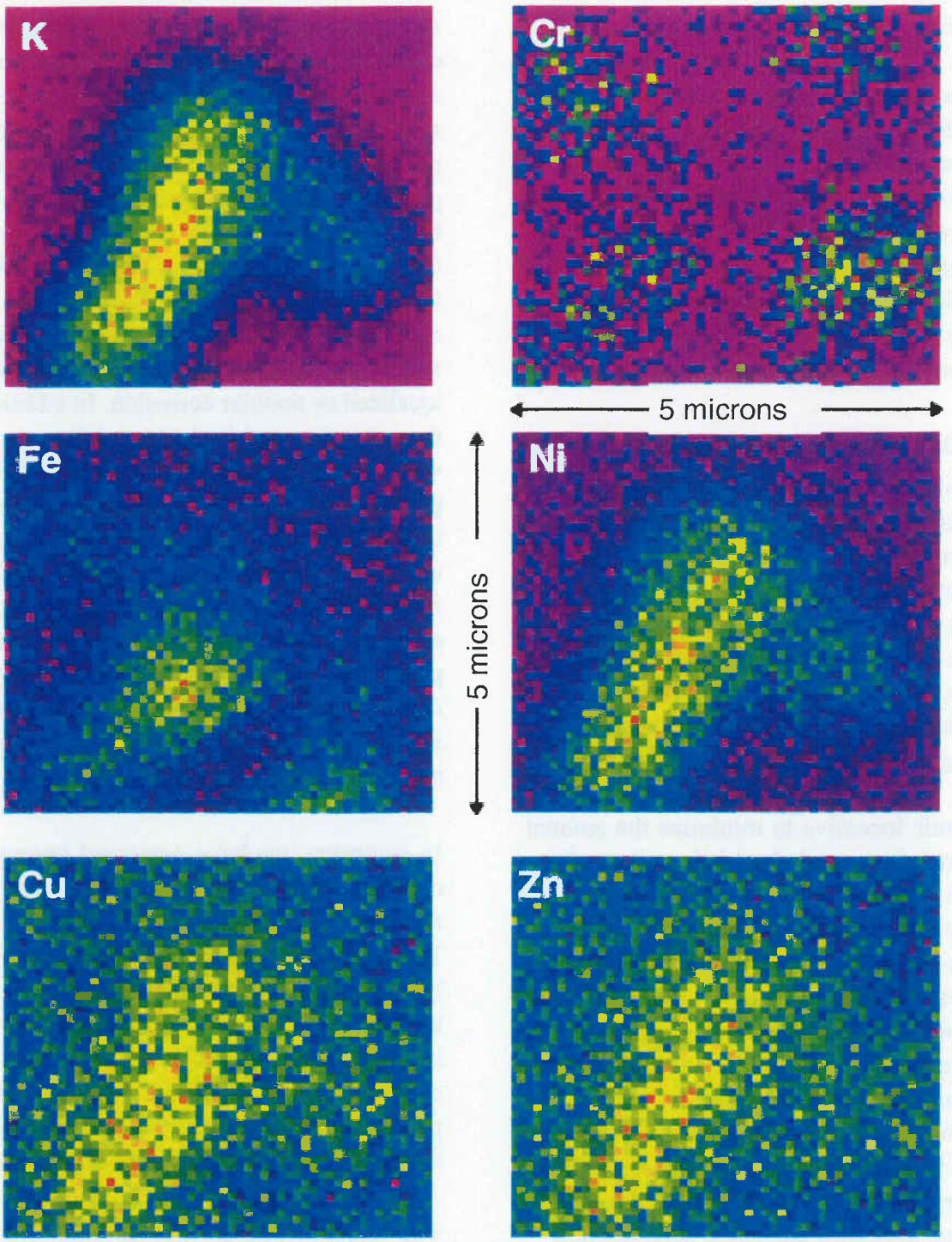

Fig. 2.15. Spatial distributions of K, Cr, Fe, Ni, Cu, and Zn in and near a hydrated Pseudomonas fluorescens *bacterium, as measured by scanning x-ray fluorescence imaging.*

reduction of the Cr from the 6+ state in which it was originally introduced. Recent studies have also demonstrated the ability of the XRF technique to spatially resolve the distribution of elements for single hydrated bacteria adhered to a thin-film mineral surface. The further development of these techniques for such applications promises to provide unique opportunities in the field of microbiology, geomicrobiology, and environmental research.

2.3.4.3 Nuclear materials studies

Zirconium alloys are extensively used in the nuclear industry as nuclear fuel cladding and structural fuel assembly components primarily because Zr is essentially transparent to neutrons. In nuclear reactors, one of the main degradation processes of Zr alloys, such as Zircaloy, is corrosion in high-temperature water. Corrosion and hydrogen ingress limit the useful lifetime of these alloys, and thus there is great economic incentive to minimize the amount of oxidation and hydriding that these materials experience in the reactor. The ability of Zircaloy to withstand corrosion and in-reactor degradation is impacted by its microstructure, in particular by the intermetallic precipitate size, morphology, and distribution and by the concentration of alloying elements in the Zr matrix. In addition, small changes in alloy chemistry, such as reduced tin content, have been implemented during the past decade to improve in-reactor corrosion performance.

A great amount of empirical knowledge exists correlating precipitate size, morphology and distribution (all of which depend on the thermomechanical treatment as expressed by the annealing parameter) to corrosion performance, hydrogen pickup and in-reactor deformation. For instance, a surprising observation is the correlation of precipitate size on corrosion rate in pressurized water reactors (PWR) and boiling water reactors (BWR) reported by Garzarolli and Stehle (1986). In PWRs, large precipitates are desirable, as they decrease uniform corrosion rates. In BWRs, small precipitates are needed to decrease localized or nodular corrosion. In addition to the corrosion and hydrogen pickup varying with thermomechanical treatment for a given alloy, corrosion is also dependent upon alloy composition. Although relationships between microstructure and corrosion rates are understood empirically (i.e., the optimum annealing parameter to create a particular microstructure is well characterized), there is little mechanistic understanding of this process (Lemaignan and Motta, 1994).

In summary, we have empirical knowledge on the behavior of some alloys in both autoclave tests and in-reactor environments. This empirical knowledge relates corrosion behavior to heat treatment and therefore to the as-fabricated microstructure. It is thus important to characterize in detail the existing microstructure, in terms of precipitate structure and volume fraction, as well as the alloying content in the Zr matrix.

The second-phase precipitates are not detectable with standard bulk x-ray techniques, because their volume fraction in the alloy is on the order of 0.2 - 0.4%. These particles have traditionally been studied using transmission electron microscopy

(TEM), but, using TEM, it is difficult to obtain precise crystallographic information, as well as a true bulk picture of the types and quantities of second phases present after different heat treatments and irradiation schedules. The high brilliance and low background of the x-ray beams at the APS allowed us to determine the quantity and types of precipitates present in a material, by quickly acquiring enough diffraction information to estimate the phases present and their volume fraction in both unirradiated and neutron-irradiated samples.

The levels of alloying elements in the matrix are so low that they cannot be measured by traditional measurement techniques, such as energy-dispersive x-ray (EDX) analysis with TEM. There are chemical and spectroscopic techniques that can measure very low levels of alloying elements, in the bulk, but these are not suited to determining the alloying element content in specific regions in the microstructure. The unique combination of spatial and elemental resolution needed to measure to study the alloying elements in the hcp matrix of Zr alloys is available at the microbeamline at SRI CAT.

Answering these questions would have great technological benefit and would lead to the design of better cladding and more accurate predictions of corrosion in existing cladding, through more mechanistic and physically based corrosion models.

Microchemistry of the Zr alloy base metal

The solubility of transition metal alloying elements in the Zr matrix is very small (< 100 ppm) and cannot be detected with traditional analysis techniques. This is because the techniques that have the spatial resolution to distinguish the matrix from the precipitates, such as TEM, do not have the elemental sensitivity to measure matrix concentrations below about 0.5% (5000 ppm). On the other hand, bulk techniques with higher compositional sensitivity do not have the spatial resolution to analyze only the Zr matrix. With the microbeam facility at the 2-ID-D/E beamline, we have the ideal combination of spatial and compositional sensitivity to measure these small concentrations of Fe and other transition elements in the matrix.

This facility was used to study the alloying content in the matrix of well-annealed Zircaloy 2 and Zircaloy 4, as well as the alloying element content of various standards including the above alloys in the quenched state, ultrapure zone-refined Zr. We examined TEM foils to avoid beam spreading resulting from the beam transversing the thickness of the sample. The results show very good agreement with the standards and allow the quantification of the alloying content of the matrix (Erwin et al., in press). To aid in this quantification, we have recently acquired a Monte Carlo program that can simulate the x-ray fluorescence process and can predict the results of the experiments.

Precipitate volume fraction as a function of thermal processing

We have used the 2-BM beamline to examine the precipitation kinetics of second phases in Zr alloys and to relate specific thermomechanical fabrication routes to a *quantitative* measure of second-phase particles present in the alloy in unirradiated

samples. This is, to our knowledge, the first time that such low levels of second phases in an alloy were detected in a bulk diffraction experiment.

Experiments on this beamline last year and earlier this year, indicated that the APS was capable of identifying by bulk diffraction analysis very small amounts of second-phase particles in Zr alloys (volume fraction ~ 0.2%). We have examined ZIRLO, Zircaloy 2 and Zircaloy 4, identified the precipitate peaks as corresponding to the appropriate phases. and showed that their evolution could be followed with diffraction measurements in the APS (Delaire et al., in press). This research data has helped resolve other outstanding questions, such as which intermetallic phases are present in advanced alloys, such as ZIRLO.

To quantify the precipitate volume fraction, we are using Rietveld refinement, with the GSAS program, from Los Alamos National Laboratory. To that end we need a fairly complete data set for the 2-theta region of interest, as well as measurements performed on well-defined standards. We examined a series of samples with varying annealing parameters, either isochronally (different temperatures, fixed time of 1 h) or isothermally (different times, fixed temperature of 700°C), and are currently performing the Rietveld analysis. This research is being prepared for submission to the *Journal of Nuclear Materials*.

2.3.4.4 Nanotomography of chips

Over the last two years, we have seen an improvement in both spatial resolution and overall image quality in the tomography of integrated circuit components at beamline 2–ID-B. In collaboration primarily with a research group at the National Institute of Standards and Technology, we have been developing tomographic imaging techniques capable of resolving submicron-sized structures, hence the term *nanotomography*. Our goal is to perform non-invasive imaging of buried integrated circuit constructions on the tens of nanometer length scale. These structures are not only excellent references for general nanoscale imaging development, they are also driving the development of a much-needed inspection tool for next-generation devices having defects on the order of 20 nm or smaller.

Our samples were taken from a test suite of electromigration-voided samples having a critical dimension of 0.35 μm for the transistor level and consisting of a two-level aluminum metallization stack (Ti/Al/Ti/TiN) joined by a tungsten via. An electro-migration sample was prepared by maintaining a 2.3 mA current and a temperature of 220°C for 300 h, conditions that are typical of accelerated life testing. Although a void was formed in the interconnect, it still had electrical continuity because the Ti or TiN barrier layers or both were still intact. The samples were prepared for standard TEM measurements, meaning that the interconnect junctions with the W vias were in free-standing SiO_2 membranes ~10 μm thick.

We employed scanning transmission x-ray microscopy to collect 2D projections of the samples over a range of angular orientations to the beam. The 2-ID-B scanning transmission x-ray microscope (STXM) utilizes coherent soft x-ray radiation from a

5.5 cm undulator after monochromatization by a spherical grating monochromator (McNulty et al., 1998). The STXM uses either an Au or a Ni zone plate having 100 nm or 45 nm finest zone widths, producing a near-diffraction-limited transverse resolution of 150 or 60 nm, respectively. The preliminary work was performed with both the 100 nm zone plate due to its higher diffraction efficiency, and the 45 nm zone plate was used in subsequent work for its better spatial resolution. We chose optimum photon energies in the region spanned by the Al and Si 1*s* absorption edges at 1559 and 1839 eV, respectively.

On a typical experimental run, we were able to acquire 12-14 projections evenly spaced over an angular range of ±70°. This angular increment was initially limited by the rotational stage; the range was limited by the working distance between the sample and an order-sorting aperture pinhole, as well as by decreasing sample transmission at larger angles of incidence.

Tomographic reconstructions of these limited data sets involve solutions to underdetermined systems of equations. Different algorithms have been developed that work better or worse depending on the nature of the measured data set, e.g., in terms of signal to noise and number of projections. Also, one method may be preferable given certain *a priori* information about the sample. One aim of our work is to optimize the reconstruction quality, while at the same time trying to work with as reduced a set of projections as possible. These conditions will be common in upcoming high-throughput measurements in production-line environments.

Figure 2.16(a) shows the first results from STXM data acquired with the 100 nm zone plate (Levine et al., 1999). This reconstruction employed the simultaneous iterative reconstruction technique (SIRT). Two density isosurfaces are shown, green for medium and red for high (~ twice medium) density. Tungsten is known to be present in the higher density via region. Surprisingly, similar densities were also observed in the centers of the two focused ion beam (FIB) markers, which are primarily aluminum with a TiN liner.

A comparison between the acquired and the reconstructed data for the normal incidence plane gives an indication of the uncertainties of the reconstruction method. These are seen to be about 400 nm, compared to an aluminum linewidth of 1.1 μm. Most of the small line artifacts can be ignored, but where they cross one of the FIB markers they increase its distortion. The set of angles sampled is much less than the Nyquist sampling limit, $\pi/2$ times the number of horizontal samples, or 394 in this case. Our number of projections is at least an order of magnitude less. As a consequence, there is no possibility that the 3D resolution will be as fine as the 2D resolution.

A Bayesian reconstruction algorithm was applied to the same projection data used to produce Fig. 2.16(a) (Levine et al., 2000). A view is presented in Fig. 2.16(b). No additional preprocessing was done. The image is much smoother than the SIRT reconstruction and more in accord with the acquired normal incidence projection in Fig. 2.16(c), which shows straight edges. The roughness present in the SIRT

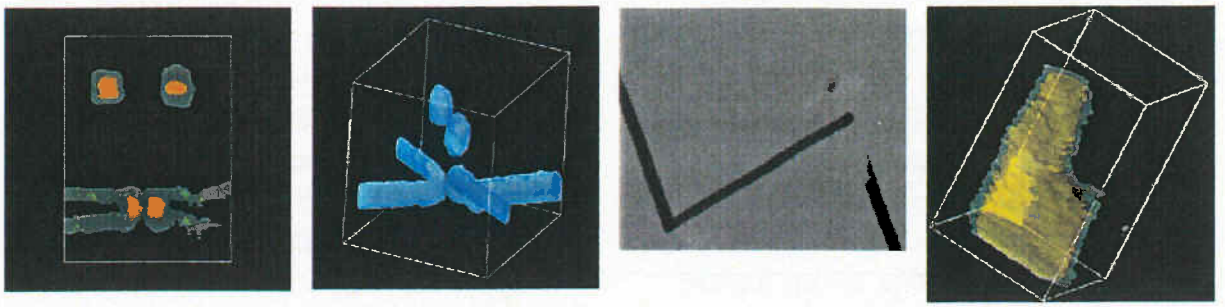

(a) (b) (c) (d)

Fig. 2.16. (a) SIRT reconstruction of the integrated circuit with the ordinate y and the abscissa z. The two levels of interconnect are connected by vias. The two FIB markers are at the top of the image. This in-plane side view in practice cannot be observed directly in transmission. (b) Bayesian reconstruction of an integrated circuit interconnect using same data as in (a). The distance from the plane of the FIBs to the center of the upper interconnect line is 5.4 ± 0.5 μm. (c) Normal incidence projection of an integrated circuit interconnect with an electromigration void, imaged with 301 x 301 pixels with 57 nm step size and the 100 nm zone plate. The total field of view is 17.1 μm. The dark marks at the intersection of aluminum metallization are the tungsten vias, which join two different levels. The light regions near the vias are the remnants of focused ion beam markers which fell out during sample preparation. (d) Bayesian reconstruction of the ragged end of the aluminum interconnect shown in the right side in (c).

reconstruction was used to estimate its spatial resolution at 400 nm. Here, an estimate is made based on the distance for a change in value by a factor of 0.735 when an abrupt change is expected. This is found to be 3.6 ± 1.0 pixel. Given a pixel size of 57 ± 5 nm, the measured resolution in the 3D Bayesian reconstructed data is 200 ± 70 nm, i.e., about twice as good.

Similarly, the Bayesian method was applied to a projection set acquired using the 45 nm zone plate from a circuit with an electromigration void. We failed to obtain a reconstruction with the Bayesian method for coarsely scanned data using the 100 nm zone plate, despite a successful SIRT reconstruction. For fine resolution data, Bayesian reconstructions were obtained without further preprocessing. The region of the wire end is shown in Fig. 2.16(d). The resolution is estimated as above to be 7 ± 1 pixel, or 140 ± 30 nm. This is comparable to a resolution of 10 ± 3 pixel or 200 ± 70 nm for SIRT. The uncertainty in the resolution is higher for SIRT because the isosurfaces generated by SIRT are rougher than those by the Bayesian method. The relative resolution of the two methods is 0.7 ± 0.2 and is independent of the pixel size and its uncertainty.

2.3.4.5 Noninterferometric quantitative x–ray phase imaging

Until recently, absorption was the principal contrast mechanism in transmission x-ray imaging and x-ray tomography experiments. As in medical applications, this leads to the ability to observe the projected density distribution in the object. However, imaging

based on absorption contrast can subject the specimen under study to a significant radiation dose leading to possible structural changes. This is particularly the case for x–ray imaging of biological structures at submicrometer resolution, where the imparted radiation dose can exceed 10^6 Gy in order to obtain high-quality images.

Consequently there has been considerable interest in the development of phase-contrast x-ray microscopy, especially under conditions where the absorption may be relatively low. This work is of interest in both full-field or direct-imaging microscopy and in soft x-ray holography. Moreover, away from absorption edges in the specimen, the phase-contrast mechanism becomes increasingly dominant at higher photon energies (absorption contrast decreases roughly as the third power of the photon energy, while phase contrast decreases linearly with it). For very energetic x-rays, objects may exhibit negligible absorption contrast yet show substantial phase contrast. In parallel, the importance of phase-contrast mechanisms has been accentuated by the availability of third-generation x-ray sources. These devices, by virtue of their high brilliance, have enabled phase-contrast imaging to become a simple and standard imaging technique. Phase-contrast tomography, while not yet commonplace, is also developing rapidly.

Early x-ray phase imaging arose from scanning transmission electron microscopy techniques and utilized quadrant detectors for phase analysis. Quadrant detectors have since been used in scanning transmission x-ray microscopy, and a similar technique has been used in visible light microscopy. An advantage of this method is its spatial resolution, which is governed by the focal spot size of the scanning apparatus. The disadvantage is the time required to acquire a high-resolution image. Alternatively, whole image detection, for example with Shack-Hartmann arrays, is instrumentally complex and provides only limited spatial phase resolution. Whole image phase analysis in x-ray microscopy was also considered using Wigner deconvolution techniques. This is computationally intensive as it requires four-dimensional data sets. Multiple defocusing methods have also been developed, and various other iterative algorithms have appeared that successively approximate the phase by numerically propagating the complex amplitude between spatially separated planes. These techniques often intermix phase with absorption contrast or pose additional difficulties separating them. We tested a new method for x-ray phase determination that is neither computationally intensive nor depends upon complex x-ray optical schemes. This deterministic technique, which makes use of the derivative of the intensity over two or more longitudinally separated observation planes to retrieve the phase of the wave, utilizes the transport of intensity approach developed by Paganin and Nugent (1998). Its appeal is that it directly (noniteratively) retrieves spatially accurate, quantitative phase via an efficient numerical algorithm and uses standard x-ray microscopy techniques. We used it to explore the ability to extract the phase quantitatively from the absorption contrast, with a variety of samples ranging from essentially pure-absorption to pure-phase objects (Allman et al., 2000).

The experiments were performed with 1.83 keV x-rays at beamline 2-ID-B using two experimental configurations. The first was a holographic geometry (Fig. 2.17) in which test objects were illuminated from the diverging point source formed by the focus of a Fresnel zone plate lens. Holograms formed by interference between the waves scattered by the object and those that passed through unscattered were detected by a CCD camera. The second was a full-field imaging geometry (Fig. 2.18) in which points in the test object were directly imaged onto the CCD camera by the zone plate, functioning as an objective lens. The CCD camera in both cases used a thinned, backside-illuminated 1024 x 1024 pixel chip with 24-μm-square pixels and liquid nitrogen cooling, operated in direct x-ray detection mode. The spatial resolution obtained with the holographic geometry, ~60 nm, approached the diffraction limit of the zone plate that was used. The resolution obtained with the imaging geometry was limited to ~150 nm by the x-ray beam flight path (1 m) and CCD pixel size.

Figures 2.19 - 2.22 show intensity images and the retrieved phase images of various test objects obtained with both geometries. Of note is that the spider web segment in Fig. 2.22, a nearly pure phase object, showed significant phase but negligible absorption contrast. Overall, the measured phase obtained from the images obtained holographically agrees with the geometrically estimated phase to within ±7%. That obtained with the imaging method agrees within ±10%. In both cases the accuracy of the phase measurement was limited by the detected pixel resolution and precision to which the geometrical parameters were known.

These initial results indicate the promise of this technique for quantitative phase imaging of submicrometer structures. When fully developed, this method will help minimize the radiation dose and attendant artifact in high-resolution x-ray microscopy, as well as providing a valuable addition to the x-ray microscopist's toolbox.

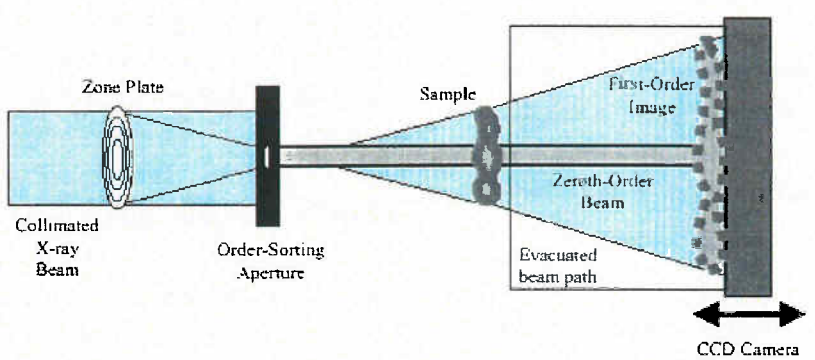

Fig. 2.17. Holographic geometry. The zone plate forms a near-diffraction-limited focal spot used to illuminate the sample. Coherent x-rays scattered by the sample interfere with those unscattered by it to form a hologram (first-order beam), which is recorded by the CCD camera. The zeroth-order beam from the zone plate is ignored.

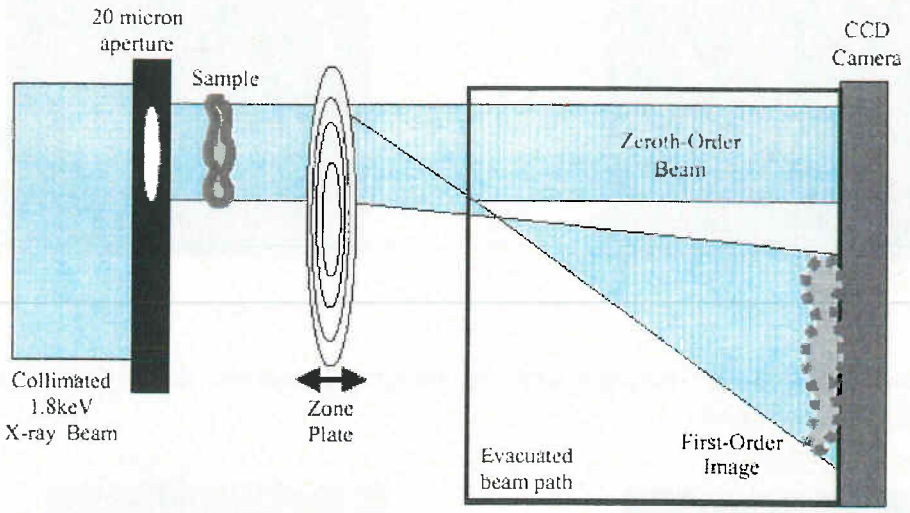

Fig. 2.18. Imaging geometry. The sample is illuminated by a coherent x-ray beam through a 20 μm pinhole. The zone plate incoherently images points in the sample onto the CCD camera (first-order image). The zeroth-order beam from the zone plate is ignored.

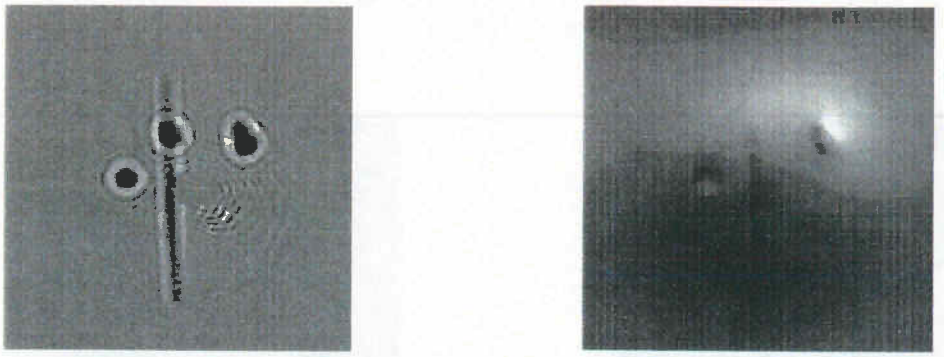

(a) (b)

Fig. 2.19. Images of aluminum spheres (1-3 μm diameter) supported on a 100 nm formvar membrane, recorded with the holographic geometry. (a) Hologram intensity distribution after white-field (sample removed) background correction. (b) Image of retrieved phase. Visible in both images is a vertical fold in the formvar that displays signifcant phase distortion but low absorption.

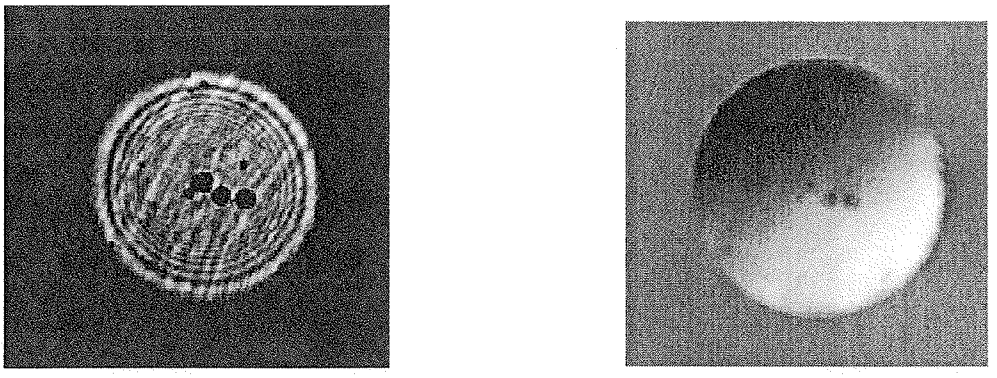

(a) (b)

Fig. 2.20. Aluminum spheres recorded with the imaging geometry. (a) In-focus intensity distribution. (b) Retrieved phase.

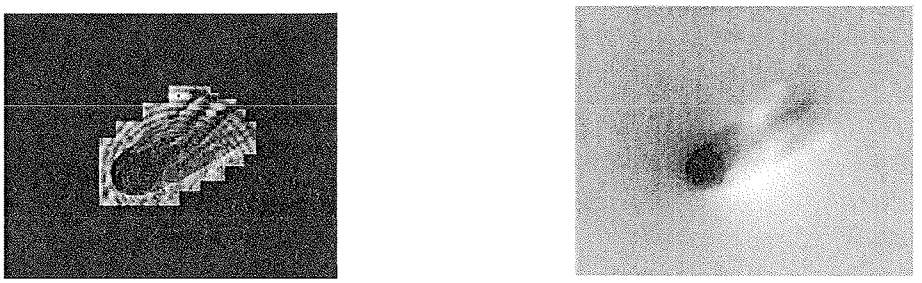

(a) (b)

Fig. 2.21. A 3.7-μm-diameter plastic optical fiber, folded upon itself, recorded with the imaging geometry. (a) In-focus intensity distribution. Note that the absorption contrast of this predominantly phase object is weak. (b) Retrieved phase.

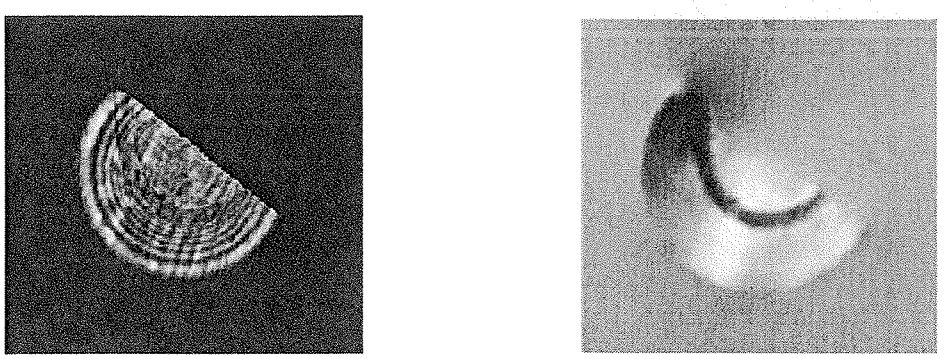

(a) (b)

Fig. 2.22. A segment of spider web silk (1.8 μm diameter) recorded with the imaging geometry. (a) In-focus intensity distribution, showing barely detectable absorption contrast. This is essentially a pure phase object at 1.83 keV. (b) Retrieved phase.

2.3.4.6 Interferometry

The triple Laue (LLL) interferometer is one of the most widely used x-ray interferometers, be it in ultraprecise metrology (Chetwynd et al., 1998) or in imaging techniques (Momose, 1995). One feature of the LLL interferometer is that it can be used over a wide range of energies and is relatively easy to manufacture. As a first attempt into x-ray interferometry, we have built and tested (on 1-ID) a triple Laue interferometer (Fig. 2.23) achieving better than 90% fringe visibility.

An example of the imaging capability of the LLL is shown in Fig. 2.24. Figure 2.24(a) shows the interferogram obtained with a glass capillary [Fig.2.24(b)] placed in one of the LLL beam paths. The recorded fringes are for equal optical thickness and indicate the direction and modulus of the gradient. Since the thickness of the glass varies in a smooth and continuous fashion, this phase information would not be attainable with single-beam or in-line interferometric techniques.

The Laue transmission geometry has two significant problems: 1) absorption losses in each of the blades reduce intensity, and 2) Borrmann broadening in the last blade limits spatial resolution. An interferometer with all Bragg reflections has neither of these problems and has been proposed by Graeff and Bonse (1997). Their idea was to simultaneously excite the Si (440) and Si (404) reflections, creating split beams, and then to combine the branches after several Bragg reflections. Our version of this interferometer is shown in Fig. 2.25. This type of interferometer is dispersive and has a fixed operating energy with a narrow energy range (Fezzaa and Lee, 2000). Our interferometer was designed to have an operating energy of 7.46 keV.

Figure 2.26 shows the setup and results for a measurement where the intensity through a 50 μm aperture was monitored while sliding a 4° plastic wedge in one branch of the interferometer. A thin piece of plastic attenuator in the other arm compensates for the absorption loss through the wedge. The measured contrast was 93%.

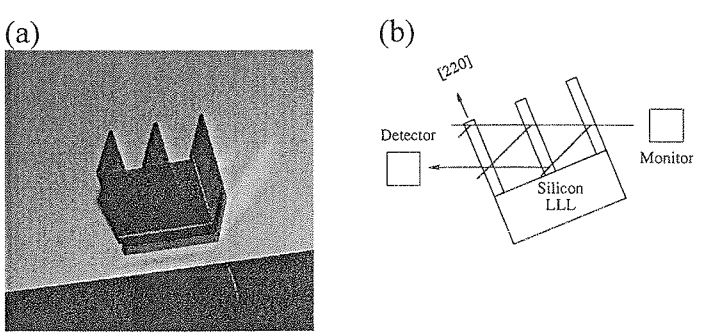

Fig. 2.23. The LLL interferometer (a) and a schematic of its operating mode (b).

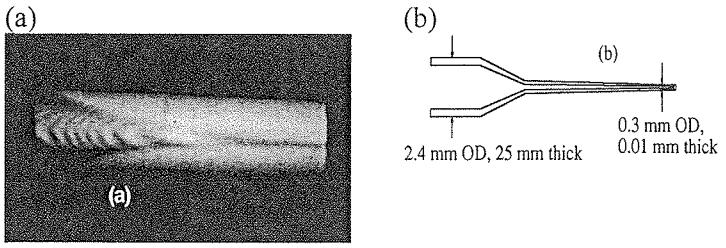

Fig. 2.24. An LLL interferogram of a glass capillary (a) and a schematic of the glass capillary (b).

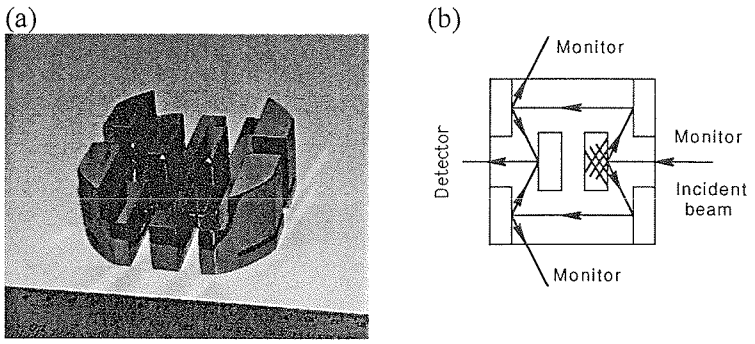

Fig. 2.25. Bragg reflection interferometer (a) and a schematic of its operating mode (b).

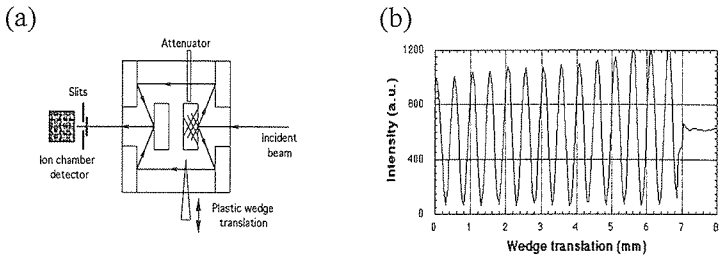

Fig. 2.26. Schematic of the Bragg reflection interferometer with a plastic wedge as a sample (a) and the resultant fringes (b).

We also tested this interferometer using 14.91 keV and the (880) and (808) reflections. Figure 2.27 shows the resultant Moiré pattern from an 8° plastic wedge that was inserted to cover half of one of the branches of the interferometer. The resulting effect of this linear phase gradient is a tilt of the fringes, which confirms that the Moiré pattern is indeed a two-beam interference effect. No fringes were seen when one branch of the interferometer was blocked.

A modified version of the above interferometer with a variable optical path difference was fabricated by putting

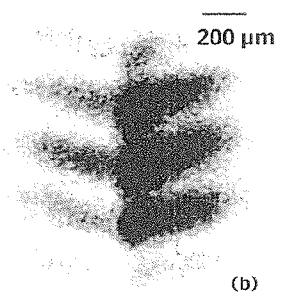

Fig. 2.27. An image of the fringes produced by putting a plastic wedge into the Bragg reflection interferometer operating at 14.91 keV.

a 1° angle into the faces in one of the arms of the interferometer. This angle allows a variation of the path length when the crystal is translated laterally. A wedge scan was made for each position, and the resulting fringes contrast was measured. Ideally, this interferometer would have no defocusing effect, and the fringe contrasts would only depend on the longitudinal beam coherence. However, due to fabrication imperfections, both longitudinal (λ_L) and transverse (λ_T) coherence lengths were involved. The data give $\lambda_L = 50$ μm and $\lambda_T = 14$ μm at 7.46 keV and $\lambda_L = 350$ μm and $\lambda_T = 100$ μm at 14.92 keV, which is within 10% of the calculated values. These coherence lengths are for the beam transmitted through the interferometer and not for the incident beam. The interferometer has a much smaller bandpass and angular acceptance than the incident beam. This smaller bandpass and angular acceptance are the determining factors for these coherence lengths.

2.4 Microfabrication and Deep X–ray Lithography

2.4.1 Novel X-ray Optical Elements

Micromachining processes available in the recently commissioned microlithography cleanroom at the APS are becoming known in the users' community for their capabilities. We were successful in fabricating several x-ray optical components, such as beam stops, pinholes, microslits, orientation grids for microtomography, arrays of compound refractive x-ray focusing lenses, and collimation structures. Beam stops in the range from 10 to 80 μm diameter, and thickness from 15 to 45 μm were fabricated on top of silicon nitride membranes by optical lithography and thick photoresist technology followed by gold electroforming (Fig. 2.28). Similar techniques are used for fabricating pinholes with diameters of 1 to 10 μm.

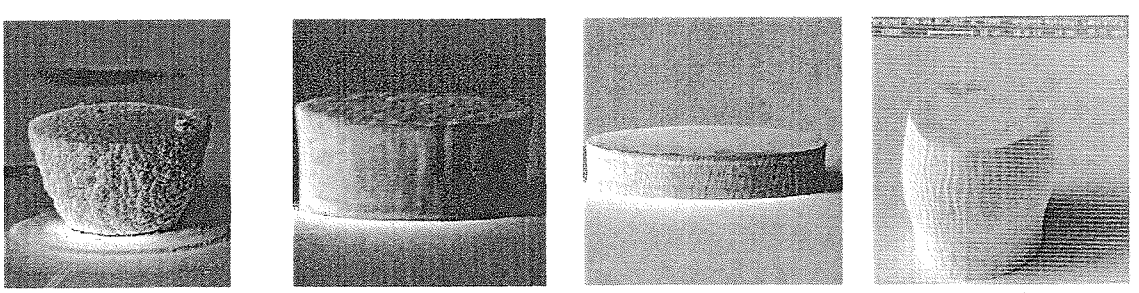

(a) (b) (c) (d)

Fig. 2.28. Scanning electron micrographs of beam stops of various dimensions. (a) D = 40 μm, h = 32 μm; (b) D = 40 μm, h = 20 μm; (c) D = 50 μm, h = 16 μm; and (d) D = 20 μm, h = 40 μm, where D is the diameter, h is the height of each structure.

Orientation grids for x-ray tomography were made by optical lithography and electroforming on silicon nitride membranes (Fig. 2.29). Arrays of refractive compound focusing cylindrical lenses for hard x-rays were fabricated by deep x-ray lithography in polymethylmethacrylate (PMMA) plates of thickness from 1 to 6 mm (Fig. 2.30). The focusing distance has values between 2-5 m for the APS bending magnet beamline spectrum, and the lens aperture is 1 mm. Special effort has been made to decrease the roughness of the refractive structures and to control the exposure-induced deformation in PMMA (Moldovan, 1999). The focusing effect was tested and showed focusing capabilities in the 20-50 μm range for the x-ray spot size, limited mainly by the spherical aberration (Fig. 2.31). New arrays of parabolic lenses (under fabrication) are expected to reduce the spot size down to 0.5-5 μm.

Deep x-ray lithography, in conjunction with Au, Pb, Cu, or Pt electroforming, has been used for fabricating x-ray collimators. Preliminary tests showed capabilities of producing arrays of columns with 20:1 to 40:1 aspect ratios in 1-mm-thick PMMA (Fig. 2.32). These arrays will be used as electroforming molds for the collimators. As a result of a collaborative effort with NASA, the University of Melbourne, and Sandia National Laboratory, we have begun the fabrication of prototype structures for soft-x-ray lobster-eye lenses.

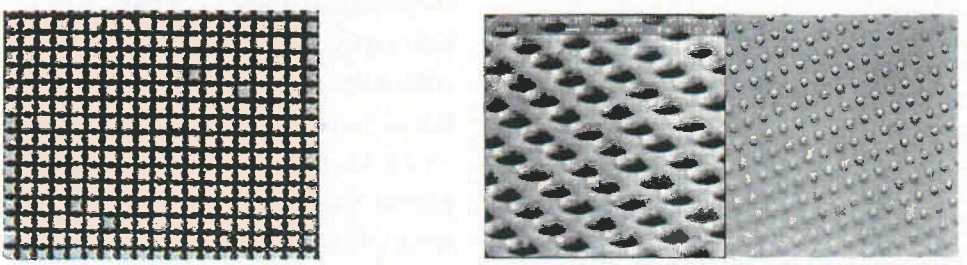

(a) (b)

Fig. 2.29. Arrays of gold squares and dots of various dimensions. (a) 4 μm pitch, 1 μm spacing and (b) 4 μm pitch, 1 μm diameter.

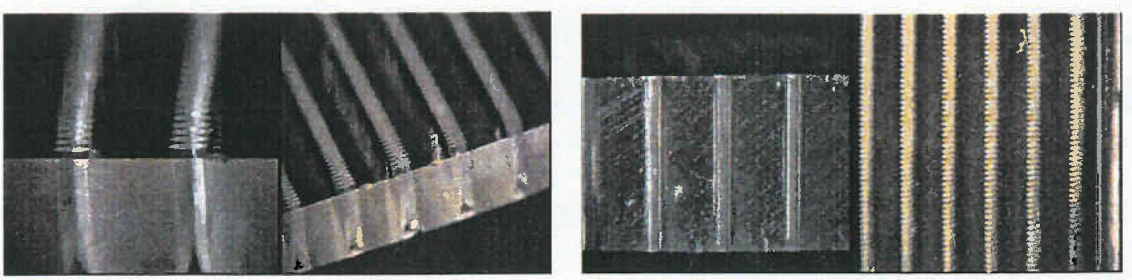

(a) (b)

Fig. 2.30. Arrays of cylindrical refractive lenses in (a) 3-mm-thick PMMA, and (b) 6-mm-thick PMMA.

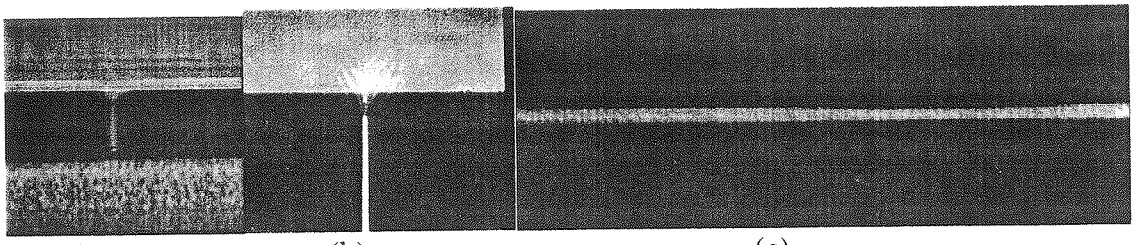

(a) (b) (c)

Fig. 2.31. Focusing effect in a 1-mm-thick lens structure (a), in a 3-mm-thick structure (b), and along a 6-mm-high PMMA lens (c). The intensity in the upper half of (a) and (b) corresponds to the unfocused, direct 10 keV beam, passing above the lenses.

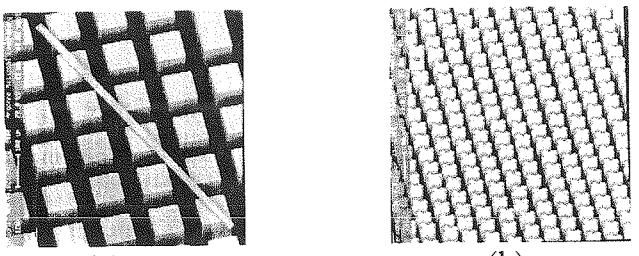

(a) (b)

Fig. 2.32. Arrays of columnar structures made of PMMA, prepared for electroforming x-ray collimators.

2.4.2 Zone Plate Fabrication by Focused Ion Beams

Fresnel zone plates (FZPs) are successfully used at APS beamlines to focus an x-ray beam to a submicron size. Currently x-ray FZPs were fabricated using a combination of electron-beam and x-ray lithography. New developments of FZPs concentrated on increasing the resolution and the efficiency, which means smaller linewidths and thicker zones, hence higher aspect ratios. For this reason, we investigated alternative fabrication methods. As a prototype, an x-ray zone plate was fabricated using the novel approach of focused ion beam (FIB) milling. A focused ion beam had been successfully used for x-ray mask repair and is an attractive tool for fabrication of high-aspect-ratio structures. During FIB milling, material is removed by the physical sputtering action of ion bombardment. The sputtering yield is high enough to remove a substantial amount of material. Therefore FIB milling provides a direct (maskless) patterning method with accuracy in the range of tens of nanometers. Using the 9500HT FIB station from Micrion, which has a 50 keV Ga^+ column, we succeeded in fabricating an x-ray phase zone plate (Fig. 2.33) with an aspect ratio of up to 6:1. Circular Fresnel zones were milled in a 1.0-μm-thick TaSiN film deposited on a silicon wafer. The outermost zone width of the zone plate is 170 nm at a radius of 60 μm. The time it took to mill each zone was about 90 s, and 70 zones were made. The electron micrograph shows that the zone plate structures are rather well defined. The focusing characteristics of this zone plate are being tested at 2-ID-D. In terms of achieving structures with an even higher aspect ratio, the beam profile and redeposition of the material during milling will need to be considered carefully.

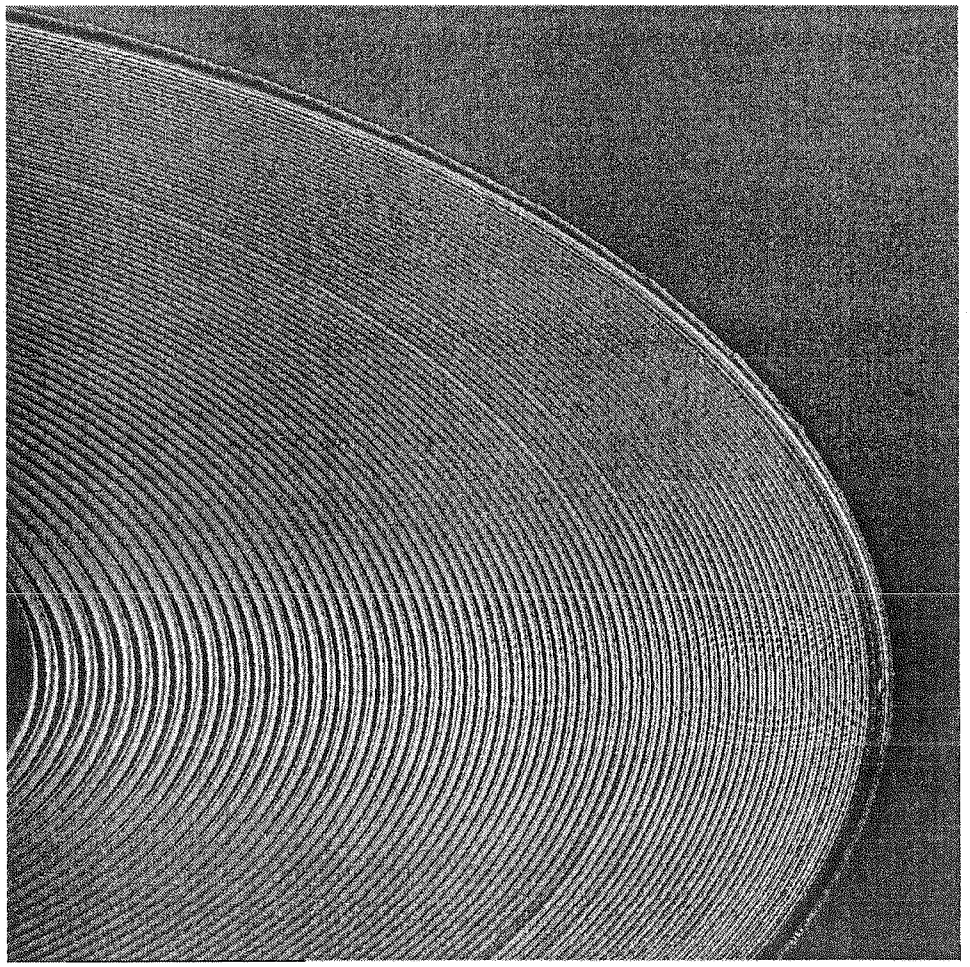

Fig. 2.33. Scanning electron micrograph of the TaSiN zone plate fabricated by FIB. The outermost zone width and thickness are 170 nm and 1.0 μm.

2.5 High-Energy X-ray Scattering

The SRI CAT high-energy program is part of the activities of the x-ray physics program. This program is based on the 1-ID beamline, which it shares with the other sector 1 programs. The activities of the high-energy program are divided into two main areas: optics development and experimental technique development.

The high-energy optics development effort has focused on developing monochromators that deliver high-quality x-ray beams in the energy range of 50-100 keV. We have based this program on several design goals:

- the x-ray beam should have both high brilliance and high flux,
- the monochromator should be tunable over a significant energy range,

- the monochromatic beam should be delivered to a separate experimental station, and
- no compromises should be made in the throughput of the monochromator due to inefficient cooling of the crystal optics.

To achieve these goals, we have built a high-energy double-crystal monochromator that uses the standard APS undulator. The first crystal of this monochromator is cryogenically cooled and, as a consequence, does not show significant thermal distortion when used with the undulator at fully closed gap. (It should be noted that, for maximum production of high-energy x-rays, a standard APS undulator needs to be operated at closed or nearly closed gap.) This is a significant achievement, because most (if not all) other high-energy beamlines use thick thermal filters to reduce the heat load on to their monochromators, which consequently reduces their throughput (particularly in the 50-65 keV range). One version of the high-energy monochromator, the double bent-Laue, is described below. We are currently working on a focusing configuration and a narrow-energy bandpass configuration.

The effort to develop high-energy experimental techniques is very diverse and has touched on several different scientific disciplines. One area of research utilizes the Kohzu double-crystal monochromator (the standard monochromator on beamline 1-ID) with Si (311) crystals to give an energy range of 25-45 keV. This has proved to be a very valuable energy range that is not accessible at most beamlines due to their use of mirrors. Experiments in this range are relatively straightforward extensions of lower energy techniques, but often the additional penetration from the higher energy x-rays makes a crucial difference. Two examples of such experiments are the polaron and confined-fluid studies discussed below.

Another area of research for high-energy techniques is experiments using x-rays above 50 keV (utilizing the high-energy monochromators described above). Most of the experiments at 1-ID in this energy range are geared toward using the penetration capabilities of high-energy x-rays. One example of this is powder diffraction from compounds with high-Z elements to reduce absorption corrections. Another example is the profiling of stress or phases in bulk parts. Much of this work is similar to neutron diffraction studies, but, with the high-energy x-rays, we are capable of obtaining much better spatial resolution. A third example is the ability to penetrate environmental chambers (e.g., furnaces). It is much easier to design furnaces for high-energy x-rays than for lower energies, and the resultant furnaces have superior performance (see below for one such device).

For future research, we will continue the research described above with additional emphasis in the optics development effort on focusing and in the technique development effort on stress/strain/texture measurements and in the *in situ* study of transient behavior of materials.

2.5.1 A New Bent-Crystal High-Throughput Monochromator

The standard double-crystal monochromator consisting of two flat, perfect crystals in a nondispersive setting is ideal for most low-energy experiments (below 30 keV) but is much less effective at high energies (above 60 keV). Flat perfect crystals do not extract and deliver high-energy photons from the white beam in an efficient manner due to the narrow Darwin widths of the crystals, the large value of the cotangent of the Bragg angle, and the increased opening angle of the undulator radiation at high energies where wiggler-like behavior sets in. An alternative monochromator optics design composed of two bent Laue crystals has been developed, which is considerably more efficient in extracting monochromatic high-energy synchrotron radiation. This monochromator delivers over ten times more flux onto a sample with the same energy bandpass as flat Bragg crystals in the 60-100 keV range. It has made 1-ID the only high-energy beamline in the world possessing the important features of high intensity, full tunablility, and phase-space (brilliance) preservation, while maintaining an in-line geometry.

The optics are shown schematically in Fig. 2.34. The white beam is incident on the first Laue crystal, cylindrically bent to a Rowland circle going through the source S1. The singly diffracted beam emerges as if emanating directly from a virtual source S2, also located on the first Rowland circle. The second crystal is also bent, but to a Rowland circle going through the virtual source S2. The doubly diffracted beam propagates as if coming from the virtual source S3 located on the second Rowland circle and close to the original source S1. The over ten-fold flux increase results from the bending strain-induced broadening of the crystal reflection's angular acceptance. Despite this broadening, one does not experience any significant increased energy bandpass because the curvature of the crystal is matched to the angular distribution of the white beam. This is characteristic of the Rowland geometry—all rays from any given point within the source impinge at the same angle onto the bent crystal lattice, leaving only a small source-size contribution.

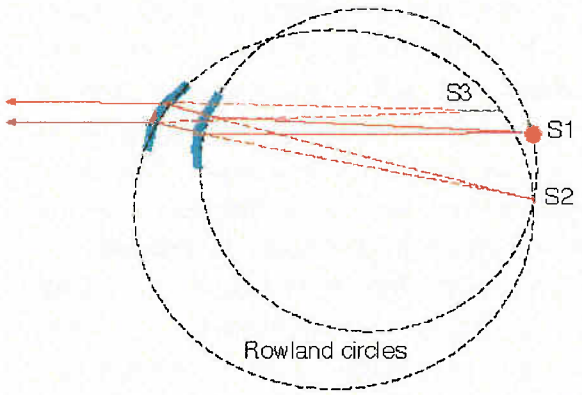

Fig. 2.34. Schematic of the high-energy, bent-Laue monochromator. S1 is the source of photons from the undulator, while S2 and S3 are virtual sources created by the crystal optics.

The technical challenge of implementing the bent double-Laue monochromator optics is achieving fine control and stability of the bend radii of the two crystals. The first crystal, in particular, poses additional difficulty due to the presence of the harsh conditions of closed undulator-gap heat load and cryogenic (liquid N_2) cooling. Crystal benders allowing excellent mechanical control and stability were developed, which operate by inducing the cylindrical bending deflection of a stiff triangular crystal by

pushing indirectly on its tip through a weak spring (see Fig. 2.35). This arrangement leaves the bend radii of the crystal insensitive to thermal or mechanical perturbations in the system. The cryogenic cooling for the first crystal is accomplished by flowing liquid N_2 through the copper blocks clamping the base of the crystal.

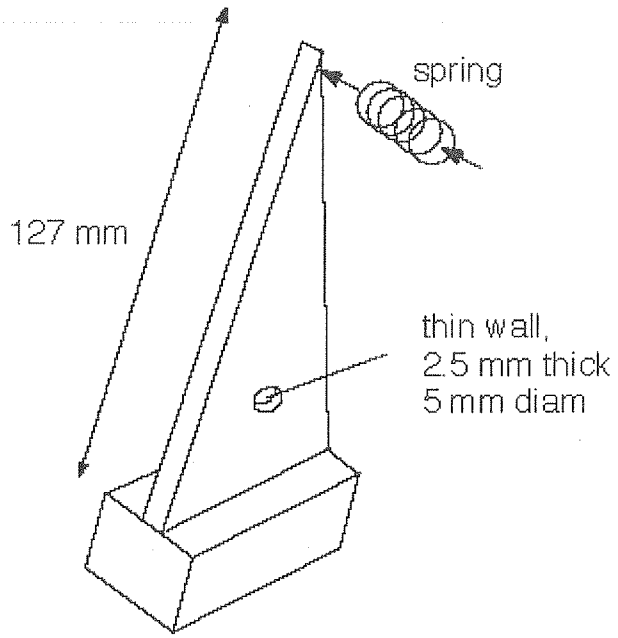

Fig. 2.35. Schematic of the mechanism to bend the Laue crystals for the high-energy monochromator.

2.5.2 High-Energy Applications

2.5.2.1 Polaron studies

The magnetic properties of the lanthanum manganese oxide class of materials have attracted tremendous interest recently because of the dramatic increase in conductivity these systems exhibit when the magnetic moments order ferromagnetically, either by lowering the temperature or by applying a magnetic field. This huge increase in the carrier mobility, which has been given the name "colossal magnetoresistance" (CMR), is of both scientific and technological interest. In particular, it is anticipated that these materials may provide the next generation of read/write heads for the magnetic data storage industry, while the "half-metallic" behavior provides fully spin-polarized electrons for use in magnetoelectronics applications and for sensors in a variety of applications, such as in the automotive industry.

Colossal magnetoresistance can be strongly enhanced in systems with reduced dimensionality, and so there has been considerable interest in the two-layer Ruddlesden-Popper compounds, $La_{2-2x}Sr_{1+2x}Mn_2O_7$. The reduced dimensionality leads to significant extension of the temperature range over which magnetic correlations are important and thereby allows a detailed examination of the link between local spin correlations and the resulting magnetotransport. One of the central questions in the field of manganites concerns the lattice involvement in the mechanism of CMR. While the relation between ferromagnetism and conductivity was explained in terms of double exchange, it is now clear that a full understanding of these materials must include the lattice degrees of freedom. In particular, the formation of lattice polarons above the Curie temperature has been inferred from a variety of measurements, but direct evidence has been lacking.

The measurements were performed on a single crystal of the double-layer compound $La_{1.2}Sr_{1.8}Mn_2O_7$, cleaved from a boule that was grown using the floating zone technique. The x-ray data were taken on the

1-ID-C diffractometer, mostly using a high-energy beam of 36 keV to provide enough penetration in transmission geometry. Additional measurements were taken in reflection geometry with 21 keV. A wide range of reciprocal space was explored, including the (*h*0*l*) and (*hhl*) planes. The crystal structure of $La_{1.2}Sr_{1.8}Mn_2O_7$ is body-centered tetragonal (space group *I*4/*mmm*) with $a \cong 3.87$ Å and $c \cong 20.15$ Å, and consists of MnO_2 bilayers separated by (La, Sr) sheets. Previous neutron scattering measurements (Osborn et al., 1998) have evidenced two-dimensional ferromagnetic correlations that peak in intensity at the combined metal-insulator and Curie transition at $T_C = 112$ K and extend over a large temperature range above T_C.

Our measurements (Vasiliu-Doloc et al., 1999) have revealed charge localization in the paramagnetic-insulating phase of the layered $La_{1.2}Sr_{1.8}Mn_2O_7$ CMR material, with the associated diffuse polaron scattering that originates from the lattice distortions around the localized charges.

Figure 2.36(a) shows a contour plot of the diffuse x-ray scattering in the [*h*, 0, *l*] plane around the (2, 0, 0) reflection. Only the $l > 0$ half is shown, but the pattern is symmetric with respect to $l = 0$. The sharp rod of scattering along the [0, 0, *l*] direction is resolution limited in the [*h*, *k*, 0] plane and is associated with stacking faults. The *h*-scans across the diffuse scattering at l=0.5 shown in Fig. 2.36(b) clearly indicate that this diffuse scattering is anisotropic and strongly temperature dependent, with a dramatic response at T_C.

Part of this diffuse scattering is due to acoustic phonons, but the sudden change at T_C cannot be due to conventional acoustic phonons, as confirmed by inelastic neutron measurements. A good description of the **q**-dependence of this diffuse scattering has been obtained in terms of Huang scattering, consistent with a Jahn-Teller type distortion around the Mn^{3+} ions.

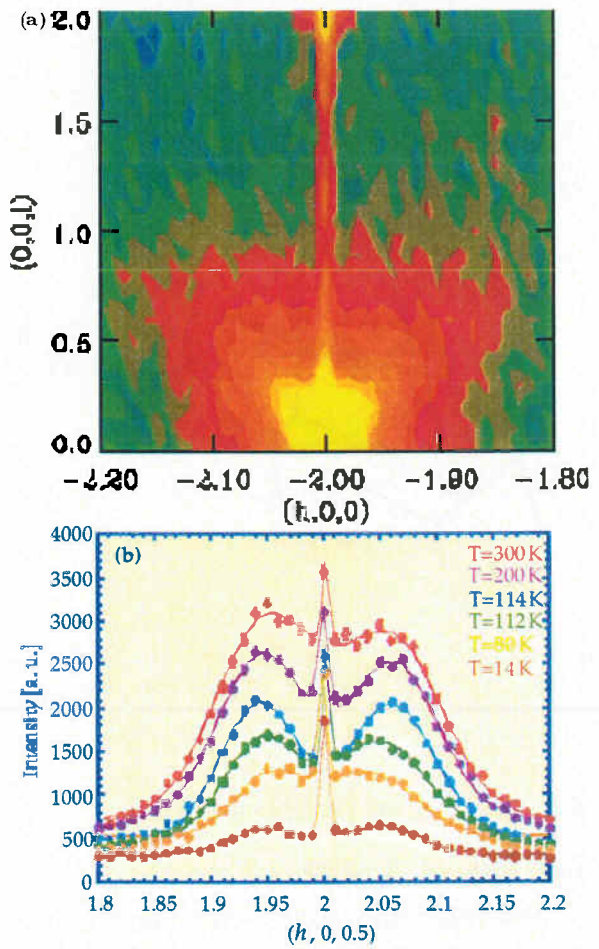

Fig. 2.36. (a) Contour plot showing the lobe-shaped pattern of x-ray diffuse scattering around (2, 0, 0). (b) X-ray h-scans across the diffuse scattering at l = 0.5 at a series of temperatures.

The measurements also reveal the presence of broad incommensurate peaks in the paramagnetic phase, as shown by the contour plot of the x-ray intensity at 125 K in the (hk) plane at $l = 18$ in Fig. 2.37(a). These peaks are characterized by a wave vector ($\pm\varepsilon$, 0, ± 1) as measured from the nearest fundamental Bragg peak, where $\varepsilon \cong 0.3$ [in terms of reciprocal lattice units ($2\pi/a$, 0, $2\pi/c$)]. The in-plane incommensurability is evident in the x-ray h-scans shown in Fig. 2.37(b) at different temperatures. Note that this peak increases and then rapidly decreases in intensity as we cool through T_C. Figure 2.37(c) shows that the temperature dependence of the incommensurate peak intensity is remarkably similar to the Huang scattering derived from the x-ray scattering by subtracting the estimated thermal diffuse scattering. This indicates that both types of scattering are associated with the development of polarons above T_C. The incommensurate peak intensity falls slightly more rapidly than the Huang scattering with increasing temperature. This is consistent with ascribing the Huang scattering to individual polarons and the incommensurate peaks to polaron correlations, which become stronger with decreasing temperature. Below T_C we observe a "melting" of the polaron correlations occurring simultaneously with the collapse of the polarons themselves. These results have been confirmed using neutron scattering at the National Institute of Standards and Technology (NIST) Center for Neutron Research and provide important new insights into the relation of polarons to colossal magnetoresistance.

Charge and orbital ordering have been observed at low temperature in a number of insulating, antiferromagnetic cubic manganites at small and large ($x \geq 0.5$) doping,

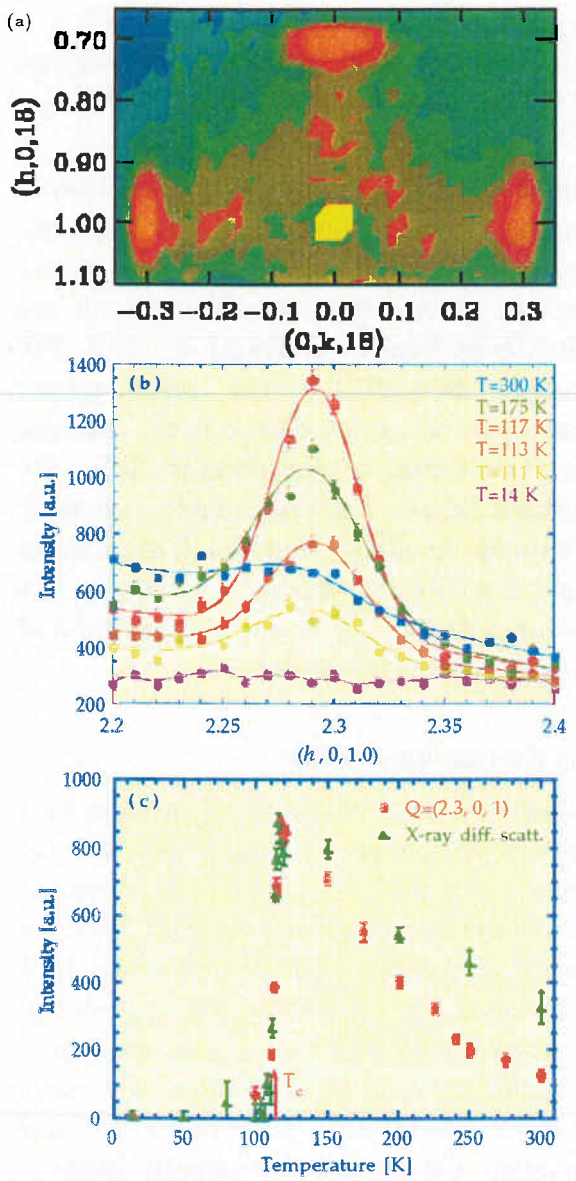

Fig. 2.37. (a) Contour plot of the x-ray intensity in the (hk) plane at l = 18, collected at T=125 K. Three incommensurate peaks due to polaron ordering are observed, characterized by the wave vector (±ε, 0, l) or (0, ±ε, l). The expected fourth peak was not accessible experimentally. (b) X-ray h-scans through the incommensurate peak (2.3, 0, 1) at different temperatures. The higher scattering at small h is due to the proximity of the lobe-shaped diffuse scattering around the Bragg peak. (c) Temperature dependence of the x-ray intensity of the (2.3, 0, 1) incommensurate peak (red closed circles), and of the diffuse scattering after correction for the phonon contribution (green closed triangles).

as well as in layered manganites with x = 0.5. However, short-range charge ordering in the paramagnetic phase of an optimally

doped CMR ferromagnet is a novel feature observed here. In the present x=0.4 system, the charge correlations are not strong enough to win the competition with the double-exchange interaction, and the charges delocalize at the ferromagnetic transition, where the charge peaks collapse and the lattice strain relaxes. It is the delicate balance between double exchange, Coulomb repulsion and the lattice strain field that dictates whether the material is a ferromagnetic metal or charge-ordered insulator at low temperatures.

2.5.2.2 Confined fluids

Fluids confined between solid surfaces have been of great interest to researchers over the last few years (Granick, 1999). This is because the structural and other properties of such fluids differ considerably from bulk fluids at the same temperature, and this has implications for our basic understanding of phenomena such as lubrication, adhesion, surface chemistry, etc. Surface force apparatus (SFA) measurements (Bhushan et al., 1995; Demirel and Granick, 1996) and computer simulation studies (Thompson et al., 1992; Gao et al., 1995; Gao et al., 1997) have found evidence for layering of the liquid molecules in liquid films confined to thicknesses of a few molecular diameters, but direct structural evidence has been lacking. [Evidence for layering near a bulk liquid/solid interface has however recently been obtained from x-ray reflectivity (Yu et al., 1999).]

X-ray reflectivity provides the most direct method for probing the structure of liquid films in the direction normal to the confining surfaces. However, such experiments on films confined at thicknesses of a few nanometers present significant challenges, such as: (a) penetration of the beam through the confining walls and minimization of the scattering from the walls (for which extremely small and high-energy x-ray beams are essential), and (b) alignment of two solid surfaces to a controllable parallel separation of nanometers over square millimeters of area (for which the surfaces must be both highly polished and flat over such length scales, as well as dust-free). In addition, the layering is rapidly destroyed by surface roughness, which typically should not exceed ~ 0.3 nm. We have utilized specially designed silicon substrates (Fig. 2.38) having a diameter of

(a)

(b)

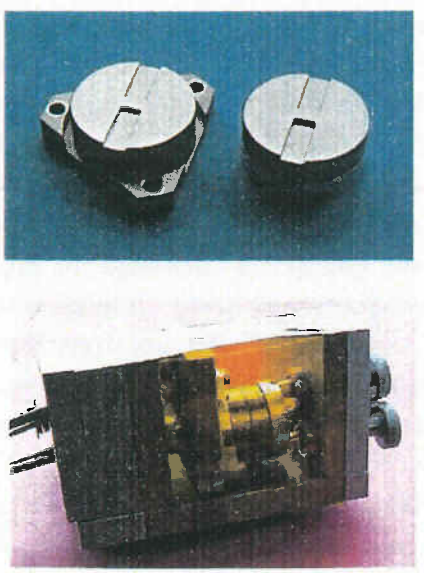

Fig. 2.38. Components of the experimental setup for x-ray scattering on confined liquids. (a) Specially designed silicon substrates (25.4 mm diameter). The area of confinement is the bridge in the center. (b) The sample cell.

1 inch (25.4 mm), an rms roughness of 3 Å (determined by x-ray scattering) and a convex curvature with a height variation of less than 100 Å over the whole sample area (determined by interferometry). Two grooves were etched in each surface, which left a bridge of the size (2 x 4) mm^2 in the center part. The bridge is the area of confinement with a resulting height variation of less than 10 Å. For the experiment, the liquid was spread over the surface of one substrate in a class 1 clean-room. Both substrates were put together so that the grooves formed tunnels that were the paths for the x-rays to the area of confinement (Fig. 2.38). The gap distance between both silicon pieces was controlled by piezodrivers.

The x-ray reflectivity experiments were performed at the SRI-CAT beamlines. The characteristics of the setup were checked at station 2-BM-B where liquid hexadecane ($C_{16}H_{34}$) was used. Some reflectivity measurements taken at 30 keV photon energy are depicted in Fig. 2.39. They show that the gap size shrinks linearly with increasing pressure of the piezodevices. A minimum gap size of 74 nm was achieved, but no evidence was found for layering.

Further reflectivity measurements using octamethylcyclotetrasiloxane (OMCTS) were performed at station 1-ID-C, again with a photon energy of 30 keV (Fig. 2.40).

We were able to achieve 10 times higher pressure compared to the run at 2-BM-B and thus could get much smaller gap distances. Also the flux was much higher so that more details of the reflectivity would be seen.

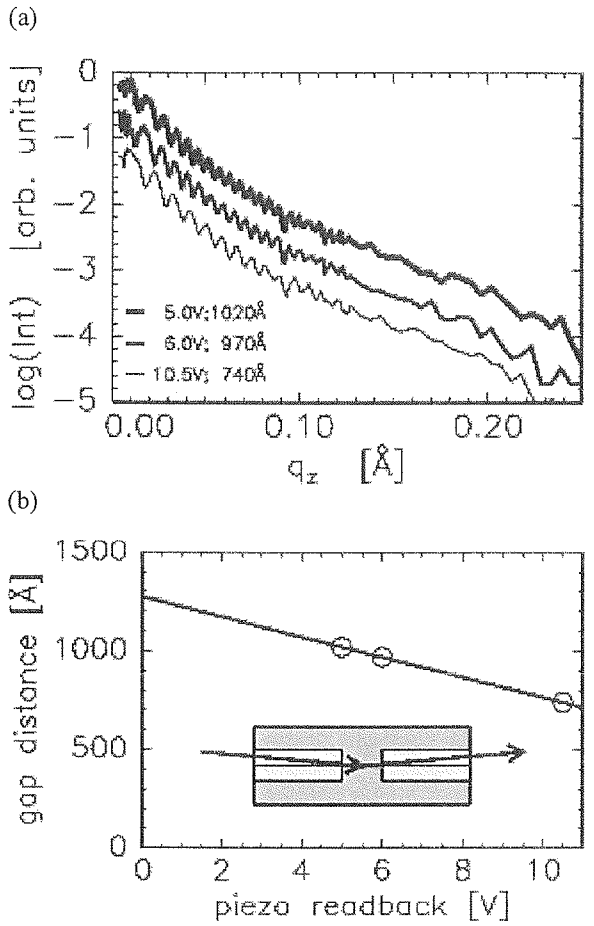

Fig. 2.39. Gap measurements of the confined liquid setup. (a) Some reflectivity measurements at different readbacks of the piezodrivers. They show oscillations due to the gap size. (b) Characteristics of the piezodrivers and a sketch of the sample with the area of confinement in the center.

The reflectivity curves from OMCTS have been fit using the following model: The silicon substrates and native oxide layers were represented with the appropriate step functions of electron density normal to the surface suitably smeared to take into account ~ 0.3 nm roughness and obtained by fitting to the reflectivity of the bare substrates. The OMCTS liquid between the substrates was modeled by a series of Gaussian peaks representing in-plane averaged electron densities of the molecular layers. Extremely

good fits were obtained in this manner (Fig. 2.41). We found that both the gap and the number of molecular layers decreased in a quantized fashion with increasing pressure, from a gap size of 25.2 Å containing three close-packed layers to a gap size of 19.9 Å at the highest pressures, containing 2 non-close-packed-layers. The width of the Gaussian peaks corresponded rather well to the size of the OMCTS molecule (diameter ~ 8 Å).

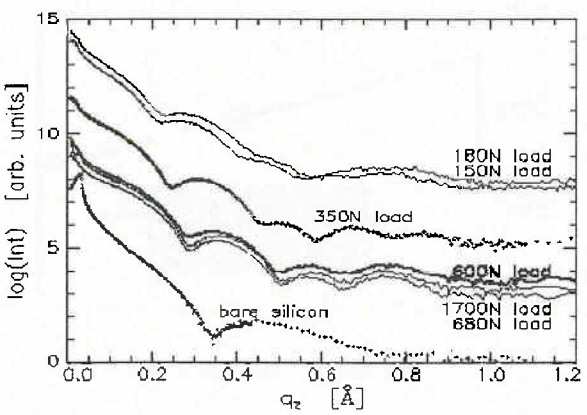

Fig. 2.40. Reflectivities on confined OMCTS. Different pressures have been applied on the silicon substrates. Essentially, only three different reflectivities can be seen.

2.5.2.3 High-temperature powder diffraction

Furnace development

Often conventional x-ray powder diffraction employing flat-plate sample geometry has surface roughness and absorption problems. The corrections for these effects are complicated and some times produce erroneous results. These corrections are eliminated by the use of transmission geometry, which is possible through the use of high-energy x-rays. Other advantages for using high-energy x-rays for powder diffraction include the ability to penetrate through environmental chambers (e.g., high-temperature furnaces) and the ability to gather data far out into reciprocal space.

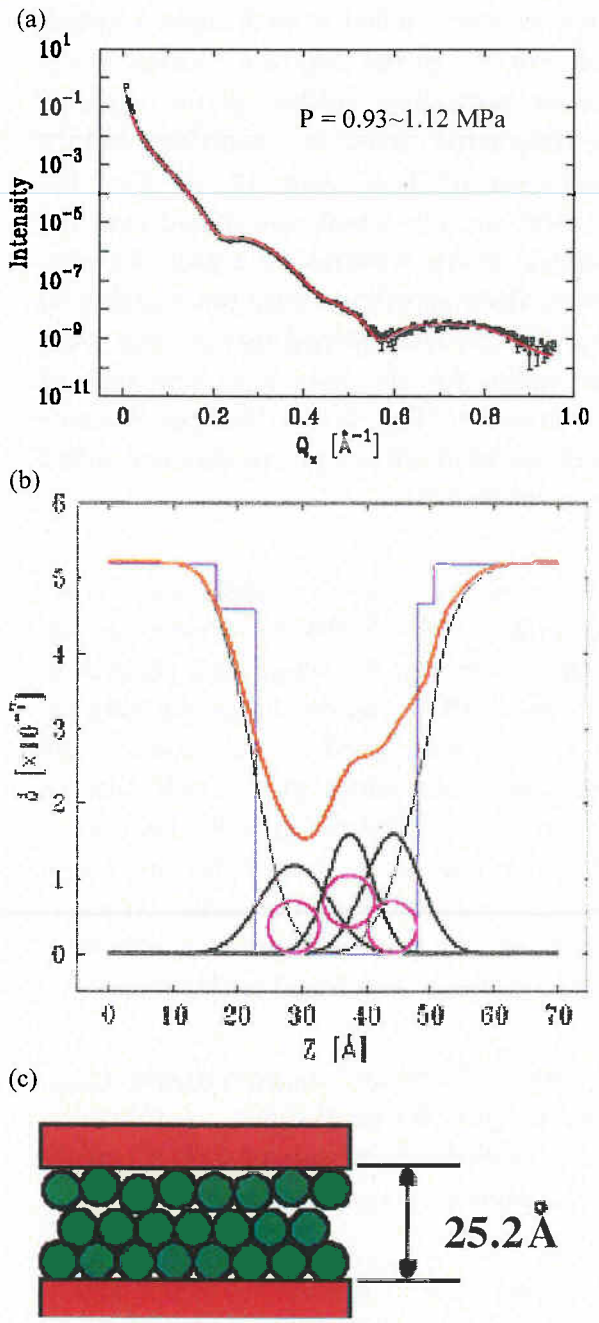

Fig. 2.41. (a) Measured and modeled reflectivity for pressures between 0.93 and 1.12 MPa. Fitted curve uses the electron density model shown in (b). This model is schematically represented in (c).

Temperature control is the most important issue for the high-temperature powder diffraction experiments. A uniform temperature applied on the entire sample volume is a critical requirement for the design of high-temperature furnaces. In collaboration with a group from Ames Laboratory, a high-energy furnace (up to 1500°C) has been designed (Fig. 2.42) specifically for use with high-energy x-rays employing transmission diffraction geometry (Margulies et al., 1999). This allows for full bulk sampling, low thermal gradients (<1°C/mm), and precise control of the sample environment. Unlike the flat-plate geometry, the transmission geometry allows the solid-liquid, as well as solid-solid, phase transitions to be studied. For example, in a study of the phase transition of α– to β–TiRh, high-quality time-resolved data was obtained at 60 keV (Fig. 2.43). There is disagreement in the literature as to whether this phase transition is first or second order. The data clearly show the coexistence of both phases over a narrow temperature range.

We are continuously developing improved versions of the furnace that can reach even higher temperatures with easier alignment and are exploring research projects that can utilize the capability of the high-temperature powder-diffraction technique.

Clathrate thermoelectric materials

There is considerable interest in developing new materials for thermoelectric applications that might allow the replacement of current refrigeration technology with efficient, all-solid-state

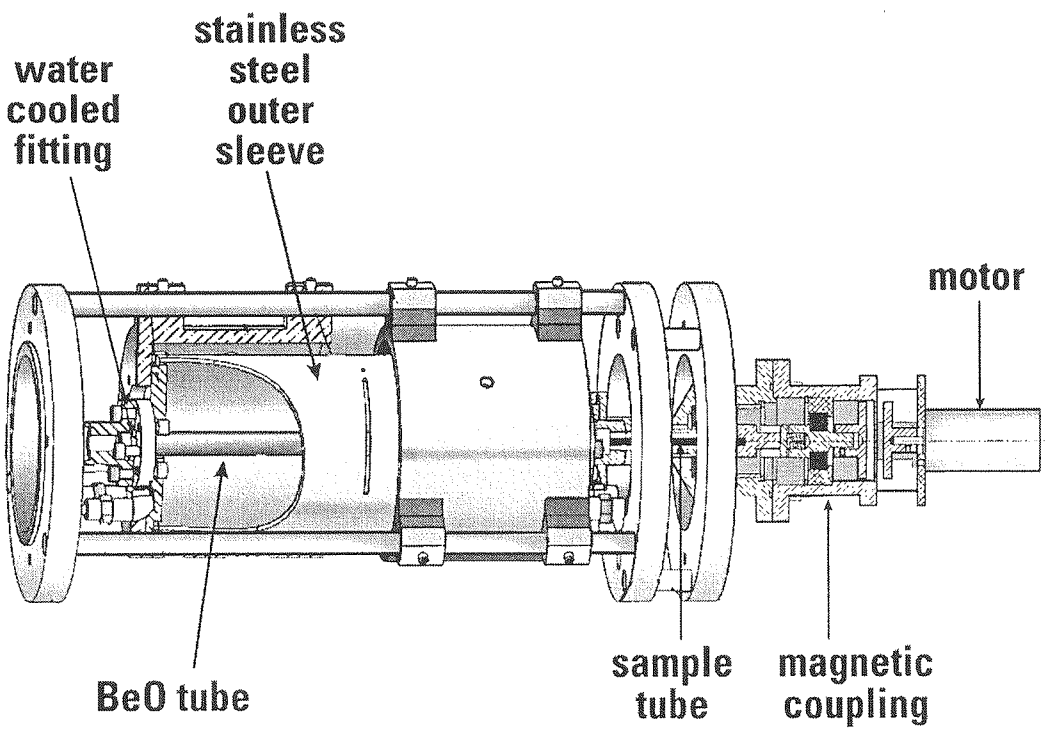

Fig. 2.42. Schematic of the furnace used in the time-resolved studies.

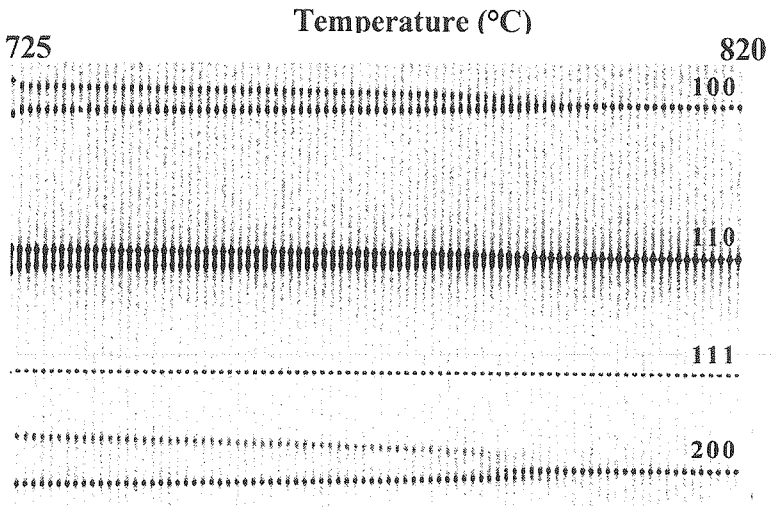

Fig. 2.43. A section of image plate showing the tetragonal to cubic phase transition in TiRh, area of transition. The stripes are individual "snap-shots" taken every 8 seconds.

devices. Semiconductors with a clathrate structure are attractive candidate thermoelectric materials. They consist of 3D frameworks of covalently bonded Si, Ge or Sn, with species, such as Cs, Rb, K, Na, Sr, or Eu, rattling inside cavities in the framework. The frameworks are typically heavily doped and can be constructed from face-sharing polyhedra of various types and sizes (see Fig. 2.44 for an example structure).

The disorder associated with the vibrational motion of species inside the framework cavities and any disorder introduced by doping the framework can have a profound impact on the thermoelectric properties of these materials. The rattling of species in the cavities ("cages") reduces the material's thermal conductivity and the distribution of dopant ("guest" atoms) over the available framework sites influences the electronic structure of the materials. A more complete understanding of the disorder induced by the guest atoms inside their oversized cages would not only lead to a better understanding of the transport properties but may also enable one to predict transport properties from a structural analysis. Therefore, accurate structure analysis is a vital part of this research project.

For this kind of analysis, a few important criteria for the powder-diffraction data are: high-order reflections, minimal absorption corrections, and good signal-to-background ratios (especially at high orders). Employing high-energy x-rays allows the collection of high-order reflections and reduces absorption effects, especially if some of the guest atoms are high-Z elements.

In collaboration with A. P. Wilkinson and R. A. Young from Georgia Institute of Technology, S. B. Schujman and G. A. Slack from Rensselaer Polytechnic Institute, and G. S. Nolas from Marlow Industrial Inc., we have examined $Cs_8Na_{16}Ge_{136}$,

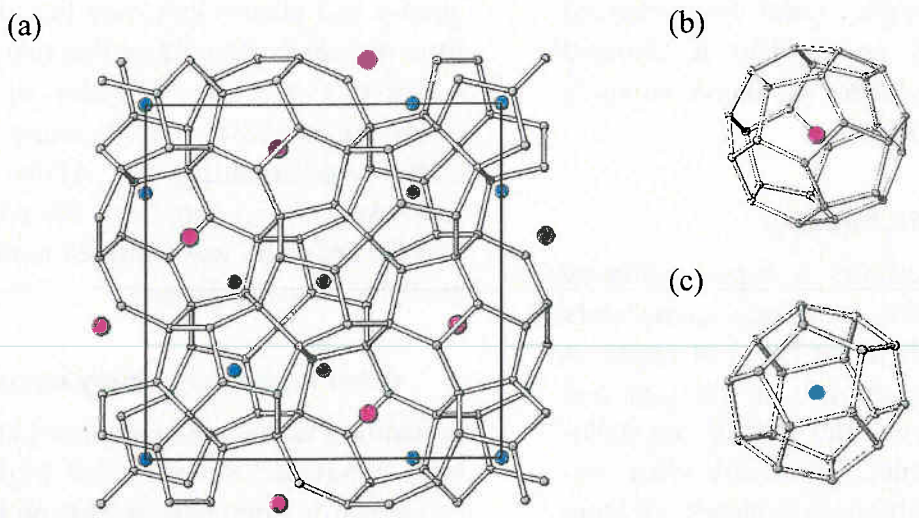

Fig. 2.44. The type II clathrate structure (a) adopted by $Cs_8Na_{16}Ge_{136}$ and its relatives can be constructed from face sharing (b) hexakaidecahedra and (c) dodecahedra.

$Eu_8Ga_{16}Ge_{30}$ and $Cs_8Cd_4Sn_{42}$. Powder diffraction data were acquired for the first two samples using 80 keV photons at temperatures of 20, 150 and 298 K. Data were obtained on the $Cs_8Cd_4Sn_{42}$ sample at 298 K using 80 keV photons and at wavelengths just below the Sn and Cd K-edges, respectively. In addition, a 20 K data set was obtained using a wavelength just below the Cd K-edge.

$Cs_8Na_{16}Ge_{136}$

In this material, Cs and Na occupy the hexakaidecahedral and dodecahedral cavities, respectively. The atomic displacement parameters (ADPs) for the Cs and Na indicate that they are heavily disordered at room temperature. However, on cooling to 20 K, the disorder associated with the Cs site disappears, but the Na still shows signs of disorder. Presumably this residual disorder is static in origin with the true location of the sodium being slightly displaced from the center of the dodecahedral cavity. The general quality of the fits to the diffraction data is good (Fig. 2.45), but the residual static disorder on the sodium site could not be modeled due to the relatively low x-ray scattering power of the sodium. A comparison of the ADPs obtained

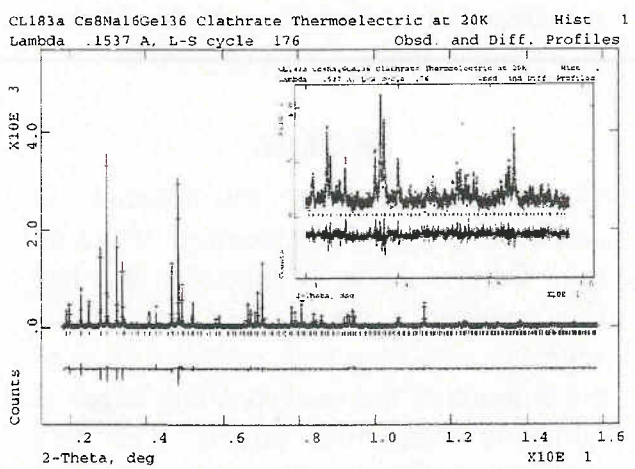

Fig. 2.45. A Rietveld fit to the data obtained on $Cs_8Na_{16}Ge_{136}$ at 20 K using 80 keV x-rays. Usable data were obtained out to ~16° 2θ, corresponding to a minimum d-spacing of around 0.55 Å (see inset).

from the powder diffraction data with those obtained from single-crystal data collected at temperatures above 100 K showed excellent agreement for the heavy atoms in the structure (Cs and Ge).

$Eu_8Ga_{16}Ge_{30}$

This material adopts a type-I clathrate structure with the europium completely occupying two different types of cages. A random distribution of the gallium and germanium over the three crystallographically distinct framework sites was assumed during the data analyses, as there was insufficient scattering contrast between the Ga and Ge to explore the possibility of dopant ordering. The ADPs for both Eu sites indicated considerable disorder at 298 K. At 20 K, the ADPs for one of the two distinct Eu sites showed very strong evidence for static disorder. As the europium scatters very strongly and data to relatively high Q were available, it was possible to model the disorder using four statistically occupied positions displaced from the cavity center. The use of a split site model gave significantly better agreement with the data than a simple model with a large ADP.

$Cs_8Cd_4Sn_{42}$

The structure analysis for this material was performed using a combination of the 80 keV, Cd K- and Sn K-edge data that had been collected at 298 K. The Cd and Sn K-edge data sets were both collected close to the bottoms of the corresponding edges to minimize absorption effects. The data analysis indicated that the cadmium predominantly occupies only one of the three available framework sites. The fit to the 20 K data set was of very high quality and clearly indicated that there was little disorder of the Cs at this temperature, suggesting that the disorder of the Cs observed at 298 K was dynamic and not static. Additionally, the ADPs for the framework atoms supported the conclusion that the cadmium was confined to one of the available framework sites.

Other high-energy x-ray research

In addition to the work mentioned above, we have conducted several other high-energy powder-diffraction experiments on beamline 1-ID with outside user groups. These groups include Argyriou and coworkers (Argonne Materials Science Division); Gray and coworkers (Griffith Univ., Brisbane, Australia); and Kramer and coworkers (Ames Lab./Iowa St. Univ.). Measurements on liquids and amorphous materials have been made with Price, Saboungi, and coworkers (Argonne Materials Science Division); Billenge, Petkov, and coworkers (Michigan St. Univ.); and Zwanziger and coworkers (Indiana Univ.). High-energy stress/strain experiments have been conducted with Noyan (IBM) and Ustundag (Cal. Tech.); Pyzalla (Hahn-Meitner Inst., Berlin); Gnaupel-Herold (NIST, Gaithersburg); Winholtz (U. of Missouri-Columbia); and Varma and coworkers (Los Alamos National Laboratory).

2.6 High-Resolution X-ray Scattering

The high-resolution x-ray scattering program is focused on developing x-ray optics and applications: in particular, nuclear resonant scattering, inelastic x-ray scattering, and the application of high-resolution x-ray scattering techniques to fundamental measurements. *Inelastic nuclear resonant scattering* allows direct determination of partial phonon density of states in samples containing a suitable isotope with a low-energy nuclear transition. *Inelastic x-ray scattering*, on the other hand, enables measurement of phonon dispersion relations and form factors in single crystals and liquids. The emphasis in nuclear resonant scattering is developing unique applications, as this technique is more advanced in its instrumentation development. The emphasis in inelastic x-ray scattering is more on spectrometer development, in terms of resolution, throughput, and accuracy. The fundamental measurements are related to in-depth analysis of normal incidence diffraction, absolute wavelength measurements, and analysis of radiation from rotating frames, in the long pursuit of μeV-resolved spectroscopy.

2.6.1 Nuclear Resonant Scattering

Phonon-assisted nuclear resonant scattering of synchrotron radiation is a method originally developed by the group in 1995 (Sturhahn et al., 1995), following the successful development of meV resolution, tunable monochromators (Toellner et al., 1992; Mooney et al., 1994). With the availability of the 3-ID undulator beamline, the group continued to improve the method, by first reducing the energy resolution to under 1 meV (Toellner et al., 1997), and then applying it to samples under extreme *high pressure*, to *thin films and multilayers*, and to *biological systems*.

These applications are chosen based on their scientific merit, the unique nature of inelastic nuclear resonant scattering, or because other established methods in particular areas can be considered limited.

2.6.1.1 High-pressure applications

Properties of materials change drastically under high pressure. In particular, accurate knowledge of the equation of state of iron under high pressure has special importance in geophysics, since iron is the dominant component in the earth's core.

In collaboration with Geophysical Laboratories of the Carnegie Institute of Washington, the high-pressure group at the University of Paderborn, Germany, and the GSE-CARS-CAT of The University of Chicago, we have developed the necessary technology to measure phonon density of states under high pressure. The x-rays must be focused to a size smaller than 5 microns in diameter, and multiple avalanche photodiode (APD) detectors need to be mounted a few millimeters from the sample for a large solid-angle coverage. The final setup, shown in Fig. 2.46, incorporated a Kirkpatrick-Baez mirror system (Eng et al., 1998), a modified diamond anvil high-pressure cell, and three modified APD detectors. This is a permanent setup, placed in the 3-ID-B station for outside users.

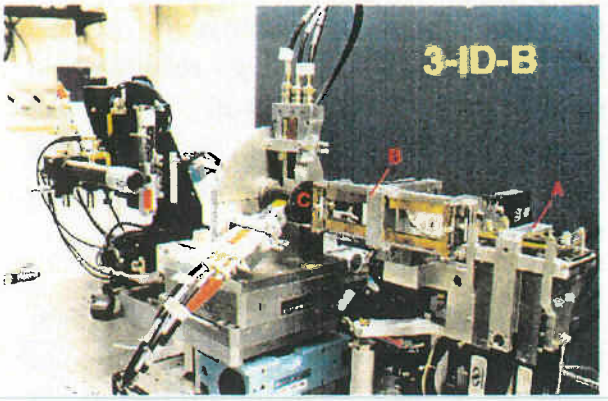

Fig. 2.46. The high-pressure setup in station 3-ID-B. Vertical (A) and horizontal (B) focusing mirrors in Kirkpatrick-Baez geometry reduce the beam size to under 5 microns in diameter. The diamond anvil cell is specially designed to accommodate three avalanche photodiode detectors (C), providing a 40% solid angle coverage. Very small samples of the order of several nanograms are sufficient.

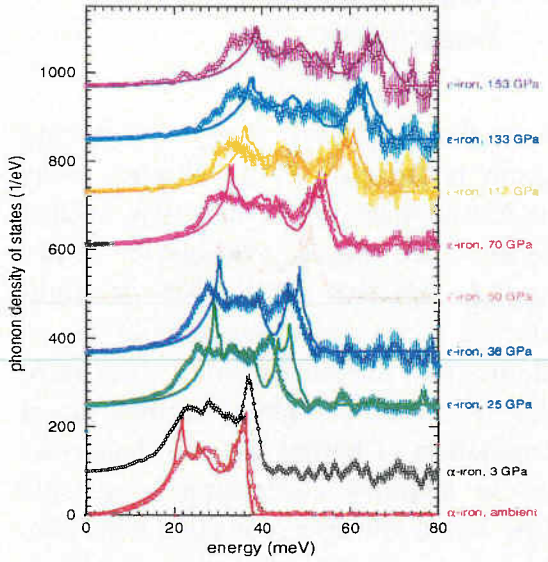

Fig. 2.47. The phonon density of states of Fe under high pressure. The solid lines are ab initio theoretical calculation (Toellner et al., 1997). The data were taken with 2 meV resolution.

The experiments were carried out for pure iron metal and wustite (FeO). The highest pressure reached is 153 GPa. Previous measurements that provided parameters for the equation of state were limited to 42 GPa.

From the data shown in Fig. 2.47, one can also extract model-free vibrational kinetic energy, zero-point energy, heat capacity, entropy, and Debye temperature (Mao et al., submitted) (see Fig. 2.48). Furthermore, using the Debye-like low-energy region of the excitation spectrum between 2-13 meV, it is possible to extract phonon velocities, which in turn, allow determination of bulk and shear moduli. This study shows that it is possible to measure complete elastic parameters up to pressures reaching that of earth's outer core. The elastic, thermodynamic, and energy parameters are essential for interpretation of seismological

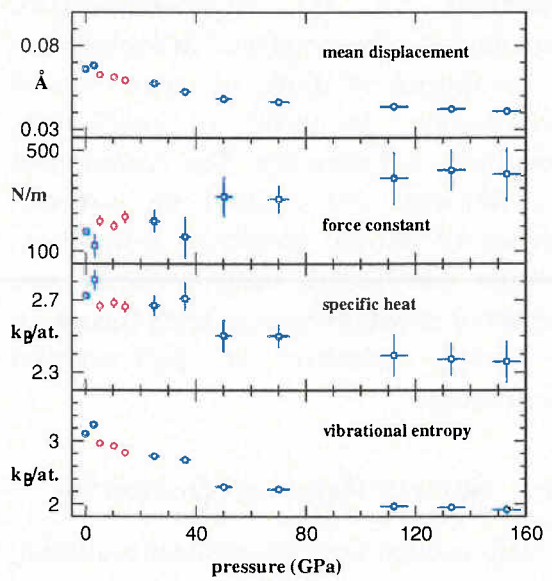

Fig. 2.48. The derived dynamical properties of iron metal as a function of pressure. The red data points are taken with a pressure medium to insure isotropic distribution.

observations and for numerical modeling of planetary cores.

One critical aspect of these measurements is the resolution function. The sharper the resolution function, both in terms of width and tails, the more reliable is the extraction of phonon velocities. Currently, the lowest possible resolution function with practical flux for measurements is 0.66 meV at the 14.4 keV ^{57}Fe nuclear transition. However, this 2-bounce monochromator is not compatible with microfocusing optics. A new type, 4-bounce nested monochromator, consisting of a novel mechanical concept called "artificial channel-cut" is being developed by the XFD synchrotron radiation instrumentation engineering group (Shu et al., submitted). Following the first successful implementation of this concept at 21.6 keV, we are now ready to build a 1 meV, in-line geometry monochromator to improve the quality of these experiments at 14.4 keV for ^{57}Fe and at 23.88 keV for the ^{119}Sn nuclear resonance.

The high-pressure measurements have also been extended to the ^{119}Sn isotope with an energy resolution of 1 meV at 23.88 keV (Fig. 2.49).

Improvements in monochromatization band-pass are considered to be a high priority. Along this line, the energy bandpass at 23.880 keV ^{119}Sn nuclear resonance has been further reduced to 0.5 meV by using two dispersive Si (12 12 12) crystals. The result, shown in Fig. 2.50 indicates that, as the resolution improves, the low dispersion points become more visible, thus providing even more stringent tests for the theoretical models and calculations.

The methodology for ^{119}Sn was developed as part of the PhD thesis of Dr. Michael Hu (Hu, 1999; Hu et al., 1999a; Hu et al., 1999b).

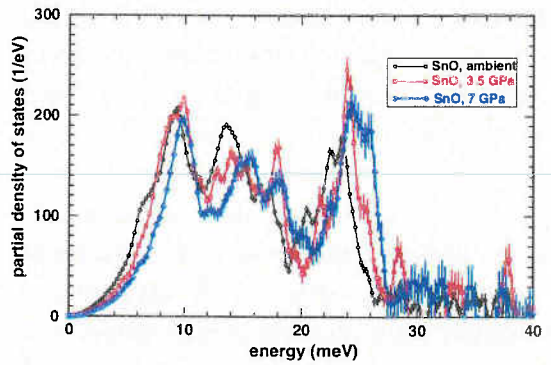

Fig. 2.49. The partial phonon density of states of SnO, measured up to 7 GPa with 1 meV overall resolution.

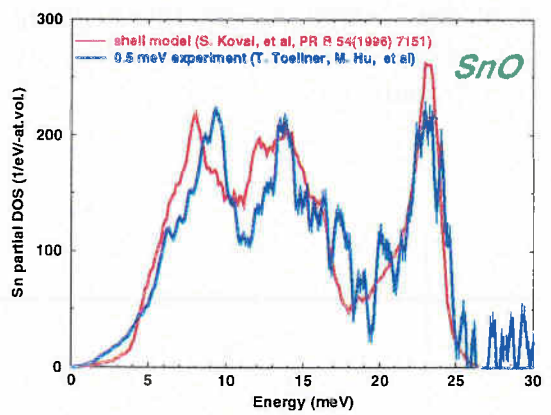

Fig. 2.50. The partial phonon density of states of SnO measured with 0.5 meV resolution and compared to the published result (Koval et al., 1996; Toellner, 2000).

2.6.1.2 Biological materials and organic molecules: Dynamics of proteins

X-ray scattering techniques have provided valuable information to understand the structure of biological systems. While diffraction techniques provide static information at the interatomic distance level and small angle scattering is used to learn about the intermediate range order, the dynamical information is limited to Debye-Waller factors. The "snap-shot" experiments provide nanosecond-resolved structural information. However, full dynamical information requires knowledge about the vibrational frequencies and dispersion of collective modes. The relationship between folding chains and active centers is an important part of the function of proteins. In this context, inelastic nuclear resonant scattering may play an important role as Fe is at the center of the heme group of protoporphyrin and acts as a binding site for O_2, CO, and H_2O.

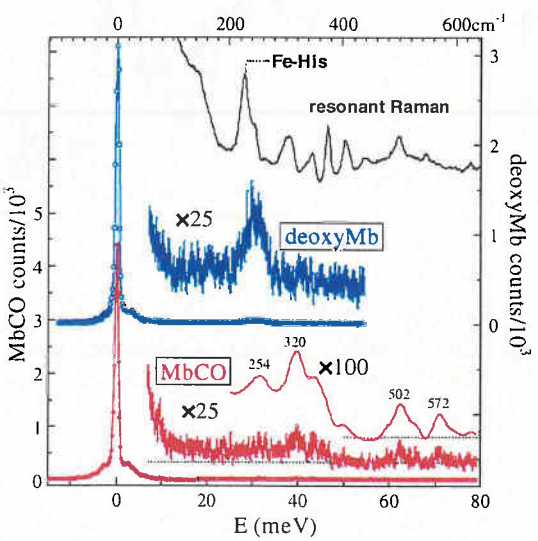

Fig. 2.51. The effect of CO on heme-group vibrations measured by inelastic nuclear resonant scattering.

Application of the nuclear resonant inelastic x-ray scattering (NRIXS) technique to biological materials with resonant isotopes at positions that are functionally important is very promising. In fact, NRIXS is the only method to provide reliable information below ~ 10 meV about such biologically active centers. The opportunity for systematic investigation of vibrational dynamics of biomolecules was realized at beamline 3-ID. We initiated outside collaborations [with T. Sage (Northeastern University), S. Durbin (Purdue University), and F. Parak and K. Achterhold (Technical University of Munich)] and initial experiments involve the oxygen-storing protein myoglobin (Mb). The NRIXS spectra of MbCO and deoxy-Mb are shown in Figs. 2.51 and 2.52. An energy resolution of 0.85 meV permits reliable determination of excitations down to ≈ 2 meV. In this experiment, the protein was

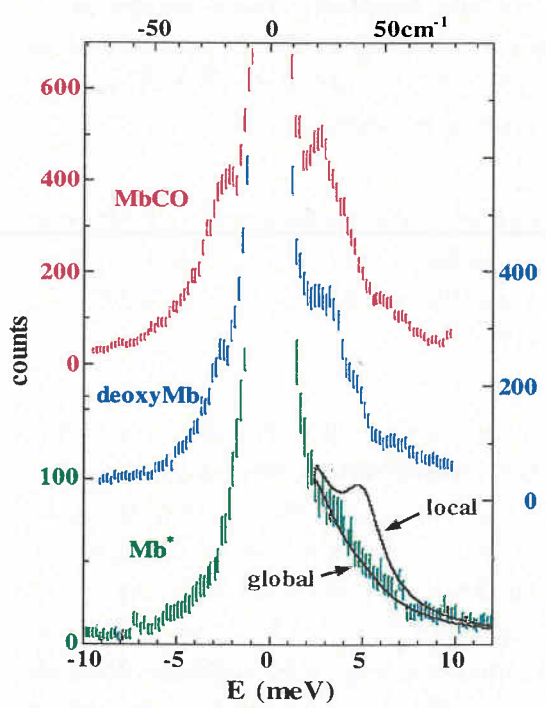

Fig. 2.52. The influence of CO ligation on the lower frequency heme vibrations.

solved in glycerol. The ^{57}Fe concentration was merely 7-10^{-5}.

In addition to NRIXS measurements, the technique of nuclear forward scattering provides unique data about interval fields and relaxation effects in the sub-meV regime (Keppler et al., 2000). The collaboration with Dr. T. Sage (Northeastern University) and Dr. S. Durbin (Purdue University) is focused on the photolysis of CO in myoglobin and on the properties of standard compounds (Sage et al., unpublished). The 3-ID beamline is the only place in any synchrotron radiation facility that has the resolution and the flux necessary to carry out such measurements at the present time.

2.6.1.3 Thin films, multilayers, and amorphous materials

The investigation of vibrational dynamics of thin films or multilayer structures has been traditionally difficult. In particular, excitation with larger momentum transfer (i.e., light scattering is not applicable), was almost inaccessible. NRIXS provides a unique solution to this situation.

The effect of confining a light element with a heavy element in a multilayer structure was studied in a Fe-Au multilayer structure, prepared in collaboration with the thin film group of the Materials Science Division of ANL (S. Bader, E. Fullerton, M. Grismdtich, and H. Sowers) and was characterized by various methods. The result is shown in Fig. 2.53.

The capability of NRIXS for determination of local phonon density of states (DOS) was demonstrated by measurements of ^{57}Fe monolayers deposited at the interface or interior of a ^{57}FeCr multilayer (Keune and Sturhahn, 1999) (see Fig. 2.54). In the Fe-Au system, we observe a pronounced softening of the vibrational modes with decreasing

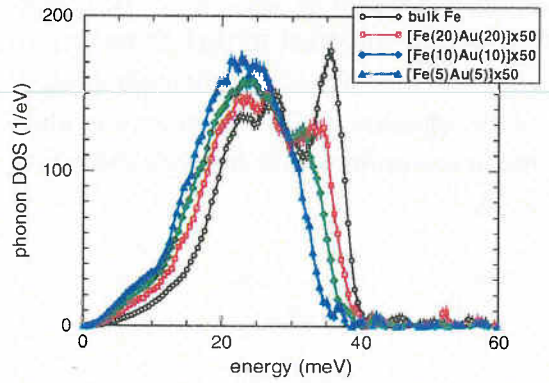

Fig. 2.53. The iron phonon density of states for Fe/Au multilayers with varying thickness. The x-ray diffraction and conversion electron Mössbauer spectroscopy results indicated that the Fe layers remain intact and magnetic, while the dynamical properties are changed drastically.

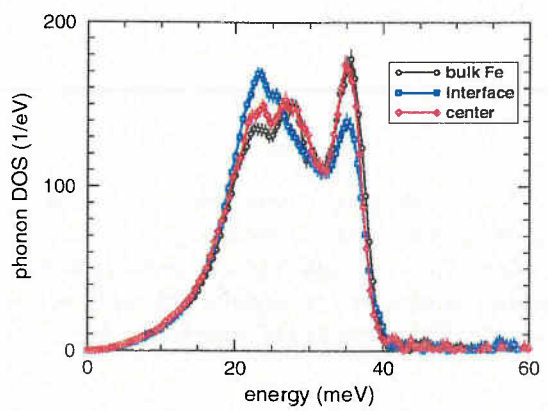

Fig. 2.54. The isotopic selectivity of nuclear resonant scattering is demonstrated in this experiment. The ^{57}Fe minelayer is selectively deposited either at the center of ^{56}Fe or at the Fe/Cr interface. When combined with nuclear forward scattering, it is possible to obtain chemical, magnetic, and dynamic behavior at the same time.

thickness of the Fe layers. Modes around 36 meV that are very strong in bcc Fe, almost completely disappear at the expense of excitations around 23 meV in the multilayer. The effects in the FeCr are subtler. The same principal behavior is observed at the interface; however, if the ^{57}Fe tracer layer is placed in the center of the ^{56}Fe layers, the DOS is almost identical to that of bcc iron. We also note a slight shift at the high-energy end of the spectrum. This technique is also applied to amorphous thin films as shown in Fig. 2.55.

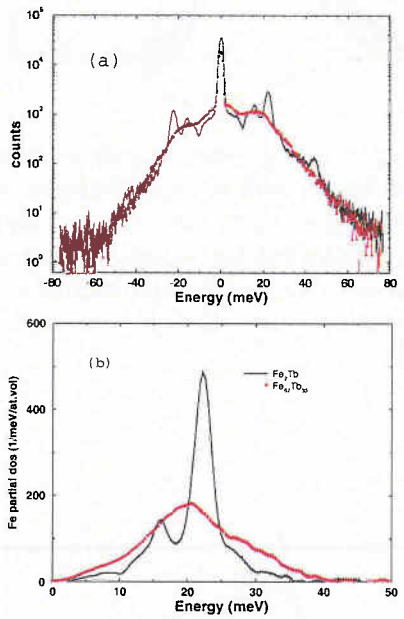

Fig. 2.55. The effect of crystalline-amorphous phase transition on phonon density of states in a Fe_2Tb alloy. The raw data clearly indicate the two-phonon contributions around 40 meV, as well as the quality of the signal over 5 decades.

2.6.2 Inelastic X-ray Scattering

2.6.2.1 A new spectrometer with 2 meV resolution for inelastic x-ray scattering

X-ray scattering with an energy resolution of a few meV provides a tool for investigating phonon excitations in condensed matter. In contrast to inelastic neutron scattering, there are virtually no limitations in the accessible energy-momentum space arising from the mass of the probe. In particular, for non-crystalline matter, this is an important advantage, because the collective dynamics has to be investigated at low momentum transfers and high energy transfers, a region difficult to access with conventional neutron scattering. Experiments at the European Synchrotron Radiation Facility (ESRF) with inelastic x-ray scattering on liquid and amorphous samples have attracted considerable attention during the past five years (see, e.g., measurements on liquid water by Sette et al., 1995; and on liquid lithium by Sinn et al., 1997).

The new spectrometer at station 3-ID-C is a state-of-the-art instrument that allows one to perform inelastic measurements with comparable or superior flux and resolution compared to the ESRF spectrometers. The monochromatization at 21.657 keV is achieved by a combination of a water-cooled diamond high-heat-load monochromator and an in-line monochromator that consists of two nested channel-cut crystals (Fig. 2.56).

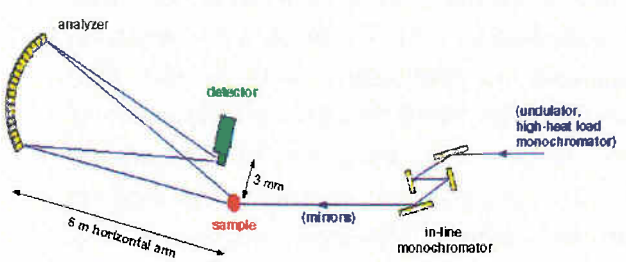

Fig. 2.56. Inelastic spectrometer at station 3-ID-C.

Development of the outer channel-cut of the monochromator, a so-called artificial channel-cut, allows one to adjust the two crystals with a mechanical precision of a few nanoradians with respect to each other.

The energy transmitted through the monochromator can be varied in a range up to about 100 eV by rotating the two channel-cuts. The flux at the sample is 3×10^8 photons/sec in a spot size of 150 μm × 150 μm.

For the energy analysis, the (18,6,0) reflection of a spherically bent silicon disk was used in backscattering geometry (θ_{Bragg}= 89.98°) at about 6 m from the sample. In order to avoid bending stress, the silicon is diced into 1 mm large pieces. The radiation from the analyzer is collected by a semiconductor (Cd-Zn-Te) detector developed for backscattering geometry.

In order to change the scattering angle at the sample, the analyzer and detector have to be rotated around the sample. To achieve this, the analyzer is mounted on a 2-m-long x-z-slide, which can position the analyzer. The detector is rotated independently. To maintain the backscattering alignment, an optical feedback system is applied.

Within the geometrical limitation of the hutch, a maximum scattering angle of 15 degrees is possible, which corresponds to a maximum momentum transfer of about 3 $Å^{-1}$. An extension to 5 $Å^{-1}$ is possible by deflecting the beam before the sample with a germanium (111) reflection in the horizontal scattering plane. The loss of intensity due to this extra reflection is about 30%.

Commissioning of the 2 meV spectrometer

The energy resolution of the spectrometer can be determined by measuring the energy width, if (ideally) a pure elastic scatterer is used as a sample. In a good approximation, Plexiglas® at the structure factor maximum (1 $Å^{-1}$) can be used as such a sample. An energy scan with a 10 mm thick Plexiglas® sample revealed an energy width of 2.2 meV (see Fig. 2.57).

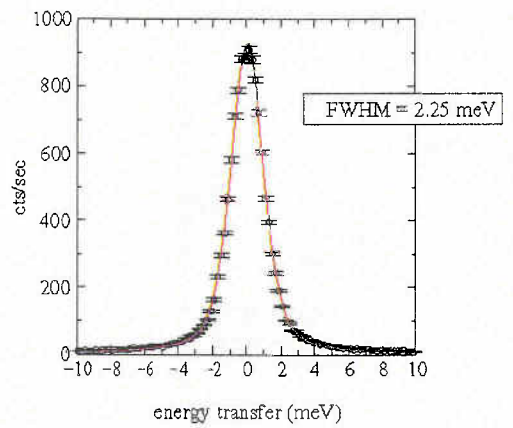

Fig. 2.57. Overall resolution function of the spectrometer.

To determine the accuracy of the energy scale, we measured phonon dispersion curves in a single crystal of beryllium. In Fig. 2.58, individual energy scans at different ζ values are shown. The position of the phonon peaks at ω≠0 yields the phonon dispersion for a particular phonon branch. The dispersions for the LA-TA and the LO-TO branches are shown in Fig. 2.59 and compared to literature from neutron experiments. The agreement is excellent and the deviations between the x-ray and neutron data are ≤ 2%, close to the statistical error of the data (Sinn et al., submitted).

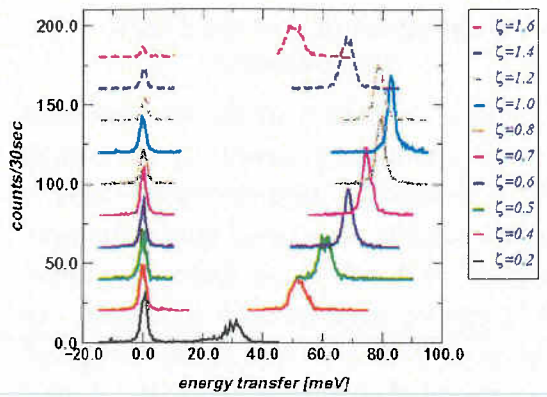

Fig. 2.58. Energy scans at different momentum transfers in a beryllium single crystal.

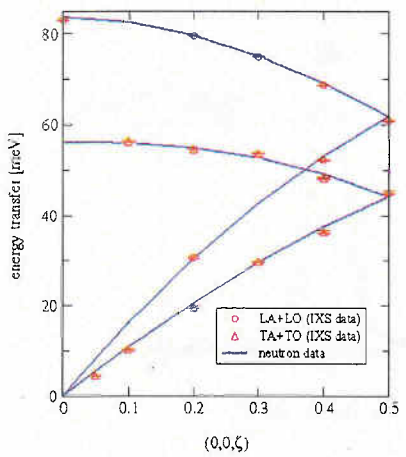

Fig. 2.59. Phonon dispersion in beryllium.

2.6.2.2 Inelastic x-ray measurements on liquid aluminum

Collective excitations in liquids have been extensively investigated in the recent years both experimentally and theoretically (see, e.g., Balucani and Zoppi, 1994). One characteristic feature of the collective excitations is the so-called positive dispersion, an increased slope in the dispersion relation compared to the macroscopic sound velocity. In alkaline metals this effect is of the order of 10-20% and can be explained by a viscoelastic shear modulus at high frequencies. In liquid water, however, a positive dispersion of more than twice the macroscopic sound velocity is observed (Sette et al., 1995); understanding the magnitude of this effect is still the subject of discussions. In one theoretical paper (Balucani et al., 1993), the authors suggest that the positive dispersion in water has the same origin as that in alkaline metals but is enlarged due to the high Einstein frequency in water. In liquid aluminum, the Einstein frequency is between those of the liquid alkaline metals and water, and therefore the magnitude of the enlargement of the sound velocity is expected to be in between water and the alkaline metals. Until now, no experimental data existed to check this hypothesis quantitatively.

We measured liquid aluminum at slightly above the melting point (at 1000°C) in a range of momentum transfers between 0.2 $Å^{-1}$ and 1.4 $Å^{-1}$. The preliminary results of the normalized intensity spectra $S(Q,\omega)$ are shown in Fig. 2.60. By transforming the data to the current-current correlation function

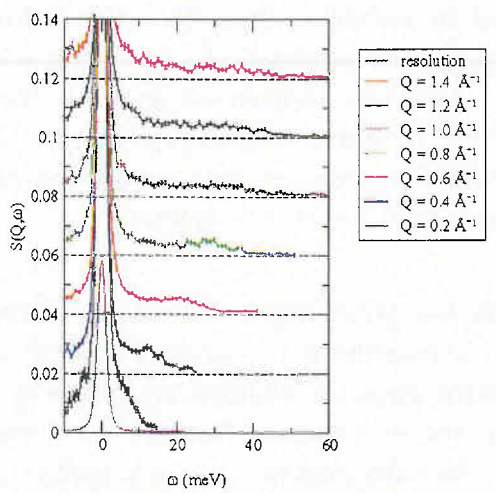

Fig. 2.60. Inelastic spectra for liquid aluminum for different momentum transfers.

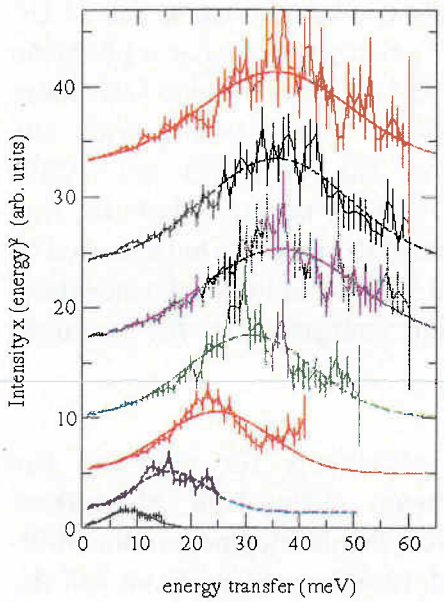

Fig. 2.61. Current-current correlation functions for the spectra shown in Fig. 2.60.

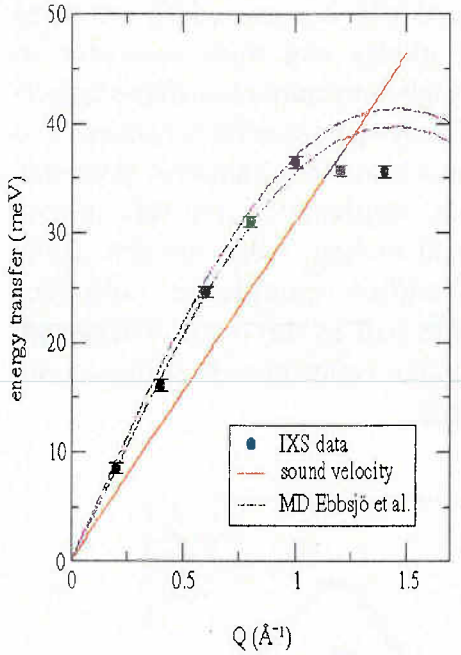

Fig. 2.62. Dispersion of the collective modes in liquid aluminum, derived from the current-current correlation function.

$C(Q,\omega) = \omega^2 S(Q,\omega)$, one can extract a dispersion relation (Figs. 2.61 and 2.62). A strong positive dispersion is observed, which also coincides with findings from computer simulations (Ebbsjoe et al., 1980). A further analysis of the data will reveal a more quantitative determination of the positive dispersion and of the damping of the modes (Sinn et al., submitted).

2.6.2.3 Investigation of collective excitation in lithium-ammonia mixtures

Solutions of alkali metals in ammonia have been investigated for over a century due to their many interesting properties. In these systems the outermost electron of the alkali metal separates from the ion, resulting in a free electron and an alkali metal ion. By variation of the metal concentration, one can change the electronic state of the system from an insulator to a liquid metal.

We performed measurements in a saturated solution of lithium in ammonia, where the system is a good metal. Energy scans at different momentum transfers are shown in Fig. 2.63. The curve at the bottom shows the resolution function of the spectrometer. As visible already in these raw data, there is a strong variation of the shape of the spectra with increasing momentum transfer. This is an indication for a collective mode dispersing at low momentum transfer with a speed close to the macroscopic sound velocity but also showing a strong softening around two times the Fermi momentum k_f for this system. This phenomenology is completely different than in pure ammonia. Rather than viewing the lithium–ammonia system as a incoherent mixture, stable complexes are most likely forming that consist of one lithium-atom surrounded by four ammonia atoms and that vibrate as one unit.

The surprisingly narrow width of these collective modes and their existence to relatively high momentum transfers suggests that the effective pair potentials between two complexes is close to a harmonic potential. A possible explanation for this unique experimental finding is that the size of the ammonia-lithium complexes coincides almost with half of the Fermi wavelength for this lithium concentration (Burns et al., unpublished).

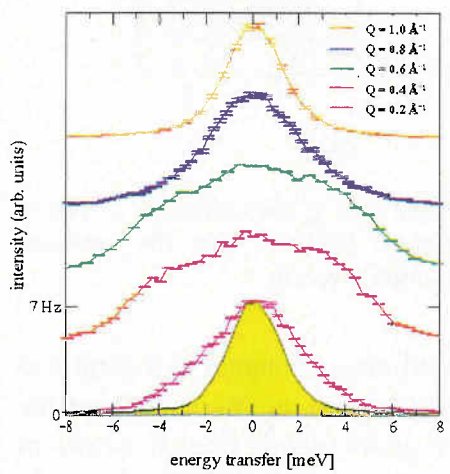

Fig. 2.63. Energy scans in a lithium-ammonia mixture for different momentum transfers.

2.6.3 Fundamental Measurements

2.6.3.1 Normal incidence diffraction in Si and Al_2O_3

High-resolution x-ray scattering takes advantage of special properties of crystals when the Bragg angle is near or at 90°, thus diffracting the beam practically onto itself. It is well known that the energy bandpass reaches its minimum value, while the angular acceptance is at its maximum. Multiple beam diffraction also accompanies the back-diffracted beam. Since this particular geometry is used for monochromatization and energy analysis, a detailed study was carried out, as part of Dr. John Stutter's thesis under joint supervision with Prof. R. Collela of Purdue University (Sutter, 2000). For silicon, with the exception of the Si (111) and (220) reflections, there is no multiple-beam free diffraction at 90 degrees. We have studied Si (12 4 0) and Si (18 6 0) in detail, since these are relevant energies for the ongoing programs.

The key ingredients for studying the multiple beam diffraction at normal incidence were the development of the milli-eV-resolved, tunable incident beam and the n-beam computer program (developed by Collela and modified by Sutter). The striking aspect of these measurements is the reduced reflectivity near the 90° Bragg angle: in an angular region of 40 μrad, the reflectivity drops to the 2% level. The shape of the resolution function is also critical, which is close to a Lorentzian with wide tails. The schematic general description is given in Fig. 2.64, and measurements are shown in Fig. 2.65.

The results of these studies have serious implications for high-resolution mono-chromatization and analysis, as well as x-ray Fabry-Perot interferometers. In an attempt to improve the efficiency of the diffracted beam, we have tried to identify other crystals with lower symmetry. It was suggested earlier that Al_2O_3 might be a good candidate.

We have pursued this option in collaboration with Dr. Yuri Shvydko (University of Hamburg). Among a dozen crystals tested, the standard and high-purity HEMEX crystals obtained from Crystals Systems,

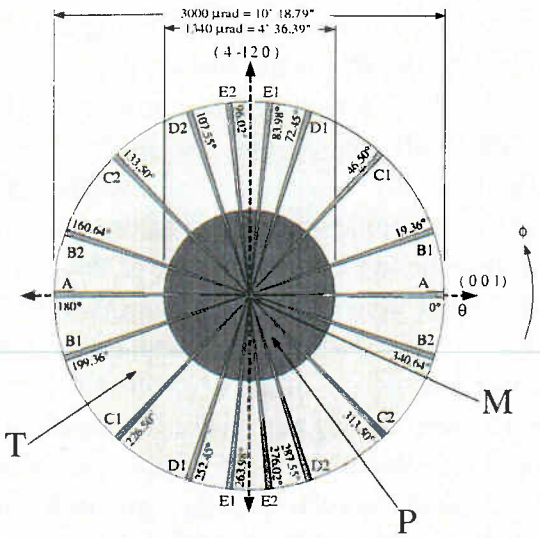

Fig. 2.64. A polar plot of all the multiple-beam cases occurring with Si (12 4 0) at 14.4381 keV. The angle ϕ is measured from the reciprocal lattice vector (001). The center of the plot is parallel to $-\mathbf{k_0}$ and antiparallel to the (12 4 0) vector. The distance from the center is proportional to the angle between $-\mathbf{k_0}$ and (12 4 0). The center region represents the strong 24-beam case close to exact backscattering. The letters A-E refer to conjugate pairs of reflections described in detail by Sutter et al. (in press).

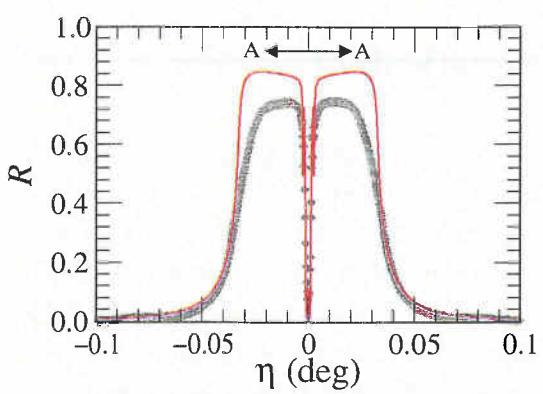

Fig. 2.65. Measured (gray) and calculated (red) reflec.6tivity of Si (12 4 0) at 14.438 keV measured under the normal incidence condition.

Inc., proved to have dislocation-free zones, and one of them gave the best result

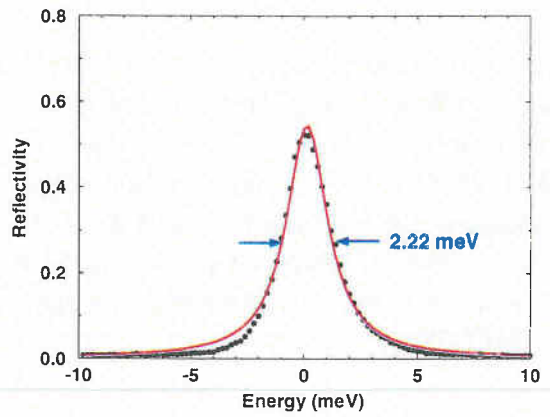

Fig. 2.66. The reflectivity of Al_2O_3 measured at 21.6306 keV, using a 1 meV bandpass incident beam. The Bragg angle is set to exactly 90°.

obtained to date, as shown in Fig. 2.66. The extinction depth for the Al_2O_3 (1 1 45) reflection is 133 μm. Therefore, dislocation-free crystals the size of the incident beam and a millimeter thick are necessary to have a good monochromator. Topographic investigations indicate a strong correlation between the dislocation density and reflectivity and resolution. These studies created the opportunity to realize the concept of exact backscattering proposed earlier.

2.6.3.2 X-ray wavelength standard

The narrow linewidth of some Mössbauer nuclei could be used as a length standard in the Angstrom scale, since they are easily reproducible with high accuracy. This wavelength is independent of temperature, pressure, and chemical condition of the sample at the part-per-trillion level. Prior to our measurements, the wavelength of the 14.4 keV Mössbauer transition of ^{57}Fe was known with an accuracy of 10 ppm: 14.413.00(15) eV (Bearden, 1965, 1967). The wavelength of ^{57}Fe Mössbauer radiation has now been determined with a relative

uncertainty of 0.19 ppm by using exact Bragg backscattering from a reference silicon crystal. The new value is 14.412497(3) eV. The new method takes advantage of the high brightness of the 3-ID beamline, with an undulator producing 14.4 keV radiation in the first harmonic (see Figs. 2.67 and 2.68).

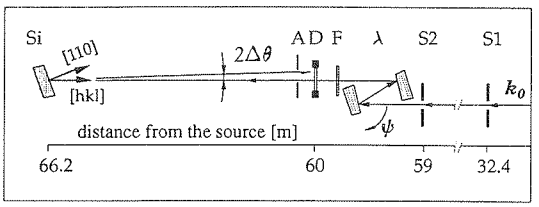

Fig. 2.67. The experimental setup. Slits S1 and S2 are set at 30 and 75 μm; λ: a λ-meter is a channel-cut Si monochromator whose temperature is kept constant within 2 mK and that is mounted on a Kohzu stage with 25 nrad resolution; F: an ^{57}Fe foil to provide Mössbauer radiation; D: a semitransparent APD detector; A: a 4 mm aperture to insure backscattering; and Si: the reference silicon crystal with a lattice constant of 5.43102030(36) Å.

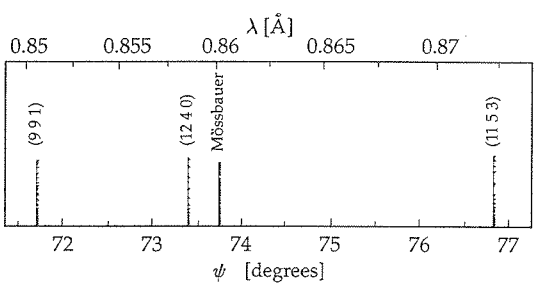

Fig. 2.68. Back-reflected and Mössbauer radiation in the detector plotted as a function of the angle of the wavelength-selecting monochromator λ, as shown in Fig. 2.67.

2.6.3.3 Instrumentation development

High-energy-resolution x-ray scattering experiments rely heavily on tunable, "in-line" crystal monochromators. When the resolution reaches 1 meV levels, the degree of asymmetry reaches near the Bragg angle, forcing the quality of the surface finish to be "mirror-like." Channel-cut single crystals are difficult to polish. In addition, a monochromatic x-ray beam delivered by a C (111) monochromator provides several millijoule power to the first face of the outer channel-cut crystal, causing a temperature difference of 100-200 mK compared to the second face of the same channel-cut. (The inside nested, higher order channel-cut crystal cuts down the energy bandpass from cV to meV level). Finally, geometrical restrictions dictated by crystal placement or allowable vertical offset makes simple-crystal channel-cut geometry impractical. These three unrelated difficulties can be overcome by separating the two faces of the outer channel-cut crystal and providing an artificial link between them. The mechanism described in section 3.3.4.4 was developed to solve this problem. The two separate crystals can be held together with better than 30 nrad angular stability, as shown in Fig. 3.28 (see section 3.3.4.4).

2.7 Polarization Studies

The main mission of the polarization studies program is to develop instrumentation and techniques that will utilize the high-brilliance, variably polarized x-ray beam produced from two undulators in sector 4. In addition, this sector will be used for application of x-ray scattering techniques and for high-heat-load testing of front-end components. To briefly review the main operational features, sector 4 has two branch lines, one for the "soft" (0.5 – 3 keV) and the other for the "hard" (> 3 keV) energy range. Variable polarization states will be provided in the soft x-ray regime by a

specialized circularly polarized undulator (CPU), while a planar undulator in combination with crystal optics will be used above 3 keV. A novel concept of spatially separating the beams from the insertion devices was implemented by placing the undulator axes at a small angle (270 μrad) with respect to each other. A dipole electromagnet between the devices introduces the angular deviation of the electron beam, so 30 m away in the first optics enclosure (FOE), the two beams are separated by 8 mm. This is sufficient to use two horizontally deflecting mirrors in the FOE to further separate the beams and direct the soft x-ray beam down the beam pipe. The implementation of this concept enables simultaneous operation of both branch lines and thus more efficient utilization of the delivered beam.

Since the last *Experimental Facilities Division Progress Report* (1998), major milestones have been accomplished. The construction and commissioning of all shielding enclosures were completed. The double-crystal monochromator for the hard x-ray branch was delivered in January of 2000, installed on the beamline in March, and the first monochromatic light was observed on April 1, 2000. Three additional components need to be installed in order to complete the construction of the hard x-ray branch: the phase-retarding tank, scheduled for installation in January of 2001, the focusing mirror chamber in April of 2001, and the flat mirror chamber in July of 2001. For the soft x-ray branch, the installation of horizontally deflecting mirrors and associated vacuum chambers are planned for January of 2001. The entire soft branch will be moved from sector 2 to sector 4 in October as well.

Despite heavy involvement in the construction of sector 4, the development and application of polarization-manipulation-related techniques continued in sector 1 for hard x-rays and, along with spectroscopic techniques, in sector 2 for soft x-rays. Several selected accomplishments are described below. They include characterization and application of a circularly polarized microprobe, temperature-dependent x-ray magnetic circular dichroism on rare-earth compounds, study of interfacial magnetism, exploration of magnetic anisotropy using polarized x–rays, microspectroscopy and imaging with photoelectron microscopy, x-ray-excited optical luminescence studies of oxidized porous silicon, and changes of a ferromagnet/insulator interface upon thermal annealing.

2.7.1 A Microfocused Circularly Polarized X-ray Probe for Energies between 5 and 10 keV

The magnetic contribution to the cross section for scattering of x-rays by matter is of significant scientific interest because of its capability to reveal information about the angular and spin momentum distribution in the scattering medium (Blume and Gibbs, 1988). We report here on a technique that combines microfocusing x-ray optics with Bragg-diffracting phase retarders for producing a circularly polarized x-ray microprobe in the energy range from 5 to 10 keV. Circularly polarized x rays are of particular interest since they couple linearly

to the magnetic moments. A microfocused x-ray beam will enable a wide variety of spatially resolved magnetic scattering experiments, yielding results in applied fields like modern magnetic materials and superconducting compounds, as well as in more basic physics. An important advantage of x-rays in the energy range from 5 to 10 keV is their relatively high penetration power, allowing real bulk measurements of magnetic samples and penetration through nonmagnetic surface layers. Unlike neutrons, x-rays can be used to probe for element-specific properties by working at a particular resonance.

For the energy range between 5 and 10 keV, Bragg-transmission phase retarders have proven to be the most practical approach for the production of a circularly polarized x-ray beam from a linearly polarized synchrotron beam (Hirano et al., 1991). Such phase retarders utilize the fact that, according to the dynamical theory of x-ray diffraction, the wave fields inside a crystal belonging to different linear polarizations propagate with different phase velocities close to a Bragg reflection. The phase difference thus induced is a linear function of the deviation of the angle of incidence from the exact Bragg condition (Lang and Srajer, 1995). Switching the beam helicity requires only minimal rotations of the phase retarder, which can be done even during the course of a measurement, thereby reducing systematic errors. Due to their low absorption, diamond crystals are exceptionally well suited for this application, with only a few crystals of different thickness required to cover the whole energy range between 3 and 12 keV. To produce x-ray beams with submicron cross section, microzone plates are a well-established tool (*X-ray Microscopy and Spectromicroscopy*, 1998). They can be understood as circular diffraction gratings with radially increasing line density, whose operation principle is based on Fresnel's theory of diffracting zones (Born and Wolf, 1980). In the non-diffraction-limited regime, zone plates focus the beam simply by de-magnifying the x-ray source. Since the different diffraction orders of a zone plate correspond to distinct focal lengths, a microfocusing experimental setup typically includes an order-sorting aperture (OSA), e.g., a pinhole, to reduce unwanted diffraction orders. The polarized microprobe was set up at the beamline 1-ID insertion device. Figure 2.69 shows the setup schematically. The undulator beam was collimated using white-beam tungsten slits close to the source. The radiation was then monochromatized using a standard liquid-N_2-cooled double-crystal Si (111) mono-chromator. An additional set of slits downstream of the monochromator was used to further define the beam to a size of 0.5×0.5 mm^2 at 60 m from the source. This beam was incident on the phase-retarding optics. For the phase retarder, a 400-μm-thick diamond in (111) reflection geometry was chosen. With an x-ray energy of 8 keV, the incident flux on the diamond was measured to be $\approx 2 \cdot 10^{12}$ photons per second, and the transmitted circularly polarized flux was $4 \cdot 10^{11}$ photons per second. The transmitted radiation had a degree of circular polarization of about 0.99. To suppress higher harmonics, the beam was reflected by a Pd-coated mirror placed behind the phase retarder. The beam path was enclosed in evacuated beam pipes to reduce the intensity loss due to air scattering. The microfocusing setup following the diamond consisted of two parts, the zone plate and the OSA. The

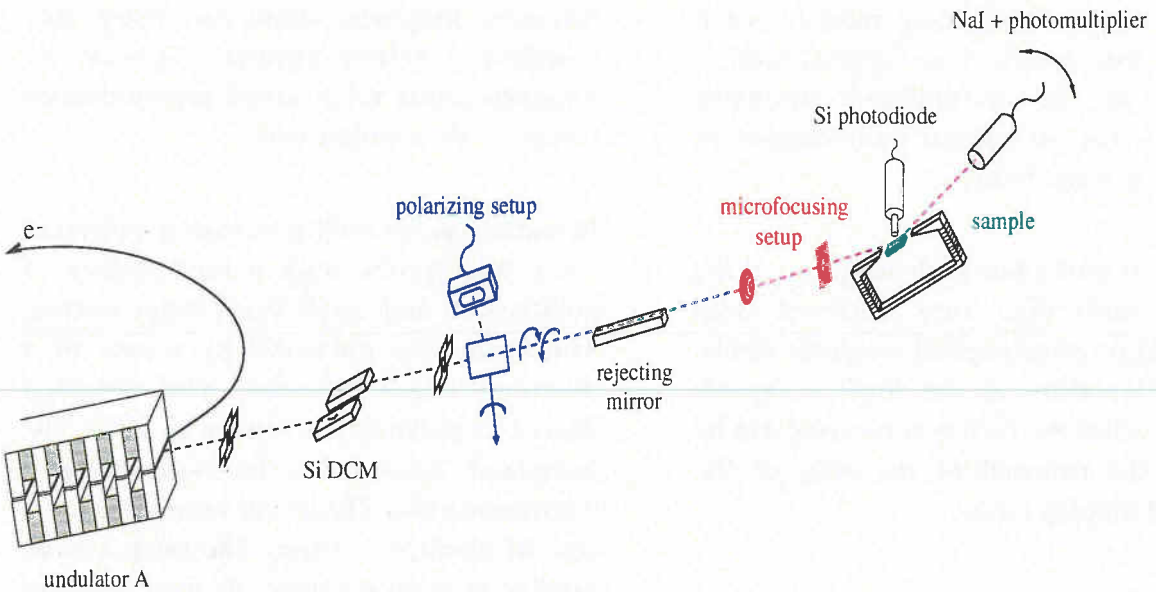

Fig. 2.69. The experimental setup on beamline 1-ID (DCM = double-crystal monochromator).

zone plate had a diameter of 250 μm and a focal length of about 40 cm at 8 keV. It was mounted on a three-axis motorized stage to allow the focused beam to be positioned on the sample. Pinholes of various sizes from 20 to 50 μm were used as order-sorting apertures. The sample was likewise mounted on a three-axis motorized stage in the center of a standard 8-circle diffractometer.

A switchable magnetic field of up to 0.8 T could be applied to the sample parallel to the beam. Two different kinds of detectors were employed to simultaneously monitor both the fluorescence yield and the Bragg-scattered intensity as a function of the position of the sample in the microfocused beam.

The size of the microfocused beam was measured by scanning a Cr-coated knife-edge horizontally and vertically through the beam. The Cr K-fluorescence of the knife-edge was measured as a function of its position in the focused beam. The optimum focus size that could be reached was 4.0×2.3 μm^2 (horiz. × vert.). Horizontally, the measured focus size agrees very well with the value calculated from the demagnification of the source. The vertical size was significantly larger than the calculated value. By temporarily clamping the knife-edge holder on the diffractometer to the zone-plate mounting, we showed that this difference is mainly due to vibrations of the knife-edge relative to the zone plate. For the mentioned focal size, we measured a flux on the order of 10^8 photons per second (Pollmann et al., 2000).

As a demonstration experiment, we used the microprobe to image magnetic domains in a $HoFe_2$ crystal at the Ho L_3 edge. Observing the (400) Bragg reflection of the crystal, two-dimensional scans were performed while reversing the helicity of the incident

beam to obtain the flipping ratio for each point on the sample. The flipping ratio is defined as the normalized intensity difference for orthogonal polarizations of the incident x-ray beam.

Figure 2.70 shows two such mappings of the flipping ratio that were obtained with oppositely oriented applied magnetic fields. The reorientation of the local magnetic moments when the field was reversed can be seen in the reversal of the sign of the measured flipping ratio.

Figure 2.71 shows the remanent magnetic structure of the $HoFe_2$ crystal, as measured without an applied field. In this case, a clear contrast of the measured flipping ratio at different regions of the sample can be discerned. These regions can be identified as different magnetic domains. Their size matched previous results obtained by magnetic force microscopy measurements (Srajer et al., unpublished).

In summary, we built a circularly polarized x-ray microprobe with a high degree of polarization and small beam cross section. The beam was polarized by means of a diamond phase retarder. The obtained degree of polarization was up to 99%. The polarized beam was focused using a microzone plate. The useful beam spot had a size of about 4 × 2 μm. The setup can be used to perform magnetic domain mapping measurements on materials like spring magnets or magnetic multilayers. To improve the spatial resolution, the use of a microzone plate with smaller zone structure is planned.

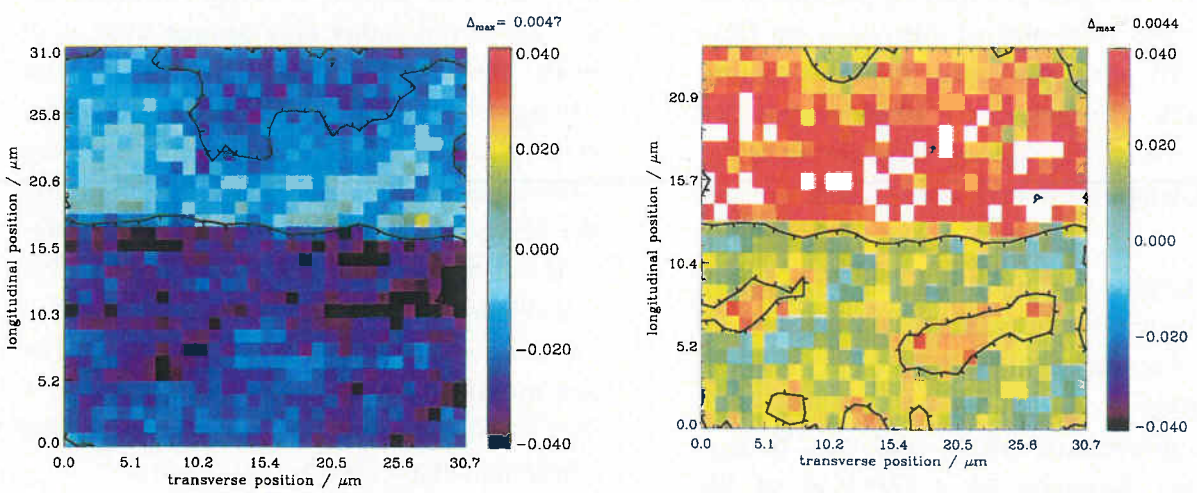

Fig. 2.70. Two-dimensional mappings of a $HoFe_2$ crystal for a field of 0.43 Tesla, applied with opposite orientations. The magnitude of the field was sufficient to align the sample parallel to the applied field. The flipping ratio changed sign.

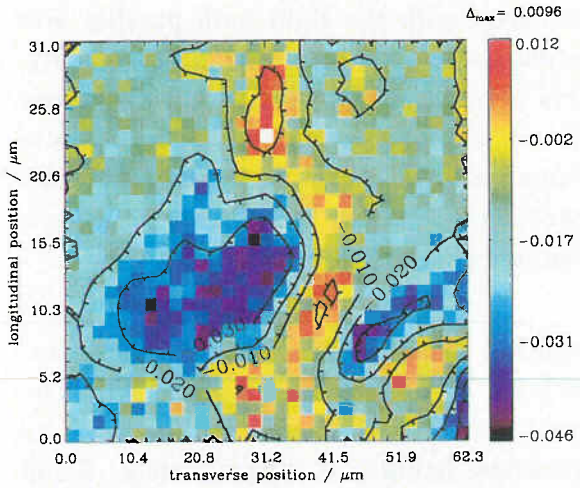

Fig. 2.71. Two-dimensional mapping of the remanent magnetic structure of the $HoFe_2$ crystal. Magnetic domains can be clearly identified.

2.7.2 Temperature Dependence of the X-ray Magnetic Circular Dichroism Signal at the RE L_3 Edge in $REFe_2$

Compounds containing rare earths (RE) and 3d transition metals (TM) are of great technological importance due to the wide range of industrial applications, such as magneto-optical disks, transducers, and most importantly high-performance permanent magnets. In these materials the RE atom is used to increase the magnetic anisotropy, while the transition metal enhances the Curie temperature. The magnetic moment on the RE atom arises primarily from the highly localized 4f orbital, which has negligible overlap with the surrounding atoms, while the moment on the TM arises on the much more delocalized 3d orbital. Thus magnetic ordering in these compounds is mediated through an indirect exchange, whereby the RE 4f orbital spin-polarizes the more diffuse RE 5d orbital, which in turn has a direct exchange coupling with the TM 3d orbital. Clearly for a well-defined understanding of the magnetic properties of these materials, knowledge of the spin-polarization and exchange-coupling mechanisms involved in the 5d orbital is essential.

X-ray magnetic circular dichroism (XMCD) provides an ideal tool for providing just such information. XMCD is defined as the difference in the absorption coefficient between right- and left-handed circularly polarized x-rays. Since wave functions of the initial core levels are well understood, the structure in the measured spectra can be directly correlated to the spin-polarization of the final state orbital allowed by selection rules. Furthermore since the core level binding energies are unique to each of the constituent atoms in a material, the information obtained is specific to a particular element and orbital.

In this report, we present XMCD measurements at the RE L_3 edge on a series of $REFe_2$ compounds (RE = Ho, Er, Tm, Lu). The mechanism behind the magnetic ordering in these materials is the well-known RKKY interaction, illustrated in Fig. 2.72. The well-localized 4f orbital spin-polarizes the 5d orbital via an exchange $\xi_{4f\text{-}5d}$, which in turn interacts with the TM 3d orbital through $\xi_{5d\text{-}3d}$ exchange. Additionally, the TM atoms also have a strong coupling between themselves though a direct overlap of their respective 3d orbitals ($\xi_{3d\text{-}3d}$). Since the direct exchange between the TM atoms $\xi_{TM\text{-}TM}$ ($\sim \xi_{3d\text{-}3d}$) is typically much stronger than the indirect exchange between the RE and TM atoms $\xi_{RE\text{-}TM}$ ($\sim \xi_{4f\text{-}5d} * \xi_{5d\text{-}3d}$), the magnetization of the RE sublattice will fall off faster than that of the TM. Previous XMCD measurements at these edges have

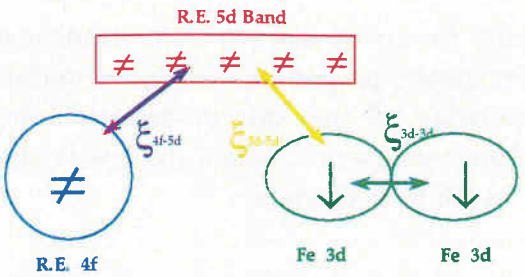

Fig. 2.72. Schematic of the magnetization process.

shown that they are composed of two distinct features. One is associated with the 5d orbital, while another has been shown to arise from transitions to the 4f orbital (Lang et al., 1995). The effect of the different exchange mechanisms on the spin polarization of the individual orbitals can be investigated by varying the RE and changing the temperature of the material. By changing the RE, the strength of the $\xi_{4f\text{-}5d}$ exchange is varied while keeping the $\xi_{5d\text{-}3d}$ exchange constant. In the case of Lu, this exchange goes to zero since it has no 4f moment, thereby isolating effects of the $\xi_{5d\text{-}3d}$ interaction alone. In the temperature behavior, features that are more tightly coupled to the TM lattice should show less temperature variation.

Powder samples were prepared of each material and placed on tapes for transmission measurements. The samples were placed inside a closed loop He displex in order to vary the temperature between 10K and 300K. In order to magnetize the sample, a 4.0 kG permanent magnet was also placed inside the displex. The magnetic field was oriented at 45° with respect to the incident beam in order to allow the transmitted beam onto the detector. The entire displex with the magnet and sample inside could be rotated by 180° in order to take data with the field both parallel and antiparallel to the incident beam helicity. This eliminated any artifacts in the signal that were not due solely to the sample magnetization. Spectra were taken by reversing the helicity at each energy using a diamond (111) phase retarder.

Figure 2.73 shows the XMCD spectra for each RE compound at 10K and 300K. The spectra of Ho, Er, and Tm each show prominent features at approximately –8 and +4 eV, which are known to come from the 4f and 5d bands, respectively. Lu on the other hand shows a single peak at ~0 eV. A peak at this energy is also clearly seen in the TM spectra at 300K (arrow). Note that the TM spectra inverts with increasing temperature since at room temperature it is above its compensation point. Taking the derivative of the XMCD spectra reveals that this feature is present in both the Er and Ho spectra also but is simply obscured by the

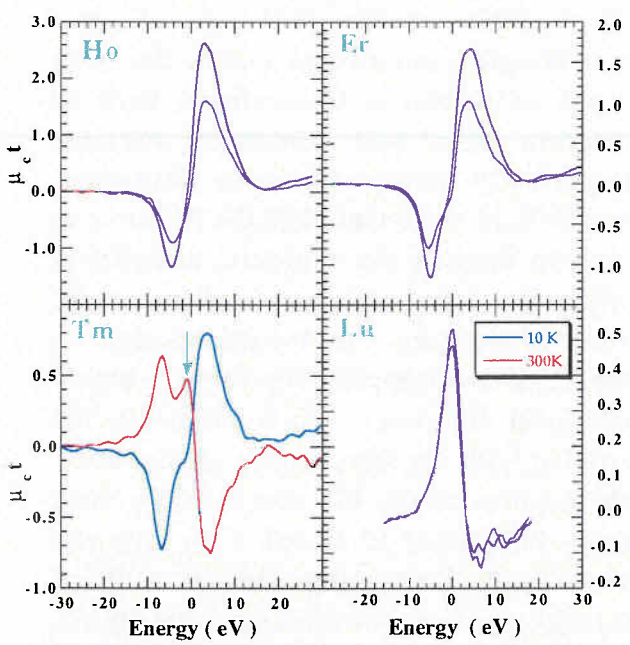

Fig. 2.73. Dichroism signal in RFe_2 at 10K (blue) and 300K (red).

much larger pre- and post-edge features. Clearly since this feature is present in Lu, it must be caused by the $\xi_{5d\text{-}3d}$ interaction. To deconvolute this small feature from the much larger nearby peaks, each spectra was fit using three Gaussian curves. This is shown in Fig. 2.74, which shows data taken at the Er edge along with the three curves used to fit the spectra. The three peaks in the spectra are labeled Q, P, and D. Peak Q is known to be associated with the RE 4f states, while peak D is known to be due to the 5d orbital. The exact nature of peak P is unclear, but as mentioned above (and shown by its temperature dependence below), its most likely source is the exchange between the TM 3d and RE 5d states, since it has nearly the same magnitude and occurs at nearly the same energy as the peak in the Lu spectra.

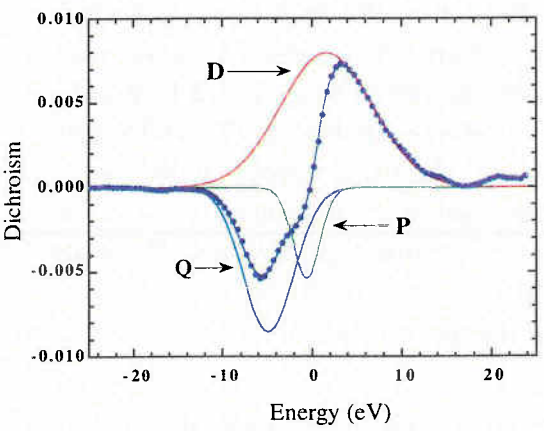

Fig. 2.74. Deconvolution of the dichroism spectra into three Gaussian curves.

The changes in each of the features in the XMCD spectra as a function of temperature are plotted in Fig. 2.75. Also plotted in this figure are single-crystal neutron diffraction measurements (Clark, 1979) of the RE sublattice magnetization for Ho, Er, and Tm. The dotted line on the Lu data is meant merely as a guide to the eye, since no neutron measurements for this material were available. There are several things to notice about the temperature variations in the signal. First the 4f and 5d features have approximately the same temperature dependence. This would indicate that the 5d band polarization probed by feature D scales nearly identically with the 4f magnetization; therefore it is dominated by the $\xi_{4f\text{-}5d}$ exchange, which is consistent with recent theoretical results (van Veenendaal et al., 1997). Feature P, on the other hand, falls off much less with increasing temperature in Ho, Er, and Tm, than the D and Q features, consistent with this feature being strongly associated with the $\xi_{5d\text{-}3d}$ exchange, since it scales with the expected magnetization of the TM sublattice. Lastly, while the D and Q features follow the general trend of the neutron measurements, substantial deviations are seen for the Er and Tm spectra. At

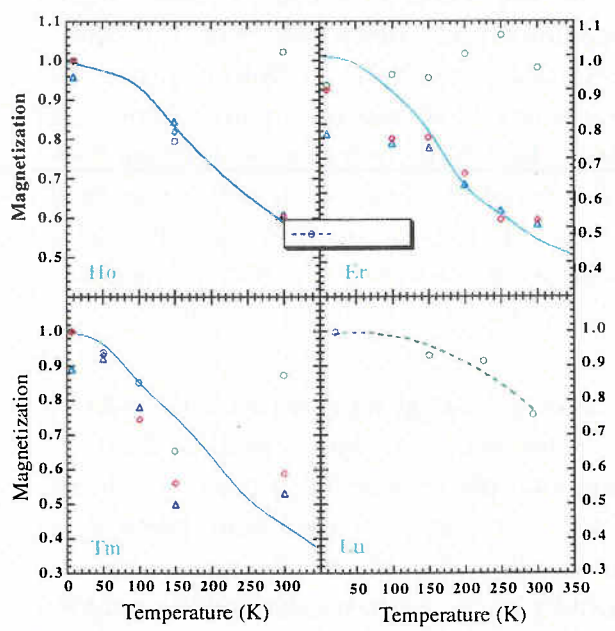

Fig. 2.75. Temperature dependence of each feature in the dichroism spectra [Q (triangle), D (diamond), and P (circles)].

low temperatures the sample becomes much harder to magnetize due to increasing anisotropy, thus the XMCD data tend to deviate away from the neutron data, which were taken on single-crystal samples. Additionally the TM data might be affected by the proximity of some of the measurements to the compensation temperature (T=250K, where the net magnetization is zero).

2.7.3 Interfacial Structure and Magnetism in Fe/Gd Multilayers

Interface structure affects many of the phenomena exhibited by magnetic films and multilayers. Yet even though the importance of interface structure is widely acknowledged, studies to date have generally ignored the magnetic component of the interface structure due to the surface sensitivity of most magnetic probes (e.g., MFM and MOKE). By using a tunable high-brilliance x-ray beam, however, the shortcomings with these techniques can be overcome to obtain information about the magnetic interfaces buried deep in the bulk of a material. Here we describe one such study of the x-ray resonant magnetic scattering (XRMS) in the reflectivity measurements of an Fe/Gd multilayer.

The experimental setup used for the XRMS measurements is shown in Fig. 2.76. A diamond phase retarder is used to convert the linear polarized undulator beam to a circularly polarized one. By alternating the helicity of the beam incident on the sample, the measurements become sensitive to the net magnetization within the sample. Therefore pure charge and charge-magnetic interference information can be extracted

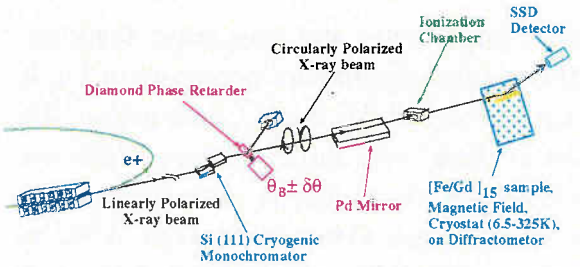

Fig. 2.76. Experimental setup.

from the data by taking the sum and difference of the measurements taken with opposite helicities. The sample was placed inside a closed loop He cryostat, which was then mounted on a 4-circle diffractometer for the reflectivity measurements. A fixed magnetic field could be applied to the sample using a permanent magnet.

Measurements of both the specular and the diffuse reflectivity scattering data have been collected in order to obtain magnetic information about the multilayer. Examples of the charge-magnetic interference reflectivity measured near the Gd L_2 and L_3 edges are shown in Fig. 2.77, while pure charge and charge-magnetic interference diffuse scattering are presented in Fig. 2.78. In all figures, Born approximation (BA) fits (Osgood III et al., 1999; Nelson, 1999) to the data are also displayed.

The fits to specular reflectivity data of the type shown in Fig. 2.77, (Nelson, 1999; Ishimatsu et al., 1999) indicate a direct proportionality between the structural roughness and the range of the Fe-Gd exchange coupling. Fits to the diffuse scattering also provide information about the relationship between the structural and magnetic properties of the multilayer. For example, the fits shown in Fig. 2.78 and fits to additional diffuse data measured from

other Fe/Gd multilayers (Nelson et al., 1999) result in longer correlation lengths for both in-plane and out-of-plane charge-magnetic roughness than for pure charge (or structural) roughness. Additional studies focusing on the temperature and energy dependencies of the XRMS data in the Fe-Gd system are already underway.

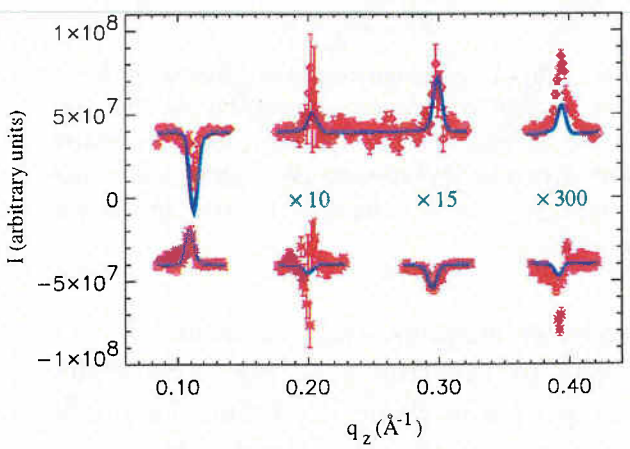

Fig. 2.77. Differences in the specular reflectivity scattering (red) at the Gd L_2 (above) and L_3 (below) edges, along with Born approximation fits (blue) to the data. The data and fit have been shifted by $4x10^7$ and enlarged, as labeled, for clarity.

2.7.4 Exploring Magnetic Anisotropy Using Polarized X-rays

As the storage density in magnetic media has increased, so too has the complexity of the materials and structures used. Most technologically relevant magnetic structures now consist of multiple interacting ferromagnetic (FM) layers. However, hysteresis and magnetocrystalline anisotropy are commonly measured using a bulk magnetization techniques. These techniques measure a weighted sum of all the FM elements in the material or device. As a result, interpretation of the data is often

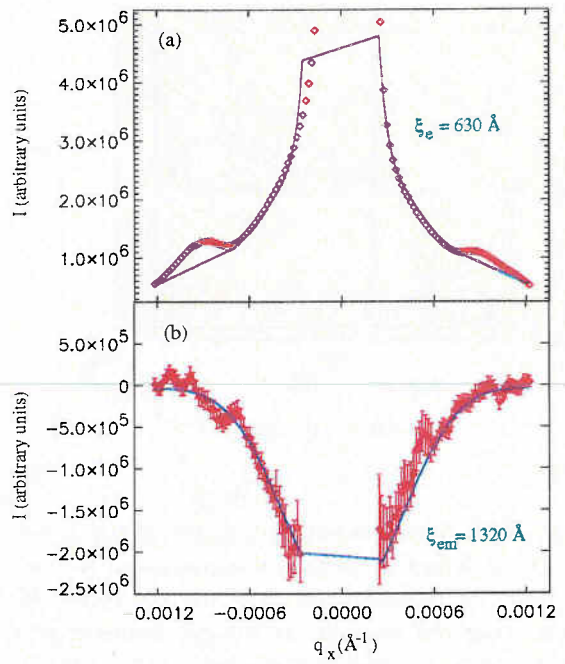

Fig. 2.78. Diffuse scattering (red) from the pure charge(a) and charge-magnetic interference (b), along with BA fits (blue) to the data.

difficult. A solution to this dilemma is to utilize an element-specific technique to separate the individual contribution of each elemental component.

Of particular interest is the study of the magnetic anisotropies that can be accomplished in an element-specific manner using x-ray magnetic linear dichroism (XMLD). XMLD is a magnetic contrast resulting from the slight absorption dependence on the angle between the beam polarization and the magnetic moment. Either by measuring the absorption for the moment and polarization parallel and perpendicular (XMLD) or by measuring the absorption while sweeping the direction of a constant field [referred to as x-ray magnetic linear loops (XMLL)], a wide variety of anisotropy information can be obtained (Fig. 2.79).

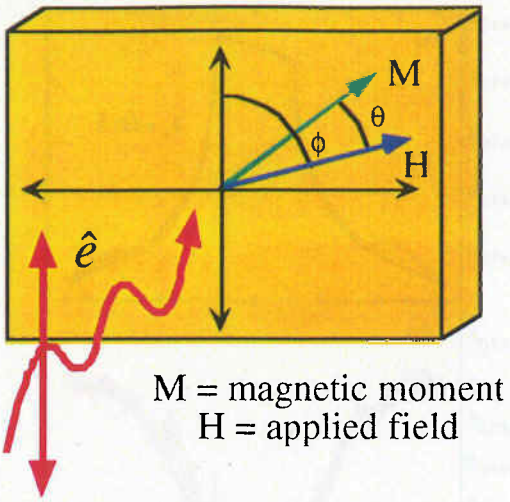

Fig. 2.79. Experimental geometry of the x-ray magnetic linear dichroism measurement. A wide variety of information can be obtained by measuring the absorption for the moment and polarization parallel and perpendicular (XMLD) or by measuring the absorption while sweeping the direction of a constant field [referred to as x-ray magnetic linear loops (XMLL)].

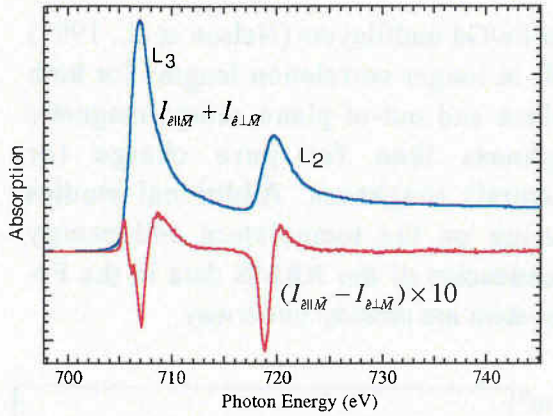

Fig. 2.80. X-ray magnetic linear dichroism for a bcc Fe(100) single crystal displaying the sum and difference spectra. The difference line shape has a strong dependence on crystal order and structure due to changes in the spin-orbit interaction.

The XMLD observed at the transition metal L edges (see Fig. 2.80) is strongly coupled to the spin-orbit interaction (van der Lann, 1999) making it potentially much better suited to the study of orbital magnetic moment variations. In addition, the spin-orbit interaction is the key link in the connection between the magnetic moment and the lattice that results in the magnetic anisotropy. Strong changes in the line shape are observed by variation in the sample crystal structure and are related to the variation in magnetocrystalline anisotropy. For example, the results for single-crystal bcc Fe(100), shown in Fig. 2.80, are quite distinct from those of polycrystalline Fe (not shown).

Another facet of this technique is the ability to directly probe the symmetry of the magnetic anisotropy. This is accomplished by monitoring the changes in absorption as a constant magnetic field is rotated in the plane of the film (see Fig. 2.81). The comparison of single crystal bcc Fe to that of polycrystalline Fe clearly shows the difference between a 4-fold magneto-crystalline anisotropy to that of no anisotropy. The solid lines show the result of magnetic calculations that through the field magnitude dependence provide quantitative information.

2.7.5 Microspectroscopy and Imaging with Photoelectron Microscopy

With the recent explosion in nano-technology, new techniques are necessary to fully explore the influence of dimensionality on materials. X-ray imaging and micro-spectroscopy are unique tools for the characterization of electronic and magnetic properties. By imaging the secondary electrons emitted due to x-ray excitation with a photoelectron microscope (PEEM), many details of the microstructure can be

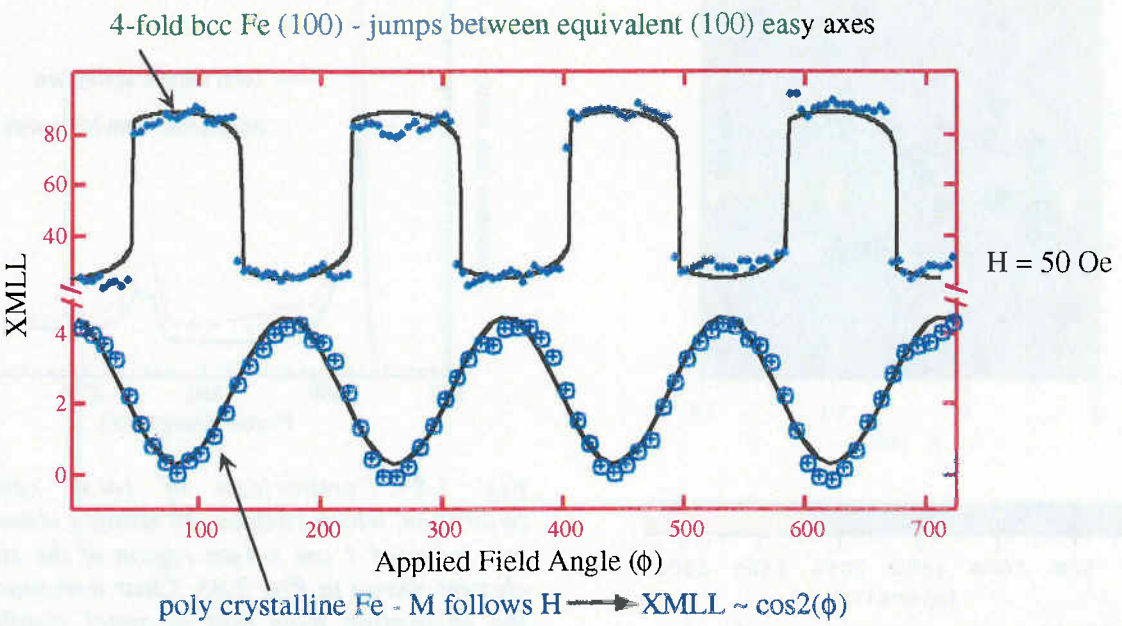

Fig. 2.81. X-ray magnetic linear loops measured by sweeping the in-plane angle of a constant magnetic field amplitude. Results show clear indications of the nature of the magnetocrystalline anisotropy that can be further understood by modeling (solid lines).

determined. Figure 2.82 shows an image of 1 μm Pd stripes on Si. In this case the x-ray energy is off resonance and the contrast is due solely to the differing electron density of the two materials. This test sample was utilized to judge the resolution during the recent commissioning of the microscope. By adjusting the optics to optimize for the highest resolution, we could resolve features in the 100 – 200 nm range.

The unique capability of PEEM is not only the ability to image, but the ability to use image intensity to track resonant phenomena and perfom microspectroscopy. Micro-fabrication techniques have enabled production of small-scale structures for technological applications. Figure 2.83 shows a 2 μm NiFe wire prepared as a prototype for nonvolatile magnetic memory elements. Element-specific maps help us

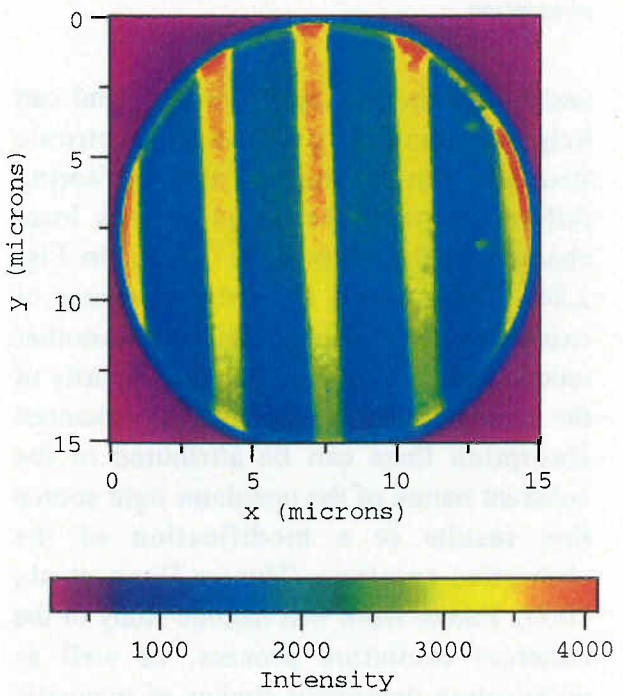

Fig. 2.82. X-ray photoelectron image of 1 μm Pd stripes on a Si wafer. This image displays a 15 μm field of view and was acquired with a 12 bit CCD camera.

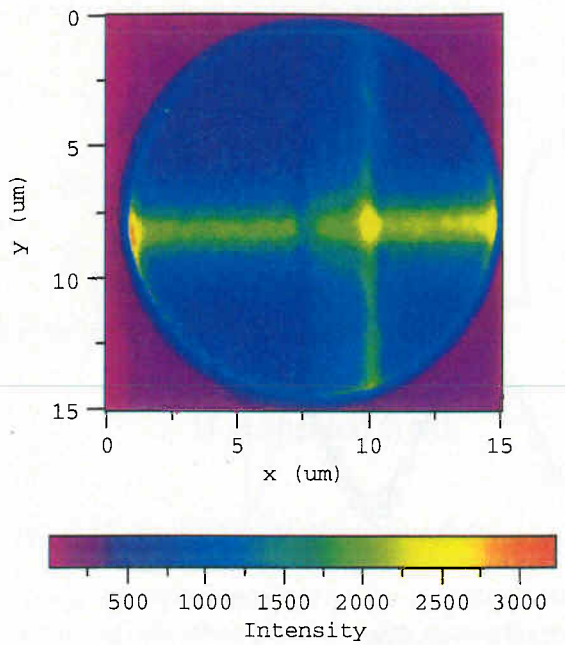

Fig. 2.83. Element-specific image of a 2-μm-wide NiFe magnetic wire with the x-ray excitation energy tuned to the Ni L_3 edge. Future capabilites in sector 4 will enable not only chemical maps, but also magnetic domain structure from polarization-dependent absorption.

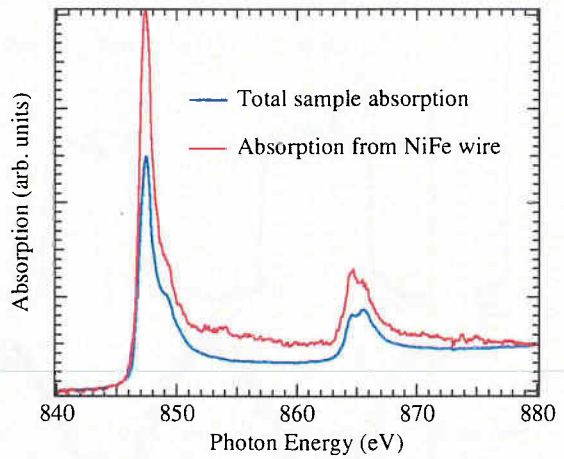

Fig. 2.84. Comparison of total sample absorption, which contains 20 memory elements, to a selected 1 μm x 1μm region of the single element shown in Fig. 2.83. Clear deviations of the absorption from that of metal standards indicate a significant oxide component.

understand the production process and can help us identify problems. Electronic structure can be studied by monitoring different parts of the image to track local changes in the absorption (shown in Fig. 2.84). These results show the prescence of oxide contamination in the wire. Another unique feature of the result is the disparity of the local and total absorption. The enhanced absorption lines can be attributed to the coherent nature of the undulator light source that results in a modification of the absorption spectrum (Hunter Dunn et al., 2000). Future work will include study of the coherent excitation process, as well as polarization-dependent studies of magnetic microstructures.

2.7.6 X-ray-Excited Optical Luminescence Studies of Oxidized Porous Silicon

Porous silicon luminescence has attracted considerable attention for application in Si-based optoelectronics (Canham, 1990). However, recent results have been unclear as to the origin of particular luminescence bands. Depending on the study, they can be attributed to either nanocrystals or oxides. To clarify this issue, a study of porous silicon as a function of oxidation conditions was undertaken. By using x-ray-excited optical luminescence, one can understand the oxide dependence by comparing the results of total x-ray fluorescence yield (TFY) to that of either total or partial luminescence yield (TLY and PLY). Figure 2.85 shows the influence of oxidation on the luminescence that provides clear evidence for overlapping luminescence bands from both Si nanocrystals and oxides. These

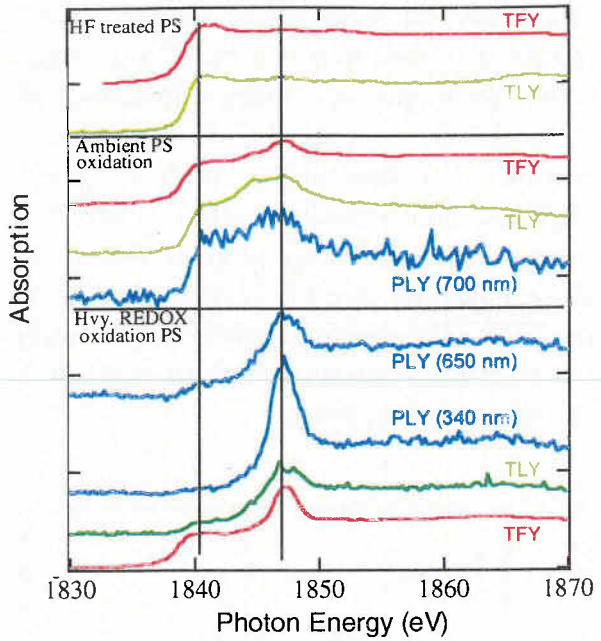

Fig. 2.85. Comparison of total fluorescence yield (TFY) to that of total and partial luminescence (TLY and PLY) as a function of oxidation. Changes in the luminescence yield for the oxide peak near 1847 eV with respect to that of the pure Si peak near 1840 eV provide clear evidence for overlapping luminescence bands from both Si nanocrystals and oxides.

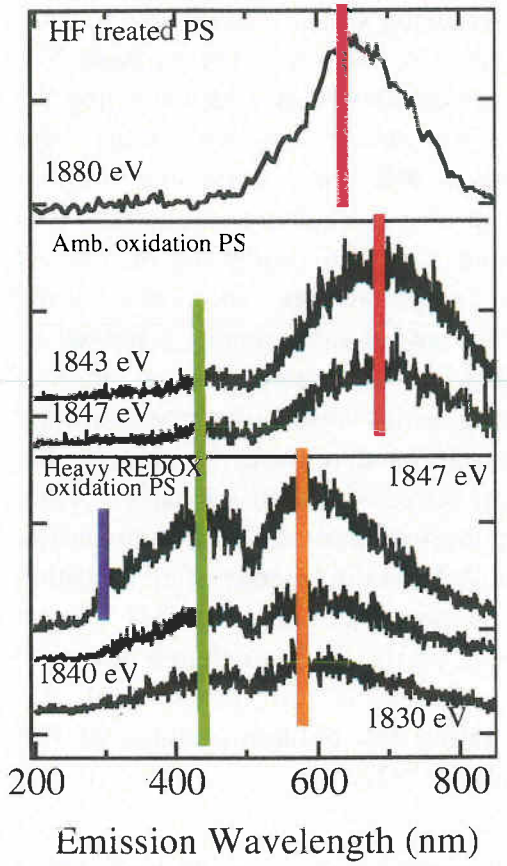

Fig. 2.86. Optical emission spectra as a function of both oxidation and photon energy.

overlapping bands are the cause of much of the confusion in the literature, and x-ray-excited optical luminescence is uniquely suited to extracting element, as well as chemical-state-specific, information for optical materials.

In addition to optical yields, this technique can also directly provide information on the shape of the optical bands. By using an optical monochromator for fixed photon excitation energies, one can follow the evolution of the emission bands (see Fig. 2.86). Future studies will utilize these bands to understand the interaction of local structure and the optical luminescence.

As well, the polarization source becoming available in sector 4 this fall will open the door to element-specific studies of magneto-optical materials.

2.7.7 Changes of a Ferromagnet/ Insulator Interface upon Thermal Annealing

Recent success in fabrication of magnetic tunneling junctions (MTJ) with magneto-resistance (MR) above 40% at room temperature has generated a great deal of interest due to potential application as efficient magnetic random access memory (MRAM) (Parkin et al., 1999). MTJs are composed of two FM electrodes separated by an insulating layer (I) with typical

structures being CoFe/ Al_2O_3/CoFe. Others have reported that these record high MR values are obtained only after annealing the MTJ to 200-300°C, which leads to ~10% increase in MR when compared with as grown structures (Parkin et al., 1999). It is suspected that the oxidation of the Al overlayer penetrates into the CoFe underlayer and is subsequently removed by annealing. To understand the influence of annealing x-ray absorption spectroscopy (XAS) was used to directly monitor the chemical states of FM in a $Co_{84}Fe_{16}/Al_2O_3$ bilayer before and after the annealing process. XAS at the L_3-edge of 3d transition metal elements and their oxides exhibit different, easily distinguishable features, which makes it an ideal tool for investigating the oxidation states of FM electrodes in MTJ.

A bilayer consisting of an Al wedge was used in order to perform a systematic study of the effect of annealing as a function of Al_2O_3 thickness (see Fig. 2.87). This is of particular importance since the Al_2O_3 barriers of MTJ are fabricated by oxidation of Al layers and an optimal FM/I interface

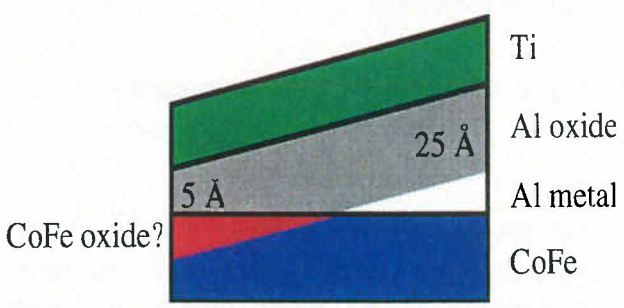

Fig. 2.87. Wedge-shaped structure used to study the Al layer thickness dependence of the oxidation process. CoFe oxide removal upon annealing is suspected to be responsible for improved magnetoresistance.

should have all of the Al and none of the FM oxidized. Absorption at the Co L edge clearly shows pre-edge features indicative of an oxide. By tracking the intensity of this feature as a function of both Al layer thickness and annealing, one can see that there is significant removal of the oxide upon annealing (see Fig. 2.88). In addition the Al K edge absorption spectra show little variation with annealing and are indicative of a disordered Al oxide.

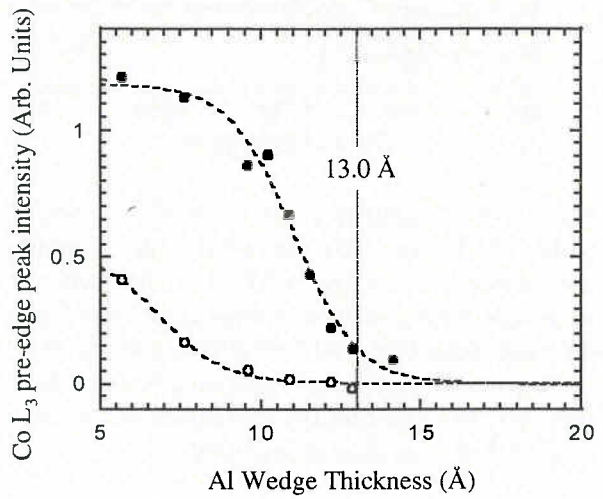

Fig. 2.88. Co pre-edge feature intensity as a function of Al thickness before (closed circles) and after annealing (open circles). Heating drives the oxygen out of the CoFe layer and results in an improved interface and subsequently improved magnetoresistance.

2.8 Time-Resolved X-ray Techniques Development

The SRI-CAT time-resolved techniques program is part of the activities of the x-ray physics group and is primarily based on the sector 1 beamlines. This program has a diverse range of activities with the common

theme of measuring temporally evolving phenomena with x-rays. A major goal of this program is to develop instrumentation that can be used by other CATs at the APS. The best example of this is the beam choppers described below, which are now primarily used in non-SRI-CAT experiments. With G. Mourou, Z. Chang, D. Umstadter (all University of Michigan), and L. Young (ANL), we also co-organized a "Workshop on the Marriage of High Intensity Lasers with Synchrotrons" to explore the field of laser-pumped, x-ray probed techniques. Other efforts center on technique development to develop new experimental methods for both the ID and bending magnet beamlines. The fuel spray studies are an example of experiments that are conceptually straight-forward but require sophisticated use of equipment (fast detectors, special injector systems) to actually execute. Several aspects of the time-resolved efforts are integrated into other sector 1 programs. One of these, the measurement of transient behavior in materials using powder diffraction, is closely coupled with the high-energy x-ray program and is described in that section.

Future efforts of the time-resolved program will fall into two categories: studies that utilize the pulsed nature of the storage ring and those that do not. In the first case, development of a fast x-ray streak camera will allow the growth of techniques, such as image-correlation spectroscopy for pump-probe experiments. For the second case, emphasis will be given to continued study of transient material behavior. In many cases, these projects will be strongly coupled to the high-energy or sector 1 optics programs.

2.8.1 Fuel Spray Studies

Detailed analysis of the fuel spray process has been recognized as an important step in the overall aim of increasing combustion efficiency and reducing emission of pollutants, particularly for diesel engines. This has spurred considerable activity in the development of both optical and nonoptical techniques for measurements in diesel fuel injection systems. Despite significant advances in laser diagnostics over the last 20 years, the region close to the nozzle has remained impenetrable to experiments designed to acquire quantitative information due to multiple scattering by the large number and high density of droplets in the region. While other researchers are looking into the possibility of using lasers of ultrahigh power and ultrashort pulse to study this region, we report here the development of a new nonintrusive and quantitative technique to characterize the dense part of the fuel spray using monochromatic x-ray absorption techniques. X-rays are highly penetrative in materials composed of extremely dense droplets made of low-Z materials, which makes x-rays an excellent tool for fuel spray studies. We have developed the technique, using x-ray absorption of monochromatic radiation, to quantitatively determine the fuel density distribution in this optically impenetrable region with a time resolution better than one microsecond. The current quantitative measurements constitute the most detailed near-nozzle study of a fuel spray to date.

The fuel spray was generated using a high-pressure injector typical of that found in a passenger car. The diesel fuel used in the test was doped with a cerium-containing additive in order to increase its x-ray

absorption. Injection was performed into a spray chamber filled with inert gas at atmospheric pressure and at room temperature. SF_6, a very heavy gas, was used to create a relatively dense ambient environment in the injection chamber. The experiments were performed at the 1-BM beamline. A 5.989 keV x-ray beam was focused and then collimated by a pair of slits to a size of 500 μm (horizontal) × 50 μm (vertical). The transient x-ray attenuation signal due to the fuel spray was measured by an avalanche photodiode (APD). The APD response was proportional to the beam intensity over the range used in our experiment and was recorded every 2 ns by a digitizing oscilloscope. Since the APD is a point detector, the injection chamber was translated vertically and horizontally with respect to the x-ray beam, allowing the beam to probe various positions within the spray plume. The x-ray absorption technique using a monochromatic beam is distinguished from conventional measurements by the quantitative nature of the measurement. With proper calibration, the x-ray absorption directly yields the absolute fuel mass quantity in the beam and the mass distribution. In addition, anomalous absorption was measured above and below the Ce L_3 edge at 5.723 keV to confirm this calibration.

A plot of the time-dependent x-ray transmission 1 mm and 6 mm from the nozzle on the spray axis is shown in Fig. 2.89. For the data taken at 1 mm from the nozzle, the spray clearly arrives and leaves the beam at t = 0.11 and 0.5 ms, respectively. The leading edge of the fuel spray appears very abruptly, indicating a very distinct boundary between ambient gas

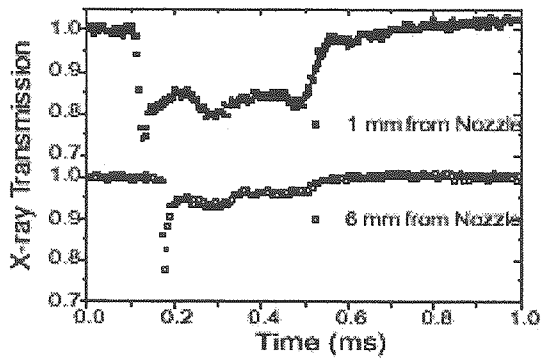

Fig. 2.89. Time evolution of the x-ray transmission on the spray axis 1 mm (solid square) and 6 mm (open square) from the nozzle.

and fuel spray with a compressed layer after the sharp edge. At 6 mm from the nozzle on the spray axis, the front edge of the spray arrives at the measuring point at a later time (0.19 ms).

The delay can be used to calculate the speed of the front edge. The absorption of the body of the spray decreased significantly, indicating a much lower fuel volume fraction there.

Based on the transmission values and the mass calibration, the amount of fuel in the path of the beam can be determined in a time-resolved manner. The normalized density (volume fraction of fuel) distribution is plotted in Fig. 2.90 for the leading edge of the spray (upper panel) and the main body of the spray (lower panel) at distances of 1 and 6 mm from the nozzle, respectively. The most striking feature of the plots in Fig. 2.90 is that the density of the fuel spray was significantly less than that of the bulk liquid fuel, even as close as 1 mm from the nozzle. The main body of the spray, the region that has been termed the "intact liquid core," is actually composed of a liquid/gas mixture.

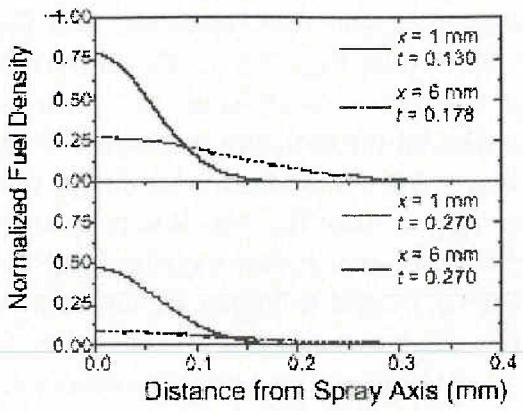

Fig. 2.90. Normalized radial distribution of the fuel density measured 1 and 6 mm from the nozzle at different instants in time (leading edge and main body of the spray intercepting the beam, respectively). A normalized density equal to unity implies the density of bulk liquid fuel (injection pressure: 500 bar; duration: 300 s).

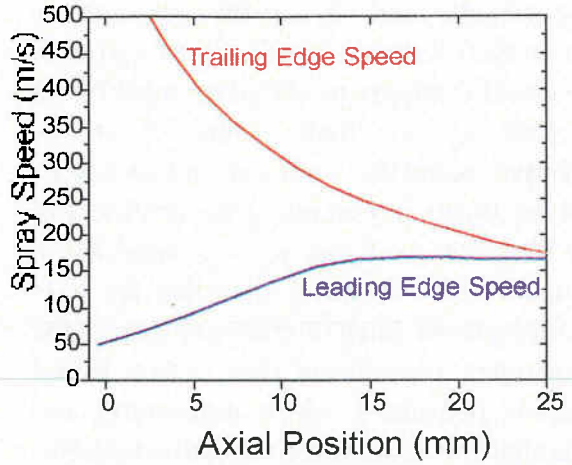

Fig. 2.91. Speed of the leading (blue line) and the trailing edge (red line) of the spray.

The speed of the leading edge has been determined in the experiment and is illustrated in Fig. 2.91. The speed increased slightly after the spray exited the nozzle, maintaining a nearly constant value that is slightly above the sonic speed in SF_6 (*ca* 140 m/s). Similarly, the speed of the trailing edge can also be derived. We note that initially the trailing edge traveled at a speed much higher than the sonic speed and gradually slowed to the value close to that for the leading edge. Thus far, the trailing-edge speed has never been determined by any other experiments. The trailing-edge speed provides invaluable information about the dynamics of the spray, such as generation of shock waves in the injection chamber.

In summary, by using monochromatic x-ray radiography, we have been able to study an optically much denser region of the spray than any study reported to date. The measurement is highly quantitative and time resolved. With further progress, a detailed spray structure of the near-nozzle region will be elucidated. These results are essential to the development of accurate theoretical models of fuel sprays and should lead to better nozzle designs. In addition, the synchrotron-based, time-resolved monochromatic x-ray radiographic technique has proven its usefulness not only in the field of spray science and technology but also in research areas dealing with transient phenomena of optically opaque materials, such as aerosols or heavy-element plasmas.

2.8.2 Polymer Thin-Film Dynamics and X-ray Damage

2.8.2.1 Polymer thin-film dynamics

On liquid surfaces, thermal excitations induce capillary waves with a long wavelength cutoff due to gravitation. The power spectrum associated with capillary waves can be expressed as $S(k) = (k_B T/\gamma)(k^2 + k_c^2)^{-1}$, where the cutoff is $k_c = \sqrt{\rho g/\gamma}$ (1 to 10 cm^{-1}), and ρ and γ are the liquid density and its surface tension,

respectively, and g is the gravitation. Theoretically, on liquid thin-film surfaces, the cutoff is simply modified by substituting g with $g_{eff} = g + F/(\rho d)$, where F is the effective interaction force per unit area (e.g., van der Waals forces) and d the thickness of the film. For $d < 1$ µm, $g_{eff} >> g$, resulting in a much larger cutoff k_c than that for bulk liquid surfaces. Such interaction prevents the long-range correlation that a free liquid surface possesses while essentially not affecting the short wavelength fluctuations. The shift of k_c to larger values can be visualized by x-ray diffuse scattering measurements, a well-suited technique for obtaining quantitative information about such thermal excitations.

Whereas bulk liquids have been investigated extensively, there are only a handful of quantitative investigations on liquid thin films, mainly due to difficulties in preparing samples with well-controlled film thickness and interfacial environment. Recently, we have attempted to study the surface behaviors of ultrathin polymer films for elucidating the capillary-wave properties on liquid thin-film surfaces and for investigating the substrate effects on these properties. True liquid-like behavior has never been observed even if the polymer-film thicknesses were much larger than the radius of gyration (R_G) and the polymer glass transition temperature (T_g). In this report, the surfaces of molten poly(tert-butyl acrylate) (PTBA) thin films on a silicon substrate have been investigated by specular and diffuse x-ray scattering.

In the experiments, we demonstrated that the surface of the polymer thin films exhibits modified capillary wave fluctuation, possibly due to the attracting van der Waals interaction between the substrates and the thin films (see Fig. 2.92). The observed capillary wave scattering is strongly dependent on the thin-film thickness. When the film thickness is close to or only a few times larger than R_G, the low-frequency cutoff of the wave-vector transfer along the surface (q_x) shifts to higher frequencies as the film thickness decreases. A signature of free liquid capillary scattering is a change of the exponent in the diffuse-scattering power law as a function of momentum transfer normal to the surface, q_z. This change was clearly observed for thicker films (Fig. 2.93).

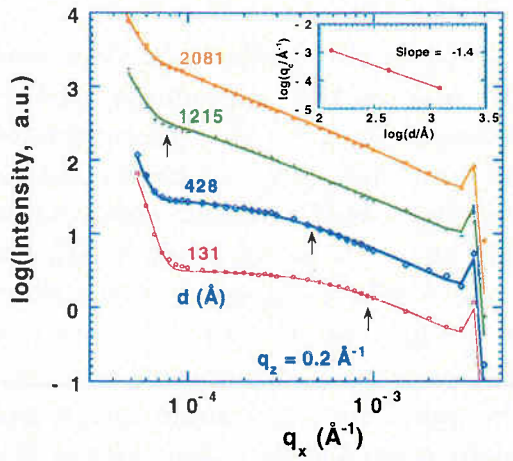

Fig. 2.92. Transverse diffuse scattering scans for the samples with various thicknesses (d) at q_z = 0.2 Å^{-1}. The fits to the data using modified capillary wave scattering theory (incorporating thin film effects) are shown as lines. The arrows indicate the cutoff locations. The inset depicts log(k_c) vs. log(d).

2.8.2.2 X-ray damage in polymer thin films

Despite the obvious occurrence of synchrotron x-ray damage to organic thin films, few attempts have been made to

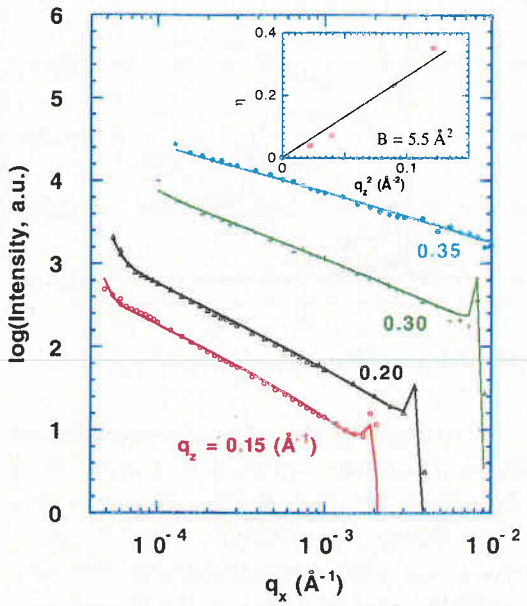

Fig. 2.93. Transverse diffuse scans from the sample with d = 2018 Å. The fits to the data using capillary wave scattering theory are shown as lines.

qualitatively determine their *morphological* changes during x-ray exposure. Frydman et al. (1997) used x-ray photoelectron spectroscopy and Fourier-transform infrared spectroscopy to study several different self-assembled monolayers (SAMs) on varying substrates. They found that the majority of the damage seems to occur at the surface of the film (especially if labile groups are present) rather than by removal of large amounts of film material. Despite the obvious surface changes, atomic force microscopy (AFM) pictures did not show any large scale increase in surface roughness but rather indicated the formation of "diamond-like" carbonaceous material with only a modest (< 4 Å) surface roughness.

We have used x-ray reflectivity at the 1-BM beamline to study x-ray damage of a polymer thin film. Reflectivity probes the electron-density profile of a film perpendicular to the surface and therefore allows us to obtain some of the important structural parameters necessary to quantify x-ray damage (such as the interfacial morphology), which cannot be obtained from spectroscopic techniques. The results indicate that most of the damage leading to a change in the reflectivity occurs at or near the film interfaces that are furthest apart. This can be deduced by the obvious disappearance of the oscillations during x-irradiation (Fig. 2.94) and by examining the surface roughness as a function of time (Fig. 2.95). We will perform further experiments, using both x-ray reflectivity and AFM, to further elucidate this important process. Especially of interest is whether AFM images will also show a pronounced increase in the top surface roughness.

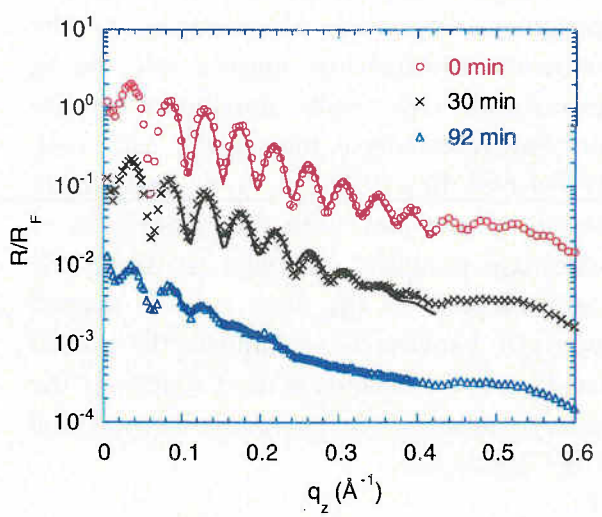

Fig. 2.94. Normalized reflectivity curves after three exposure times, including the two-layer fits. Curves are displaced for clarity.

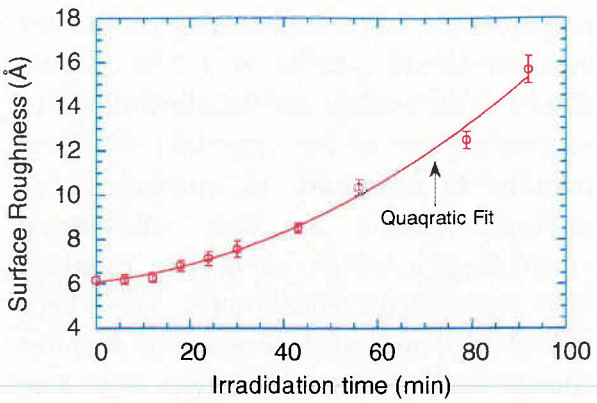

Fig. 2.95. The film-air interface width as a function of exposure time.

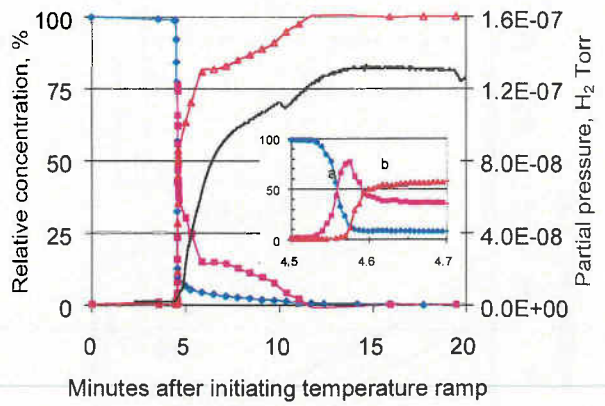

Fig. 2.96. Changes in the relative concentrations of different copper oxidation states in a $CuO/ZnO/Al_2O_3$ catalyst during reaction with a feed containing P_{O2}=6.9kPa, ramp rate = 2°C/min. Insert shows magnified area from 4.5 to 4.7 minutes after initiation of the temperature ramp, (♦) Cu^{+2}, (Ç) Cu^{+1}, (Δ) Cu^0.

2.8.3 Time-Resolved X-ray Absorption Near-Edge Spectroscopy (XANES)

Pollution regulations for automobiles have become increasingly stringent during the past several years. Attempts to curtail emissions, while maintaining the efficiency of the internal combustion have resulted in substantial improvements. For further progress, however, alternatives to the internal combustion engine are being examined. One such alternative is the polymer-electrolyte membrane fuel cell, (PEM-FC). In a PEM-FC, H_2 is catalytically oxidized to water with the generation of electrical potential. In order to supply H_2 continuously to the fuel cell, a second catalytic process incorporating the partial oxidation of methanol, is used. Currently the catalyst used for this process is an industrial $CuO/ZnO/Al_2O_3$.

With a group from Northwestern University, we employed the dispersive-crystal mono-chromator (on 1-BM) for time-resolved XANES to obtain the *in situ* information about the CuO/ZnO catalyst in the oxidative methanol reforming reaction. In Fig. 2.96, the relative concentrations of Cu oxidation states (Cu^0, Cu^{+1}, Cu^{+2}) and the H_2 content in the gas phase product were plotted. The data show clear evidence that H_2 production is only associated with metallic Cu.

2.8.4 X-ray Beam Chopper Development at SRI CAT

Beam chopper development has been part of the time-resolved program at SRI CAT. Some of the design parameters included: (a) open time windows spanning the range from seconds to picoseconds; (b) fast rise and fall time for the transmitted pulse; and (c) a slow duty cycle relative to the open time of the beam chopper. In order to facilitate the large range of open time windows, three classes of beam choppers have been developed to make use of the temporal structure of the APS storage ring.

The first type of beam chopper is a slow shutter using a double-solenoid design. It

treats the temporal structure of the storage ring as a continuous source and may have an open time window as long as a few milliseconds.

The basic design for the fast motion of the solenoid is to over-drive the solenoid with a high voltage—but only for a few milliseconds to prevent the coil from burning out. A high-voltage power supply capable of delivering several amps of current is connected to a fast high-voltage switch. The first arm of the shutter is in the normal closed position, while the second arm is in the normal open position. Setting the timing of the trigger of the high-voltage switch for the two arms adjusts the length of the open time window.

This beam chopper, shown in Fig. 2.97, was set up to protect a CCD camera used as a detector for a diesel fuel spray experiment on 1-BM. Its open time was set to 4 to 5 milliseconds. The rise and fall time of the open time window was about 400 microseconds. It was operated at 1.4 hertz. This beam chopper can be adjusted for other operating parameters. Its limits are an open time window of about 200 microseconds and a repetition rate of about 30 hertz.

The second type of beam chopper is illustrated in Fig. 2.98. It is a fast shutter with a fixed open time window. It may or may not make use of the temporal structure of the APS storage ring, depending upon the experiment and the fill pattern of the storage ring. This beam chopper is modeled after a commercial high-speed air-bearing laser scanner. Basically, it is a rotating aluminum disk with a slot through the diameter. A

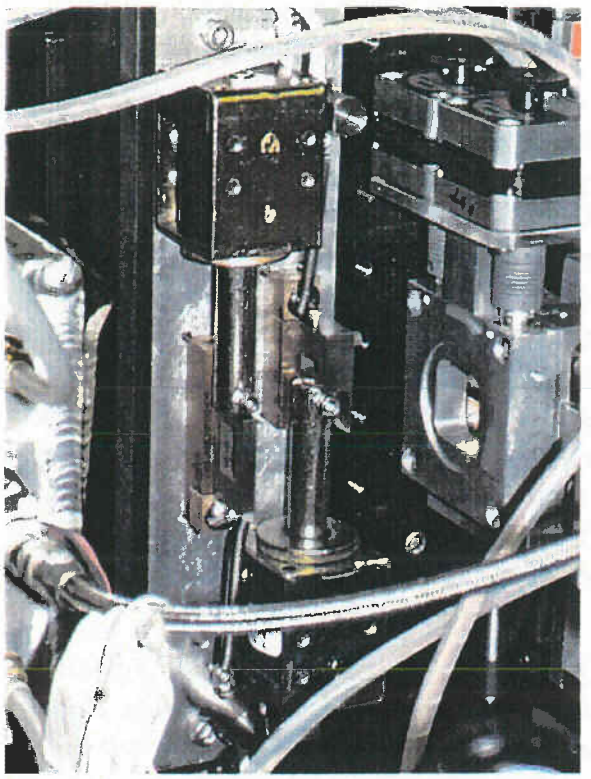

Fig. 2.97. Solenoid beam chopper.

nickel coating covers the circumference. Rotating at 1331 hertz, it has an open time window of about 2400 ns. There are two open window times per rotation of the disk. The dead time between open window times is 373 microseconds. A principal feature of this beam chopper is the high degree of rotational speed regulation of the disk. The uncertainty in the position of the transmission window (or jitter) is ± 3 ns at the 3-σ level (95% confidence level). Since the jitter is small relative to the open window time, the rotation of the beam chopper can be synchronized to the orbital frequency of the APS storage ring. This allows for the performance of time-resolved measurements. The time resolution is dictated by the experiment but may be as short as 50 ps when one filled "bucket" of the APS falls within the open time window.

If the temporal structure of the ring is not important, the beam chopper can be used to transmit a 2.4 microsecond pulse to map a time-resolved response. Carol Thompson and coworkers of Northern Illinois University have used this beam chopper to measure the time structure of the piezoresponse of a ferroelectric material at the 1-BM beamline and more recently at the BESSRC-CAT 12-ID beamline. The small size and portability of the beam chopper make it easy to transport and set up on other beamlines around the APS storage ring. This device is available to APS users upon request.

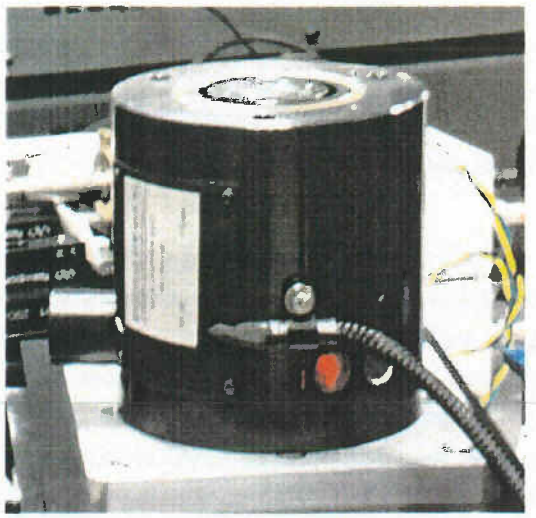

Fig. 2.98. High-speed beam chopper.

The third type of beam chopper is pictured in Fig. 2.99. It is an ultrafast shutter employing a rotating crystal mounted to the shaft of a precision high-speed motor. Using the small acceptance angle of perfect crystal reflections to produce an open window time as small as 12 ns, this beam chopper was designed to transmit only one filled bucket independent of the fill pattern of the APS storage ring. With the jitter in the time necessary to make one revolution less than 1 ns, the rotation of this beam chopper can be synchronized to the orbital frequency of the APS storage ring. Hence, it is possible to phase lock the rotation of the crystal to the temporal structure of the storage ring and work with only one selected bucket of the fill pattern.

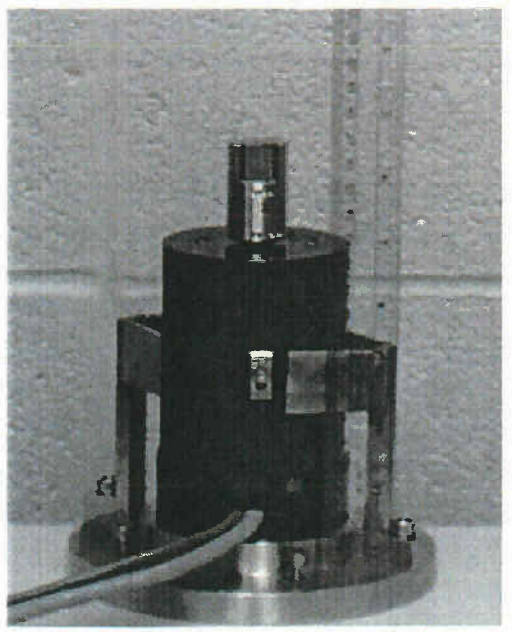

Fig. 2.99. Rotating crystal beam chopper.

The performance of this beam chopper has been tested at 1-BM, but it has not yet been used for experimental applications. It is also available to APS users upon request.

2.9 References

Allman, B.E., P.J. McMahon, J.B. Tiller, K.A. Nugent, D. Paganin, A. Barty, I. McNulty, S.P. Frigo, Y. Wang, and C.C. Retsch (2000) "Non-interferometric quantitative phase imaging with soft x-rays," J. Opt. Soc. Am. A **17**, 1732.

Balucani, U., and Zoppi (1994) *Dynamics of the Liquid State* (Clarendon Press, Oxford).

Balucani, U., et al. (1993) Phys. Rev. E **47**, 1677.

Bearden, J.A. (1965) Phys Rev. **137 B**, 455.

Bearden, J.A. (1967) Rev. Mod. Phys. **39**,78.

Bhushan, B., J.N. Israelachvili and U. Landman (1995) Nature **374**, 607.

Blume, M., and D. Gibbs (1988) Phys. Rev. B **37**, 1779.

Born,M., and E. Wolf (1980) *Principles of Optics* (Cambridge University Press, Cambridge).

Burns, C., et al. (in preparation)

Canham, L.T. (1990) *Appl. Phys. Lett.* **57**, 1046

Chetwynd, D.G., N.O. Krylova, P.J. Bryanston-Cross, and Z. Wang (1998) Nanotechnology **9**, 125.

Clark, A.E. (1979) in *Handbook of the Physics and Chemistry of Rare Earths*, K.A. Gschneidner and L. Eyring eds. (North-Holland).

Delaire, O., K.T. Erwin, A.T. Motta, R.C. Birtcher, J. Maser and B. Lai (in press) "Study of Alloying Elements in the Zr matrix of Zircaloy-4 and ZIRLO using the Advanced Photon Source at Argonne," Proc. ICONE 8, 8th International Conference on Nuclear Engineering, April 2-6, 2000, Baltimore, MD, paper 8320.

Demirel, L. and S. Granick (1996) Phys. Rev. Lett. **77**, 2261.

Ebbsjoe, I., et al. (1980) J. Phys. C: Solid St. Phys. **13**, 1865.

Eng, P., M. Newille, M.L. Rivers, S.R. Sutton (1998) "X-Ray Beam and Microtechnology Applications," SPIE Proc. p.145.

Erwin, K.T., O. Delaire, A.T. Motta, R.C. Birtcher, Y.S. Chu, and D.C. Mancini (in press) "Study of second phase particles in Zr Alloys Using the Advanced Photon Source at Argonne," Proc. ICONE 8, 8th International Conference on Nuclear Engineering, April 2-6, 2000, Baltimore, MD, paper 8319.

Experimental Facilities Division Progress Report 1997-1998, Argonne National Laboratory Report No. ANL/APS/TB-34 (Sept. 1998).

Fezzaa, K., and W.-K. Lee (2000) in *Synchrotron Radiation Instrumentation: Eleventh US National Conference,* P. Pianetta, J. Arthur, and S. Brennan, eds. (AIP CP521) p. 571.

Frydman, E., H. Cohen, R. Maoz, and J. Sagiv (1997) Langmuir **13**, 5089.

Gao J.P. et al. (1995) Science **270**, 605.

Gao, J.P., W.D. Luidtke and U. Landman (1997) J. Phys. Chem. **B101**, 4013.

Garzarolli and H. Stehle, (1986) in: IAEA Symposium on Improvements in Water Reactor Fuel Technology and Utilization (Stockholm, IAEA SM 288/24) p. 387-407.

Graeff, W., and U. Bonse (1997) Z. Physik **B27**, 19.

Granick, S. (July 1999) *Physics Today*, p. 26, and references therein.

Hirano, K., K. Izumi, T. Ishikawa, S, Annaka, and S. Kikuta (1991) Jpn. J. Appl. Phys. **30**, L407.

Hu, M. (1999) PhD thesis, Northwestern University.

Hu, M., T.S. Toellner, P.M. Hession, J.P. Sutter, E.E. Alp (1999a) Nucl. Instrum. Methods A **428**, 551.

Hu, M., T.S. Toellner, W. Sturhahn, P.M. Hession, J.P. Sutter, E.E. Alp (1999b) Nucl. Instrum. Methods A **430**, 271.

Hunter Dunn, J., et. al. (2000) Phys. Rev. Lett. **84**, 1031.

Ishimatsu, N., H. Hashizume, S. Hamada, N. Hosoito, C.S. Nelson, C.T. Venkataraman, G. Srajer, and J.C. Lang (1999) Phys. Rev. B **60**, 9596.

Keppler, C., K. Achterhold, A. Osterman, U. van Bürck, A.I. Chapman, R. Rüffer, W. Sturhahn, E.E. Alp,. F.G. Parak (2000) Eur. Biophys. J. **29**, 146.

Keune, W., and W. Sturhahn (1999) Hyperfine Interactions **123**, 847.

Koval, S., et al. (1996) Phys. Rev. B **54**, 7151.

Lang, J.C., and G. Srajer (1995) Rev. Sci. Instrum. **66**, 1540.

Lang, J.C., G. Srajer, C. Detlefs, A.I. Goldman, H. Konig, X. Wang, B.N. Harmon, R.W. McCallum (1995) Phys. Rev. Lett. **74**, 4935.

Lang, J.C., G. Srajer, J. Wang, and P.L. Lee (1999) Rev. Sci. Instrum. **70**, 4457.

Lemaignan, C., and A.T. Motta (1994) "Zirconium in Nuclear Applications," in: *Nuclear Materials*, vol. 10B, B.R.T. Frost, ed. (New York, VCH) p. 1-52.

Levine, Z.H., A.R. Kalukin, S.P. Frigo, I. McNulty, and M. Kuhn (1999) Appl. Phys. Lett. **74**, 150.

Levine, Z.H., A.R. Kalukin, M. Kuhn, S.P. Frigo, I. McNulty, C.C. Retsch, Y. Wang, U. Arp, T. Lucatorto, B. Ravel, and C. Tarrio (2000) J. Appl. Phys. **87**, 4483.

Mao, H.K., J. Xu, V.V. Sturzkin, J. Shu, R.J. Hemley, W. Sturhahn, M.Y. Hu, E.E. Alp, L. Vocadlo, D. Alfe, G.D. Price, M. J. Gillan, M. Schwoerer-Bohning, D. Häusermann, P. Eng, G. Shen, H. Giefers, R. Lubbers, G. Wortmann (submitted to Phys. Rev. Lett.).

Margulies, L., M.J. Kramer, R.W. McCallum, S. Kycia, D.R. Haeffner, J.C. Lang, A.I. Goldman (1999) Rev. Sci. Instrum. **70**, 3554.

McNulty, I., S.P. Frigo, C.C. Retsch, Y. Wang, Y.P. Feng, Y. Qian, E. Trakhtenberg, B. Tieman, B.-C. Cha, K. Goetze, T. Mooney, and W.S. Haddad (1998) SPIE Proc. **3449**, 67.

Moldovan, N. (1999) "Deformations and stress in PMMA during hard x-ray exposure for deep lithography," SPIE Proc. **3875**, 155.

Momose, A. (1995) Nucl. Instrum. Methods **A352**, 622.

Mooney, T.M., T. Toellner, W. Sturhahn, E.E. Alp, S.D. Shastri (1994) Nucl. Instrum. Methods A **347**, 348.

Nelson, C.S. (1999) Ph.D. thesis, Northwestern University.

Nelson, C.S., G. Srajer, J.C. Lang, C.T. Venkataraman, S.K. Sinha, H. Hashizume, N. Ishimatsu, and N. Hosoito (1999) Phys. Rev. B **60**, 12234.

Osborn, R., S. Rosenkranz, D. N. Argyriou, L. Vasiliu-Doloc, J. W. Lynn, S. K. Sinha, J. F. Mitchell, K. E. Gray, S. D. Bader (1998) Phys. Rev. Lett. **81**, 3964.

Osgood III, R.M., S.K. Sinha, J.W. Freeland, Y.U. Idzerda, and S.D. Bader (1999) J. Magn. Magn. Mater. **198-199**, 698.

Paganin, D., and K.A. Nugent (1998) Phys. Rev. Lett. **80**, 2586-2589.

Parkin, S.S.P., et al. (1999) J. Appl. Lett. **85**, 5828.

Pollmann, J., G. Srajer, J. Maser, J.C. Lang, C.S. Nelson, C.T. Venkataraman, and E.D. Isaacs (2000) Rev. Sci. Instrum. **71**, 2386.

Sage, T., et al. (in preparation)

Sette, F., et al. (1995) Phys. Rev. Lett. **75**, 850.

Shu, D., T. Toellner, E.E. Alp, (submitted)

Sinn, H., et al. (1997) Phys. Rev. Lett. **78**, 1715.

Sinn, H., E.E. Alp, A. Alatas, J. Barraza, G. Bortel, E. Burkel, D. Shu, W. Sturhahn, J.P. Sutter, T.S. Toellner, (submitted).

Srajer, G., et al., to be published

Sturhahn, W., T.S. Toellner, E.E. Alp, X. Zhang, M. Ando, Y. Yoda, S. Kikuta, M. Seto, C.W. Kimball, B. Dabrowski, (1995) Phys. Rev. Lett. **74**, 3832.

Sutter, J. (2000) PhD thesis, Purdue University.

Sutter, J., et al. (in press) Phys. Rev. B.

Thompson, P.A., G.S. Grest and M.O. Robbins (1992) Phys. Rev. Lett. **68**, 3448.

Toellner, T.S., T. Mooney, S. Shastri, E.E. Alp, (1992) "High Energy Resolution, High Angular Acceptance Crystal Monochromator," in *Optics for High-Brightness Synchrotron Radiation Beamlines*, ed. J. Arthur, SPIE Proc. **1740**, 218.

Toellner, T.S., M.Y. Hu, W. Sturhahn, K. Quast, E.E. Alp (1997) Appl. Phys. Lett. **71**, 2112.

Toellner, T.S. (2000) Hyperfine Interact. **125**, 3-28.

van der Laan, G. (1999) Phys. Rev. Lett. **82**, 641.

van Veenendaal, M., J.B. Goedkoop, and B.T. Thole (1997) Phys. Rev. Lett. **78** 1162.

Vasiliu-Doloc, L., S. Rosenkranz, R. Osborn, S. K. Sinha, J. W. Lynn, J. Mesot, O. Seeck, G. Preosti, A. Fedro, J. F. Mitchell (1999) Phys. Rev. Lett. **83**, 4393.

Wang, Y., F. De Carlo, I. Foster, J. Insley, C. Kesselman, P. Lane, G. von Laszewski,

D. Mancini, I. McNulty, M.-H. Su, and B. Tieman (1999) SPIE Proc. **3772**, 318.

X-ray Microscopy and Spectromicroscopy (1998) J. Thieme, G. Schmahl, D. Rudolph, and E. Umbact, eds. (Springer-Verlag, Berlin Heidelberg).

Yu, C.-J., A.G. Richter, A. Datta, M.K. Durbin and P. Dutta (1999) Phys. Rev. Lett. **82**, 2326.

3 USER TECHNICAL SUPPORT

3.1 Insertion Devices

A total of 25 IDs is presently installed in the storage ring (see Table 3.1). Almost all are hybrid permanent-magnet undulators. One is a hybrid permanent-magnet wiggler with an 8.5-cm period, and one is an electromagnetic wiggler. The most recent additions are 3.3-cm-period undulators for two new beamlines and one new 2.7-cm-period undulator added to an existing beamline. A circularly polarizing undulator is in the final stages of magnetic tuning. More details of the new devices are given below. In the future, it is expected that users will request undulators with period lengths different from these to suit their particular needs. A superconducting device is also planned.

In addition to tuning devices for the APS storage ring, nine 3.3-cm-period undulators have been measured and tuned for the APS FEL project. Details of the APS FEL project will be given in a separate publication.

At the APS, the straight sections in the storage ring have a length of 5.0 m, thus permitting the installation of two undulators of maximum length 2.4 m. In sector 4, two undulators with periods of 3.3 cm and 12.8 cm provide coverage of the energy range from 0.5 to 50 keV. These undulators have been installed in a dogleg configuration with dipole permanent magnets before, between, and after the magnets to horizontally separate the radiation fans by 270 μrad. The hard x-ray range is covered using the APS standard undulator A and a custom-built 12.8-cm-period circularly polarizing undulator (see next section) is used for the intermediate energy x-ray range. An 8 mm beam separation in the first optics enclosure at approximately 30 meters from the center of the straight section is achieved.

Table 3.1. Type and number of IDs installed in the storage ring.

Type	Number
3.3-cm-period undulator	19
5.5-cm-period undulator	1
2.7-cm-period undulaor	2
1.8-cm-period undulator	1
8.5-cm-period wiggler	1
Elliptical multipole wiggler	1

The 2-m-long, 2.7-cm-period undulator, originally designed as a prototype for the FEL project, has now been modified and tuned for installation in the APS storage ring. It was installed in addition to the 2.4-m-long, 2.7-cm-period undulator already in sector 3, bringing the combined length of undulators in that sector to 4.4 m (all with 2.7 cm period). Unlike the other standard

devices, this device was fully designed (including the support structure and the gap motion mechanism) and fabricated at the APS. Only the initial measurement and sorting of magnet blocks were done at STI Optronics. A minimum gap of 8.5 cm is achievable for both IDs. The gap can be adjusted and tapered independently for each ID.

3.1.1 Circularly Polarized Undulator

A circularly polarized undulator (CPU) was fabricated at the Budker Institute of Nuclear Physics (BINP, Novosibirsk, Russia) and delivered to the APS. The magnetic measurement and tuning of the CPU (Fig. 3.1) is being done at the APS. Although the tuning has not yet been completed, some intermediate results are given here.

Fig. 3.1. View of the CPU on the measurement bench.

After the first measurement, several problems were recognized that need to be solved before installation. One problem was the finding that the achievable horizontal field at the maximum coil current of 1400 A was slightly smaller than the vertical field (0.24 T) at the maximum vertical coil current (400 A). In order to solve this problem, the vertical gap of the horizontal poles was reduced by applying shims at the bottom of the poles. The second major problem was the existence of multipole field integral components. Almost all normal and skew multipole components did not meet the requirement. To solve this problem, additional trim coils to correct skew quadrupole, skew octupole, and normal quadrupole integrated field components were designed, fabricated, and installed. Figures 3.2 and 3.3 show the skew quadrupole corrector coil and the skew octupole corrector coil, respectively.

Especially challenging was the correction of skew quadrupole and skew octupole components that were 30 times and 10 times bigger than requirements, respectively. Pure skew quadrupole and skew octupole correction lens are not possible to use due to the aperture restrictions. A combination of a planar skew octupole lens and a skew quadrupole lens allowed us to meet the requirements for both skew components simultaneously.

Figures 3.4 and 3.5 show the vertical coil current dependence of quadrupole and octupole components, respectively, in the circular polarization mode. The handedness of circular polarization is changed by changing the polarity of the vertical coil current since the horizontal coil current is always set to positive values.

A trim coil for compensating the normal quadrupole component is integrated in the

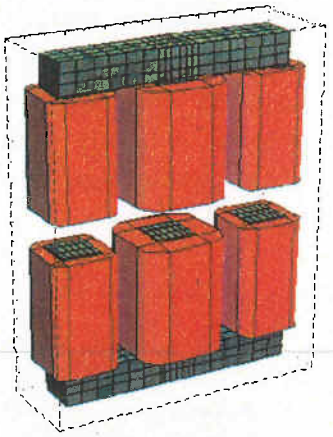

Fig. 3.2. Skew quadrupole corrector coil.

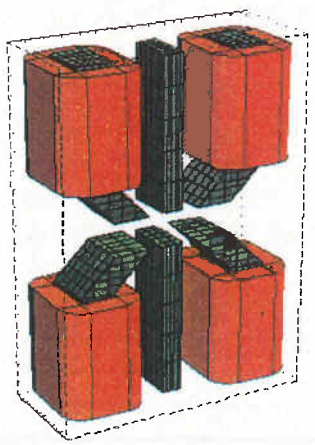

Fig. 3.3. Skew octupole corrector coil.

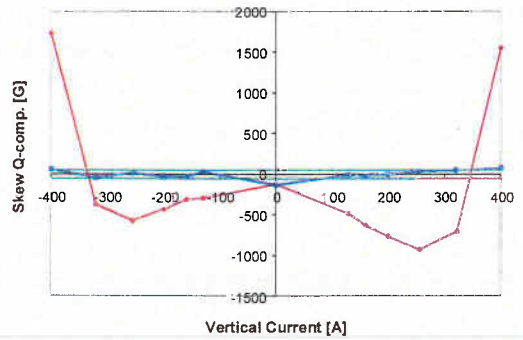

Fig. 3.4. Vertical current dependence of skew quadrupole component. Red corresponds to the field components before correction. Blue corresponds to those after correction. Green lines stand for the tolerance of the ring.

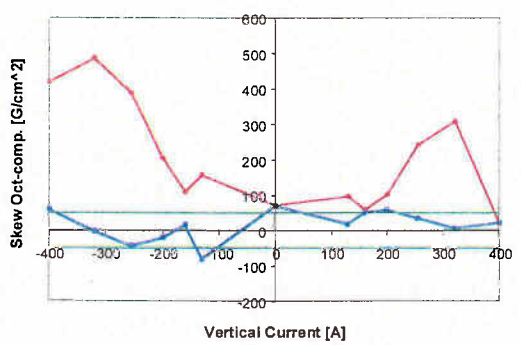

Fig. 3.5. Vertical current dependence of skew octupole component. Red corresponds to the field components before correction. Blue corresponds to those after correction. Green lines stand for the tolerance of the ring

CPU. The vertical coil current dependence of normal quadrupole is shown in Fig. 3.6.

The CPU is capable of switching the polarity of the magnetic field in the frequency range from zero to 10 Hz. In order to implement this feature, trim coils were added to produce vertical and horizontal dipole magnetic fields at each end of the undulator. An arbitrary function generator with four separate channels was designed and fabricated to provide current to the coils. These coils will compensate for vertical and horizontal, first and second field integrals during the switching time from one polarity of the main magnetic field to the other.

Compensation of the dipole field components was performed for all field regions. Figure 3.7 shows examples of

transient field compensation. The vertical switched from positive to negative at the frequency of 5 Hz in this figure. The top half in Fig. 3.7 shows the compensation for the first half period only, and the bottom half shows the compensation result for both first and second half periods. As the result of compensation, the field integral variation is within ± 50 G-cm for all field ranges.

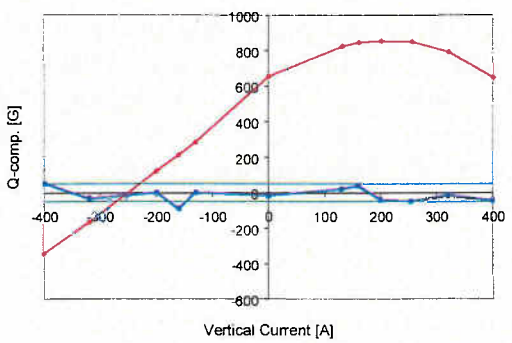

Fig. 3.6. Vertical current dependence of normal quadrupole component. Red corresponds to the field components before correction. Blue corresponds to those after correction. Green lines stand for the tolerance of the ring.

3.1.2 Fabrication of a New Gap Separation Mechanism for Insertion Devices

Four undulators utilizing the APS-designed ID gap separation mechanism have been completed and installed in the storage ring (sectors, 3, 4, 14, and 34), and components to assemble three more have been procured. A photo of the mechanism is shown in Fig. 3.8. The new design improves ID gap positioning accuracy while reducing mechanical complexity and reducing cost. The design uses four drive motors, one for each end of each jaw, which operate independently—thereby simplifying the mechanical drive trains while allowing fine adjustments to the parallelism of the jaws. The load-bearing support is assembled from stress-relieved welded structural steel beams. The system was designed to be compatible with the existing undulator A magnet assemblies and to allow a minimum gap under load of 10.0 mm.

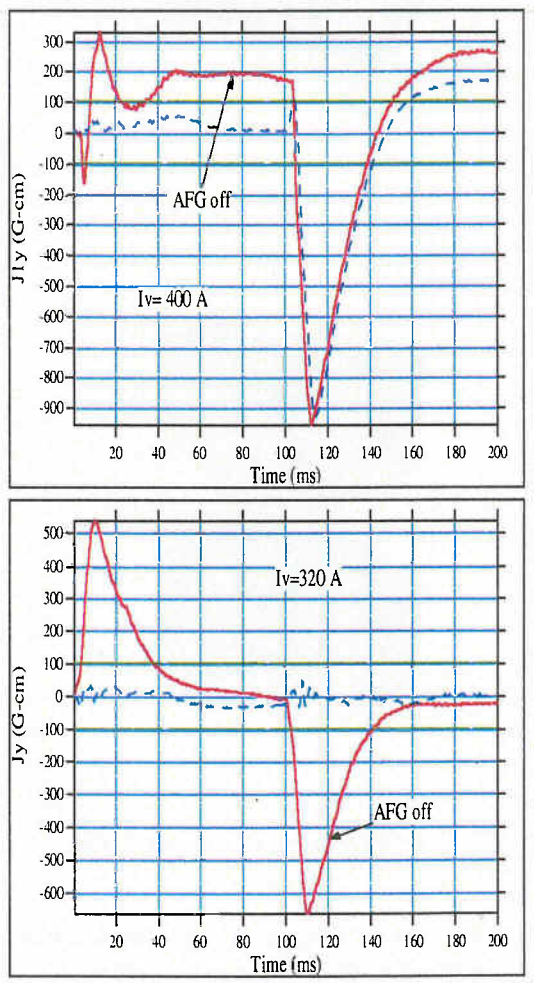

Fig. 3.7. Examples of variation of field integral. Red curves correspond to the field integral before compensation; blue curves correspond to those after compensation by using the arbitrary function generator. Green lines stand for the tolerance of the ring.

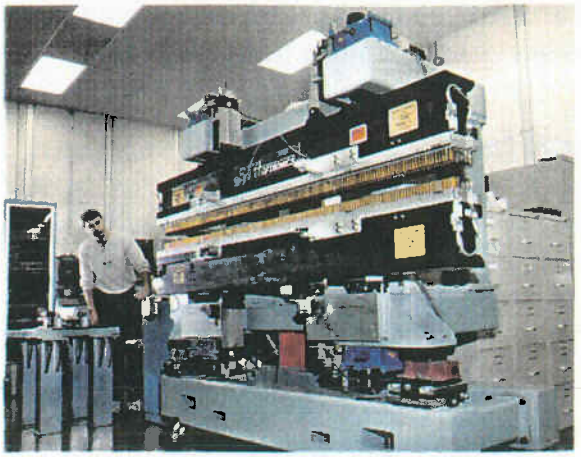

Fig. 3.8. New gap separation mechanism being tested in the magnetic measurement facility.

3.1.3 Insertion Device Vacuum Chamber Development and Fabrication

Vacuum chambers with 8 mm apertures have been installed in 24 of the 35 sectors available for ID beamlines. Construction of new 8-mm-aperture chambers continues; six of the ten chambers being built have already been welded. A 5-meter-long, 5-mm-aperture ID vacuum chamber, in addition to the 5 mm chamber installed in sector 3, has been fabricated and is now installed in sector 4. The 5-mm-aperture vacuum chamber allows the minimum gap to be decreased to 8.5 mm, which enhances the performance of both the 2.7-cm-period device in sector 3 and now the 12.8-cm-period device in sector 4.

3.1.3.1 BESSY insertion device vacuum chamber fabrication

For several years, the ID group of XFD has collaborated with the staff of the BESSY, located in Berlin, Germany, to design and fabricate ID vacuum chambers for the BESSY II project. These chambers used the innovative technology developed by the APS for small aperture vacuum chambers. Previously, nine chambers were fabricated for this facility. XFD is now working on a project to build four additional chambers

3.1.3.2 DESY FEL vacuum chamber fabrication

The Deutsches Elektronen-Synchrotron (DESY), located in Hamburg, Germany, is building a vacuum-ultraviolet (VUV) FEL based on the TESLA Test Facility linear accelerator. The APS is an official partner in this project. Towards this objective, XFD designed and fabricated the small-aperture extruded-aluminum vacuum chambers that are used for the FEL undulators. Seven 9.5-mm-aperature chambers, each 4.516 m long, were built. This project was completed in the summer of 1999, and initial FEL tests were performed at DESY during the fall and winter of 1999.

3.1.3.3 SLS insertion device vacuum chamber design and fabrication

The XFD is collaborating with the Paul Scherer Institute to design and fabricate four insertion device vacuum chambers based on the APS extruded-aluminum design for the SLS. Three of the chambers will be 2.1 m long and will use the APS 12 mm, 8 mm, and 5 mm aperture extrusions, and one chamber will be 5.15 m long and will use the 11 mm extrusion developed for BESSY. Modifications of the rf transitions and welding joints have been developed to match the requirements of the SLS ring. The BESSY-type chamber will also have additional beam position monitors and new pumping ports and end boxes. SLS will

fabricate the supports according to the APS design.

3.2 High-Heat-Load Optics

The daunting task of developing high-quality x-ray optics to withstand the formidable heat loads produced by insertion devices at the APS has been addressed by a considerable XFD/UPD research effort over the last decade. This effort has paid significant dividends, and the optics developed in this program can handle the heat load from two APS undulators operating at closed gap. We continue to pursue several high-heat-load-related projects, including refinement of mono-chromator designs (in particular to get better vacuum performance from cryogenically cooled silicon monochromators) and to develop high-heat-load (HHL) multilayer optics for use with undulators. In addition, the staff involved in the high-heat-load program is stepping up research efforts in other x-ray optics areas, including the development of x-ray interferometers and phase-contrast imaging techniques.

3.2.1 Cryogenically Cooled Silicon Monochromators

The use of cryogenically cooled silicon monochromators on undulator beamlines has become routine at the APS. To provide for a better understanding of the limits for this technology, we have measured the performance limits of two such mono-chromator designs. The results provide quantitative data that can be used to predict the performance of x-ray cryogenic monochromators under increased heat-load conditions that may occur with enhanced APS operations (e.g., higher storage-ring currents or use of longer insertion devices).

Schematics of the tested crystals are shown in Fig. 3.9 (direct cooling) and Fig. 3.10 (indirect cooling). In this context, "direct

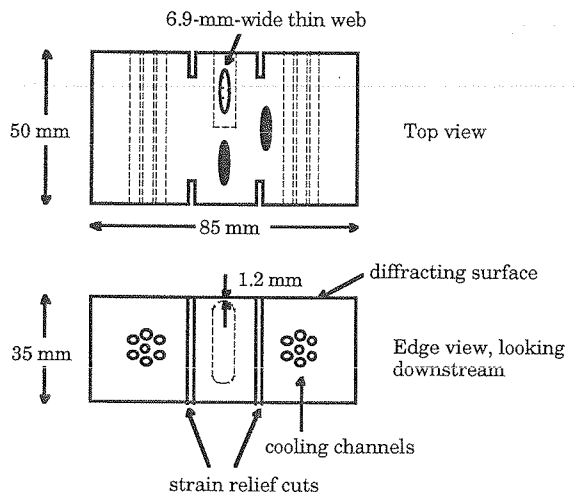

Fig. 3.9. Schematic of the directly cooled silicon monochromator crystal. The diffraction planes are (111).

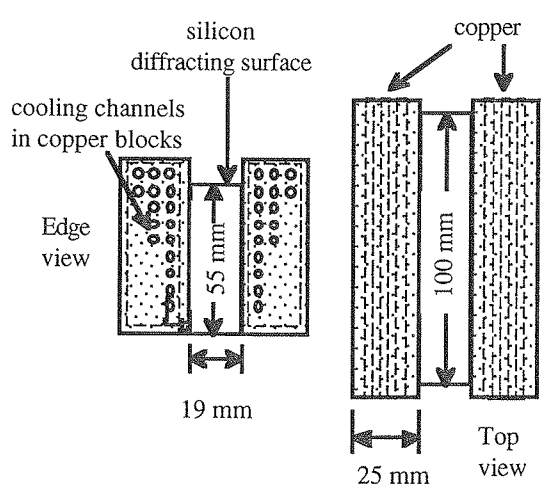

Fig. 3.10. Schematic of the indirectly cooled silicon monochromator crystal. The diffraction planes are (111).

cooling" refers to a monochromator in which the coolant (in this case liquid nitrogen) is in direct contact with the crystal. An "indirectly cooled" monochromator is one in which the crystal is in contact with an intermediary part(s) that is in contact with the coolant.

Special arrangements were made with APS Operations for the use of two standard APS undulators for the directly cooled crystal-monochromator experiments. The standard 1-ID configuration of one APS undulator A was used for the indirectly cooled monochromator. In both cases, calorimetry was performed to experimentally measure the power incident on the crystal. The thermally induced crystal distortion was measured by looking at the full-width, half-maximum (FWHM) widths from double-crystal rocking curves using the Si (333) reflections. For the directly cooled crystal, measurements were performed on both the thin web (see Fig. 3.9) and the thick parts of the crystal.

During the experiments, data were taken for many different x-ray energies with a variety of power densities and power levels. A parametric plot of the data showing total absorbed power and absorbed power density in the first 10 microns of the crystal surface reveals the limits of perfect-crystal performance. Figure 3.11 summarizes the data for the thick and thin part of the directly cooled crystal and shows similar data for the indirectly cooled crystal. The three black traces are drawn, based on experimental data, to denote the acceptable (less than 2 arc seconds of thermal distortion) and unacceptable operating regions. The acceptable regions are to the left and below these lines. The thin blue (100 mA) and thick red (200 mA) lines show the traces of total absorbed power and average absorbed power density in the first 10 μm of a thick crystal for different monochromator energies (7-20 keV) with the corresponding undulator settings (i.e., either the first or third undulator harmonic was matched to the monochromator energy). These "heat-load-tuning-curves" are for 1.5 mm horizontal by 0.5 mm vertical white-beam slits That are about 27 m from the source. This corresponds to the FWHM of the undulator radiation central cone.

These results clearly show that, for the directly cooled crystal shown in Fig. 3.9, the thick part of the crystal performs much better than the thin part. Although the thick part absorbs more power, it has better thermal-conduction paths for heat dissipation. The results also show that the power-absorption profile as a function of depth in the crystal is an important consideration. This is especially true at third-generation synchrotron sources where the critical energy is relatively high. This can be seen from the data plots—at the same total absorbed power, the measured widths are larger for higher absorbed power density in the first 10 μm of silicon.

The results show that this directly cooled monochromator will perform well at thermal loads *twice* the current standard APS operation at 100 mA with a single undulator A (minimum gap of 11 mm) provided the white beam is limited to the size of the undulator central cone. As expected, the performance of the indirectly cooled crystal is not as good as the directly cooled one. Nevertheless, the data show that the

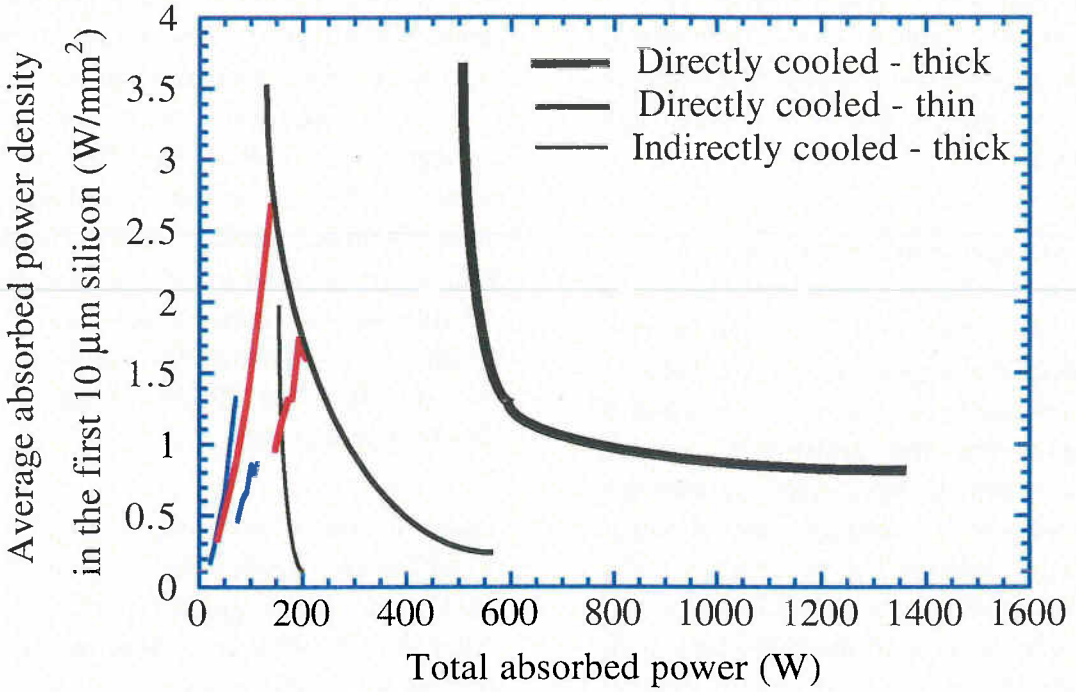

Fig. 3.11. Operating parameters of cryogenically cooled silicon crystals used in the high-heat-load monochromators, which are subject to varying total power and power density as a function of energy, undulator gap, and slit size used. Since diffraction takes place in the first 10 micrometers, the absorbed power density in this region is plotted against total power incident on the crystals. Two different cooling mechanisms, direct cooling with liquid nitrogen flowing inside the crystal and indirect cooling, where the coolant is not in contact with the crystal but with its base, were tested. The lower left part of each curve indicates the region where the measured rocking curve widths were less than 10 microradians, comparable to the vertical divergence of the incident beam. The indirectly cooled thick crystal does not perform well above 160 watts of total power, whereas a directly cooled thick crystal can operate safely up to 500 watts. The thin, directly cooled crystal (which is built into the models prepared for these tests) does not perform as well as the adjacent thick parts, mainly due to difficulties in removing the heat and to mounting strains. For comparison, "heat-load-tuning-curves" are shown for 100 mA (thin blue) and 200 mA (thick red) ring current, with white-beam slits (located at about 27 m from the source) of 1.5 mm horizontal by 0.5 mm vertical.

indirectly cooled crystal can perform well with a single undulator at 100 mA, with the same proviso about white-beam sizes as given above.

3.2.2 Diamond High-Heat-Load Tests

An alternative to cyrogenically cooled silicon for HHL monochromators is the use of diamonds. One figure of merit that is commonly used to evaluate crystals for HHL performance is the ratio of thermal conductivity (k) to thermal expansion

coefficient (α). Liquid-nitrogen-cooled silicon and water-cooled diamond crystals have a α/k ratio roughly 40 times greater than that of room temperature silicon.

We have tested a double-crystal diamond monochromator (both diamonds in Bragg geometry) in a similar manner to the tests on cryogenically cooled silicon (i.e., using both single undulators and two standard APS undulators in tandem). The maximum power incident on the monochromator was 280 W for a single undulator and 700 W for the double-undulator configuration. The diamond first crystal straddled a 3-mm-wide trough in a water-cooled copper holder, with a thin layer of Ga/In eutectic between the diamond and the nickel-plated holder to ensure good thermal contact. For the tests with the double-undulator, we used synthetic type IIa, (111) plates manufactured by Sumitomo. These plates were 10 mm by 5 mm by 0.5 mm thick, with mosaic spread of 3 to 4 arcseconds over the whole plate and 1-3 arcseconds under the beam footprint.

To gauge the performance of the monochromator, we measured the width of the double-crystal rocking curve for the (111) and (333) reflections as a function of the power and power density absorbed by the diamond first crystal. We took data at a fixed gap of 11 mm and varied the absorbed power and power density by changing the monochromator energy. We also measured the response when both the energy and the gap were changed in conjunction so that either the first or third harmonic of the undulator radiation corresponded to the monochromator energy. Figure 3.12 shows the FWHM of the (111) double-crystal rocking curve as a function of energy for one undulator and for two undulators at 11 mm gap. The deviation of the single undulator data from theory is due to the mosaic spread/strain of the crystals. The double undulator data also shows some added thermally induced mounting strains but no appreciable widening due to thermal strain in the first crystal.

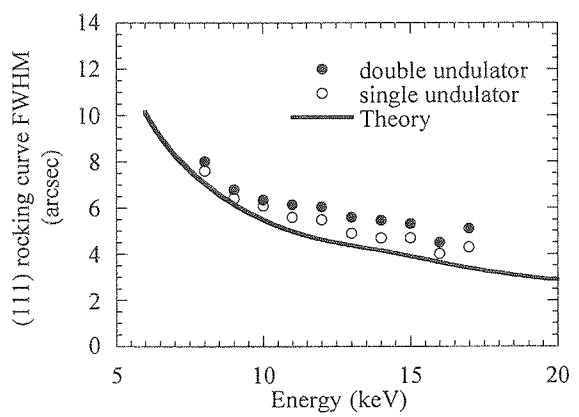

Fig. 3.12. FWHM of the (111) double-crystal rocking curve as a function of energy for one and two undulators at 11 mm gap.

The maximum power and power density absorbed by the first crystal were 37 W and 4.3 W/mm^2 with a single undulator, and 140 W and 17 W/mm^2 for two undulators. Under these conditions, finite element analysis calculations predicted a maximum thermal strain of less than 0.8 and 1.2 arcseconds, respectively, in good agreement with the data. We thus expect that the water-cooled diamond monochromator will perform well under the highest heat-load conditions currently envisaged at the APS.

3.3 Synchrotron Radiation Instrumentation Engineering

The Experimental Facilities Division develops instrumentation, beamline components, and front-end components, for SRI CAT, for other CATs, and for the APS facility. In addition, engineering support is provided to APS users and to the APS Operations Division.

3.3.1 Undulator-Only Front End

The original design of the ID beamline front ends was based on compatibility with various undulators and wigglers. These front ends are standardized and modularized to reduce the cost and engineering effort. They are easy to install and are reliable (Shu and Kuzay, 1994). However, since the standard APS ID, undulator A, achieved excellent performance in generating high-intensity x-ray radiation in the spectral range of 3.2 to 45 keV by using the first, third, and fifth harmonics of radiation, a great majority of the APS users have chosen an undulator as the only source for their ID beamline. Compared with a wiggler source, the undulator source has a much smaller horizontal divergence, providing an opportunity to optimize the beamline front-end design to a new level.

The front end designed for beamline 32-ID is the prototype for a new undulator-only beamline (Shu et al., 2000a). It is called the version 1.5 undulator-only front end. The major design change between the new front end and the original is the optical apertures of the front-end fixed masks. Smaller horizontal optical apertures on the fixed masks allowed us to design the V-shaped compact photon shutter P2-30 shown in Fig. 3.13. This new photon shutter is made from GlidCop™ and stainless steel using the APS-developed box-type explosive bonding technique (Shu et al., 2000b). Compared with the original P1-20 photon shutter, P2-30 provides 150% thermal loading capacity with more than 50% manufacturing cost savings. Figure 3.14 shows the internal water-cooling surfaces and the explosive bonding structure. Table 3.2 shows a comparison of the aperture parameters between the new front end and the original one.

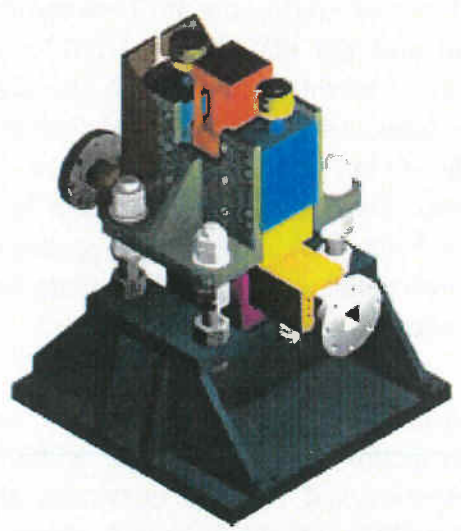

Fig. 3.13. V-shaped compact photon shutter P2-30.

During the past year, the 32-ID front end has been fully commissioned and is now operational. The construction of three more undulator-only v.1.5 front ends is in progress. Figure 3.15 is a schematic layout of the 32-ID beamline front end.

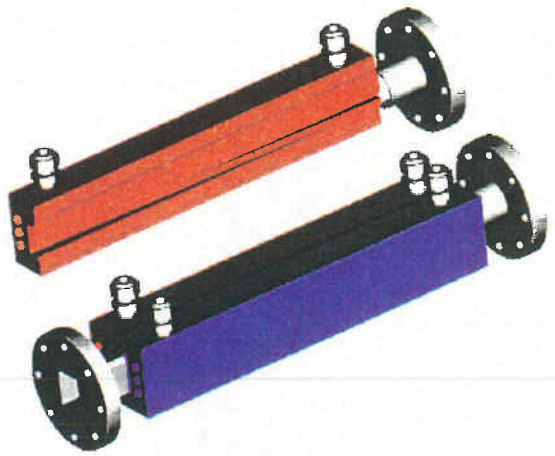

Fig. 3.14. Internal water-cooling surfaces and the explosively bonded structure of the photon shutter P2-30.

3.3.2 Double-Undulator Split Beamlines

The dogleg bend between the sector 4 undulator beamlines is also of interest to other APS CATs. We have examined several preliminary designs for new straight sections and front ends with double-undulator configurations:

- 13.0-mrad dogleg double undulator
- 1.0-mrad dogleg double undulator
- 0.3-mrad dogleg double undulator
- 5-meter undulator

The design for the large-angle 13.0-mrad dogleg double-undulator configuration requires two independent front ends with independent vacuum control for each undulator branch and considerable redesign of storage ring vacuum components. Limited by maintenance space in the storage ring tunnel, these two front ends would need to share supporting systems and specially designed twin photon shutters.

Table 3.2 Comparison of the front-end design parameters.

Aperture parameters		Original front end	New undulator front end
Pre-fixed mask optical aperture	(input)	N/A	38 mm (H) x 26 mm (V)
	(output)	N/A	20 mm (H) x 12 mm (V)
1st fixed mask optical aperture	(input)	38 mm (H) x 26 mm (V)	24 mm (H) x 16 mm (V)
	(output)	24 mm (H) x 12 mm (V)	11 mm (H) x 6 mm (V)
1st photon shutter coverage		70 mm (H) x 16 mm (V)	20 mm (H) x 20 mm (V)
Lead collimator (optical aperture)		62 mm (H) x 20 mm (V)	32 mm (H) x 20 mm (V)
	(shielding aperture)	68 mm (H) x 26 mm (V)	38 mm (H) x 26 mm (V)
Fast valve			70 mm (H) x 18 mm (V)
2nd fixed mask optical aperture	(input)	66 mm (H) x 18 mm (V)	21.5 mm (H) x 14 mm (V)
	(output)	54 mm (H) x 6 mm (V)	12.7 mm (H) x 5.2 mm (V)
2nd photon shutter coverage		70 mm (H) x 10 mm (V)	20 mm (H) x 20 mm (V)
Wall collimator (optical aperture)		72 mm (H) x 20 mm (V)	32 mm (H) x 20 mm (V)
	(shielding aperture)	78 mm (H) x 26 mm (V)	38 mm (H) x 26 mm (V)
Exit fixed mask (input)		40 mm (H) x 12 mm (V)	21 mm (H) x 11 mm (V)
	(output)	4.5 mm (H) x 4.5 mm (V)	3 mm (H) x 2 mm (V)
Exit Be-window		5 mm (H) x 5 mm (V)	3.6 mm (H) x 2.6 mm (V)

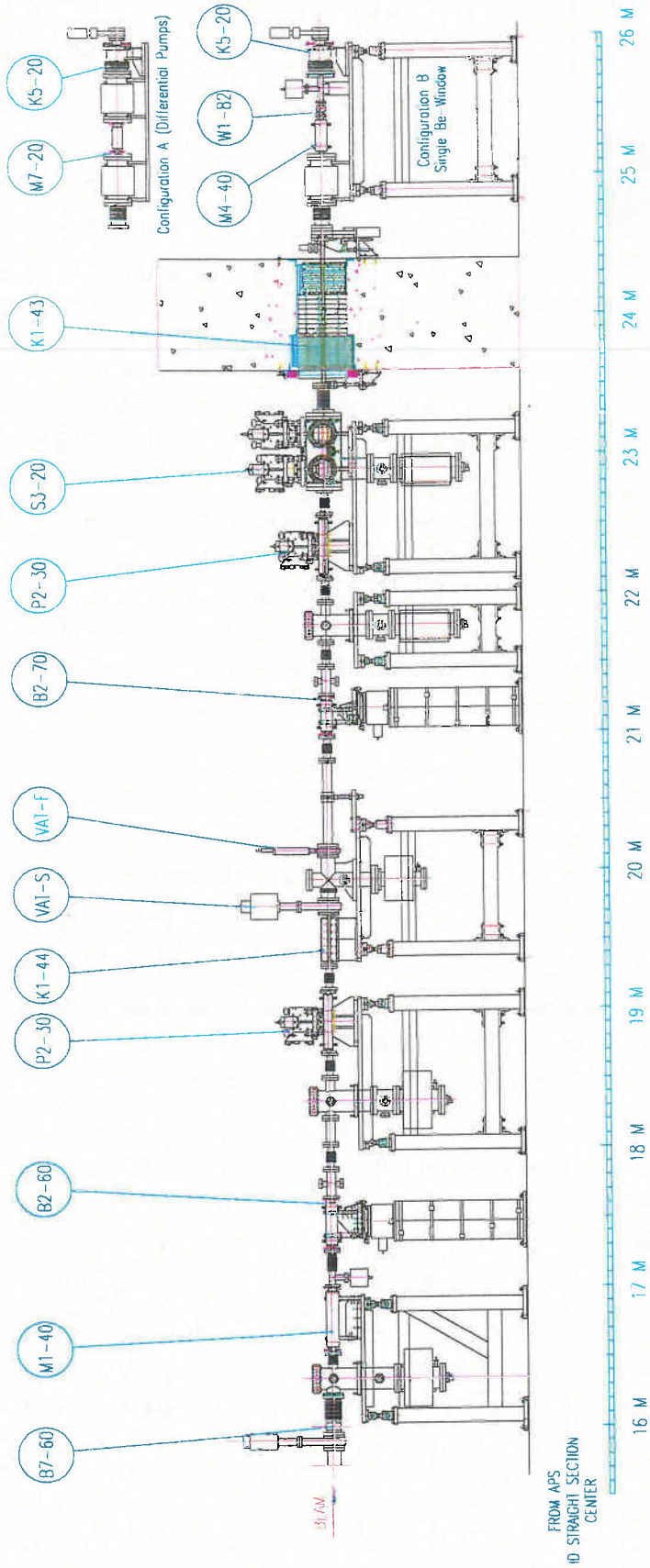

Fig. 3.15. Schematic layout of the 32-ID beamline front end. Beam enters from the left and travels to the right. B7-60*: BM mask, M1-40: ID mask, B2-60: first XBPM/mask, P2-30: first photon shutter, K1-44: collimator, VAT-S: UHV valve, VAT-F: fast valve, B2-70: second XBPM/mask, P2-30: second photon shutter, S3-20: safety shutter, M4-40: exit mask for Be-window, W1-82: single Be-window, K5-20: in-vacuum collimator, M7-20: exit mask for differential pumps.*

For the 0.3-mrad dogleg double-undulator configuration, a single shared front end is a better solution. The SRI-CAT 4-ID front end is an example of such a shared front end, having a 0.27-mrad dogleg separation. We have analyzed the thermal load on the second photon shutter with 0.3-mrad dogleg double-undulator A configuration.

As shown in Fig. 3.16, the peak power density at the front-end second photon shutter in this configuration is 30% higher than the peak power density in the single 2.4-m undulator A case due to the overlap of the two beams. Figure 3.17 shows a finite element analysis result of the maximum surface temperature on the original second photon shutter with this new thermal load. To control the surface temperature, we would need to design a set of new fixed masks with smaller optical apertures for this configuration and reduce the second photon shutter glancing incidence angle from 2 degrees to 1.5 degrees. The x-ray fans from each undulator are separated on the first photon shutter in the 1.0-mrad dogleg configuration, reducing the power density on the shutter. Based on user interest and the feasibility studies, a 1.0-mrad beamline separation has been selected as the most practical.

With the same technical approach, we can upgrade existing undulator/wiggler front ends to be compatible with a 5-meter undulator configuration. More experimental studies at the SRI-CAT 4-ID test facility will help us to optimize the final design.

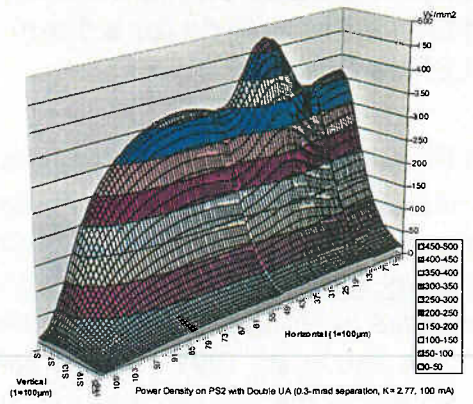

Fig. 3.16. Peak power density at the front-end second photon shutter location in the 0.3-mrad dogleg double-undulator configuration.

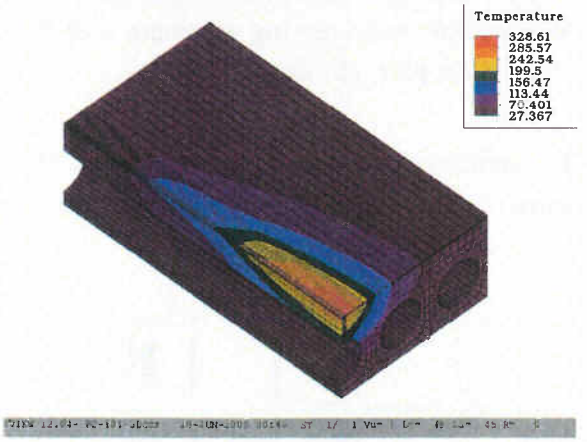

Fig. 3.17. A finite element analysis result of the maximum surface temperature on the original second photon shutter with the thermal load with the 0.3-mrad dogleg double-undulator configuration.

3.3.3 Impact Studies on the Bending Magnet Front Ends for a 6-mm Lattice Offset

At the APS, beam stability and orbit control at the micron level have been design requirements. For both the electron beam and the x-ray beam significant effort has been expended to achieve this (Decker and Singh, 1999; Shu et al., 1997). Decker and Singh summarize the current position on these developments and make several proposals to achieve precise closed-loop local feedback. With the proposed schemes, the well-demonstrated interference of the x-ray beam position monitor (XBPM) signals by the bending magnet (BM) radiation and the corrector and steering magnets will be, for the most part, eliminated.

The primary proposal is to move the upstream and downstream dipole magnets in two consecutive sectors on the APS lattice by 6 mm inboard leaving the IDs untouched. We have studied the potential impact of the lattice offset would be on the APS BM front ends. This impact was investigated by comparing the bremsstrahlung and the synchrotron-radiation ray tracings in regards to the beam missteering with or without the offset alignment implementation in the front ends. Figure 3.18 is a synchrotron radiation ray tracing in the BM front end with the fixed masks realigned. As shown in Fig. 3.18, the BM source is displaced by 6.364 mm inboard. The three fixed masks will be displaced in the horizontal plane by 3.621, 2.278 and 0.846 mm so that they end up on the new beam centerline, which then defines an improved offset angle of 0.298 mrad compared to an unaligned front-end configuration with an offset angle of

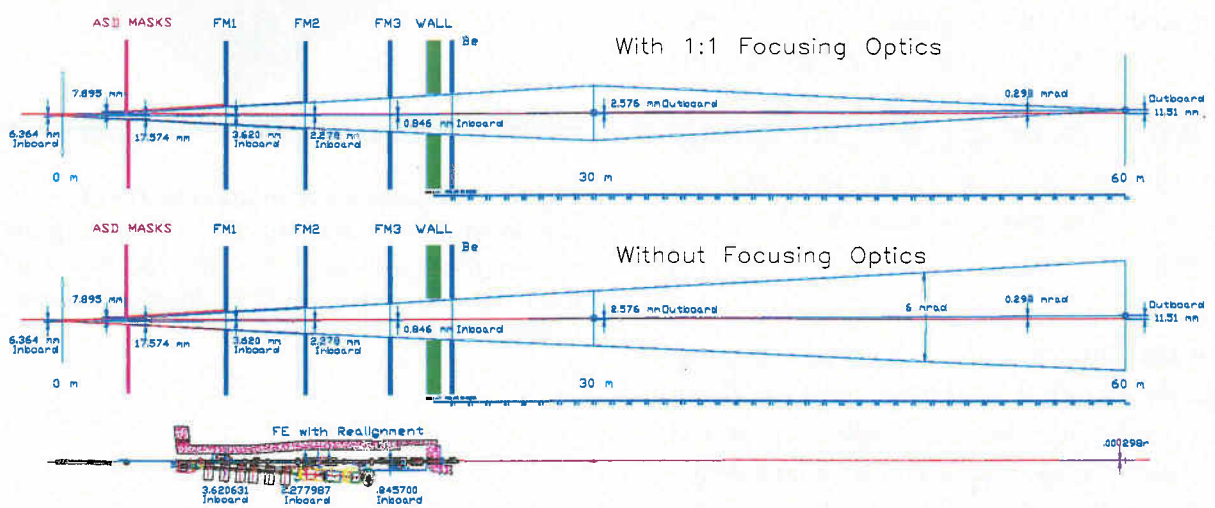

Fig. 3.18. Synchrotron radiation ray tracing in the BM front end with fixed masks realigned for the lattice offset.

0.376 mrad. With the realignment, the BM radiation horizontal fan will be preserved at 6 mrad normal value.

An examination of the bremsstrahlung ray tracings shows no impact as far as the bremsstrahlung is concerned.

3.3.4 Beamline Components Development

3.3.4.1 New XBPM development

Smaller optical apertures on the fixed masks in the new front end create new technical challenges for the XBPM design. To solve the problems experienced during the 32-ID commissioning process, a new compact photoemission-type chemical-vapor-deposition (CVD)-diamond XBPM has been designed (Fig. 3.19) and was tested on the 32-ID front end.

A new XBPM that uses shadowed BM radiation has been proposed for the dogleg double-undulator configurations. Preliminary tests of this new BM-radiation-based XBPM are in progress.

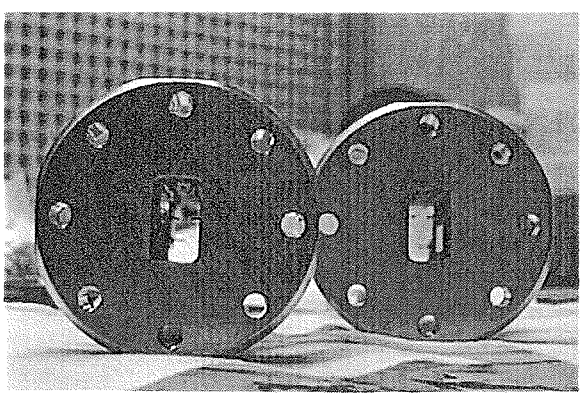

Fig. 3.19. A new compact photoemission-type CVD-diamond XBPM for the 32-ID front end.

3.3.4.2 Wide-angle monochromatic photon shutter

A special wide-horizontal-angle monochromatic photon shutter was designed for the IMM-CAT 8-ID troika-type hard-x-ray multiple-branched beamline. The shutter will be used to regulate the beam reflected from the diamond single-bounce ESRF monochromator in the 8-ID-D hutch. When closed, the shutter must completely prevent the monochromatic beam and any associated stray radiation from entering the 8-ID-E station. When open, the shutter will permit reflected radiation over a range of two-theta from 15 to 50 degrees.

3.3.4.3 Technology development for white-beam components

Beamline components test facility at 4-ID

The SRI-CAT 4-ID-A station houses a vacuum chamber immediately following the front-end differential pump for the testing of new front-end and beamline components. It is called the beamline components test facility (BCTF). This vacuum chamber is equipped with large access flanges for the testing components. Numerous smaller flanges are used for thermocouple, electrical and water-cooling feedthroughs. An infrared mirror is mounted inside the chamber, so that an infrared camera is able to image the temperature distribution on the internal thermal-loading surface of the testing devices as shown in Fig. 3.20. A motorized table is used for varying the angle of incidence on the component under test. The BCTF started commissioning activity in April 2000.

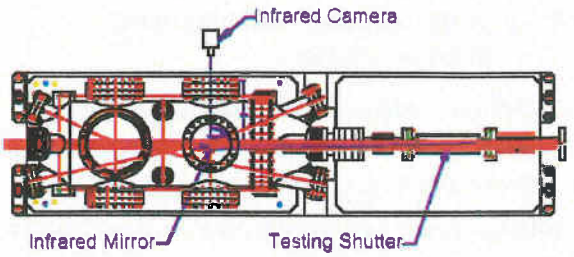

Fig. 3.20. BCTF with infrared mirror and camera.

Recent beamline experiments using infrared thermal imaging

Several experiments have been performed on various beamline components. Typically, thermal images are obtained by viewing through a sapphire window into a vacuum chamber where the component strike surface is located. Often, due to physical constraints, images must be viewed off highly reflective gold infrared mirrors designed to allow a line of sight down the beamline to the target of interest.

Several experiments were conducted at 1-ID-B using a variety of filter materials. The goal was to characterize the maximum operating temperatures of various filter materials commonly used in beamlines. This information can be used to determine maximum allowable operating conditions. Figure 3.21 shows the results of various filter materials of different thicknesses, including graphite, aluminum, diamond, and copper. The full open beam was allowed to strike the filter materials at various undulator gap positions. Note that the maximum surface temperature does not necessarily occur at closed-gap conditions, because the wavelength distribution of the beam changes as a function of undulator gap.

Another set of experiments was performed at 1-ID-A to assess the performance of the new B2-20 beam position monitor under both single- and double-undulator operation modes. Figure 3.22 shows the maximum surface temperature versus undulator gap for both double- and single-undulator configurations. With double-undulator operation, the upstream first undulator is in the closed-gap 11-mm position throughout the tests. Results agree well with predicted operating temperatures.

The new P4-39 white beam photon shutter was recently tested at 4-ID-A with excellent results. Figure 3.23 shows the maximum surface temperature versus undulator gap down to the closed-gap position. Although the ring current was only 75 mA during the test run, the extrapolated results at maximum ring current agree with analytically predicted values.

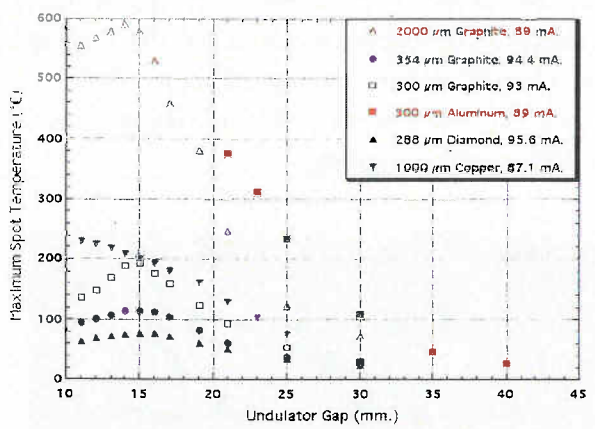

Fig. 3.21. Filter experiments at 1-D-B. Various filter materials of different thicknesses were exposed to the full open beam at various undulator gap positions. There were 250 μm and 300 μm Be windows upstream.

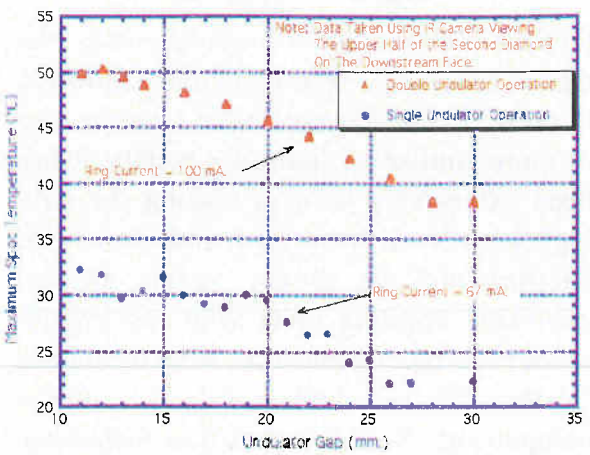

Fig. 3.22. B2-20 beam position monitor tests. Data taken at 1-ID-A with double- and single-undulator operation.

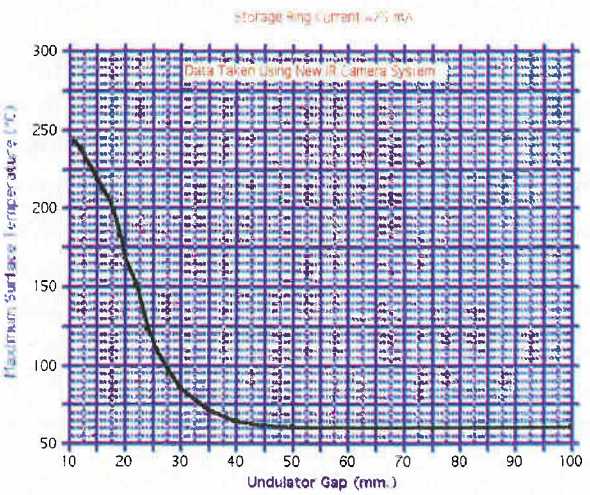

Fig. 3.23. P4-39 white-beam photon-shutter test at the 4-ID-A BCTF. Storage-ring current was 75 mA.

Erosion/corrosion of machinable tungsten in water

As a result of a beamline mishap with a water-cooled tungsten slit, we discovered that significant erosion/corrosion occurs with machinable tungsten when exposed to water. Figure 3.24 shows a cut-away section of a tungsten slit, the water passages are

Fig. 3.24. Cut-away section of a tungsten slit, showing the corroded water passages.

severely corroded from the water used to cool the slit.

Machinable tungsten consists of 95% tungsten, 3.5% nickel and 1.5% iron and is manufactured using a powder metallurgy process. The nickel and iron are used to bind the matrix together, forming a very strong yet machinable material. Oxygen present in water reacts with the iron in the matrix forming iron oxide. The brittle iron oxide then erodes away locally leaving the machinable tungsten without a binding matrix. As this occurs, the tungsten particles erode away from the material without the matrix to keep them bound in place. Once the erosion/corrosion process begins, it progressively accelerates as more and more surface area is exposed to the water.

Four samples were tested for a period of one year; two of the samples were nickel coated and the other two samples were uncoated. Each sample was subjected to 1 gpm of continuous water flow, and the samples were periodically removed and weighed. The weight loss of the samples over time was recorded. Figure 3.25 shows the results of the uncoated machinable tungsten

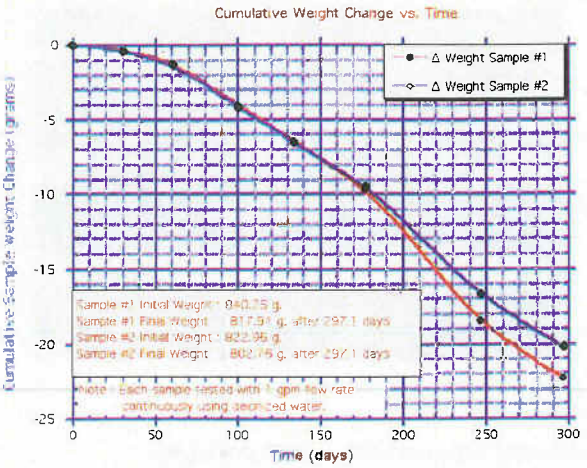

Fig. 3.25. Tests of uncoated machinable tungsten samples exposed to 1 gpm of continuous water flow. Samples were periodically removed and weighed.

samples. Significant weight loss occurred over a very short period, and the weight loss accelerated as more and more material was eroded away. Initially, the nickel coating seemed to reduce the erosion/corrosion rate; however, after a period of time, the nickel was worn away, and the erosion rate increased to the level of the uncoated samples.

It seems that the long-term solution to the erosion/corrosion problem is to remove the oxygen from the water. This prevents iron oxide from being formed, thus corrosion and subsequent erosion can not begin without the oxidation mechanism in place. A better solution for new components made of machinable tungsten is to design them in such a way as to prevent water from ever coming into contact with the tungsten surface. This is the design for the new L5-92 tungsten slits, the cooling water flows through copper tubes that are brazed into the tungsten body.

Explosive bonding

Explosive bonding technology uses the controlled energy of a detonating explosive to create a metallurgical bond between two or more similar or dissimilar metals. It has been extensively used in making the APS high-heat-load beamline and front-end components. In recent years, special explosive bonding units with rectangular joints (box-type) geometries were developed for the APS new high-heat-load beamline components. Based on this new technique, the box form of the component could be built in two halves first, then welded together as shown in Fig. 3.26. Therefore, beamline designers have more freedom to optimize the cooling surface geometry.

Five different high-heat-load beamline components have been designed using this new technique. These include: two white beam photon shutters for beamline integral shutters at 32-ID and 4-ID, a white-beam collimator for 3-ID x-ray collimating lens, a white-beam splitter at 4-ID-A (Fig. 3.26), and an upgraded white-beam grazing-incidence knife-edge slit for 2-ID, shown in Fig. 3.27.

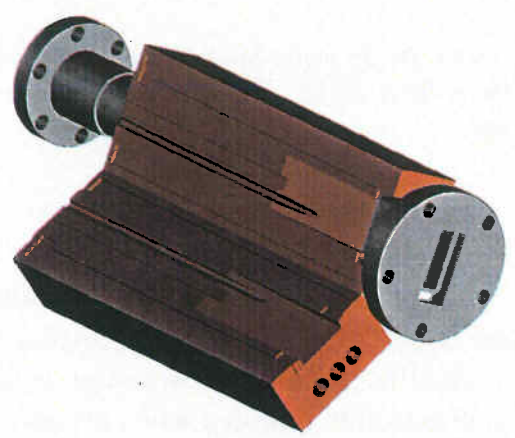

Fig. 3.26. White-beam splitter at 4-ID-A.

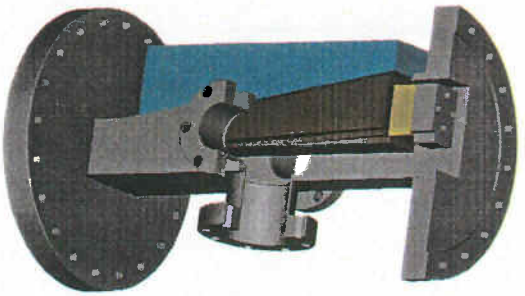

Fig. 3.27. Upgraded white-beam grazing-incidence knife-edge slit for 2-ID.

3.3.4.4 High-resolution and precision instrumentation

Mechanism for artificial channel-cut crystal

We have developed a novel high-stiffness weak-link mechanism having the precision and stability to allow us to align or adjust an assembly of crystals to achieve the same performance as does a single channel-cut crystal. We call it an "artificial channel-cut crystal." Using this mechanism, we can make an outer channel-cut crystal large enough to optimize the nested monochromator's performance and compensate the crystal local temperature and strain variations. This new technique presents a significant opportunity to support the instrumentation development for a high-resolution hard x-ray monochromator with meV energy resolution at the SRI-CAT 3-ID beamline.

Figure 3.28 shows the design of the miniature multiaxis driving structure for the artificial channel-cut crystal. The structure consists of three subassemblies: one base weak-link mechanism and two crystal holders.

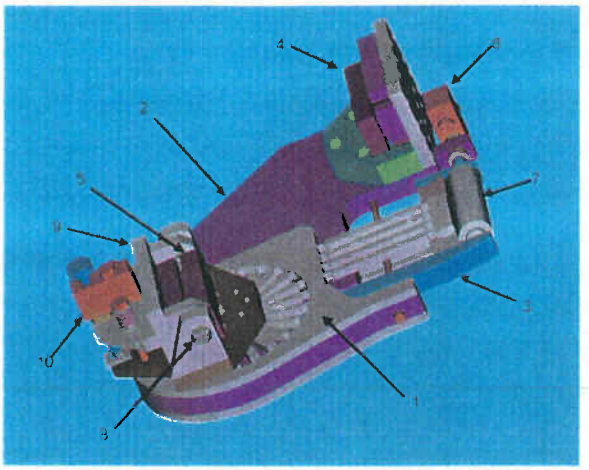

Fig. 3.28. The base mechanism includes a compact sine-bar driving structure for the crystal pitch alignment, which is the key component of the mechanism. There are two groups of stacked thin metal weak-link structures (1) mounted on each side of the base plate (2). A sine-bar (3) is installed on the center of the planar rotary shaft for the pitch alignment between the two (4 4 0) single crystals (4, 5). Two linear drivers are mounted on the base plate serially to drive the sine-bar. The rough adjustment is performed by a Picomotor™ (6) with a 20-nm to 30-nm step size. A Queensgate™ closed-loop controlled PZT (7) with capacitance sensor provides 1-nm resolution for the pitch fine alignment.

To optimize the system stiffness, we have chosen overconstrained mechanisms in this design. The precision of modern photo-chemical machining processes using lithography techniques makes it possible to construct a strain-free (or strain-limited) overconstrained mechanism on a thin metal sheet. By stacking these thin-metal weak-link sheets with align-pins, we can construct a solid complex weak-link structure for a reasonable cost.

A pair of commercial flexure bearings is mounted on one of the crystal holders, and a

Picomotor™-driven structure provides the roll alignment for the crystal.

We have tested the sensitivity of the weak-link sine-bar structure with a laser Doppler angular encoder. A 200-mm-long aluminum arm is mounted on the center of the planar rotary shaft, perpendicular to the sine-bar. A set of prisms is mounted at the end of the arm as a multireflection displacement sensor. During this test, a series of 5-nm incremental steps was applied to the sine-bar by a Queensgate piezoelectric transducer (PZT). The average angular step size measured by the laser Doppler angular encoder is 33 nrad with a 7 nrad rms deviation, which meets the design specification of the weak-link mechanism.

We have tested the first prototype artificial channel-cut crystal as an outer crystal for a 4-bounce high-resolution monochromator with nested configuration at the APS 3-ID-B experiment station. The outer crystals of the monochromator are asymmetrically cut silicon (4 4 0), and the inner channel-cut crystal is silicon (15 11 3). This combination yields a bandpass of 1 meV at 21.6 keV. The monochromator is turnable between 21.5 - 21.7 keV. As a typical case, Fig. 3.29 shows a forty-minute stability result with a 1-meV bandwidth monochromatic beam. The change in transmitted intensity reflects the change in beam position, thermal changes, and crystal angle variations combined. At this point we have not isolated the contribution of the artificial channel-cut crystal assembly alone. However, we infer that the contribution of the angular drift of two crystals attached to each other with the mechanism described here is less than 25 nrad per hour.

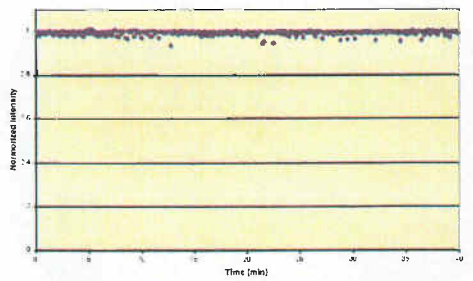

Fig. 3.29. Forty-minute stability result with a 1–meV bandwidth monochromatic beam.

X-ray mirrors for the polarized x-ray facility

The emerging facilities in sector 4 of SRI CAT will provide linearly and circularly polarized x-rays in the intermediate (0.5 to 3 keV) and hard (3-100 keV) x-ray ranges. Intermediate-energy x-rays are created by a novel electromagnetic circularly polarized undulator capable of producing switchable circular and linear polarization, while polarized hard x-rays are formed using a linear undulator with diamond phase-retarding optics. One of the unique features of this sector is the canting of the undulators in the straight section to allow the spatial separation of hard and intermediate x-rays into two separate beamlines that can operate simultaneously.

This separation is made possible with the use of two horizontally deflecting mirrors. The angular adjustments for the beam path require extremely precise rotational motions, with a resolution of 0.15 μrad. For these motions, large-diameter precision ball bearings are chosen over axial bearings. Large open-frame linear stages accomplish the task of moving the mirrors transverse to the beam. These stages allow a compact and symmetrical design.

Rhodium, platinum and multilayer coatings along the water-cooled mirror body enable operations at different energy levels. To move the beam to the individual coatings, each mirror travels a total of 30 mm vertically. All required motions, transverse, vertical, and rotational are applied externally. For optimum performance and ease of maintenance, the mirrors are mounted to large horizontal conflat flanges and covered with bell jar chambers.

3.4 X-ray Optics Fabrication and Metrology

The APS users have continued to avail themselves extensively of our capabilities in the areas of metrology, thin film deposition, crystal fabrication, and mirror design. New capabilities have been acquired and improvements have been made to further enhance the range of x-ray optics that can be made and characterized for users. An atomic force microscope (AFM) has been commissioned, and its operation has been steadily improved to allow characterization of surface roughness at the Angstrom rms level. A vestibule was constructed in the metrology clean room that served to improve the environmental isolation of this microscope (and the entire metrology lab). This was needed because the AFM was found to be extremely sensitive to environmental conditions. A facility improvement was also made in the main polishing room. Cleanliness in this room was much improved by simple changes in the floor and ceiling materials and with the implementation of dust isolation. These improvements were effective in significantly reducing the occurrence of fine scratches in the polished crystal surfaces. A CCD camera has recently been procured for use in x-ray topography. Heretofore the optics fabrication and metrology (OFM) group has used film, and the CCD detector was obtained with the intent both to speed up data taking and to facilitate quantitative analyses of strain in fabricated crystal optics. Also a specialized dicing saw has been procured, which will be used for separating wafers into chips after x-ray lithography and subsequent wafer-level device processing has been performed. This saw will be useful for separating micro- and nanomachines made on large wafers. The saw will also be useful for the sawing of fine grooves for strain release of bent x-ray optics. Improvements in the thin-film deposition facility were made. Software to permit long deposition runs to be automated has been implemented. Multilayers with more than 200 individual layers were made in this way. Reactive sputtering for the deposition of TiO_2 has recently been accomplished by the addition of a simple gas-handling apparatus. Furthermore, a vacuum heater was added to permit deposition by evaporation, as well as by sputtering. A stand-alone x-ray reflectometer has been fully commissioned and is being used to calibrate layer thicknesses using the software package known as IMD (Windt, 1998). A mirror for SRI-CAT sector 4 has been designed. This mirror required special design considerations because the beamline employs two undulators that are not in line and are intended for separate beamline paths. The beamline layout is such that beams from both undulators impinge upon the main heat-load mirror simultaneously; this fact complicated the mirror design considerably. A water-cooled x-ray monochromator to reflect and render useful off-axis radiation from an undulator

beamline has also been designed. Finally, an international workshop to chart out the future of metrology for x-ray and neutron optics was held at the APS.

3.4.1 X-ray Optics Metrology Laboratory

The x-ray optics metrology laboratory is located in a 10,000 Class clean room in the APS experiment hall and houses four different instruments that are fully operational:

1) a long trace profiler (LTP) for measuring slope error and curvature of mirrors up to 2 m in length (Takacs et al.,1999; Assoufid and Her, 1999),

2) a TOPO3D/2D surface roughness microscope that has a height resolution on the order of 1 Å resolution rms,

3) a WYKO-6000 surface profiler for measuring figure error with a maximum aperture of 150 mm and accuracy and repeatability of 1/100 λ and 1/200 λ, respectively,

4) an Explorer atomic force microscope.

During the last two years, we handled 161 metrology measurements. This grand total is broken down as follows: 27 for SRI-CAT, 3 for MU-CAT, 3 for MHATT-CAT, 2 for IMM-CAT, 3 for CMC-CAT, 4 for MR-CAT, 6 for BESSERC-CAT, 5 for CARS-CAT, 3 for SBC-CAT, 2 for COM-CAT, and 16 for UNI-CAT. Also included are 59 measurements performed for the OFM/UPD group that were indirectly for the benefit of the APS users, and 28 measurements performed for non-APS users including BNL, ESRF (Optics Group), Beamline Technology Corp., and the ANL Chemistry Division.

3.4.1.1 Recent enhancements in the metrology cleanroom

Several features were recently implemented to enhance the metrology laboratory environment and measurement accuracy:

1) A vestibule was constructed at the entrance of the metrology cleanroom.

2) A control box was added to allow one to adjust airflow speed, as well as temperature, from the inside of the cleanroom. The airflow velocity can now be lowered to minimize airflow-induced vibration during mirror measurements while still maintaining adequate cleanness of the room. The vestibule provides an additional barrier against dust particles when the airflow velocity is reduced or when the airflow system is completely shutdown.

3) All of the instrument computers are now connected to the APS network, and a single printer located outside of the main cleanroom is used, thus eliminating printer paper, which was one the major source of dust particles.

A mapping of particle measurement performed within the cleanroom, before and after modification, showed a substantial reduction in particle count.

3.4.1.2 Mirror metrology

Over 200 optical measurement requests have been handled since the operation of the metrology laboratory began. The measurement requests included beamline mirrors and mirror bender assemblies, as well as a

variety of small components and substrates. The chart in Fig. 3.30 shows the evolution of optical measurement handled at the metrology laboratory since 1996, with a constant increase in the total volume of measurement. Requests related to beamline mirrors and mirror-bender assemblies make up about 29% of the total. Mirrors are typically 1 m long, and the most common substrate materials are silicon and ULE, and their optical quality has constantly improved during the last seven or eight years.

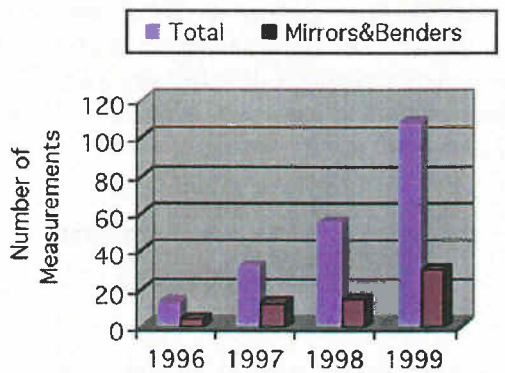

Fig. 3.30. Volume of metrology measurement requests handled over years. The total number of measurements is indicated in blue, and the volume of the mirror- and mirror-bender-assembly related measurements is shown in red.

Nowadays mirrors with surface roughness and slope error on the order of 1.5 Å rms, and <2 μrad rms, respectively, can be easily obtained. The most common substrate (39% of the ones we characterized) is silicon. The pie charts in Fig. 3.31 show the distribution of suppliers of mirrors used at the APS.

The large majority of the evaluated components were from APS CATs and users, but requests have also been handled for other non-APS users, as well as for

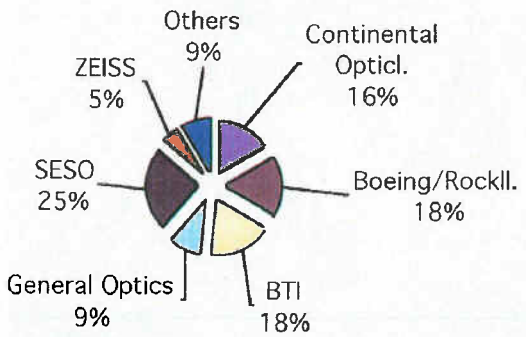

Fig. 3.31. Suppliers of APS mirrors evaluated at the metrology laboratory.

private businesses, such as BTI and SSG corporations. In particular, the APS metrology laboratory has supplied crucial measurement data for developing a Kirkpatrick-Baez (KB) mirror in collaboration with Oak Ridge National Laboratory (ORNL) and BTI (G. Ice et al., 2000).

Figure 3.32 shows a GlidCop mirror from UNI-CAT being carried to the TOPO3D/2D instrument for surface roughness evaluation. It is the largest (1.4 m long) and heaviest (150 kg) mirror to be evaluated. The mirror width (180 mm) allows the user to intercept a 6-mrad x-ray beam fan from the 33-BM beamline. Because of its size and weight, special care was necessary during metrology measurement.

3.4.1.3 Atomic force microscope

The AFM is a very useful metrology tool because it can probe features with sizes and a range of spatial wavelength that are relevant to x-rays. It is particularly useful in studying thin films and in the development of multilayer optics.

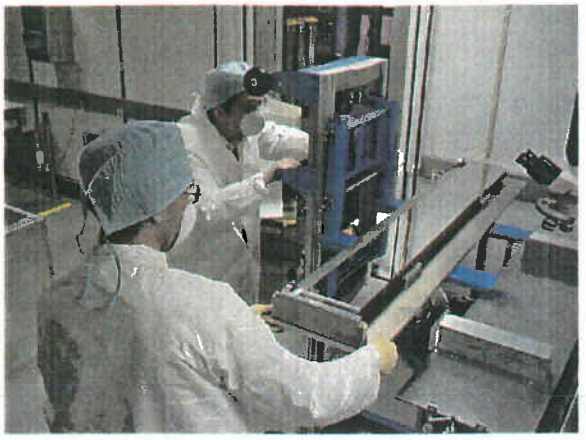

Fig. 3.32. Photograph of the UNI-CAT 1.4-m-long water-cooled GlidCop mirror being moved under the TOPO3D/2D system for surface roughness evaluation. The mirror is 180 mm wide and weighs 100 kg and so requires careful handling. It will be used for focusing a 6-mrad beam from the 33-BM beamline

At the APS metrology laboratory, an AFM Explorer system is used, and we have seen a growing demand in measurement requests with this instrument. It is a stand-alone unit that can be used to evaluate surface topography of samples up to 2 cm x 2 cm area, and it has two different scanners that can probe areas of 130 μm x 130 μm, and 3μm x 3 μm, with a height range of 12 μm and 0.8 μm, respectively. The system works either in contact or noncontact modes. The noncontact mode is very important when evaluating optical surfaces.

Figure 3.33 shows AFM images of a C/W/Si test sample at the OFM deposition facility. The sample is to be used to study the growth of C/W mutilayers for hard x-ray use. The AFM image revealed a structure that cannot be seen by an optical interference microscope.

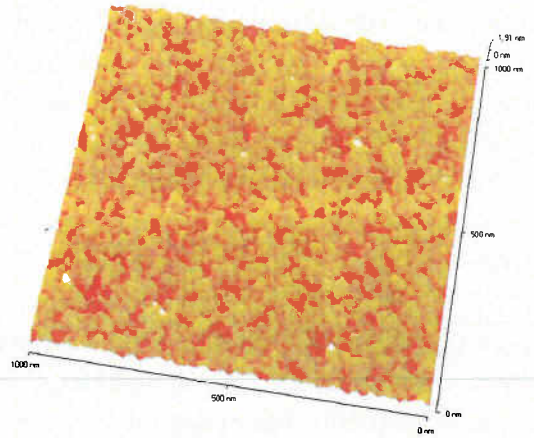

Fig. 3.33. An AFM image of a C/W/Si test sample. The image was taken using a Topometrix Explorer system equipped with a 12-μm Z scanner. The sample has a root mean square surface roughness of 0.182 nm. The AFM revealed details that cannot be resolved with an optical interference microscope.

3.4.2 International Workshop on Metrology for X-ray and Neutron Optics

A two-day International Workshop on Metrology for X-ray and Neutron Optics, the first of its kind, was held at the APS on March 16-17, 2000, and was attended by 64 world-class scientists and engineers, from government laboratories around the world. Several corporate representatives were also among the attendees. The workshop announcement, schedule, and corporate sponsor information are posted on the web at www.aps.anl.gov/conferences/xnom/

Workshop topics and discussions centered around state-of-the art and future needs in metrology instrumentation and techniques used to characterize x-ray and neutron optical substrates, particularly long grazing-incidence mirrors, supermirrors, and multilayers for use in x-ray synchrotron radiation, x-ray FEL and neutron beamlines.

The workshop included formal presentations, as well as informal presentations and group discussions, which allowed tackling a broad area of topics and issues. Among the main topics were the long trace profiler, stitching interferometry, metrology and mirror characterization with x-ray synchrotron radiation, standard issues, and metrology environment requirements.

3.4.3 Deposition Laboratory

Since September 1998, we have made over 370 regular depositions, and more than 500 mirrors and experimental samples have been made in this period. Among them over 160 Au/Cr and Au/Ti on Si samples were fabricated for SRI-CAT x-ray lithography experiments. Other coatings include: Ti, Cr, Al, B_4C, etc., on Si_3N_4 membranes and Be windows for SRI and UNI CATs; Cr on Mylar high-pressure ion chamber windows for ANL-Physics; Al, B_4C/Al, MgF_2/Al on Si visible light reflective mirrors for the undulators in the APS low-energy undulator test line (LEUTL) project; Au and W on Si_3N_4 membranes and Ti on Be x-ray beam detectors for SRI CAT; Al/Cr, Pd/Ti, and Pt/Cr on Si, ZERODUR or glass harmonic rejection mirrors for SRI, IMCA, Bio, and BESSRC CATs; and Rh/Cr, Pt/Cr mirrors for PNC and GSE-CARS CATs.

Additionally, multilayers for sagittal focusing and complicated multilayer structures, such as laterally graded and multistrip multilayers, have been developed. Reactive sputtering has been implemented to make compound thin films such as TiO_2. ^{57}Fe waveguides using multilayer structures have been fabricated in the large sputter deposition system by incorporating a house-invented precision-temperature-controlled evaporator into the system.

Both the large and small deposition systems have been fully automated. An electronic circuit coordinates the sputter-gun power supplies and the substrate movement. It turns the gun on and off at a desired moment for each layer deposition. In the old process, the guns were on all the time. This automation allows us to make more uniform multilayers, save target materials, and fabricate multilayers with larger number of bilayers. An example of the control that we have achieved is shown in Fig. 3.34, which is a transmission electron micrograph of a multilayer structure consisting of 100 layers of W and 100 layers of C (Courtesy of M. Kirk, R. Csencsits, and R. Cook at ANL/MSD). The period thickness is 25.3 Å, and the peak reflectivity is 78% (Macrander et al., 2000). The regularity of the layer thickness and the low roughness are seen to be very good. This deposition control is only possible after repeated calibration from preparatory growths. The thicknesses are then measured rapidly with a stand-alone x-ray reflectometer. Example data for a specular reflection scan are shown in Fig. 3.35. The accompanying simulation was obtained using the IMD software package (Windt, 1998). This figure shows data for a specular scan (in red) and a simulation (green line).

This example is chosen because i) the data exemplifies data obtained with the reflectometer, ii) the thickness of the W layer invoked for the simulation, 0.53 nm, is near the limit of our technological ability, iii) the incomplete agreement between the simulation and the data and the fact that the

invoked rms roughness, 0.5 nm, is roughly the same as the W layer thickness is taken to mean that the modeling software needs to be improved/updated.

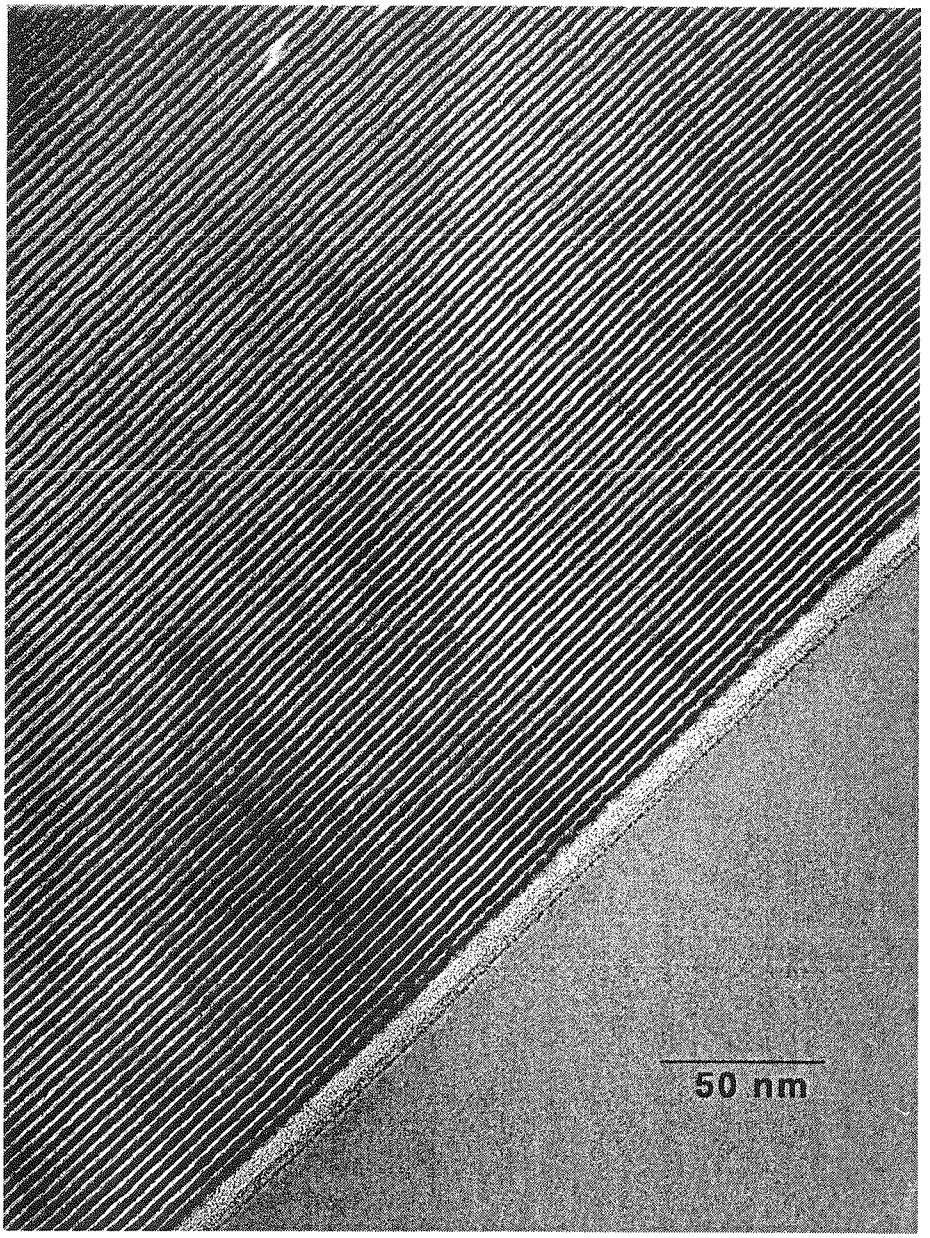

Fig. 3.34. A transmission electron micrograph of a multilayer structure consisting of 100 layers of W and 100 layers of C (courtesy of M. Kirk, R. Csencsits, and R. Cook at ANL/MSD).

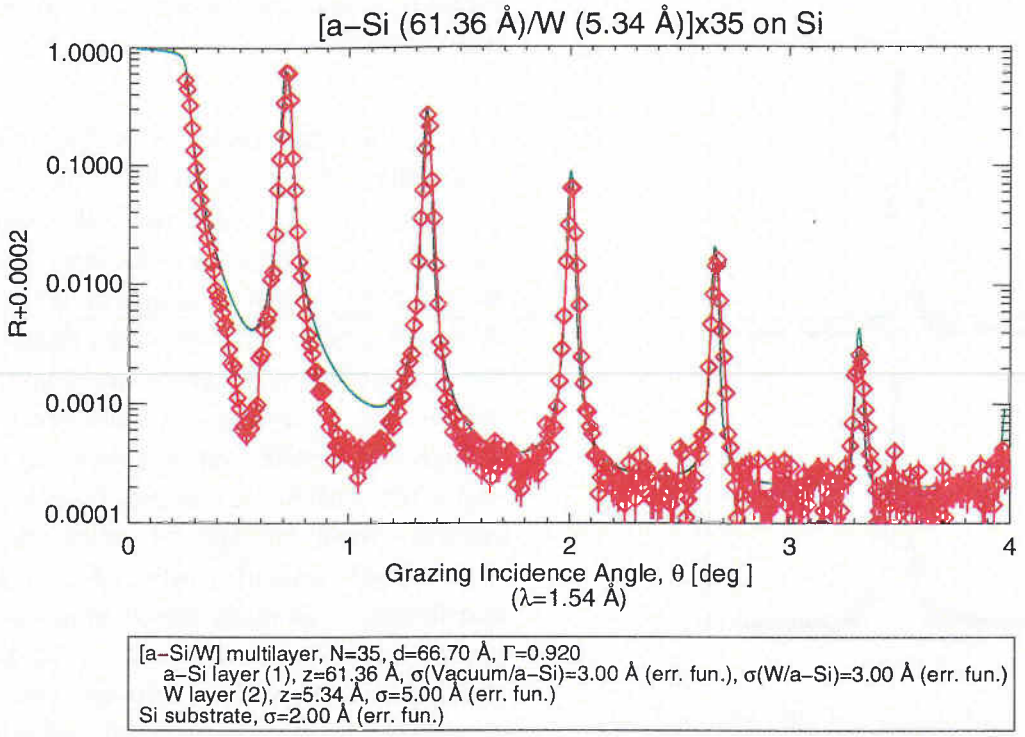

Fig. 3.35. Example data for a specular scan (in red). The accompanying simulation (green line) was obtained using the IMD software package (Windt, 1998).

Recently, we have designed and installed a vacuum heater in the large deposition system. We made novel use of permanent magnets to overcome the challenge of mounting vacuum heaters in an existing vacuum system. Vacuum heaters are important for sample annealing and vacuum baking.

3.4.3.1 Microfocusing mirrors

Kirkpatrick-Baez grazing-incidence mirrors are widely used at the APS as micro-focusing optics. We have coated ~100 of these mirrors for our users. Most mirrors consist of 5 nm Cr and 40 nm Rh (or Pt, or Pd) on Si single crystals or float glasses. We have studied the film growth and roughness of these systems using *in situ* spectroscopic ellipsometry measurements. We found that too thick a Cr underlayer will increase the film roughness, while a 5 nm Cr underlayer will provide both a good adhesion and a smooth surface (Liu et al., 1999). Good results have been obtained for these mirrors. CARS-CAT demonstrated that a system of two 100-mm-long, actively bent mirrors in a KB arrangement could achieve a double-focused beam of 0.8 μm x 0.85 μm and flux density gain greater than 10^5 from 10 keV undulator x-rays. Figure 3.36 shows their focusing results using a fluorescence knife-edge coated at the APS deposition lab. Other CATs, such as PNC-CAT and UNI-CAT, are also using KB mirrors coated at the deposition lab.

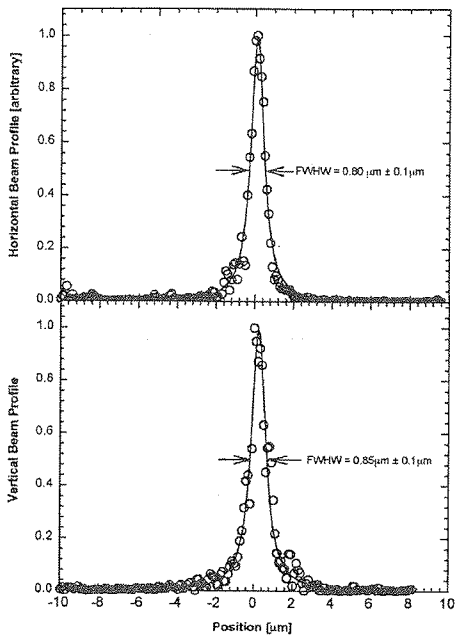

Fig. 3.36. A doubly focused 10 keV undulator x-ray beam obtained from actively bent KB mirrors by CARS-CAT.

3.4.3.2 Graded multilayer deposition

Laterally graded multilayers consisting of uniform W layers and wedge-shaped C layers have been made at the deposition lab for tunable x-ray double-monochromator applications in collaboration with HASY-LAB. The double monochromator has two identical graded multilayers in series, as in the conventional double-crystal mono-chromator arrangement. By letting the x-ray beam hit slightly different (bilayer) d–spacings on each multilayer, one can adjust the bandpass and peak energy of the transmitted beam. Also, since the Bragg angles of the two multilayers are not constrained to be the same, the angle of the transmitted beam can be varied in the vertical plane. This option may be an attractive alternative to the conventional way for studying liquid surfaces in reflectivity and grazing-incidence diffraction measurements.

The films were made by DC magnetron sputtering with the sputtered atoms passing a contoured mask while the substrate was moving. Two different masks were designed to produce either a uniform or graded thickness profile. The mask was fixed on the top of the shielding can of the sputter gun. To determine the shape of these two masks, a thickness profile was measured for a film deposited without any masks installed. The results were compared with that of theoretical calculations of thickness distribution. The mask was then designed to appropriately increase or reduce the flux of the sputtered atoms along the axis perpendicular to the moving direction of the substrate.

Two identical graded multilayer samples were made in the small deposition system for testing at HASYLAB in a double-crystal monochromator arrangement. The multi-layer comprised 60 bilayers of W and C on 100 x 25 x 3 mm float glass with a d-spacing varying from 35 to 60 Å and an average gradient of 0.27 Å/mm along the long direction. The W layer was uniform, while the C layer thickness was graded. Figure 3.37 shows the bilayer spacing as a function of lateral distance as measured from x-ray diffraction data (Macrander et al., 1999).

In addition to W/C, Mo/Si and W/Si graded multilayers have also been fabricated. Graded multilayers have many other novel applications. For example, test samples have been provided to Bio-CAT for x-ray fluorescence detection experiments, and

experiments with x-ray standing waves have also been planned.

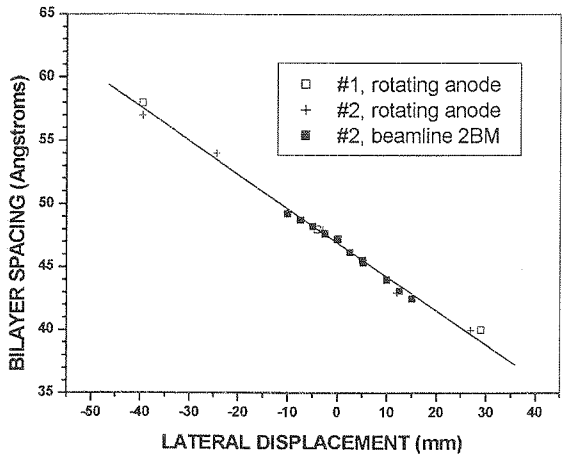

Fig. 3.37. Combined data for the bilayer spacing as a function of lateral distance as measured from the x-ray diffraction data for a W/C graded multilayer.

3.4.3.3 Double-multilayer monochromator for beamline 2-BM

Four stripes of W/C and W/Si multilayers have been coated on two identical Si multilayer (ML) mirrors (100 x 145 x 50 mm) in the large deposition system. Each of the stripes on one of MLs pairs up with a matched stripe on the second ML in a (+,–) double-multilayer monochromator (DMM) configuration. The four stripes on each ML provide four different d-spacings. The stripes are 22 mm wide, coated on two mirrors in the same runs. The thick W/C strip (1.55 nm W / 2.15 nm C x 100 bilayers) has to be coated in two separated runs, with the C-gun cleaned in between, to prevent the C target from arcing. This strip needed a total of 17 hours of deposition. To coat every C layer in the W/C multilayer, the mirrors were moved over the C target 18 times during the coating to provide needed uniformity. Our fully automated system enabled us to accomplish all these smoothly. Test results showed a nonuniformity of ~5%.

3.4.3.4 Reactive sputter deposition

We have succeeded in reactive sputtering for the first time at the APS. TiO_2 films have been made in the large deposition system by sputtering a Ti target in a mixture of Ar and oxygen (85 Ar / 15 oxygen). Two MKS (2159) gas flow controllers together with a MKS (247) power supply (set point source) were used to control the ratio of Ar and O_2 flows. A MKS (250) pressure controller was used to control the total pressure. The gas pressure and composition were stable during the deposition. The TiO_2 films could also be annealed in an O_2 environment after the growth using our house-made vacuum heater.

Spectroscopic ellipsometry was used to measure these films. Our collaborators have shown that these thin TiO_2 films could be used to adsorb/desorb Sr ions as previously done using TiO_2 single crystals. This is important for future x-ray standing wave studies of electrical double-layer structure at the TiO_2-water interface using W/C multilayers.

We are now able to make complicated thin-film structures involving multilayers, graded multilayers, MBE-type isotope thin films, and compound thin films in the same vacuum chamber without the need to break the vacuum.

3.4.4 Fabrication Laboratories

The OFM fabrication laboratory continued to serve user communities of the APS. It has also proved possible to help other synchrotron facilities. The lab prepared new crystal elements (such as monochromators, in particular, cryomonochromators, interferometers, and diced analyzers) for x-ray beamlines and/or improved (i.e., reshaped, re-etched and repolished) crystals that had been already used on the beamlines. All together, in the past two years, the lab delivered to users 394 optical elements. Of these, 158 crystals were for SRI-CAT (including the old and new XFD, and UPD), 8 crystals were for Bio-CAT, 29 crystals for BESSRC-CAT, 2 crystals for IMM-CAT, 40 crystals for PNC-CAT, 14 crystals for MU-CAT, 4 crystals for MHATT-CAT, 12 crystals for UNI-CAT, 17 crystals for CARS-CAT, 38 crystals for DND-CAT, 17 crystals for IMCA-CAT, 2 crystals for CMC-CAT, 4 crystals for SBC-CAT, 3 crystals for HP-CAT, 1 crystal for MR-CAT, 3 crystals for MSD-ANL, 6 crystals for IPNS-ANL, 2 crystals for Physics Dept.-ANL, 2 manifolds for SSRL-Stanford, 6 crystals for Rockefeller University, 4 crystals for Albert Einstein College of Medicine, 16 crystals for Northwestern University, 2 crystals for University of Washington, and 4 crystals for LBL-Berkeley.

Parallel to production activities, some R&D projects were carried out.

1) The polishing room underwent essential reconstruction. A new entrance with a vestibule was added, walls were sealed along the floor, the floor was covered with special linoleum, and the ventilation system was enhanced and air quality improved. With all these modifications, the room was converted into a semi-clean room. As a result, we no longer have problems with scratches that previously often occurred on polished surfaces due to particles entering the room from the nearby loading dock.

2) The lab was equipped with a new polisher (Fig. 3.38) that was built by the Strasbaugh company according to our specifications. The machine is equipped with: a 36" polishing table that can be totally submerged into the polishing slurry, three motorized polishing rings of 12" diameter, and a motorized cutter for making groves in the polishing pads. It is possible, using this machine, to polish crystals (up to 12" dia.) in the so-called floating mode (crystals fully submerged in the slurry, no additional load imposed on the polished object). This type of polishing should result in surfaces of very low roughness and very high flatness. So far, using Rodel pads IC-1000 with a square pattern 0.25" x 0.25", we were able to polish 4" dia. silicon slabs to a roughness of 3.25 Å rms and a flatness of $\lambda/3$.

Fig. 3.38. New polisher from Strasbaugh.

3) In order to enhance our capabilities of crystal cutting, a new saw (Kulicke&Soffa dicer Model 984-10) was purchased. After pre-installation preparations (bringing electrical power, water, sewer and compressed air lines), the machine was installed by the manufacturer. The machine will allow dicing of different materials (e.g., manufacturing of silicon-focusing analyzers and separation of micromechanical objects) and precise cutting of small, mainly silicon, crystals.

3.4.5 X-ray Characterization Laboratory

The x-ray laboratory continued to serve the APS users by offering them opportunities to test their crystals or thin layers deposited on different substrates. Available to any authorized user, a single-axis diffractometer, a Laue camera, and a double-axis diffractometer (all of which are installed at conventional x-ray generators—Rigaku and Spellman) were used to obtain the crystallographic orientation and to do further testing of numerous crystals. The instruments were primarily used for the needs of the fabrication laboratory. The main experimental activities in the x-ray lab were concentrated at the Topo Test Unit (TTU) and the triple-axis diffractometer installed at the rotating anode generator.

In the past two years, the TTU was used for 162 topographic test runs. Predominantly silicon crystals (monochromators and analyzers already manufactured, and sometimes ingots to be used for fabrication) but also 31 diamond crystals, were investigated. A majority of the runs were performed on samples for XFD and/or UPD. However, many crystals for UNI-CAT, IMCA-CAT, MU-CAT, IMM-CAT, CMC-CAT, COM-CAT, HP-CAT, SBC-CAT, CARS-CAT, Bio-CAT, and MHATT-CAT were also tested.

The triple-axis diffractometer was predominantly used for reflectivity measurements (all together 50 single- or multilayers were investigated) and for testing samples that were later used at the beamlines (all together about 18 different samples were checked). Most single-and multilayer samples measured in the lab were produced in the OFM deposition laboratory. Measurements supplied data needed for correction of deposition procedures or constituted testing of final products (e.g., four big 100 mm x 120 mm tungsten/carbon graded multilayers were tested that were used later in Denmark as monochromators). In addition, four beryllium single crystals were investigated under compressive stress. Stress was applied either in the c crystallographic direction (2 samples) or in the a crystallographic direction (another 2 samples). The measurements were carried out in the stress range 0 to 700 MPa using specially designed load frames. A typical triple-axis arrangement with a Ge (111) monochromator and a Ge (111) analyzer was utilized. Additionally, a CCD camera was used for image data acquisition. As the compressive stress on a sample increases, the single crystal fractures into smaller crystal grains of a very complex behavior. The stress-strain response exhibits strong anisotropy. Results are currently under evaluation.

Although there were no major changes to the equipment used in the x-ray laboratory

in the past two years, some small developments are worth noting.

1) Operation of the Topo Test Unit was improved by adding new monochromators and new software that significantly accelerated sample orientation (finding the correct sample tilt position with respect to the monochromator crystallographic planes). Another major improvement of the TTU is to come soon. A new CCD camera (built to our specifications by Roper Scientific) was purchased. It will allow the collection and storage of digitized images. The camera was put into operation temporarily at the triple-axis diffractometer and used for Be experiments. Mounting of the camera on the TTU requires essential mechanical reconstruction of the diffractometer.

2) Upgrading of the triple-axis diffractometer continued.

- A new sample holder was constructed and built. It allows load frames (e.g., hydraulic press) or big slabs with deposited multilayers to be mounted in the center of the four-circle goniometer and translated in two directions normal to each other.
- A second detector that monitors the intensity of the monochromatic beam was added.
- The main detector subassembly was reconstructed. The analyzer table was improved and a platform for mounting a CCD camera was added.
- In addition to EPICS control, the diffractometer can now be run under SPEC control.

3.5 Beamline Controls and Data Acquisition

3.5.1 Overview and General Remarks

The principal tasks of the beamline controls and data acquisition (BCDA) group are to develop, test, maintain, distribute, and support new software and hardware solutions for APS users, and to implement those solutions on SRI-CAT beamlines. The tasks of development and maintenance have become increasingly mixed in recent years, as new features are required in old software, and known problems in mature software must be fixed before new software can be layered on top.

In general, the group's development objectives have become somewhat more complex in recent years as experimental programs have matured on some stations, while new programs have started at others. New programs frequently need new software urgently enough to tolerate the bugs and shortcuts expected from rapid development, while mature programs want incremental improvements in well-tested software and no new bugs. However, the bulk of the software both programs use is the same. EPICS allows custom software in a program's local directory to override specific pieces of base software—in fact it provides two levels of this override support. This allows us to preserve some software-development efficiencies and still serve a variety of different user priorities. But the housekeeping required to maintain several different versions of base software with a variety of custom overrides for each of

roughly 30 experimental programs makes development slower and more error prone.

In past years, most of our effort went into new software development, software distribution, and providing technical support to CAT developers. As the total amount of software has increased, more of our effort has gone into maintaining old software through changes in hardware and in the underlying EPICS and VxWorks software. Increasingly sophisticated applications layered on top of established software (e.g., automated alignment support based on scan software) have exposed problems that were previously ignored. In some cases, our requirements have become unique in the EPICS collaboration, and this has required us to take over development of a custom version of software that we used to rely on other collaboration members to support.

Software distribution absorbs much less effort than it did in years past, partly because maintaining our web-based system has become routine, but mostly because CAT developers now require less thorough documentation of new software, and because they are upgrading less frequently since their focus has moved from development systems to actual users. Now the distribution problem has evolved into a problem of merging software from different developers into a package distributable to all, and this too is essentially a maintenance activity.

As a software group's effort moves from development of new software to maintenance of old software, development teams normally begin to lose developers, in part because people capable of development do not want to become software "babysitters." We cannot afford to lose people. Argonne's Hot Technology program has helped to lower the financial incentive for developers to leave, and we are working to minimize other incentives. We now have an understanding within the group that a minimum of 20 percent of a developer's time should be spent on challenging projects that are interesting and that require development of new skills. Thus far, the group has lost only two developers.

The technical-support problem has changed significantly. CAT developers have become quite proficient, and their technical-support requirements have changed from mostly hand holding to mostly troubleshooting. Instead of a large number of simple tech-support problems, we are getting a small number of difficult ones. The time required is roughly the same, but different group members are involved.

What follows is a listing of software modules and objectives along with descriptions of new developments.

3.5.2 Scan-Related Software

Previously, scan software acquired a single data point at a time, and our storage and visualization tools were layered on top of this software. But the APS provides enough photons that hardware-assisted scanning is required for many applications, notably imaging applications like tomography and microscopy. The scan software was modified to acquire arrays directly from multichannel analyzers, transient digitizers, etc., and this required minimal modifications to the storage and visualization layers.

We developed a system for very rapid acquisition of image data using a waveform generator to drive a 2D piezostage and a multichannel scaler to acquire x-ray data. To implement the system, we rewrote waveform-generator software originally developed by CEBAF, and used MCS software developed by CARS-CAT. We have demonstrated a peak acquisition rate of 10^5 data points per second. No real data have been acquired with the system, as x-ray microscope users apparently are not interested in the technique, and x-ray transmission tomography can be acquired more rapidly with a CCD detector. X-ray fluourescence tomography, however, will require very fast point-by-point acquisition.

Also, users required acquisition of many more than the 15 signals our scan software supported; the latest software allows users to trigger up to four detector modules and acquire up to 85 signals at each data point. In one application, users trigger a scaler, a multichannel analyzer, and a CCD detector. In another application, 64 signals from a bank of multichannel scalers acquire data from a 16-element x-ray detector with four regions of interest per detector.

In some cases, users want the scan software to set up conditions and trigger a separate client program, such as the multichannel analyzer display program, to acquire and store the data. The previous wait-for-client support in the scan software was adequate for use by beamline staff but was not robust or simple enough for outside users.

Users wanted scan software to go straight to the peak of a finished scan, to take some of the tedium out of beamline alignment and to support peak-following scans. This capability, coupled with existing scan-parameter support, has been used to implement one-dimensional (1D) automated alignment of the zone plate and order-sorting aperture for the 2XFM x-ray microscope. The user interface for this microscope is being considered for use on other SRI-CAT x-ray microscopes.

As the scan software became more frequently driven by other software, we discovered a rare condition in the procedure used to verify the links through which the scan software drives positioners. We also discovered that the linking software was not behaving correctly when the client's request for a completion callback was denied. Both of problems have been fixed. Currently, we are testing a solution to another long-standing link-related problem: the scan software was unable to read changes in positioner limits that occurred after the link had been made.

We have developed new tools for manipulating and viewing scan data in the MDA (multidimensional archive) file format written by VME resident software; mdaTools is a collection of programs and libraries supporting this format. Currently, we have a basic listing program; a display program for 1D, 2D, and 3D data; and a program that converts a directory of MDA files into a NeXus file. We also have a modified version of the old data catcher program that displays 2D data as they are being acquired.

3.5.3 EPICS String-Sequence Record

A CAT developer asked for a new EPICS record type to facilitate the development of software for serial and general purpose interface bus (GPIB) devices. The new record extends the EPICS sequence record in the same way the string-calculation record we developed last year extended the EPICS calculation record. The record also simplifies the development of custom user interfaces and is a key element of our multistep-measurement software.

3.5.4 EPICS Optical Table Record

Previously, our optical-table software used first-order approximations to the equations relating real motor positions to virtual motor positions (e.g., tilt angles). We found an exact solution to the system of six coupled transcendental equations that describes the real-to-virtual transformation, and with help from XFD's engineering group, demonstrated an accuracy of a few microns in the position of the point about which the optical table rotates (at the National Design Engineering Show).

3.5.5 Java Interface to EPICS Channel-Access Library

EPICS modules communicate with each other using a facility named "channel access." We would like to develop EPICS client software in the Java programming language, so our programs will run on many different platforms (Unix, Windows, etc.) without modification. A first step in this development is to connect Java with channel access. Java channel access (JCA) does this. Though usable as-is, JCA is not yet implemented entirely in Java, which would require the channel-access protocol definition. When this definition becomes available, we hope to continue the development of JCA.

3.5.6 Conversion to EPICS Message Passing Facility

Previously, EPICS support for analog-to-digital converters (ADCs), digital-to-analog converters (DACs), serial and GPIB devices, and miscellaneous other devices was implemented on a second VME processor using a facility named Hideos. Hideos was too difficult to maintain and port to new VME processors and was replaced by the EPICS message passing facility (MPF). We assisted in the development of MPF by developing VxWorks board-support software. MPF requires more memory than Hideos—too much memory to run on the processors typically installed at APS beamlines. To preserve the investment in these processors, and simplify the conversion from Hideos to MPF, we produced a version of the VxWorks image that could be loaded into flash memory.

3.5.7 Merging Third-Party Software

One function of the BCDA group is to collect software applicable to APS beamlines from all sources and integrate it into a package that is easily distributed and deployed at APS beamlines. Software collected in this way includes a large amount of code from CARS-CAT: support for multichannel analyzers and multichannel scalers, fast proportional integral differential (PID) loops, and MPF versions of serial support we wrote. Also included are support for Heidenhain encoder-interpolation hardware, written by a developer at BESSY; waveform-generator support from CEBAF;

generic subroutine support from the Royal Greenwich Observatory; and slit-control software from UNI-CAT.

In one application of this software, we implemented lookup table support within a feedback loop, to maintain 10 microradian crystal alignment between a linear stage and a rotary stage. This allowed the two stages to be used together to emulate a four-meter-diameter rotation stage.

Among other developments driven directly by user requests are the following:

- Modified and tested support for Heidenhain encoder interpolators.
- Designed and tested interface board for a bank of 16-bit ADCs.
- Designed transition boards for digital and analog output devices.
- Converted Omega temperature controllers to RS232 and made cables for EPICS operation in sector 1.
- Wrote software to run and acquire data from a transient digitizer.
- Updated, fixed, and added to the BCDA web pages. Most significantly added a hardware "home page."
- Fixed problems in support for Oxford ILM202 liquid N2 level controller for MHATT-CAT.
- Converted GPIB support for Queensgate AX301 piezocontroller to serial.
- Designed and implemented remote-shutter electronics for the topography lab.
- Implemented a custom DAC channel to control the mirror bender in 3-ID.
- Designed and built a gate-valve controller.
- Designed and built a Personnel Safety System remote shutter control interface.
- Designed a standard glue-logic electronics module.
- Fabricated and tested 100 new motor-transition boards.
- Wrote software support for Omega, Lakeshore, Oxford, Wavelength Electronics temperature controllers.
- Implemented EPICS access security for the mirror lab.
- Studied wavelet signal processing techniques.
- Wrote software to perform multiple-step measurements (e.g., for dichroism experiments).
- Investigated optimization algorithms for multidimensional automated alignment.
- Modified spherical-grating mono-chromator software to use multiple gratings.
- Developed software support for the Canberra triple channel analyzer.

3.5.8 CCD Image-Grabber Software

The Portable Channel Access Server allows the core functionality of EPICS to exist on a multitude of platforms. One place where it is very desirable to take advantage of this functionality is cheap and/or specialized PC hardware. Over the last couple of years, a significant amount of work has been done with the Portable Channel Access Server to ease the merging of PC-based control and acquisition systems into the EPICS control structure. To date, PC-based CCD camera systems from four separate manufacturers

have been successfully merged into our EPICS-based control system. Also, work has begun to add EPICS control of a PC-based motion control system.

In each case, we were able to use vendor-supplied drivers in their native environment in combination with in-house-developed software to provide virtually seamless EPICS-based control over these systems. This has allowed the users to expand the tools available to them without adding new and unfamiliar control systems for them to learn.

3.5.9 Insertion Device Support

Users who routinely scan the ID along with their monochromator encountered occasional difficulties in unusual circumstances, such as scans interrupted by electron-beam fill operations. To avoid these problems, we wrote a front end to the ID software that makes an ID look more like a simple motor, and that has a more robust command-completion handshake.

3.5.10 Progress toward a Standard Scripting Language

We are in the early stages of what we hope will become a collaboration with developers at ESRF and the National Synchrotron Light Source (NSLS) to implement a standard scripting language for use at synchrotron-radiation beamlines. Users of EPICS-based beamline software have long requested scripting support, and attempts have been made to use the languages tcl and Rexx for this purpose, but defects in these languages or in their availability on different platforms have so far limited progress. The language, Python, now seems to be the best candidate. EPICS developers at Fermilab and KEK (Japanese High Energy Accelerator Research Organization) have produced good connections with the EPICS channel-access layer, and we have assembled some of the required infrastructure (e.g., numeric support, plotting widgets). The project has been set aside for several months.

3.5.11 Parameter Management Software

The software that preserves beamline parameters (e.g., motor speeds and positions) through reboots of the VME crate has become reliable enough that users seldom run the manual parameter-management tools anymore. The software now defends parameters against crashes that occur while they are being saved and detects directory permissions that allow the parameter file to be written but that do not allow its length to be changed.

3.5.12 Motor Support

Motor-control software has undergone a thorough revision with four goals: to reorganize device-support software so that it is easier for third-party developers to write software for new motor controllers, to address a long list of minor problems in the motor-record definition, to support servomotors, and to allow the motor record to be used as an interface to other software, making what some users call a pseudomotor. We have also added motor support for a few new controllers and developed driver electronics for small servos.

3.5.13 System/Network Administration

- Upgraded to redundant file server and new disk array.
- Recovered from failed disks, a failed disk interface, and a failed central processing unit board.
- Upgraded network from 10 Mb hubs to 10/100 Mb switches, 1 Gb backbone.
- Tripled the number of network connections per experiment station in sectors one, two, and three.
- Installed a new network in sector four.
- Installed new tape-library system for system backups.
- Installed new operating system patches and security patches.
- Investigated technologies suitable for an SRI-CAT data store.
- Moved the file server and related equipment, as well as the computer support lab, to new locations.

3.6 References

Assoufid, L., and P. Her (1999) "Recent enhancement of the APS LTP capabilities," to appear in the conference proceeding for *The 11th Conference on Synchrotron Radiation Instrumentation*, Stanford, CA, Oct. 13-15, 1999.

Decker, G., and O. Singh (1999) "Method for Reducing X-ray Background Signals from Insertion Device X-ray Beam Position Monitors," *Physical Review Special Topics – Accelerators and Beams*, Vol. **2**, 112801.

Ice, G., J-S Chung, J. Tischler, A. Lunt, L. Assoufid (2000) Rev. Sci. Instrum. **71**, 2635.

Liu, C., J. Erdmann, and A. Macrander (1999) Thin Solid Films **355-356,** 41.

Macrander, A.T., J. Als-Nielsen, C. Liu, S. Krasnicki, J. Maj, D. Mancini, J. Erdmann, and P. Gaarde (1999) SPIE Proc. **3773,** 100-106.

Macrander, A.T., C. Liu, R. Csencsits, R. Cook, M. Kirk, and R. Headrick, (2000) Physica B **283**, 157-161.

Shu, D., and T.M. Kuzay (1994) "General Layout Design for the Advanced Photon Source Beamline Front Ends," Nucl. Instrum. Methods A**347**, 584-590.

Shu, D., J. Barraza, H. Ding, T.M. Kuzay, and M. Ramanathan (1997) "Progress of the APS High Heat Load X-ray Beam Position Monitor Development," *Synchrotron Radiation Instrumentation: Tenth U.S. National Conference*, E. Fontes, ed. (AIP) pp. 173-177.

Shu, D., M. Ramanathan, and T.M, Kuzay, (2000a) "General Design of the Layout for New Undulator-Only Beamline Front Ends," to be published in the *Proceedings of 7th International Conference on Synchrotron Radiation Instrumentation*, August 21- 25, 2000, Berlin, Germany.

Shu, D., J. Chang, T.M. Kuzay , and D.G. Brasher (2000b) "Development and Applications of Rectangular Box-Type

Explosively Bonded Structures for High-heat-load Beamline Components," to be published in the *Proceedings of 7th International Conference on Synchrotron Radiation Instrumentation*, August 21- 25, 2000, Berlin, Germany.

Takacs, P.Z., E. L. Church, C. Bresloff, and L. Assoufid (1999) "Long Trace Profiler Measurement," to appear in the conference proceeding for *The 11th Conference on Synchrotron Radiation Instrumentation*, Stanford, CA, Oct. 13-15, 1999.

Windt, D.L. (1998) Computers In Physics **12**, 360-370.

4 MAJOR PLANS FOR THE FUTURE

4.1 Plans for Future Instrumentation and Technique Development

4.1.1 X-ray Imaging and Microscopy

In the future, the x-ray imaging and microscopy program will shift from serving primarily as a development and proving ground for strategic instrumentation and techniques to a more balanced program with greater emphasis on scientific applications. This shift is consistent with completion of the planned technical capabilities of the SRI-CAT beamlines and experimental stations. One area to be scaled back is the microfabrication and lithography effort, which will be taken over by the Center for Nanoscale Materials (CNM, see below). The development program will focus on three technical areas: soft and hard x-ray focusing optics with spot sizes down to the nanoscale; high-resolution imaging, diffraction, and coherent scattering using these optics; and high-throughput tomography. X-ray nano-probe development and nanoscience applications, especially in the soft x-ray region, will be conducted in support of the CNM to complement hard x-ray experiments at the proposed NanoCAT. Other applications of these techniques and instrumentation will emphasize investigation of outstanding problems in the biological, biomedical, environmental, and materials sciences. Examples include trace-elemental analysis by microfluorescence of phagosomes infected by pathogenic mycobacteria, and study of layer dynamics in liquid-crystal gels near phase transitions by x-ray intensity fluctuation spectroscopy.

4.1.2 High-Energy X-ray Scattering

The SRI-CAT high-energy program will continue to pursue research along two complementary lines: high-energy x-ray optics development and high-energy experimental technique development. The optics portion of the program will continue to develop state-of-the-art high-energy x-ray optics, including focusing and narrow energy bandpass monochromators, micro-focusing with zone plates, and the use of multilayers and refractive lenses. The experimental-techniques portion of the program will emphasize the areas of high-energy experimentation that exploit the high-brilliance, high-energy x-rays provided by undulators at the APS. Brilliance is used by experiments that need small beams (e.g., 3D stress or compositional profiling), or by those needing very good angular resolution (e.g., high-resolution powder diffraction). Additionally, we will emphasize the development of *in situ* measurements and the study of transient behavior in materials. In the long term, the future of the high-energy x-ray program is strongly coupled with the proposed HEX-CAT. If the HEX-CAT beamlines are built, they will have a strong scientific focus and most of the programmatic science will be moved from 1-ID to HEX-CAT. The high-energy program will continue to use 1-ID for optics and other instrumentation development, consistent with the SRI-CAT mission.

4.1.3 High-Resolution X-ray Scattering

The scientific programs for inelastic nuclear resonant scattering will be extended to

liquids in addition to current high-pressure studies exceeding 1 Mbar, thin films and surfaces and dynamics of proteins. The studies with Fe and Sn will be extended to Dy, Sm, Eu and Kr, as a regular part of the user program at 3-ID. The momentum-resolved inelastic x-ray scattering spectrometer will be enhanced with multiple analyzers. The overall performance of both programs will be improved by implementing cryogenically cooled, artificially linked monochromators. A new initiative will be evaluated in x-ray metrology for high-precision determination of x-ray wavelengths, lattice constant measurements, and x-ray interferometry, in particular with Michelson-Morley and Fabry-Perot type interferometers, taking advantage of exact backscattering or normal incidence diffraction beamline at sector 1.

4.1.4 Polarization Techniques

Magnetic x-ray diffraction, reflectivity, diffuse scattering, and spectromicroscopy techniques will be extended to the study of nanoscale magnetic structures, spin-polarized electronic excitations and organic magnets. Of particular interest is the characterization of periodic magnetic arrays. Modern fabrication techniques have reduced the size of individual elements to as small as 40 nm, and our goal is to achieve a comparable spatial resolution with the circularly polarized microprobe. An upgrade of the existing photoemission microscope (PEEM) is planned in order to study structures down to 20 nm. Furthermore, we will work towards acquiring high magnetic field (B>5 T) capabilities on both branch lines to fully exploit the study of hard and dilute magnetic systems with polarized radiation. In addition, by employing resonant coherent x-ray beams at L-edges of magnetic transition metal and rare-earth atoms the study of magnetic speckle and magnetic domain dynamics will be explored.

4.1.5 Time-Resolved Program

Future efforts of the time-resolved program will fall into two categories: studies that utilize the pulsed nature of the storage ring and those that do not. In the first case, development of a fast x-ray streak camera will allow the development of techniques, such as image-correlation spectroscopy for pump-probe experiments. These will serve as prototype experiments for the kinds of experiments planned for the x-ray FEL sources when they come on-line. For the second case, emphasis will be given to the continued study of transient material behavior and of the dynamics associated with slow fluctuations in condensed matter. Coherent x-ray beams will be used to probe slow dynamics in condensed matter systems through the detection of speckle and the application of photon intensity correlation spectroscopy. This technique should lead to wide application in studying surface fluctuations in various solids and liquid films. In addition, using the technique of x-ray fluorescence correlation spectroscopy demonstrated by us on sector 2, we plan to study the dynamics and relaxation of nanoparticles inserted in complex fluids, interdiffusion at interfaces, and related phenomena. In many cases, these projects will be strongly coupled to the high-energy program or sector 1 optics programs.

4.2 User Support

4.2.1 Synchrotron Radiation Instrumentation Engineering

Engineering and technical support for users will continue to be the priority for both divisions. The main emphasis of this effort will be to develop beamline components and x-ray instrumentation for SRI CAT and other CATs. New front ends capable of handling the thermal loads of double-undulator straight sections will be developed. Users will be assisted with thermal, vibration, and beam stabilization studies, with nanomotion control, and with imaging software development. Some R&D in the area of magnetic systems, vacuum techniques, and software will be required to maintain state-of-the-art capabilities.

4.2.2 Insertion Devices

A program of occasionally swapping out insertion devices will be instituted to allow for improvements in the magnetic tuning of IDs that have been installed for a long time. The ID magnetic field will then be refined to meet the more stringent requirements of smaller storage ring emittance, and the devices will be checked for any magnetic degradation. Undulators with new period lengths will be designed and built as requested by users. The engineering of new, state-of-the-art insertion devices, such as the CPU, will continue and novel short-period superconducting devices will be developed. Effort will be directed towards providing a solid experimental basis for engineering the next-generation synchrotron facility through the engineering and operations support of the APS FEL (LEUTL) and the continuing collaboration with the LCLS.

4.2.3 Optics Fabrication and Metrology

New or enhanced x-ray optics fabrication and characterization facilities in support of new initiatives have been under development. The demand from the synchrotron user community has been for more control over reflecting and diffracting surfaces and interfaces. These demands are expected to increase with the arrival of x-ray FEL beamlines. Precise measurement of the power spectrum for surfaces at long length scales is accomplished with a long trace profiler, and we have added a second LTP instrument to our facility. This unit is currently set up and will serve as a test bed for LTP improvements. The power at short length scales will be measured with an atomic force microscope, and the addition of a near-field scanning optical microscope is planned. Diffuse x-ray scattering is an excellent tool to measure the power spectrum, and a program to implement such measurements on surfaces and interfaces of importance to APS users has been under active development. This program addresses the perpetual issue of the meaningfulness of non-x-ray-based metrology tools for the measurement of the performance of x-ray optics. Fabrication facilities for improved polishing have been built up and will be enhanced incrementally. Commercial suppliers of superpolished surfaces have been able to supply "roughnesses" at the sub-0.1-nm level (rms).

We will be in position to not only fabricate, but also to characterize, such surfaces over the full power spectrum and to verify these assessments with x-ray measurements. The deposition facility continues to be improved and enhanced in several areas. Control over

uniformity for long deposition runs has been a focused activity. These efforts are important for achievement of high-reflectivity multilayers and supermirrors. Design and use of sputtering masks will continue to be emphasized for the growth of laterally graded multilayers and for making the next-generation Kirkpatrick-Baez mirrors using the differential deposition technique. Finally, we will exploit two capabilities that have recently been added. A dicing saw has been commissioned for nanofabrication purposes and for making x-ray analyzers. This saw has already seen significant use for these purposes. A CCD camera has been added to the rotating anode facility for the purpose of making quantitative assessment of topography data and to facilitate the collection of diffraction data. A program to evaluate stress in thin films and multilayers will be undertaken with the addition of this new CCD. Assessment of multilayer performance at cryogenic temperatures is planned.

4.2.4 High-Heat-Load Optics

The high-heat-load optics program has been focused for several years on solving the problem of developing monochromators to handle the heat load from APS undulators. This goal has been met, and the work on high-heat-load monochromators has sub-sided to some degree. We still have several high-heat-load projects (refinement of monochromator designs, multilayer mono-chromators, high-energy monochromators) on which we are working, but a substantial part of our research efforts is now being directed to other optical related areas, such as x-ray interferometry and phase-contrast imaging.

4.3 New Initiatives

4.3.1 Center for Nanoscale Materials

The Center for Nanoscale Materials is one of the five nanoscience research centers proposed by the Department of Energy (DOE). This center builds on strengths at ANL in nanosciences and hard x-ray microprobes to create a unique national capability for nanoscale synthesis, fabrication, and analysis of materials. The CNM will explore the behavior of materials confined to length scales smaller than those that define macroscopic physical behavior. In addition, it will draw extensively on a wide range of resources at ANL, especially the APS, to create an organization at the forefront of nanoscale materials research. The CNM will include an approx. 40,000 sq. ft. building attached to the APS on the southwest side of the Experiment Hall. The CNM will include the development of a new sector at the APS and establishment of NanoCAT. The aim of NanoCAT is to apply a multitude of x-ray techniques to the study and development of advanced nano-structured materials and nanoscale devices at the CNM. The efforts within the proposed NanoCAT will be integrated with the design, characterization, and fabrication efforts within the CNM. In addition, beamlines in the existing SRI CAT will work cooperatively with the CNM to carry out upgrades and subsequent experimental programs in support of the research activities at the CNM.

The XFD will be providing effort for the conceptual design of the NanoCAT sector, including a hard x-ray nanoprobe ID beamline, an x-ray scattering ID beamline

for *in situ* real-time analysis of nanomaterial processing, an x-ray scattering BM beamline for rapid turn-around analysis of nanostructures in support of nanofabrication, and an x-ray lithography BM beamline. XFD scientists are working with scientists from MSD and the ANL Chemisty Division to provide the project planning for the CNM and R&D in support of construction for both synchrotron radiation techniques and microfabrication techniques critical to its success. During construction, XFD will provide scientific and engineering support in the completion of the NanoCAT sector and related facilities at the CNM. XFD scientists will continue to develop experimental techniques and conduct preliminary experiments that will contribute to the basis of the x-ray science that will be part of the CNM.

4.3.2 Inelastic X-ray Scattering (IXS) CAT

A dedicated inelastic x-ray scattering beamline at the APS is proposed, building on the experience obtained at sector 3 of SRI CAT and at other third-generation sources. This proposal, submitted to DOE and the National Science Foundation by a group of scientists at national laboratories, universities and industrial research laboratories, would deliver a state-of-the-art beamline in two complementary energy regimes and would attack a broad scientific program. One spectrometer will focus on very high-resolution work, with energy resolutions in the sub-meV regime. This spectrometer will have the highest resolution in the world and significant projected flux increases of the order of 10. It will carry out seminal work in the study of dynamics in systems, such as high-temperature superconductors, solids under high pressure, proteins and polymers. The second spectrometer will be optimized for the study of higher energy excitations, with resolutions in the 0.05-1 eV range. Here studies will be carried out on electronic excitations in electronically active materials, such as the colossal magnetoresistance manganites, high-temperature superconductors, semiconductors and other novel materials, including the C_{60}-based conductors and Mott-Hubbard insulators.

These two components of the CAT will be designed and operated as essentially separate beamlines, with independently optimized undulators, monochromators and spectrometers. It will take advantage of the next-generation short-period and/or superconducting undulators. In a certain sense, the IXS-CAT beamline may be said to be the "first second-generation beamline at a third-generation source" to constitute the premier facility for the study of dynamics with x-rays in this country.

4.3.3 Normal Incidence Diffraction Beamline at Sector 1

The possibility of building a normal incidence diffraction beamline at the APS was considered early, during the construction phase of the APS, and provisions were made in the storage ring magnets in sector 1 and the storage ring tunnel to extract the photons into the "Early Assembly Area" where there are no other beamlines. In 2000, efforts were made to observe the beam and to characterize the reflectivity and energy bandpass of the back-reflected beam. The encouraging results obtained with sapphire and silicon crystals provided the possibility to generate high-energy-resolution x-rays with a bandpass of

1-to-100 meV in the energy range of 4-to-40 keV. The tunability of up to 20 eV at many different energy points is feasible, with the additional possibility of matching absorption edges of elements. The photon flux exceeding 10^{13} ph/sec/100 meV at 6 keV, or 10^{11} ph/sec/10 meV at 15 keV, or even 10^{10} ph/sec/1 meV at 25 keV can be reached. The total length of the beamline can exceed 130 m, if the backscattering crystal is placed at the end of sector 1.

There are a variety of scientific possibilities offered by a normal incidence diffraction beamline: x-ray metrology, x-ray interferometry, high-energy resolution spectroscopy above 30 keV, and microfocusing for a submicron-resolution Mossbauer microscope. We plan to pursue all of these possibilities.

4.3.4 High-Energy X-ray (HEX) CAT

HEX-CAT is an effort to form a collaborative access team for the construction and operation of an APS sector dedicated to the use of high-energy x-rays for a diverse scientific agenda. HEX-CAT has primarily grown out of the high-energy x-ray program based on sector 1, and the CAT director and several members of the CAT are from the x-ray physics group of UPD. If HEX-CAT is funded and built, some members of the x-ray physics group will become essentially full-time HEX-CAT staff members. A letter of intent was submitted to the APS Program Evaluation Board in October of 2000. This letter of intent was accepted, and the Board invited HEX-CAT to submit a scientific proposal.

The ID beamline of the HEX-CAT will be a "second-generation" APS beamline, with specially designed undulators, state-of-the-art x-ray optics, and dedicated experimental instrumentation. The two primary goals of the beamline will be to maximize the x-ray brilliance in the 40 keV to 90 keV energy range and to have efficient operations to accommodate large numbers of experiments. An optimized high-energy BM beamline will also be built to provide for experiments that do not require the high levels of brilliance of the undulator beamline.

The scientific scope for the CAT is the use of high-energy x-rays for single-crystal and powder diffraction, diffuse scattering, scattering from amorphous materials, determination of stress/strain and texture in materials, phase-contrast imaging, fluorescence mapping and the study of solid/liquid or liquid/liquid interfaces. Dedicated instrumentation will be developed for each of these techniques. The intention of HEX-CAT is to serve a wide range of scientific interests including (but not limited to): condensed-matter physics, both applied and basic materials science research, chemistry, environmental and geological sciences, engineering, and nontraditional synchrotron users such as archaeologists. We believe that this facility will be highly complementary to other APS CATs and to the users of neutron scattering facilities.

Appendix 1

1999 & 2000 XFD and UPD Publications

Adams, B., P. Fernandez, W.-K. Lee, G. Materlik, D.M. Mills, D.V. Novikov, "Parametric Down Conversion of X-ray Photons," J. Synchrotron Rad. **7**, 81-88 (2000).

Alp, E.E., W. Sturhahn, T. Toellner, "Synchrotron Radiation and the Mössbauer Effect: Recent Develpoments," Mossbauer Effect Reference and Data Journal **22**, 167-169 (1999).

Alp, E.E., W. Sturhahn, T.S. Toellner, "Polarizer-Analyzer Optics," Hyperfine Interact. **125**, 45-68 (2000).

Alp, E.E., W. Sturhahn, H. Sinn, T. Toellner, M. Hu, J. Sutter, A. Alatas, "Inelastic Scattering of Synchrotron Radiation from Electrons and Nuclei for Lattice Dynamics Studies," in *X-ray and Inner Shell Processes*, R. W. Duncford, et al., eds. (AIP, 2000) pp. 713-718.

Andruszkow, J., ...P. Den Hartog, ..., E. Gluskin, ...E. Trakhtenberg, et al. (a total of 146 authors listed alphabetically), "First Observation of Self-Amplified Spontaneous Emission in a Free-Electron Laser at 109 nm Wavelength," Phys. Rev. Lett. **85**, 3825-3829 (2000)

Assoufid, L., D.M. Mills, A. Macrander, G. Tajiri, "Is Colder Better? - Exploring the Feasibility of Liquid-Helium-Cooled Optics," SPIE Proc. **3773** (SPIE, 1999) pp. 39-48.

Assoufid, L., P. Her, "A Simple Way of Characterizing X-ray Downwards-Deflecting Mirror-Bender Assemblies Using the Long Trace Profiler," Synchrotron Radiation Instrumentation: Eleventh US National Conference, P. Pianetta, et al., eds. (AIP, 2000) pp. 225-229.

Badyal, Y., M. Karabulut, K. Marasinghe, M.- L. Saboungi, D. R. Haeffner, S. D. Shastri, D. E. Day, C. S. Ray, "The Effects of Uranium Oxide High-Level Waste on the Structure of Iron Phosphate Glasses," Mater. Res. Soc. Symp. Proc. **556** (MRS, 1999) p. 297.

Badyal, Y.S., M.-L. Saboungi, D.L. Price, S.D. Shastri, D.R. Haeffner, A.K. Soper, "Electron Distribution in Water," J. Chem. Phys. **112**, 9206-9208 (2000).

Biedron, S.G., S.V. Milton, Y.C. Chae, R.J. Dejus, H.P. Freund, B. Faatz, H.D. Nuhn, S. Reiche, "The APS SASE FEL: Modeling and Code Comparison," Proc. 1999 Particle Accelerator Conference **4**, A. Luccio and W. MacKay, eds. (IEEE, 1999) pp. 2486-2488.

Biedron, S.G., L.H. Yu.M. Babzien, I. Ben-Zvi, L.F. DiMauro, A. Doyuran, W. Graves, E. Johnson, S. Krinsky, R. Malone, I. Pogorelsky, J. Skaritka, G. Rakowsky, L. Solomon, X.J. Wang, M. Woodle, V. Yakimenko, J.N. Galayda, E. Gluskin, J. Jagger, V. Sajaev, I.

Vasserman, "First Lasing of a High-Gain Harmonic Generation Free-Electron Laser Experiment," Nucl. Instrum. Methods A **445**, 301-306 (2000).

Biedron, S.G., Y.C. Chae, R.J. Dejus, B. Faatz, H.P. Freund, H.D. Nuhn, S. Reiche, S.V. Milton, "Multi-Dimensional Free-Electron Laser Simulation Codes: A Comparison Study," Nucl. Instrum. Methods A **445**, 110-115 (2000).

Bilderback, D.H., A.K. Freund, G.S. Knapp, D.M. Mills, "The Historical Development of Cryogenically Cooled Monochromators for Third-Generation Synchrotron Radiation Sources," J. Synchrotron Rad. **7**, 53-60 (2000).

Bortel, G., E.E. Alp, W. Sturhahn, T.S. Toellner, "Wavelength-Dispersive Double Flat-Crystal Analyzer for Inelastic X-ray Scattering," J. Synchrotron Rad. **7**, 333-339 (2000).

Butler, B.D., D.R. Haeffner, P.L. Lee, T.R. Welberry, "High-Energy X-ray Diffuse Scattering Using Weissenberg Flat-Cone Geometry," J. Appl. Crystallogr. **33**, 1046-1050 (2000).

Cai, Z.-H., W. Rodrigues, P. Ilinski, D. Legnini, B. Lai, W. Yun, E. D. Isaacs, K. E. Lutterodt, J. Grenko, R. Glew, S. Sputz, J. Vandenberg, R. People, M. A. Alam, M. Hybertsen, L. J. P. Ketelsen, "Synchrotron X-ray Microdiffraction Diagnostics of Multilayer Optoelectronic Devices," Appl. Phys. Lett. **75**, 100-102 (1999).

Cai, Z., B. Lai, W. Yun, P. Ilinski, D. Legnini, J. Maser, W. Rodrigues, "A Hard X-ray Scanning Microprobe for Fluorescence Imaging and Microdiffraction at the Advanced Photon Source," X-ray Microscopy: Proceedings of the Sixth International Conference, W. Meyer-Ilse, T. Warwick, and D. Attwood, eds. (AIP, 2000) pp. 472-477.

Cai, Z., B. Lai, I. McNulty, A. Khounsary, J. Maser, P. Ilinski, D. Legnini, E. Trakhtenberg, S. Xu, B. Tieman, G. Wiemerslage, W. Yun, E. Gluskin, "Performance of a High-Resolution X-ray Microprobe at the Advanced Photon Source," Synchrotron Radiation Instrumentation: Eleventh US National Conference, P. Pianetta, et al., eds., (AIP, 2000) pp. 31-34.

Chumakov, A.I., W. Sturhahn, "Experimental Aspects of Inelastic Nuclear Resonant Scattering," Hyperfine Interact. **123**, 781-808 (1999).

Coulthard, I., J.W. Freeland, R. Winarski, D.L. Ederer, J.S. Jiang, A. Inomata, S.D. Bader, T.A. Calcott, "Soft X-ray Absorption of a Buried SmCo Film Utilizing Substrate Fluorescence Detection," Appl. Phys. Lett. **74**, 3806-3808 (1999).

Coulthard, I., D.T. Jiang, Y.J. Zhu, T.K. Sham, "A Systematic Study of Synchrotron Light Induced Luminescence from Porous Silicon: Implications to Morphology and Chemical Effect Dependent Electronic Behaviour," J. Porous Mater. **7**, 165-168 (2000).

Coulthard, I., W.J. Antel, Jr., S.P. Frigo, J.W. Freeland, J. Moore, W.S. Calaway, M.J. Pellin, M. Mendelsohn, T.K. Sham, S.J. Naftel, A.PJ. Stampfl, "Resonant Auger Studies of Metallic Systems," J. Vac. Sci. Technol. A **18**, 1955-1958 (2000).

Coulthard, I., W.J. Antel, Jr., J.W. Freeland, T.K. Sham, S.J. Naftel, P. Zhang, "Influence of Sample Oxidation on the Nature of Optical Luminescence from Porour Silicon," Appl. Phys. Lett. **77**, 498-500 (2000).

Decker, G., O. Singh, H. Friedsam, J. Jones, M. Ramanathan, D. Shu, "Reduction of X-BPM Systematic Errors by Modification of Lattice in the APS Storage Ring," Proc. 1999 Particle Accelerator Conference **3**, A. Luccio and W. MacKay, eds. (IEEE, 1999) pp. 2051-2053.

Dejus, R.J., O.A. Shevchenko, N.A. Vinokurov, "An Integral Equation Based Computer Code for High Gain Free-Electron Lasers," Nucl. Instrum. Methods A **429**, 225-228 (1999).

Dejus, R.J., O.A. Shevchenko, N.A. Vinokurov, "Calculations of the Self-Amplified Spontaneous Emission Performance of a Free-Electron Laser," Proc. 1999 Particle Accelerator Conf. **4**, A. Luccio and W. MacKay, eds. (IEEE, 1999) pp. 2492-2494.

Dejus, R.J., O.A. Shevchenko, N.A. Vinokurov, "A Linear Integral-Equation-Based Computer Code for Self-Amplified Spontaneous Emission Calculations of Free-Electron Lasers," Nucl. Instrum. Methods A **445**, 19-23 (2000).

Fenter, P., P. Geissbuehler, E. DiMasi, G. Srajer, L. Sorensen, N. C. Sturchio, "Surface Speciation of Calcite Observed in situ by High-Resolution X-ray Reflectivity," Geochim. Cosmochim. Ac. **64**, 1221-1228 (2000).

Freeland, J.W., K. Bussmann, Y.U. Idzerda, C.-C. Kao, "Understanding Correlations between Chemical and Magnetic Interfacial Roughness," Phys. Rev. B **60**, R9923-R9930 (1999).

Freeland, J.W., K. Bussmann, Y. U. Idzerda, "Connecting Disorder and Magnetic Properties in CoFe Thin Films," Appl. Phys. Lett. **76**, 2603-2605 (2000).

Friedman, E.S., Y. Sato, A. Alatas, C.E. Johnson, T.J. Wilkinson, K.A. Yener, B. Lai, G. Jennings, S.M. Mini, E.E. Alp, "An X-ray Fluorescence Study of Lake Sediments from Ancient Turkey Using Synchrotron Radiation," Advances in X-ray Analysis **42**, 151-160 (2000).

Fultz, B., T.A. Stephens, E.E. Alp, M.Y. Hu, J.P. Sutter, T.S. Toellner, W. Sturhahn, "Atom Clusters and Vibrational Excitations in Chemically Disordered $Pt_3{}^{57}Fe$," Phys. Rev. B **61**, 14517-14522 (2000).

Fultz, B., W. Sturhahn, T.S. Toellner, E.E. Alp, "An Inelastic Nuclear Resonant Scattering Study of Partial Entropies of Ordered and Disordered Fe_3Al," Mat. Res. Soc. Symp. Proc. **590**, S.R. Stock, S.M. Mini, and D.L. Perry, eds. (MRS, 2000) pp. 91-102.

Gluskin, E., E.E. Alp, I. McNulty, W. Sturhahn, J. Sutter, "A Classical Hanbury Brown-Twiss Experiment in the Hard X-ray Wavelength Range," J. Synchrotron Rad. **6**, 1065-1066 (1999).

Gluskin, E., C. Benson, R.J. Dejus, P.K. Den Hartog, B.N. Deriy, O.A. Makarov, S.V. Milton, E.R. Moog, V.I. Ogurtsov, E.M. Trakhtenberg, K.E. Robinson, I.B. Vasserman, N.A. Vinokurov, S.Xu, "The Magnetic and Diagnostics Systems for the Advanced Photon Source Self-Amplified Spontaneously Emitting FEL," Nucl. Instrum. Methods A **429**, 358-364 (1999).

Gluskin, E., N. Vinokurov, V. Tcheskidov, A. Medvedko, Yu. Evtushenko, V. Kolmogorov, P. Vobly, E. Antokhin, P. Ivanov, I. Vasserman, E.M. Trakhtenberg, P.K. Den Hartog, B. Deriy, M. Erdmann, O. Makarov, E.R. Moog, "An Electromagnetic Helical Undulator for Polarized X-rays," AIP Conf. Proc.: Synchrotron Radiation Instrumentation Vol. 521, P. Pianetta, J. Arthur, and S. Brennan, eds. (AIP, 2000) pp. 344-347.

Hahn, U., J. Pflüger, M. Rüter, P.K. Den Hartog, M. Erdmann, E.M. Trakhtenberg, G. Wiemerslage, S. Xu, "The Vacuum Chambers for the VUV SASE FEL at the TESLA Test Facility (TFF FEL) at DESY," Proc. IEEE Particle Accelerator Conference **2**, A. Luccio and W. MacKay, eds. (IEEE, 1999) pp. 1369-1371.

Hahn, U., P.K. den Hartog, J. Pflüger, M. Rüter, G. Schmidt, E.M. Trakhtenberg, "Design and Performance of the Vacuum Chambers for the Undulator of the VUV FEL at the TESLA Test Facility at DESY," Nucl. Instrum. Methods A **445**, 442-447 (2000).

Hashizume, H., S. Miya, T. Tanaka, N. Ishimatsu, Y. Yamaguchi, N. Hosoito, A. Sakuma, G. Srajer, "Internal Magnetic Roughness in an Iron-Gadolinium Multilayer," Phil. Trans. R. Soc. Lond. **357**, 2817-2825 (1999).

Haskel, D., E. A. Stern, F. Dogan, A. R. Moodenbaugh, "XAFS Study of the Low-Temperature Tetragonal Phase of La_{2-x} Ba_xCuO_4: Disorder, Stripes, and T-c Suppression at x=0.125," Phys. Rev. B **61**, 7055-7076 (2000).

Hu, M.Y., W. Sturhahn, T.S. Toellner, P.M. Hession, J.P. Sutter, E.E. Alp, "Data Analysis for Inelastic Nuclear Resonant Absorption Experiments," Nucl. Instrum. Methods A **428**, 551-555 (1999).

Hu, M.Y., T.S. Toellner, W. Sturhahn, P.M. Hession, J.P. Sutter, E.E. Alp, "A High-Resolution Monochromator for Inelastic Nuclear Resonant Scattering Experiments Using ^{119}Sn," Nucl. Instrum. Methods A **430**, 271-276 (1999).

Hwu, Y., B. Lai, D.C. Mancini, J.H. Je, D.Y. Noh, M. Bertolo, G. Tromba, G. Margaritondo, "Coherence Based Contrast Enhancement of X-ray Radiography with a Photoelectron Microscope," Appl. Phys. Lett. **75**, 2377-2379 (1999).

Hwu, Y., H.H. Hsieh, M.J. Lu, W.L. Tsai, H.M. Lin, W.C. Goh, B. Lai, J H. Je, C.K. Kim, D.Y. Noh, H.S. Youn, G. Tromba, G. Margaritondo, "Coherence-Enhanced Synchrotron Radiology: Refraction versus Diffraction Mechanisms," J. Appl. Phys. **86**, 4613-4618 (1999).

Hwu, Y., W.L. Tsai, B. Lai, D.C. Mancini, J.H. Je, D.Y. Noh, H.S. Youn, C.S. Hwang, F. Cerrina, W. Swiech, M. Bertolo, G. Tromba, G. Margaritonda, "Use of Photoelectron Microscopes as X-ray Detectors for Imaging and Other Applications," Nucl. Instrum. Methods A **437**, 516-520 (1999).

Ice, G.E., J-S. Chung, J. Tischler, A. Lunt, L. Assoufid, "Elliptical X-ray Microprobe Mirrors by Differential Deposition," Rev. Sci. Instrum. **71**, 2635 (2000).

Ishimatsu, N., H. Hashizume, S. Hamada, N. Hosoito, C.S. Nelson, C.T. Venkataraman, G. Srajer, J.C. Lang, "Magnetic Structures of Fe/Gd Multilayers Revealed by Resonant X-ray Magnetic Scattering," Phys. Rev. B **60**, 9596-9606 (1999).

Jäschke, J., H.D. Rüter, E. Gerdau, G.V. Smirnov, W. Sturhahn, J. Pollmann, "A Single-Line Linearly Polarized Source of 14.4 keV Radiation by Means of Resonant Absorption," Nucl. Instrum. Methods B **155**, 189-198 (1999).

Job, P.K., M. Pisharody, E. Semones, "Measurement of Absorbed Dose by 7-GeV Bremsstrahlung in a PMMA Phantom," Nucl. Instrum. Methods A **438**, 540-547 (1999).

Job, P.K., M. Pisharody, E. Semones, "Dose Measurements of Bremsstrahlung-Produced Neutrons from Thick Targets at the Advanced Photon Source," Proc. 4th Specialists Meeting on Shielding Aspects of Accelerators, Targets and Irradiation (OECD-NEA, 1999) pp. 17-24.

Job, P.K., M. Pisharody, E. Semones, "Further Measurements of Bremsstrahlung from the Insertion Device Beamlines of the Advanced Photon Source," Proc. 4th Specialists Meeting on Shielding Aspects of Accelerators, Targets, and Irradiation O(ECD-NEA, 1999) pp. 25-33.

Kaendler, I.D., O.H. Seeck, J.-P. Schlomka, M. Tolan, W. Press, J. Stettner, L. Kappius, C. Dieker, S. Mantl, "Structural Characterization of Oxidized Allotaxially Grown $CoSi_2$ Layers by X-ray Scattering," J. Appl. Phys. **87**, 133-139 (2000).

Karablut, M., G. K. Marasinghe, C. S. Ray, G. D. Waddill, D. E. Day, Y. S. Badyal, M.- L. Saboungi, S. Shastri, D. Haeffner, "A High-Energy X-ray and Neutron Scattering Study of Iron-Phosphate Glasses Containing Uranium," J. Appl. Phys. **87**, 2185-2193 (2000).

Kemner, K.M., W. Yun, Z. Cai, B. Lai, H.-R. Lee, J. Maser, D.G. Legnini, W. Rodrigues, J.D. Jastrow, R.M. Miller, S.T. Pratt, M.A. Schneegurt, C.F. Kulpa, Jr., "Using Zone Plates for X-ray Microimaging and Microspectroscopy in Environmental Science," J. Synchrotron Rad. **6**, 639-641 (1999).

Kemner, K.M., B. Lai, J. Maser, M. A. Schneegurt, Z. Cai, P. Ilinski, C. F. Kulpa, D. G. Legnini, K. H. Nealson, S. T. Pratt, W. Rodrigues, M. Lee Tischler, W. Yun, "Use of the High-Energy X-ray Microprobe at the Advanced Photon Source to Investigate the Interations between Metals and Bacteria," X-Ray Microscopy: Proceedings of the Sixth International Conference, W. Meyer-Ilse, T. Warwick, and D. Atwood, eds. (American Institute of Physics, 2000) pp. 319-322.

Keppler, C., K. Achterhold, A. Ostermann, U. van Bürck, A.I. Chumakov, R. Rüffer, W. Sturhahn, E.E. Alp, F.G. Parak, "Nuclear Forward Scattering of Synchrotron Radiation by Deoxymyoglobin," Eur. Biophys. J. **29**, 146-152 (2000).

Keune, W., W. Sturhahn, "Inelastic Nuclear Resonant Absorption of Synchrotron Radiation in Thin Films and Multilayers," Hyperfine Interact. **123**, 847-861 (1999).

Khounsary, A., "Thermal Management of Next-Generation Contact-Cooled Synchrotron X-ray Mirrors," SPIE Proc. **3773** (SPIE, 1999) pp. 78-87.

Kuzay, T.M., J.T. Collins, J. Koons, "Boiling Liquid Nitrogen Heat Transfer in Channels with Porous Copper Inserts," Int. J. Heat Mass. Tran. **42**, 1189-1204 (1999).

Kuzay, T.M., J.T. Collins, "Heat Transfer Augmentation in Channels with Porous Copper Inserts," in *Heat Transfer Enhancement of Heat Exchangers*, S. Kakac, A.E.Bergles, F. Mayinger, and H. Yüncü, eds. (Kluwer Scientific Printers, 1999) pp. 223-231.

Kuzay, T.M., "Thoughts on Reshaping the Engineering Curriculum," Proc. of NATO Advanced Studies Institute, Heat Transfer Enhancement of Heat Exchangers S. Kakac, A. E.Bergles, F. Mayinger, and H. Yüncü, eds. (Kluwer Scientific Printers, 1999) pp. 669-670.

L'abbe, C.L., R. Coussement, J. Odeurs, E.E. Alp, W. Sturhahn, T.S. Toellner, C. Johnson, "Experimental Demonstration of Time-Integrated Synchrotron-Radiation Spectroscopy with Crossed Polarizer and Analyzer," Phys. Rev. B **61**, 4181-4185 (2000).

Labrenz, M., G.K. Druschel, T. Thomsen-Ebert, B. Gilbert, S.A. Welch, K.M. Kemner, G.A. Logan, R.E. Summons, G. De Stasio, P.L. Bond, B. Lai, S.D. Kelly, J.F. Banfield, "Formation of Sphalerite (ZnS) Deposits in Natural Biofilms ofSulfate-Reducing Bacteria," Science **290**, 1744-1747 (2000).

Lai, B., K. M. Kemner, J. Maser, M. A. Schneegurt, Z. Cai, P. P. Ilinski, C. F. Kulpa, D. G. Legnini, K. H. Nealson, S. T. Pratt, W. Rodrigues, M. Lee Tischler, W. Yun, "High-Resolution X-Ray Imaging for Microbiology at the Advanced Photon Source," X-Ray and Inner-Shell Processes, R. W. Dunford et al., ed. (American Institute of Physics, 2000) pp. 585-589.

Lang, J.C., G. Srajer, J. Wang, P.L. Lee, "Performance of the Advanced Photon Source 1-BM Beamline Optics," Rev. Sci. Instrum. **70**, 4457-4462 (1999).

Lee, H.-R., D. Kupperman, W. Yun, Z. Cai, W. Rodrigues, "X-ray Microdiffraction Studies to Measure Strain Fields in a Metal Matrix Composite," Rev. Sci. Instrum. **70**, 175-177 (1999).

Lee, S.-H., C.F. Majkrzak, S.K. Sinha, C. Stassis, H. Kawano, G.H. Lander, P.J. Brown, H.F. Fong, S.-W. Cheong, H. Matsushita, K. Yamada, Y. Endoh, "Search for Orbital Moments in Underdoped Cuprate Metals - A Sisyphian Task," Phys. Rev. B **60**, 10405-10417 (1999).

Lee, W.-K., P. Fernandez, D. M. Mills, "Performance Limits of Direct Cryogenically Cooled Silicon Monochromators - Experimental Results at the APS," J. Synchrotron Rad. **7**, 12-17 (2000).

Leupold, O., A.I. Chumakov, E.E. Alp, W. Sturhahn, A.Q.R. Baron, "Noniron Isotopes," Hyperfine Interact. **123/124**, 611-631 (1999).

Levine, Z.H., A.R. Kalukin, S.P. Frigo, I. McNulty, M. Kuhn, "Tomographic Reconstruction of an Integrated Circuit Interconnect," Appl. Phys. Lett. **74**, 150-152 (1999).

Levine, Z.H., A.R. Kalukin, M. Kuhn, S.P. Frigo, I. McNulty, C.C. Retsch, Y. Wang, U. Arp, T.B. Lucatorto, B.D. Ravel, C. Tarrio, "Tomography of Integrated Circuit Interconnect with an Electromigration Void," J. Appl. Phys. **87**, 4483-448 (2000).

Liu, C., J. Erdmann, J. Maj, A. Macrander, "Thickness Determination of Metal Thin Films with Spectroscopic Ellipsometry for X-ray Mirro and Multilayer Applications," J. Vac. Sci. Technol. A **17**, 2741-2748 (1999).

Liu, C., J. Erdmann, A. Macrander, "*In situ* Spectroscopic Ellipsometry as a Surface Sensitive Tool to Probe Thin Film Growth," Thin Solid Films **356**, 41-48 (1999).

Ma, Q., D.C. Mancini, R.A. Rosenberg, "Synchrotron-Radiation-Induced Anisotropic Wet Etching of GaAs," Appl. Phys. Lett. **75**, 2274-2276 (1999).

Ma, Q., N. Moldovan, D.C. Mancini, R.A. Rosenberg, "Synchrotron-Radiation-Induced, Selective-Area Deposition of Gold on Polyimide from Solution," Appl. Phys. Lett. **76**, 2014-2016 (2000).

Ma, Q., N. Moldovan, D.C. Mancini, R.A. Rosenberg, "Sample size effect in photoelectrochemical etching of n-GaAs," Appl. Phys. Lett. **77**, 1319-1321 (2000).

Macrander, A.T., J. Als Nielsen, C. Liu, S. Krasnicki, J. Maj, D. Mancini, J. Erdmann, P. Gaarde, "Laterally Graded Multilayer Double-Monochromator," SPIE Proc. **3773** (SPIE, 1999) pp. 100-106.

Macrander, A.T., C. Liu, R. Csencsits, R. Cook, M. Kirk, R. Headrick, "Roughness in Sputtered Multilayers Analyzed by Transmission Electron Microscopy and X-ray Diffuse Scattering," Physica B **283**, 157-161 (2000).

Marasinghe, G.K., M. Karabulut, C.S. Ray, D.E. Day, P.G. Allen, J.J. Bucher, D.K. Shuh, Y. Badyal, M.L. Saboungi, M. Grimsditch, S. Shastri, D.R. Haeffner, "Effects of Nuclear Waste Components on Redox Equilibria, Structural Features, and Crystallization Characteristics of Iron Phosphate Glasses," Ceram. Trans. **93**, 195-202 (1999).

Margulies, L., M.J. Kramer, R.W. McCallum, S. Kycia, D.R. Haeffner, J.C. Lang, A.I. Goldman, "A New High Temperature Furnace for Structural Refinement by Powder Diffraction in Controlled Atmospheres Using Synchrotron Radiation," Rev. Sci. Instrum. **70**, 3554-3561 (1999).

Matkin, L.S., H.F. Gleeson, P. Mach, C.C. Huang, R. Pindak, G. Srajer, J. Pollmann, J. W. Goodby, M. Hird, A. Seed, "Resonant X-ray Scattering at the Se Edge in Liquid Crystal Free-Standing Films and Devices," Appl. Phys. Lett. **76**, 1863-1865 (2000).

McPherson, A., J. Wang, P.L. Lee, D.M. Mills, "A New High-Speed Beam Chopper for Time-Resolved X-ray Studies," J. Synchrotron Rad. **7**, 1-4 (2000).

Milton, S.V., S.G. Biedron, P. Den Hartog, J.W. Lewellen, E.R. Moog, A. Nassiri, G. Travish, "The APS SASE FEL: Status and Commissioning Results," Proc. 1999 Particle Accelerator Conference **4**, A. Luccio and W. MacKay, eds. (IEEE, 1999) pp. 2483-2485.

Milton, S.V., N.D. Arnold, C. Benson, S. Berg, W. Berg, S.G. Biedron, Y.C. Chae, E.A. Crosbie, G. Decker, B. Deriy, R.J. Dejus, P. Den Hartog, R. Dortwegt, M. Erdmann, Z. Huang, H. Friedsam, H.P. Freund, J.N. Galayda, E. Gluskin, G.A. Goeppner, A. Grelick, J. Jones, Y. Kang, K.J. Kim, S. Kim, K. Kinoshita, R. Lill, J.W. Lewellen, A.H. Lumpkin, G.M. Markovich, O. Makarov, E.R. Moog, A. Nassiri, V. Ogurtsov, S. Pasky, J. Power, B. Tieman, E. Trakhtenberg, G. Travish, I. Vasserman, N. Vinokurov, D.R. Walters, J. Wang, X.J. Wang, B. Yang, S. Xu, "The FEL Development at the Advanced Photon Source," SPIE Proc. **VOL ?** (SPIE, 1999) pp. 86-95.

Milton, S.V., E. Gluskin, S.G. Biedron, R.J. Dejus, P.K. Den Hartog, J.N. Galayda, K. J. Kim, J.W. Lewellen, E.R. Moog, V. Sajaev, N.S. Sereno, G. Travish, N.A. Vinokurov, N. D. Arnold, C. Benson, W. Berg, J.A. Biggs, M. Borland, J.A. Carwardine, Y.C. Chae, G. Decker, B.N. Deriy, M.J. Erdmann, H. Friedsam, C. Gold, A.E. Grelick, M.W. Hahne, K.C. Harkay, Z. Huang, E.S. Lessner, R.M. Lill, A.H. Lumpkin, O.A. Makarov, G.M. Markovich, D. Meyer, A. Nassiri, J.R. Noonan, S.J. Pasky, G. Pile, T.L. Smith, R. Soliday, B.J. Tieman, E.M. Trakhtenberg, G.F. Trento, I.B. Vasserman, D.R. Walters, X.J. Wang, G. Wiemerslage, S. Xu, B.X. Yang, "Observation of Self-Amplified Spontaneous Emission and Exponential Growth at 530 nm," Phys. Rev. Lett. **85**, 988-991 (2000).

Moldovan, N., "Deformations and Stress in PMMA during Hard X-ray Exposure for Deep Lithography," SPIE Proc. **3875** (SPIE, 1999) p. 155.

Montano, P.A., A.T. Macrander, "Inelastic X-ray Scattering Study of Cr (110): From Low Momentum Transfer to the Compton Scattering Limit," J. Phys. Chem. Solids **61**, 415-418 (2000).

Mooney, T.M., N.D. Arnold, E. Boucher, B.-C. Cha, K. A. Goetze, M.R. Kraimer, M.L. Rivers, R.L. Sluiter, J.P. Sullivan, D.B. Wallis, "EPICS and its Role for Data Acquisition and Beamline Control," AIP Conf. Proc.: Synchrotron Radiation Instrumentation Vol. 521, Pianetta, J. Arthur, and S. Brennan, eds. (AIP, 2000) pp. 322-327.

Nelson, C.S., G. Srajer, J.C. Lang, C.T. Venkataraman, S.K. Sinha, H. Hashizume, N. Ishimatsu, N. Hosoito, "Charge-Magnetic Roughness Correlations in an Fe/Gd Multilayer," Phys. Rev. B **60**, 12234-12238 (1999).

Osgood III, R.M., S.K. Sinha, J.W. Freeland, Y.U. Idzerda, S.D. Bader, "X-ray Scattering from Magnetically and Structurally Rough Surfaces," J. Magn. Magn. Mater. **198-199**, 698-702 (1999).

Petkov, V., S.J L. Billinge, S. D. Shastri, B. Himmel, "Polyhedral Units and Network Connectivity in Calcium Aluminosilicate Glasses from High-Energy X-ray Diffraction," Phys. Rev. Lett. **85**, 3436-3439 (2000).

Petkov, V., S.J.L. Billinge, J. Heising, M.G. Kanatzidis, S. Shastri, S. Kycia, "High Real-Space Resolution Structure of Materials by High-Energy X-ray Diffraction," Mat. Res. Soc. Symp. Proc. **590**, S.R. Stock, S.M. Mini, and D.L. Perry, eds. (MRS, 2000) pp. 151-156.

Pisharody, M., E. Semones, P.K. Job, "Dose Measurements of Bremsstrahlung-Produced Neutrons from Thick Targets," Nucl. Instrum. Methods A **430**, 542-558, (1999).

Pollmann, J., G. Srajer, J. Maser, J.C. Lang, C.S. Nelson, C.T. Venkataraman, E.D. Isaacs, "Characterization of a Microfocused Circularly Polarized X-ray Probe," Rev. Sci. Instrum. **71**, 2386-2390 (2000).

Powell, C.F., Y. Yue, R. Poola, J. Wang, "Time-Resolved Measurements of Supersonic Fuel Sprays Using Synchrotron X-rays," J. Synchrotron Rad. **7**,. 356-360 (2000).

Retsch, C.C., Y. Wang, S.P. Frigo, I. McNulty, L.B. Lurio, G.B. Stephenson, "Effect of Focusing Optics on X-ray Speckle Contrast," AIP Conf. Proc.: Synchrotron Radiation Instrumentation Vol. 521, P.Pianetta, J. Arthur, and S. Brennan, eds. (AIP, 2000) pp. 123-127.

Röhlsberger, R., W. Sturhahn, T.S. Toellner, K.W. Quast, P. Hession, M. Hu, J. Sutter, E.E. Alp, "Phonon Damping in Thin Films of Fe," J. Appl. Phys. **86**, 584-587 (1999).

Röhlsberger, R., W. Sturhahn, T.S. Toellner, K.W. Quast, E.E. Alp, A. Bernhard, J. Metge, R. Rüffer, E. Burkel, "Vibrational Density of States of Thin Films Measured by Inelastic Scattering of Synchrotron Radiation," Physica B **263-264**, 581-583 (1999).

Röhlsberger, R., E.E. Alp, E. Gerdau, O. Leopold, K.W. Quast, R. Rüffer, W. Sturhahn, T.S. Toellner, E. Burkel, "Techniques for Inelastic X-ray Scattering with μeV-Resolution," Physica B **263-264**, 574-576 (1999).

Röhlsberger, R., T. Toellner, W. Sturhahn, K.W. Quast, E.E. Alp, A. Bernhard, E. Burkel, O. Leupold, E. Gerdau, "Coherent Resonant X-ray Scattering from a Rotating Medium," Phys. Rev. Lett. **84**, 1007-1010 (2000).

Rosenkranz, S., R. Osborn, J. F. Mitchell, L. Vasiliu-Doloc, J. W. Lynn, S. K. Sinha, "Spin Correlations of the Magnetoresistive Bilayer Manganite $La_{1.2}Sr_{1.8}Mn_2O_7$," Int. J. Mod. Phys. B **13**, 3820-3822 (1999).

Schwoerer-Böhning, M., A.T. Macrander, "Phonons in Large-Band-Gap Materials," J. Phys. Chem. Solids **61**, 485-487 (2000).

Sepiol, B., M. Kaisermayr, H. Thiess, G. Vogl, E.E. Alp, W. Sturhahn, "Quasielastic Scattering of Synchrotron Radiation from Non-Resonant Atoms," Hyperfine Interact. **126**, 329-333 (2000).

Shu, D., P.K. Job, J. Barraza, T. Cundiff, T.M. Kuzay, "CVD-Diamond-Based Position Sensitive Photoconductive Detector for High-Flux X-rays and Gamma Rays," Proc. 1999 Particle Accelerator Conference **3**, A. Luccio and W. MacKay, eds. (IEEE, 1999) pp. 2090-2092.

Shu, D., R. Varma, S. Krasmicki, S. Sinha, "Design of a Miniature Hydraulic Compression Load Frame for Microdiffraction Tests at the Advanced Photon Source," AIP Conf. Proc.: Synchrotron Radiation Instrumentation Vol. 521, P. Pianetta, J. Arthur, and S. Brennan, eds. (AIP, 2000) pp. 198-203.

Shu, D., T.S. Toellner, E.E. Alp, "Design of a High-Resolution High-Stability Positioning Mechanism for Crystal Optics," AIP Conf. Proc.: Synchrotron Radiation Instrumentation Vol. 521, P. Pianetta, J. Arthur, and S. Brennan, eds. (AIP, 2000) pp. 219-224.

Shvyd'ko, YuV., M. Lerche, J. Jäschke, M. Lucht, E. Gerdau, M. Gerken, H.D. Rüter, H.-C. Wille, P. Becker, E.E. Alp, W. Sturhahn, J. Sutter, T.S. Toellner, "Gamma-Ray Wavelength Standard for Atomic Scales," Phys. Rev. Lett. **85**, 495-498 (2000).

Sinha, S.K., "New Developments in the Application of Synchrotron Radiation to Material Science," Jpn. J. Appl. Phys. **38**, 1-7 (1999).

Sinha, S.K., "Small-Angle Scattering from Porous Materials," in *Experimental Methods in the Physical Sciences*, Vol. 35, Po-Zen Wong, ed., (Academic Press, 1999) pp. 223-262.

Sinha, S.K., "Physics Research Opportunities with XFEL's," Synchrotron Radiation Instrumentation: Eleventh US National Conference, P. Pianetta et al., eds. (AIP, 2000) pp. 435-440.

Srajer, G., C.J. Yahnke, D.R. Haeffner, D.M. Mills, L. Assoufid, B.N. Harmon, Z. Zuo, "Magnetic Compton Scattering Studies of the Invar Alloy Fe_3Pt," J. Phys. Condens. Matter **11**, L253-L260 (1999).

Smither, R.K., D.E. Roa, "Crystal Diffraction Lens for Medical Imaging," Medical Imaging 2000: Physics of Medical Imaging, SPIE Proc. Vol. 3977, J.T. Dobbins III and J. M. Boone, eds. (SPIE, 2000) pp. 342-352.

Solak, H.H., Y. Vladimirsky, F. Cerrina, B. Lai, W. Yun, Z. Cai, P. Ilinski, D. Legnini, W. Rodrigues, "Measurement of Strain in Al-Cu Interconnect Lines with X-ray Microdiffraction," J. Appl. Phys. **86**, 884-890 (1999).

Srajer, G., C.J. Yahnke, D.R. Haeffner, D.M. Mills, L. Assoufid, B.N. Harmon, Z. Zuo, "Magnetic Compton Scattering Studies of the Invar Alloy Fe_3Pt," J. Phys. Condens. Matter **11**, L253-L260 (1999).

Stepanov, S.A., S.K. Sinha, "X-ray Resonant Reflection from Magnetic Multilayers: Recursion Matrix Algorithm," Phys. Rev. B **61**, 15302-15311 (2000).

Strey, H.H., J. Wang, R. Podgornik, A. Rupprecht, L. Yu,V. A. Parsegian, E.B. Sirota, "Refusing to Twist: Demonstration of a Line Hexatic Phase in DNA Liquid Crystals," Phys. Rev. Lett. **84**, 3105-3108 (2000).

Sturhahn, W., A. Chumakov, "Lamb-Mossbauer Factor and Second-Order Doppler Shift from Inelastic Nuclear Resonant Absorption," Hyperfine Interact. **123**, 809-824 (1999).

Sturhahn, W., V.G. Kohn, "Theoretical Aspects of Incoherent Nuclear Resonant Scattering," Hyperfine Interact. **123**, 367-399 (1999).

Sturhahn, W., R. Röhlsberger, E.E. Alp, T. Ruckert, H. Schrör, W. Keune, "Phonon Density of States in Fe/Cr(0 0 1) Superlattices and Tb-Fe Thin-Film Alloys," J. Magn. Magn. Mater. **198-199**, 590-592 (1999).

Sturhahn, W., "CONUSS and PHOENIX: Evaluation of Nuclear Resonant Scattering Data," Hyperfine Interact. **125**, 149-172 (2000).

Su, X., C. Stagarescu, G. Xu, and D. E. Eastman, I. McNulty, S. P. Frigo, Yuxin Wang, and Cornelia C. Retsch, I. C. Noyan and C.-K. Hu, "Quantitative Nanoscale Metrology Study of Cu/SiO_2 Interconnect Technology Using Transmission X-ray Microscopy," Appl. Phys. Lett. 77, 3465-3467 (2000).

Tajiri, G., W.-K. Lee, P.B. Fernandez, D.M. Mills, L.A. Assoufid, F. Amirouche, "Cryogenically Cooled Silicon Monochromator Thermal Distortion Predictions," AIP Conf. Proc.: Synchrotron Radiation Instrumentation Vol. 521, P. Pianetta, J. Arthur, and S. Brennan, eds. (AIP, 2000) pp. 299-303.

Takacs, P.Z., E.L. Church, C.J. Bresloff, L. Assoufid, "Improvements in the Accuracy and the Repeatability of Long Trace Profiler Measurements," Appl. Opt. **38**, 5468-5479 (1999).

Toellner, T.S., "Monochromatization of Synchrotron Radiation for Nuclear Resonant Scattering Experiments," Hyperfine Interact. **125**, 3-28 (2000).

Tolan, M., O. Seeck, J. Wang, S.K. Sinha, M. Rafailovich, and J. Sokolov, "X-ray Scattering from Polymer Films," Physica B **283**, 22 (2000).

Trakhtenberg, E.M., V. Tcheskidov, P.K. Den Hartog, B. Deriy, M. Erdmann, O. Makarov, E.R. Moog, "A New Gap Separation Mechanism for APS Insertion Devices," AIP Conf. Proc.: Synchrotron Radiation Instrumentation Vol. 521, P. Pianetta, J. Arthur, and S. Brennan, eds. (AIP, 2000) pp. 363-367.

Trenkler, J., H. Abe, P. Wochner, D. Haeffner, J. Bai, H. D. Carstanjen, S. C. Moss, "Change from a Bulk Discontinuous Phase Transition in V[sub2]H to a Continuous Transition in a Defective Near-Surface Skin Layer," Model. Simul. Mater. Sci. Eng. **8**, 269-275 (2000).

Vasiliu-Doloc, L., S. Rosenkranz, R. Osborn, S.K. Sinha, J.W. Lynn, J. Mesot, O. Seeck, G. Preosti, A.J. Fedro, J.F. Mitchell, "Charge Melting and Polaron Collapse in $La_{1.2}Sr_{1.8}Mn_2O_7$," Phys. Rev. Lett. **83**, 4393-4396 (1999).

Vasserman, I.B., R.J. Dejus, P.K. Den Hartog, M. Erdmann, E. Gluskin, E.R. Moog, E.M. Trakhtenberg, "Magnetic Measurements and Tuning of Undulators for the APS FEL Project," Proc. 1999 Particle Accelerator Conference **4**, A. Luccio, and W. MacKay, eds. (IEEE, 1999) pp. 2489-2491.

Wang, J., M. Tolan, O.H. Seeck, S.K. Sinha, O. Bahr, M.H. Rafailovich, J. Sokolov, "Surfaces of Strongly Confined Polymer Thin Films Studied by X-ray Scattering," Phys. Rev. Lett. **83**, 564-567 (1999).

Wang, Y., F. DeCarlo, I. Foster, J. Insley, C. Kesselman, P. Lane, G. von Laszewski, D. Mancini, I. McNulty, M.-S. Su, B. Tieman, "A Quasi-Realtime X-ray Microtomography System at the Advanced Photon Source," SPIE Proc. **3772** (SPIE, 1999) pp. 318-327.

Wassermann, S.R., P.G. Allen, D.K. Shuh, J.J. Bucher, N.M. Edelstein, "EXAFS and Principal Component Analysis: A New Shell Game," J. Synchrotron Rad. **6**, 284-286 (1999).

Winn, B., H. Ade, C. Buckley, M. Feser, M. Howells, S. Hulbert, C. Jacobsen, K. Kaznacheyev, J. Kirz, A. Osanna, J. Maser, I. McNulty, J. Miao, T. Oversluizen, S. Spector, B. Sullivan, Yu Wang, S. Wirick, H. Zhang, "Illumination for Coherent Soft X-ray Applications: The New X1A Beamline at the NSLS," J. Synchrotron Rad. **7**, 395-404 (2000).

Yu, L.H., M. Babzien, I. Ben-Zvi, A. Douryan, W. Graves, E. Johnson, S. Krinsky, R. Malone, I. Pogorelsky, J. Skaritka, G. Rakowsky, L. Solomon, X.J. Wang, M. Woodle, V. Yakimenko, S.G. Biedron, J.N. Galayda, V. Sajaev, I. Vasserman, "The Status of the High-Gain Harmonic Generation Free-Electron Laser Experiment at the Accelerator Test Facility," Proc. 1999 Particle Accelerator Conference **4**, A. Luccio and W. MacKay, eds. (IEEE, 1999) pp. 2471-2473.

Yu, L.H., M. Babzien, I. Ben Zvi, L.F. DiMauro, A. Doyuran, W. Graves, E. Johnson, S. Krinsky, R. Malone, I. Pogorelsky, J. Skaritka, Rakowsky, L. Solomon, X.J. Wang, M. Woodle, V. Yakimenko, S.G. Biedron, J.N. Galayda, E. Gluskin, J. Jagger, V. Sajaev, I. Vasserman, "High-Gain Harmonic-Generation Free-Electron Laser," Science **289**, 932-934 (2000).

Yun, W., B. Lai, Z. Cai, J. Maser, D. Legnini, E. Gluskin, Z. Chen, A.A. Krasnoperova, Y. Vladimirsky, F. Cerrina, E. Di Fabrizio, M. Gentili, "Nanometer Focusing of Hard X-rays by Phase Zone Plates," Rev. Sci. Instrum. **70**, 2238-2241 (1999).

Yun, W., B. Lai, A.A. Krasnoperova, E. Di Fabrizio, Z. Cai, F. Cerrina, Z. Chen, M. Gentili, E. Gluskin, "Development of Zone Plates with a Blazed Profile for Hard X-ray Applications," Rev. Sci. Instrum. **70**, 3537-3541 (1999).

Zhang, R.-G., G. Evans, F.J. Rotella, E.M. Westbrook, D. Beno, E. Huberman, A. Joachimiak, F.R. Collart, "Characteristics and Crystal Structure of Bacterial Inosine-5-Monophospahate Dehydrogenase," Biochemistry-US **38**, 4691-4700 (1999).

Zhang, X., H. Solak, F. Cerrina, B. Lai, Z. Cai, P. Ilinski, D. Legnini, W. Rodrigues, "X-ray Microdiffraction Study of Cu Interconnects," Appl. Phys. Lett. **76**, 315-317 (2000).

Appendix 2

1999-2000 Presentations by XFD and UPD Staff

Alp, E.E.,International Conference on Applications of Mossbauer Effect, Aug. 29- Sept. 3, 1999, Garmisch-Partenkirchen, Germany

Alp, E.E., Scientific Program at SESAME: A Synchrotron Radiation Source for the Middle East, Aug. 21, 1999, BESSY, Berlin, Germany

Alp, E.E., Inelastic X-Ray Scattering Workshop, Jan 21, 2000, Argonne National Laboratory, Argonne, IL

Alp, E.E., Workshop on Structural Biology at SESAME, April 17-20, 2000, Athens, Greece

Alp, E.E., Festschrift in honor of Dr. Sunil Sinha, May 2, 2000, Argonne, Illinois

Alp, E.E., Workshop on Experiments at New Generation Synchrotron Machines, May 18, 2000, Leuven, Belgium

Alp, E.E., Workshop on Surface and Thin Films Studied by Synchrotron Radiation, May 19, 2000, Leuven, Belgium

Alp, E.E., Euro-School on Dynamics of New Materials, 28-Aug. 28 - Sept. 8, 2000, Warnemunde, Germany

Alp, E.E., Festcolloqium to honor Prof. E. Gerdau, University of Hamburg, Sept. 9, 2000, Hamburg, Germany

Alp, E.E., Workshop on Materials Science Beamlines at SESAME, Sept. 21-22, 2000, Ankara, Turkey

Alp, E.E., Energy Recovery Linac Workshop, Dec. 2-3, 2000, Cornell University, Ithaca, NY

Chu, Y., "Surface X-ray Scattering Studies of Conducting Ruthenium Oxide under Electrochemical Control," Sixth International Conference on Surface X-ray and Neutron Scattering, Sept. 1999, Noordwijkerhout, The Netherlands

Chu, Y., "Novel Diffraction Technique for Measuring Strain," SRI-CAT Annual Meeting, Oct. 2000, APS, Argonne National Laboratory, Argonne, IL

DeCarlo, F., "The Message Passing Interface (MPI) Standard: A Tool for X-ray Tomography Reconstruction," SRI-CAT Meeting, May 2000, APS, Argonne National Laboratory, Argonne, IL

DeCarlo, F., "X-ray Tomography at 2-BM," SRI-CAT Annual Meeting, Oct. 2000, APS, Argonne National Laboratory, Argonne, IL

DeCarlo, F., "Quasi-Real-Time Reconstruction X-ray Tomography at 2BM," PRT Organizing Meeting for the ALS Tomography Project, Dec. 2000, Lawrence Berkeley National Laboratory

Dejus, R.J., "A Linear Integral-Equation-Based Computer Code for Self-Amplified Spontaneous Emission Calculations of Free-Electron Lasers," FEL99, Aug. 23-28, 1999, Hamburg, Germany

Dejus, R.J., "Calculations of the Self-Amplified Spontaneous Emission Performance of a Free-Electron Laser," PAC99, Mar. 29 – Apr. 2, 1999, New York City, NY

Freeland, J., "Understanding Correlations between Chemical and Magnetic Interfacial Roughness," X-ray Dichroism Workshop, Aug. 1999, Argonne, IL

Freeland, J., "An Undulator Beamline for High-Resolution Intermediate-Energy (0.5 - 3 keV) Spectroscopy at the Advanced Photon Source," Synchrotron Radiation Instrumentation Conference, Oct. 1999, Stanford, CA

Freeland, J., "Exploring Magnetic Structures with Polarized X-ray Reflectivity," Spallation Neutron Source- Reflectivity Workshop, May 2000, Argonne, IL

Frigo, S., "Two and Three Dimensional Imaging of Buried Integrated Circuit Components," Auburn University, March 4, 1999, Auburn, AL

Frigo, S., "Neutral Desorption Products Produced by Molecular Core Excitation," APS Annual Meeting, March 21, 1999, Atlanta, GA

Frigo, S., "Two and Three Dimensional Imaging of Buried Integrated Circuit Components," APS Annual Meeting, March 23, 1999, Atlanta, GA

Frigo, S., "Two and Three Dimensional Imaging of Buried Integrated Circuit Components," NSLS Users' Meeting, May 24, 1999, Brookhaven, NY

Frigo, S., "Overview of Integrated Circuit Imaging at Advanced Photon Source Beamline 2-ID-B," SRI 99 Conference, Oct. 11, 1999, Stanford, CA

Frigo, S., "Overview of Integrated Circuit Imaging at Advanced Photon Source Beamline 2-ID-B," SRI-CAT User's Meeting, Oct. 26, 1999, APS, Argonne National Laboratory, Argonne, IL

Gluskin, E., "Recent Experiment Results at APS ," Oct. 27-31, 1999, Brunnen, Switzerland

Gluskin, E., "Developments of Undulator Lines for 4th Generation SR Sources," April 7-13, 2000, Osaka, Japan

Gluskin, E., "Superconducting Undulator Prospects and Challenges for SASE FEL," July 8-12, 2000, Karlsruhe, Germany

Gluskin, E., "Predicted Performance of the LCLS X-Ray Diagnostics," Sept. 9-16, 2000, Arcidisso,Italy

Gluskin, E., "APS Experience with Long Undulator Lines," Nov. 5-15, 2000, Toyko, Japan

Lai, B., "Fluorescence Microanalysis Using a Zone-Plate-Based Microprobe," Workshop on APS Innovations in Instrumentation, Tenth Users Meeting for the Advanced Photon Source, May 2000, APS, Argonne National Laboratory, Argonne, IL

Lang, J., "Temperature Dependence of Rare Earth L Edge Dichroism," XAFS 99- Workshop on Dichroism, Aug. 1999, Argonne, IL

Lang, J., "X-rays and Magnetism," Bradley University Colloquium, Sept. 1999, Bradley University,

Makarov, O.A., "A New Gap Separation Mechanism for APS Insertion Devices," SRI99, Oct. 13-15, 1999, Stanford, CA

Maser, J., "X-ray Fluorescence Analysis Using Microprobes with Zone Plate Optics," Workshop on APS Innovations in Instrumentation, Tenth Users Meeting for the Advanced Photon Source, May 2000, APS, Argonne National Laboratory, Argonne, IL

McNulty, I., "Structure Determination by Flash X-ray Holography," BESAC Panel on Novel Coherent Light Sources, January 1999, DOE Headquarters, Gaithersburg, MD

McNulty, I., "X-ray Holography at the Advanced Photon Source," SPIE Chicago Regional Chapter Meeting, April 1999, Chicago, IL

McNulty, I., "Flash X-ray Holography," ICFA Advanced Beam Dynamics Workshop on Future Light Sources, April 1999, APS, Argonne National Laboratory, Argonne, IL

McNulty, I., "Realtime X-ray Microtomography," Advanced Photon Source Technical Working Group Meeting, April 1999, APS, Argonne National Laboratory, Argonne, IL

McNulty, I., "The 1-4 keV X-ray Microscopy and Coherence Program at APS Beamline 2-ID-B," National Synchrotron Light Source Annual Users Meeting, May 1999, NSLS, Brookhaven National Laboratory, Upton, NY

McNulty, I., "Nanotomography with Intermediate Energy X-rays at the APS," Sixth International Conference on X-ray Microscopy, Aug. 1999, University of California at Berkeley, Berkeley, CA

McNulty, I., "Coherent Imaging with LCLS," Workshop on the Science and Instrumentation for the LCLS, Oct. 1999, SLAC, Stanford, CA

McNulty, I., "Radiation Damage and Other Issues in Coherent Imaging with LCLS," LCLS Scientific Advisory Committee Workshop, March 2000, SLAC, Stanford, CA

Mills, D.M., "Some Thoughts on Photon Delay Techniques," Workshop on Methods and Instrumentation for an X-FEL, June 26 and 27, 2000, HASYLAB, Hamburg, Germany

Moog, E.R., "The Undulator Line for the Advanced Photon Source Free-Electron Laser", invited talk presented at CAARI 2000, the 16th International Conference on the Application of Accelerators in Research and Industry, Nov. 1-4, 2000, Denton, TX

Moog, E.R., Presentations on Insertion Device Magnetic Design and Tolerances at two LCLS Technical Advisory Committee Meetings, Feb. 11-12, 2000 and May 19-20, 2000

Moog, E.R., "Optimization of the Design for the LCLS Undulator Line", FEL2000, Aug. 13-18, 2000, Durham NC.

Moog, E.R., "APS Insertion Devices", seminar for ANL floor coordinators, Oct. 21, 1999, Argonne National Laboratory. Presentation was videotaped for later re-use with new coordinators.

Moog, E.R., "The APS FEL Undulator", ICFA 17th Advanced Beam Dynamics Workshop on Future Light Sources, April 6-9, 1999, Argonne, IL

Moog, E.R., "Radiation Measurements of the APS FEL," FEL99, Aug. 23-28, 1999, Hamburg, Germany. (Poster was prepared by Pat Den Hartog and won the award for best poster of the session!)

Mooney, T., "EPICS and its Role in Data Acquisition and Beamline Control," SRI 99 Meeting, Oct. 14, 1999, Stanford, CA

Retsch, C., "Effects of Focusing Optics on X-ray Speckle Contrast," SRI-CAT Meeting, Oct. 1999, Argonne National Laboratory, Argonne, IL

Retsch, C., "Effect of Focusing Optics on X-ray Speckle Contrast," SRI 99 Meeting, Oct. 1999, Stanford, CA

Shastri, S., " XFEL Event Rates for a Simple Multi-Photon Process: Two-Photon Absorption," Workshop on Nonlinear Optics, Quantum Optics, and Ultrashort Phenomena, July 13-14, 2000, DESY, Hamburg, Germany

Shastri, S., " Femtosecond X-Ray Dynamical Diffraction - XFEL Implications," SPIE session on X-Ray FEL Optics and Instrumentation, July 30-31, 2000, San Diego, CA

Shastri, S., " Femtosecond X-Ray Dynamical Diffraction," XFEL Workshop, Oct 12-13, 2000, Argonnne National Laboratory

Shu, D., "Front End and Beamline Instrumentation Development at the APS," Advanced Light Source, Oct. 12, 1999, LBNL, Berkeley, CA

Shu, D., "Preliminary Test of an Automated Precision Crystal Sample Mounting Mechanism," International Workshop on Bio-Sample Mounting Automation, May 11, 2000, SSRL, Stanford, CA

Shu, D., "Ultraprecision Motion Control Technique for High-Resolution X-ray Instrumentation," 1st International Workshop on Mechanical Engineering Design of Synchrotron Radiation Equipment and Instrumentation, July 14, 2000, PSI-SLS, Switzerland

Sinha, S., "Scientific Uses for the X-ray FEL," Jan 18, 1999, Leone Panel Mtg. for BESAC

Sinha, S., "Charge and Spin Ordering in CMR Materials," University of San Diego Physics Colloquium, Mar 11, 1999, San Diego, CA

Sinha, S., "Charge and Spin Ordering in CMR Materials," Amer. Phys. Society 1999 March Centennial Mtg., Mar 20-26, 1999, Atlanta, GA

Sinha, S., "Synchrotron X-ray Studies of Confined Fluids," NATO ASI Mtg., Apr 13, 1999, Geilo, Norway

Sinha, S., "X-ray and Neutron Scattering Studies of Magnetic Roughness in Thin Films," European Synchrotron Radiation Facility Physics Colloquium, Apr 28, 1999, Grenoble, France

Sinha, S., "Synchrotron Radiation Studies of Surface Fluctations and Surface Phase Transition in Liquids," Andriatico Research Conference, Jun 29, 1999, Trieste, Italy

Sinha, S., "Introduction to X-rays and Neutron Scattering," DOE Summer School, Argonne National Laboratory, July 16-17, 1999, Argonne, IL

Sinha, S., "Synchrotron X-ray Studies of Confined Fluids," Complex Materials Conference, Aug 22-27, 1999, Santa Barbara, CA

Sinha, S., "Spin and Charge Ordering in Layered Manganites," University of Illinois, Chicago Physics Colloquium, Oct 8, 1999, Chicago, IL

Sinha, S., "Spin and Charge Ordering in Layered Manganites." RISO National Laboratory, Oct 19, 1999, Denmark

Sinha, S., "X-ray Studies from Surfaces and Thin Films," Workshop on Off-Specular Scattering, Jan 29-Feb 1, 2000, Abingdon, UK

Sinha, S., "Resonant Magnetic X-ray and Neutron Scattering from Rough Interfaces," 5th Int'l Conference on the Physics of X-ray Multilayer Structures, Mar 5-9, 2000, Chamonix Mont-Blanc, France

Sinha, S., "Spin and Charge Ordering in Layered Manganites," University of Minnesota Physics Colloquium, Apr 13, 2000, Minneapolis, MN

Sinha, S., "Synchrotron X-ray Studies of Confined Fluids," LANL Physics Colloquium, Apr 27, 2000, Albuquerque, NM

Sinha, S., "Impact of Neutron Scattering on Science and Society," SNS User Meeting, May 22, 2000, Washington, DC

Sinha, S., "Inelastic X-ray Scattering Lectures," DOE Summer School, Argonne National Laboratory, August 14-16, 2000, Argonne, IL

Sinha, S., "Inelastic X-ray Scattering Lectures," Euro Summer School 2000, Aug 28-30, 2000, Rostock, Germany

Sinha, S., "Resonant Magnetic Scattering from Thin Films," 19th European Crystallography Mtg., Aug 31-Sep 2, 2000, Nancy, France

Sinha, S., "X-ray and Neutron Scattering Studies of Magnetic Roughness in Thin Magnetic Films," American Vacuum Society Mtg., Oct 2-6, 2000, Boston, MA

Sinha, S., "Novel Applications of Synchrotron Radiation to Semi-Conductors," A.K. Ramdas Symposium, Purdue University, Oct 21-22, 2000, Lafayette, IN

Sinha, S., "Diffuse Magnetic X-ray Scattering from Magnetic Films," Nano-Magnetism Mtg., Nov 7-12, 2000, Santa Fe, NM

Sinha, S., "Synchrotron X-ray Studies of Molecular Ordering in Confined Liquids," Material Research Society's 2000 Fall Mtg., Nov 26-28, 2000, Boston, MA

Sinha, S., "What We can learn about Phonons from Inelastic X-ray Scattering," Synchrotron Radiation Research Center, Dec 6, 2000, Hsinchu, Taiwan

Sinn, H., "Inelastic X-ray Scattering Technique," EuroSchool 2000, Aug. 2000, Rostock, Germany

Srajer, G., "Investigating Magnetic Materials at the Advanced Photon Source," Workshop on Scientific Opportunities for Neutron Scattering at 30-Tesla, Jan. 14-15, 1999, Los Alamos, NM

Srajer, G., "Measurements of Magnetic Properties by X-rays," Department of Physics Seminar, March 5, 1999, Tulane University, New Orleans, LA

Srajer, G., "Magnetic Roughness Measurements at the Advanced Photon Source," Gordon Research Conference on X-ray Physics, July 29, 1999, Plymouth State College, NH

Srajer, G., "Interfacial Structure and Magnetism in an Fe/Gd Multilayer," Workshop on X-ray Dichroism, Aug. 28, 1999, Argonne National Laboratory, Argonne, IL

Srajer, G., "Measurements of Magnetic Properties Using X-rays," Department of Physics Seminar, Jan, 21, 2000, Purdue University, Lafayette, IN

Srajer, G., "Magnetic Domains Mapping," 10th APS User Meeting, May 2000, Argonne National Laboratory, Argonne, IL

Sturhahn, W., "Inelastic Nuclear Scattering Applications," National Conference on Synchrotron Radiation Instrumentation, Oct. 12-15, 1999, Stanford, CA

Sturhahn, W., "Focusing for and with NRS," Nuclear Resonance Scattering at the X-FEL, April 27-28, 2000, Hamburg, Germany

Sturhahn, W., "Sensivity Limits for NRIXS," Nuclear Resonance Scattering at the X-FEL, April 27-28, 2000, Hamburg, Germany

Sturhahn, W., "Nuclear Transitions with Short Lifetimes," Nuclear Resonance Scattering at the X-FEL, April 27-28, 2000, Hamburg, Germany

Sturhahn, W., "Interferometry with Nuclear Resonant Radiation," Nuclear Resonance Scattering at the X-FEL, April 27-28, 2000, Hamburg, Germany

Toellner, T., "Sub-meV Monochromators for X-FEL Sources," Workshop: Nuclear Resonant Scattering with X-FEL Radiation, April 27-28, 2000, HASYLAB, Hamburg, Germany

Vasserman, I., "Insertion Device Magnetic Measurements," LCLS Technical Advisory Committee Meeting, May 19-20, 2000

Wang, J., "Sprays Studied by Synchrotron X-rays," seminar, Department of Mechanical Engineering, University of Illinois, Jan. 2000, Chicago,.IL

Wang, J., "A Quantitative Measurement of Fuel Sprays Using Synchrotron X-rays," seminar, Corporate Research and Development, Robert Bosch GmbH, April 2000, Stuttgart, Germany

Wang, J., "A Quantitative Measurement of Fuel Sprays Using Synchrotron X-rays," seminar, Department of Aerospace and Mechanical Engineering, University of Missouri, April 2000, Columbia, MO

Wang, J., "The Characteristics of an X-ray Synchrotron Liquid Spectrometer," SNS Liquids Reflectometer Workshop, June 2000, Argonne, IL

Wang, Yu., "A Quasi-Realtime X-ray Microtomography System at the Advanced Photon Source," SPIE Annual Technical Symposium, Aug. 1999, San Diego, CA

Wang, Yu., "A Quasi-Realtime X-ray Microtomography System at the APS," Workshop on APS Innovations in Instrumentation, Tenth Users Meeting for the Advanced Photon Source, May 2000, APS, Argonne National Laboratory, Argonne, IL

Appendix 3
SRI CAT

SRI CAT Management

Executive Director	Director	Associate Director	CAT Manager	Secretary
Dennis M. Mills	Efim Gluskin	Deming Shu	Trudy Bolin	Linda Shoudis

Scientific Staff

Sector 1	Sector 2	Sector 3	Sector 4	Beamline Controls
Dean Haeffner	Ian McNulty	E. Ercan Alp	George Srajer	Tim Mooney
Peter Lee	Zhonghou Cai	Harold Sinn	John Freeland	
Wah Keat Lee	Yong Chu	Wolfgang Sturhahn	Jonathan Lang	**Instrumentation**
Armon McPherson	Francesco Decarlo	Tom Toellner	Mike Lehmuller	Pat Den Hartog
Tammy Middleton	Sean Frigo	Jiyong Zhao	Sunil Sinha	
Ali Mashayekhi	Peter Ilinski			
Sarvjit Shastri	Barry Lai			
Bob Smither	Dan Legnini			
Jin Wang	Derrick Mancini			
	Jörg Maser			
	Christian Roehrig			
	Shenglan Xu			

External Developers

J. Arthur	SSRL	D. Bilderback	CHESS
R. Colella	Purdue	S. Durbin	Purdue
T. Jach	NIST	S. Moss	Univ. Houston
A. Thompson	LBNL	Q. Shen	CHESS
A. Stampfl	Australia/ASRP		

Scientific Members

T.W. Barbee	LLNL	F. Cerrina	Univ. Wisconsin/Madison
C.T. Chen	SRRC, Taiwan	T.C. Chang	Univ. Illinois
R. Deslattes	NIST	D. Ederer	Tulane Univ.
B. Fultz	Cal. Tech.	M. Howells	ALS/LBNL
G. Ice	ORNL	E. Isaacs	Lucent Technologies
N. Ishimatsu	Toyko Inst. Tech.	C. Jacobson	SUNY/Stony Brook
J. Kirz	SUNY/Stony Brook	O. Leupold	Univ. Hamburg
P. Montano	ANL/MSD	J. Mullen	Purdue
G. Neyes	Katholieke Univ. Leuven	P. Platzman	AT&T Bell Labs
R. Simmons	Univ. Illinois	J. Stohr	IBM/Almaden
J. Tischler	ORNL	J. Tobin	LLNL
J. Trebes	LLNL		